Tampere University

AYUSH MISHRA

Phosphate Glasses and Fibers as an Alternative to Silicate Bioactive Glasses

Tampere University Dissertations 120

Tampere University Dissertations 120

AYUSH MISHRA

Phosphate Glasses and Fibers as an Alternative to Silicate Bioactive Glasses

ACADEMIC DISSERTATION
To be presented, with the permission of
the Faculty of Medicine and Health Technology
of Tampere University,
for public discussion in the auditorium TB109
of Tietotalo, Korkeakoulunkatu 1, Tampere,
on 20th September 2019, at 12 o'clock.

ACADEMIC DISSERTATION
Tampere University, Faculty of Medicine and Health Technology
Finland

Responsible supervisor and Custos	Associate Prof. Jonathan Massera Tampere University Finland	
Supervisor(s)	Associate Prof. Jonathan Massera Tampere University Finland	
Pre-examiner(s)	Associate Prof. Ifty Ahmed University of Nottingham United Kingdom	Prof. Annelise Faivre Université de Montpellier France
Opponent(s)	Prof. Mario Affatigato Coe College United States of America	

The originality of this thesis has been checked using the Turnitin Originality Check service.

Cover design: Roihu Inc.

ISBN 978-952-03-1224-4 (print)
ISBN 978-952-03-1225-1 (pdf)
ISSN 2489-9860 (print)
ISSN 2490-0028 (pdf)
http://urn.fi/URN:ISBN:978-952-03-1225-1

PunaMusta Oy – Yliopistopaino
Tampere 2019

Abstract

The field of bioactive glasses started with the discovery of the first bioactive glass composition 45S5 or Bioglass® in 1969. In the 1980s, the glass particulates of 45S5 depicted the ability to induce osteogenesis, as opposed to the then prevalent bioinert metallic implants. Later, the dissolution products of 45S5, which was a silicate glass, were found to stimulate the genes in human osteoblasts and act as growth factors, providing signals to the cells. Over the years, other bioactive glass compositions such as 13-93 and BonAlive® (S53P4) were discovered, which were also silicate glasses. Even today, 45S5 remains the gold standard for bioactive glasses. However, in recent times, there has been a rise in the demand for more sophisticated implants, such as scaffolds made from polymer and glass, or only glass. Furthermore, bioactive glass fibers are also appealing to the researchers for mechanically reinforcing the scaffolds, owing to their better mechanical properties than polymers. However, in this regard, the silicate glasses are known to pose serious challenges to the researchers, due to their incongruent dissolution mechanism and poor thermal processability. Moreover, for short term applications, ranging from a few weeks to a few months, the degradation rate of the commercially available silicate glasses is considered too slow.

In light of the above facts, the main aims of this thesis are: (i) to develop new glasses within the phosphate glass family, which possess good thermal processability, have additional functionalities such as antimicrobial properties and invoke favorable cell response for developing novel biomaterials in future, and (ii) to develop glass fibers based on these compositions for advanced applications such as biosensing, and possessing decent mechanical properties for reinforcing composites.

To accomplish these objectives, a new series of phosphate glasses doped with metallic ions such as Ag, Cu and Fe was developed based on a promising phosphate glass composition studied earlier. These glasses were analyzed in terms of their structural, thermal and in-vitro dissolution properties. Furthermore, the antimicrobial properties of Ag and Cu glasses were also tested, relative to com-

mercial silicate bioactive glass. Then, preliminary cell culture tests were conducted using glass discs, and glass extracts (glass dissolution products containing cell culture medium). Moving forward, two approaches were taken simultaneously to improve the cell response to these glasses. Firstly, the glasses were subjected to a series of surface treatments to improve protein adhesion at their surface, which in-turn should play a role in improving the cell attachment at their surface. In the second approach, a small addition of borate at the expense of phosphate was done to increase the glass' resistance to aqueous dissolution. Cell culture tests were then performed using glass extracts obtained from the new borophosphate glasses, and cell viability and proliferation were assessed and cytotoxicity of the extracts obtained. Finally, newly developed single core and core-clad glass fibers were also studied in terms of their mechanical properties and their potential in biosensing.

The newly developed phosphate glasses depicted a high degree of thermal processability and promising in-vitro dissolution characteristics. The Ag and Cu glasses presented antimicrobial properties even superior to the commercially available S53P4 in eliminating *Staphylococcus epidermis*. The surface treatments performed on the glass discs revealed an improvement in the protein adhesion, which in-turn vastly improved the cell attachment at their surface. In the other approach to improve cell growth and proliferation in the glass extracts, a small addition of borate at the expense of phosphate resulted in an improved cell response to the glass extracts, barring that of the Cu-doped glass. Indeed, the undiluted Cu extract exhibited a much higher cytotoxicity than all the other glass extracts, and hence was toxic to cell survival. In the study on phosphate glass fibers, the core-clad fiber was found to be promising for biosensing, owing to its ability to guide light effectively and maintain decent mechanical properties in-vitro (up to 4 weeks, and ~6 weeks in TRIS buffer solution respectively).

In summary, phosphate glasses with favorable cell response were obtained by tailoring their composition and using suitable surface treatments. These glasses were found to possess favorable thermal properties for fiber drawing and scaffold sintering, and the fibers drawn from these glass compositions showed promise in biosensing. Furthermore, they possessed high mechanical strength, and in the future, they can be considered for reinforcing scaffolds. These new glasses and

glass fibers should pave the way for a new family of bioresorbable implants for a wide array of biomedical applications in future.

Preface

This study was carried out at Tampere University in the doctoral programme of the Faculty of Medicine and Health Technology. The project was financially supported by the Academy of Finland, through the Academy Research Fellow Grant (#275427) and the Initial Funding for Research Cost (#284492).

I would like to express my sincere gratitude to my supervisor, Assoc. Prof. Jonathan Massera for his guidance and support throughout the duration of my PhD project, and for giving me the opportunity to work under his supervision. I also wish to extend my gratitude to Prof. Minna Kellomäki and Dr. Miina Ojansivu, for their guidance and suggestions during my follow up group meetings. I would further like to thank Miina Ojansivu for helping me with cell culture experiments. I am also thankful to the pre-examiners of my thesis, Prof. Annelise Faivre and Assoc. Prof. Ifty Ahmed for their constructive criticism and feedback to help improve my thesis. I would like to further thank Prof. Delia Brauer and Prof. Johann Troles, and their research groups, for hosting me as a visiting researcher at their universities, and helping me with my research.

I would like to acknowledge my co-authors, Jean Rocherulle, Laeticia Petit, Maria Pihl, Martin Andersson, Turkka Salminen, Frederic Desevedavy, Frederic Smektala, Susanna Miettinen, Sari Vanhatupa and Reija Autio for their contributions to my research and sharing their expertise with me. I am also thankful to the present and former members of our “Glass group”, especially Jenna Tainio and Amy Nommeots-Nomm for creating a nice work atmosphere during the years. I also extend my thanks to everyone at the “Biomaterials group”, including the laboratory and technical personnel Suvi Heinämäki and Heikki Liejumäki for all the help over the years. A big cheers goes out to Aleksi, Janne, Mart and Inari for all the lunch talks and shared experiences. I am also grateful to Anna-Maija Honkala and Sari Kalliokoski, the laboratory personnel at the Adult Stem Cells group at Arvo, for training and helping me with the cell culture tests.

I am eternally grateful to my parents, and the rest of my family in India for their unending support. Thank you for not letting the long distance between us matter much during these years. Finally, my deepest gratitude goes out to my wife Priya, who has been my rock over the years, and the source of unconditional support. Cheers to my sister Amisha too, for sharing in this journey.

Tampere, August 2019

Ayush Mishra

Table of Contents

List of Publications

I A. Mishra, J. Rocherulle, J. Massera, Ag-doped phosphate bioactive glasses: Thermal, structural and in-vitro dissolution properties, Biomed. Glas. 2 (1) (2016) 38–48. doi:10.1515/bglass-2016-0005

II A. Mishra, L. Petit, M. Pihl, M. Andersson, T. Salminen, J. Rocherullé, J. Massera, Thermal, structural and in vitro dissolution of antimicrobial copper-doped and slow resorbable iron-doped phosphate glasses, J. Mater. Sci. 52 (15) (2017) 8957–8972. doi:10.1007/s10853-017-0805-3

III A. Mishra, M. Ojansivu, R. Autio, S. Vanhatupa, S. Miettinen, J. Massera, In-vitro dissolution characteristics and human adipose stem cell response to novel borophosphate glasses, J. Biomed. Mater. Res. - Part A. 107 (9) (2019) 2099–2114. doi:10.1002/jbm.a.36722

IV A. Mishra, F. Désévédavy, L. Petit, F. Smektala, J. Massera, Core-clad phosphate glass fibers for biosensing, Mater. Sci. Eng. C. 96 (2019) 458–465 doi:10.1016/j.msec.2018.11.038.

Unpublished manuscripts

I A. Mishra*, L. Azizi*, C. Palma*, N. B. Huynh, R. Rahikainen, P. Turkki, A. S. Ribiero, V. P. Hytönen, J. Massera “Surface modified phosphate glasses for improved protein adsorption and cell viability” (2019)

*authors contributed equally.

Author's contribution

I. The author was responsible for writing the paper, planning the work and analyzing the data with co-authors. The author also contributed partly to the manufacturing of the glasses used in this study. Further, the author was responsible for conducting all the experiments pertaining to the characterization of the glasses, except the SEM-EDS and ICP-OES analysis.

II. The author was responsible for writing the paper, planning the work and analyzing the data with co-authors. The author also contributed partly to the manufacturing of the glasses used in this study. Further, the author was responsible for conducting all the experiments pertaining to the characterization of the glasses, except the SEM-EDS and ICP-OES analysis, and the antimicrobial tests.

III. The author was responsible for writing the paper, planning the work and analyzing the data with co-authors. The author was solely responsible for manufacturing the glasses used in this study. Further, the author was responsible for conducting all the experiments pertaining to the characterization of the glasses, except the SEM-EDS analysis. The author also performed the cell culture tests reported in this study.

IV. The author was responsible for writing the paper, planning the work and analyzing the data with co-authors. Further, the author was responsible for conducting all the experiments pertaining to the in-vitro dissolution characteristics of the glass fibers, including the light loss experiments. The author also conducted the tests for obtaining the mechanical strength of the glass fibers.

V. The author was responsible for writing the paper, planning the work and analyzing the data with co-authors. Further, the author was partly responsible for manufacturing and surface functionalization of the glasses.

List of Symbols

η	refractive index
ρ	Density
μ	Micro
c	Concentration
m	mili
t	Time
x	Dopant metal ion concentration
D	Diffusivity
M	Mol/l
T_g	Glass transition temperature
T_x	Onset of crystallization temperature
ΔT	Thermal processing window
T_c	Crystallization temperature

List of Abbreviations

APTS	3-Aminopropyltriethoxysilane
BM	Basic Medium
BO	Bonding oxygen
CaP	Calcium phosphate
CD	Classification determinant
CFU	Colony forming unit
DMEM	Dulbecco's modified eagle medium
DNA	Deoxyribo nucleic acid
DTA	Differential thermal analysis
EthD-1	Ethdium homodimer-1
FDA	U.S. Food and Drugs Administration
FTIR-ATR	Fourier-transform infrared spectroscopy-Attenuated total reflection
HA	Hydroxyapatite
hASC	Human adipose stem cells
HCA	Carbonated hydroxyapatite

HLA-DR	Human leukocyte antigen – DR isotype
ICP-OES	Inductively coupled plasma - optical emission spectrometry
L/D	Live/dead
LDH	Lactase dehydrogenase
M_nO_m	Metal oxide
NBO	Non-bonding oxygen
PDMS	Polydimethylsiloxane
PG	Phosphate glasses
PGF	Phosphate glass fibers
PLA	Polylactic acid
RNC	Relative number of clusters
RTF	Relative total fluorescence
S. epidermis	*Staphylococcus epidermis*
SBF	Simulated body fluid
SEM	Scanning electron microscopy
SG	Silicate glasses

TRIS	tris(hydroxymethyl)aminomethane (IUPAC: 2-Amino-2-hydroxymethyl-propane-1,3-diol), or a buffer solution obtained using it
UV-Vis	Ultraviolet-visible
V_m	Molar volume
WA	Washed in acidic buffer solution
WAS	Washed in acidic buffer solution and silanized
WB	Washed in basic buffer solution
WBS	Washed in basic buffer solution and silanized
WN	Washed in neutral buffer solution
WNS	Washed in neutral buffer solution and silanized

1 Introduction

Biomaterials are defined as the materials used to replace or supplement the functions of living tissues [1]. The different kinds of biomaterials in use today are a) natural or synthetic polymers (like collagen or PLA respectively), b) metals (titanium), c) ceramics (such as calcium phosphate) and d) composites (for instance, scaffolds made from polymer and bioceramics). Among these, some composites and ceramics are known to be bioactive, i.e., they are able to illicit a specific biological response from the surrounding tissue, resulting in a bond between the tissue and the material [2,3]. In the 60's the discovery of the silicate-based glass 45S5 (known as Bioglass®) by Prof. Larry Hench led to extensive research in the field of bioactive glasses [4]. The main characteristics of Bioglass® were: a) unlike polymers and metals, its constituent ions were found in the body, hence inhibiting "foreign body reaction", and b) the ability to form a bone-like hydroxyapatite layer, which is the main mineral phase of natural bone tissue [4]. Cao et. al. and Hench et. al., later reported the use of Bioglass in treating broken bones [5,6]. Hench's study on Bioglass® have been comprehensively reviewed by Montazerian and Zanotto [7]. Another, bioactive silicate glass (SG), S53P4 (known as BonAlive®), discovered by Andersson et al. [8] was found to be osteostimulative and antimicrobial [9–12]. Consequently, SG remained at the forefront of bioactive glass research, and efforts were directed towards tailoring them for fiber drawing or powder sintering to meet the requirements for reinforced bioresorbable composites and bone tissue engineering [13–15]. However, further studies established that the crystallization kinetics of typical SG are unsuitable for hot processing [13,16]. Additionally, the incongruent dissolution mechanism of SG led to the remnants of bioactive SG 14 years post operation [17]. Consequently, over time, other glass types such as borate and phosphate came into reckoning.

In an attempt to overcome some of the SG drawbacks, new glass families have been investigated.

This thesis deals with phosphate and borophosphate glasses, and fibers intended for bone regeneration and biosensing respectively. Phosphate glasses (PG) are known to have a congruent degradation, and the degradation rate can be adjusted, from days to years to suit different applications, by varying the composition [18]. They have a high solubility towards metal ions, and metal oxide doped PG are used in a wide array of applications, such as vitrification of nuclear waste [19–22] to biocompatible glass and ceramics [23–27]. In view of these interesting properties, new doped PG with added functionalities, high thermal processability and favorable cell response are proposed here. Additionally, single core and core-clad PG fibers (PGF) are also reported to have potential in biosensing and as reinforcements in composites. The main drawbacks of the developed phosphate glasses and their fibers was the poor cell attachment at their surface and lack of significant protein adsorption. To enhance the biocompatibility of these glasses, two approaches were taken simultaneously. First, their compositions were modified by introducing boron into the network for enhanced durability, without compromising the thermal processability [28–32]. In the other approach, new surface modification methods were investigated to improve protein adsorption and cell attachment at their surface. The findings in these thesis pave way for a new family of biomaterials based on PG and PGF for a wide range of biomedical applications.

Broadly, this thesis is composed of a literature review, materials and methods, results, and discussion. In literature review, the state-of-the-art within the field of bioactive glasses is discussed, with a focus on the inherent differences between the properties of SG and PG. Furthermore, the use of bioactive glass fibers as reinforcements in composites and in biosensing is explored. Metal ions used in doping the glasses, and, surface treatments to confer additional functionalities to the glasses, are reviewed. The materials and methods section comprises of the protocols for obtaining the glasses and glass fibers, and the methods used for studying their properties. The results of characterization of the new glasses, cell culture and surface treatments for enhancing cell attachment are discussed. Finally, in Conclusions and Outlook, the findings of this thesis are summarized, with an eye towards the future.

2 Literature Review

2.1 Evolution of biomaterials

The state of the art in bone regeneration has been reviewed in detail by several researchers [33–35]. Autografts are still the gold standard today in bone regeneration [36], where the grafts are harvested from other sites of the patient's body, typically from the iliac crest. Autografts are however offset by limitations such as the need for an additional surgery, longer hospital stay, quantity restrictions, high cost in addition to the well documented discomfort to the patient [37–41]. An alternative to autografts are allografts, obtained from human cadavers or living donors. They are known to be less osteoinductive, lacking a cellular component, as the grafts are devitalized during irradiation or freeze drying after harvest [42]. Furthermore, allografts are known to suffer from immunogenicity and rejection reactions, potential transmission of diseases and cost [42,43]. Consequently, a surge in the development of new biomaterials has been witnessed over the years.

Despite sustaining a generally stable temperature and pH, the biological environment presents a highly hostile environment to foreign materials such as implants. Different biomaterials invoke different responses from the surrounding tissue, based on their function and/or reactivity, as reviewed earlier [44,45]. Bioinert materials are those that do not interact with surrounding tissue, such as metals and alloys like cobalt-chromium and stainless steel, and ceramics like alumina (Al_2O_3), zirconia (ZrO_2) [45]. For instance, dental implants are usually bioinert, made from materials like titanium, zirconium and roxolid,

and are biocompatible, corrosion-resistant, other than having favorable strength properties for being placed in oral cavity [44]. However, in post hip replacement with bioinert implants, problems like localized inflammation with tissue damage and bone degradation have surfaced [46]. This is indeed unfortunate given that hip replacement has been hailed as a high point in the field of orthopedics [47]. With the use of metal-on-metal implants for total hip replacement, patients reported severe pain at the implantation site and reduced range of motion. This was due to the release of wear particles from the implants as confirmed by the high metal concentration in patient's blood, which elicit adverse tissue reactions [48–50]. Consequently, the adverse reactions to metallic implants have been reported in the literature [51,52]. Bioactive coatings were developed to compensate for the inertness of metallic implants [53–60]. The major function of these coatings was to be osteoconductive and osteoinductive, and hence accelerate osteointegration. The development of bioactive coatings for orthopedic implants has been reviewed in detail by Zhang et al [61].

For applications where the implants were supposed to be temporary, bioresorbable and bioactive materials were developed. They are known to degrade and be disposed of by the patient's body, hence eliminating the need for a follow-up surgery to remove the implant. Natural polymers such as collagen, and synthetic polymers such as poly lactic acid (PLA), polyglycolic acid (PGA) are known to be bioresorbable, and have been reviewed in detail for biomedical applications [62–64]. Similarly, both α and β Tricalcium phosphate (TCP), Ca-P based ceramics with different dissolution rates are also bioresorbable material, popular as bone substitute/filler as they dissolve gradually while being replaced by regenerated bone [65–69]. While, bioresorbable bioceramics are known to release ions beneficial to the bone regeneration, they lack chemical interaction with the newly formed tissue. To increase the interaction between biomaterials and tissues, bioactive bioceramics were developed.

Hydroxyapatite (HA) is another Ca-P based bioceramic, which is known to be bioactive, i.e., it can bond to bone, and can demonstrate osteoinductivity depending on factors such as geometry and microporosity of the implant [70,71,80,81,72–79]. Similar to TCP, the in vivo and in vitro dissolution of HA is known to depend on the composition, crystallinity and pH of the solution [82–85]. Overall, HA has low resorbability compared to TCP and other biomaterials, with in-vitro dissolution studies showing nearly no dissolution of phase pure HA after 30 days in distilled water [86].. However, doping with Si has been shown to increase the resorbability and osteogenic properties of HA [87–89]. Conse-

quently, it is a popular biomaterial for use as a bone substitute, scaffold for tissue engineering, carrier for drug delivery and can be employed as porous or dense blocks, granules, paste, cement or coatings [90–93]. HA is classified as class B bioactive materials, meaning it is able to bond to the bone. However, pertaining to the high similarity between synthetic HA and natural HA, the HA reaction in vivo is slow and the new bone formation is slow and incomplete across the array. As the dissolution rate of HA is too slow and that of TCP is considered too fast, the common approach taken is to use a mixture of the two Ca-P ceramics to attain the desired dissolution rate [94–99]. Class A bioactive materials, such as the bioactive glass 45S5 discovered by Larry Hench, are known to bond rapidly to bone and to enhance bone proliferation. Bioactive glass are classified as class A bioactive materials, meaning that they are osteoinductive, and are able to induce bone growth even in non-bone sites [100]. Class A bioactive materials were also found to bond to the soft connective tissues as explained in [5,101–103].

2.2 Glass

Glass is a versatile material used in a wide range of applications from construction to photonics owing to its compositional freedom. SG are widely used in food and beverage container, windows or fiber optics. When used in harsh environment the higher durability of borosilicate glasses and its higher resistance to thermal cycles have been seen as an advantage and is nowadays the material of choice in laboratory/kitchen glassware, external lighting or industrial equipment. Hubert et al. reviewed the role of boron in SG, and summarized the various applications of borosilicate glasses in today's world [104]. Glass can also be shaped into lenses or fibers. Fibers have had a tremendous impact on communications, and glass and process development for optical fibers has been reviewed in detail by [105]. Indeed, the ability of glass to efficiently guide light over very long distances has revolutionized data transfer by encoding data into a light wave. However, one should remember that, at the start optical cable were developed for endoscopes to allow medical doctors to "see" inside the human body. Therefore, the use of glass in the medical field is not new [106].

While most of the glass research is focused on SG, other type of glasses have emerged with time. Some exotic compositions, like the chalcogenide glasses have had tremendous impact on night-vision pertaining to their transparency in the infrared. Tellurite based glasses have been developed for their ability to efficiently guide light in the mid-infrared region. PG and glass-ceramics have found great application as ion hosts for

solid state lasers or as low temperature sealing glasses. However all these glasses also found application in the medical field. IR and MIR transparent glasses, despite possessing toxic elements, have been used as sensors, as it allows recording fingerprints of most biomolecules [107]. The use of PG in place of calcium phosphate crystalline materials also seemed as an obvious path to follow in order to replace the use of the existing TCP and HA. PG could also have potential to substitute the well-known and FDA approved bioactive SG glasses.

2.2.1 Bioactive Silicate glasses

2.2.1.1 Structure

The structural backbone of a typical SG structure is formed by amorphous SiO_4 tetrahedral network. These tetrahedra connect at the corners in different orientations to form a continuous 3D network, with the oxygen atoms acting as a bridge between them. The configuration around the silica atoms are expressed with a Q^n notation, with n indicating the number of bridging oxygen (BO) ranging from 0-4. Alkali and alkaline earth metals modify the properties of SG as they disrupt the network connectivity, by replacing BO with non-bridging oxygen (NBO), thereby opening up the structure. A typical SG network can be illustrated as in Figure-1. The strength of the metal-oxygen bond and the number

of NBOs dictate properties such as viscosity and chemical durability of the glass. Therefore, by controlling the concentration of glass modifier one can tailor the speed of glass dissolution in aqueous solution.

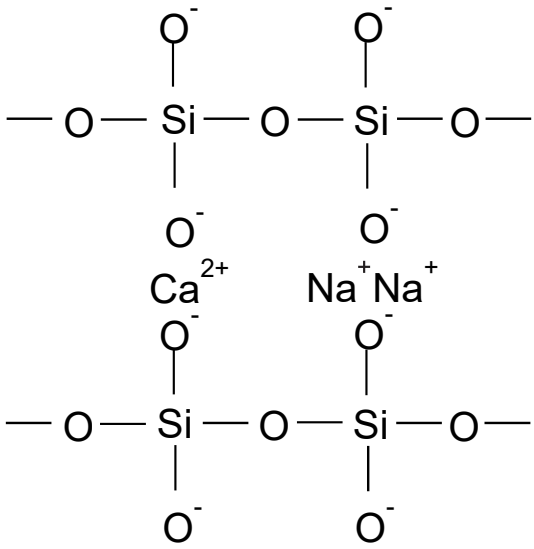

Figure 2.1 Schematic representation of silica chains in the structure of a typical SG [108]

2.2.1.2 Dissolution mechanism

Silicate bioactive glasses are normally 'invert' glasses, which are stabilized by the ionic interactions between the modifiers and NBOs. 'Invert' glasses are glasses with a low percentage of the network former, typically less than 50 mol% and high alkaline and alkaline earth content. For instance, the bioactive SG 45S5 is an invert glass with the composition 46.1SiO_2-2.6P_2O_5-24.4Na_2O-26.9CaO (mol%). The impact of other glass components on physical and chemical glass properties has been studied extensively in the past [109–111].

The glass dissolution mechanism reactions in aqueous solutions has been established in the past. [112,113,122,123,114–121]. While the reactions depend upon factors such as glass composition, type of solution, pH of the solution, surface area to volume ratio, there are two distinct types of dissolution mechanisms. Glasses may dissolve congruently, i.e., they maintain the same ratio of elements in the solution as the glass itself, or

incongruently, where some of the elements may leach preferentially [120]. SG are known to exhibit incongruent dissolution in aqueous media.

The glass reactions occurring at the glass' surface in aqueous solutions may be divided into primary and secondary reactions. The ion exchange, hydration and hydrolysis reactions are the primary reactions, whereas precipitation is considered a secondary reaction. These reaction steps, even though are listed sequentially, are known to be strongly coupled to each other[115,121,124]. These reactions of the dissolution of SG were described in detail by Hench [125], and can be summarized as:

Stage 1 Rapid exchange of ions between the glass network modifiers with H^+ from the solution. This leads to the hydrolysis of the silica groups, thereby forming silanol (Si-OH) groups at the glass' surface: The consumption of H^+ ions from the solution leads to an increase in the pH.

$$\mathrm{Si-O-Na^+ + H^+ \rightarrow Si-O-H^+ + Na^+(aq)}$$

Stage 2 The increase in the solution pH leads to an attack on the silica network, with the dissolved silica forming silicic acid ($Si(OH)_4$) in the solution. Furthermore, the creation of silanol groups at the surface continues.

$$\mathrm{Si-O-Si + H_2O \rightarrow Si-O-H + OH-Si}$$

Stage 3 An amorphous silica-rich layer depleted in Na^+ and Ca^{2+}, condenses and polymerizes at the surface of the glass.

Stage 4 Glass continues to dissolve, along with the migration of Ca^{2+} and $(PO_4)^{3-}$ from the glass as well as the solution through the silica-rich layer, leading to the formation of an amorphous calcium phosphate layer (ACP) at its surface.

Stage 5 Further dissolution of the glass, with the ACP layer incorporating $(OH)^-$ and $(CO_3)^{2-}$, leading to the formation of a carbonate substituted hydroxyapatite (HCA) layer.

In Stage 1, the reaction leads to a near instantaneous establishment of an electrochemical equilibrium of the glass surface with the aqueous solution [126–128]. The leaching of mobile ions such as Na leave the glass material more or less intact, while the charge balance is also maintained [120]. The mobility of the leaching ions is known to depend upon their field strength and radii, i.e., the charge to radius ratio. The higher this ratio is, the lower the mobility, for instance, glasses doped with K_2O were found to dissolve much

faster than those doped with Li_2O [119]. The ion exchange reaction is often described with Fick's law [129–131], which for one dimension can be stated as below:

$$\frac{dc}{dt} = \frac{d}{x}(D\frac{dc}{dx})$$

Where D stands for the diffusivity of the leaching ions. For a glass surface, the equation solves to a parabolic rate law, indicating that the amount of alkali dissolved is proportional to the square root of time [120]. However, as there are other reactions occurring simultaneously as well, the glass dissolution process and leaching of ions is not just governed by Fick's law [124].

In Stage 2, the excess OH^- ions in the solution due to the consumption of H^+ ions, act as a catalyst for network dissolution [132]. In alkaline conditions (pH<9), the hydrolysis reaction causes depolymerization of the silicate network. This reaction dominated by the nucleophilic attack of OH^- ions on the glass network leads to a more open glass structure, with formation of silanol groups. In Stage 3, the silanol groups react further to simultaneously form Si-O-Si groups due to repolymerization, as well as form soluble silica in the form of silicic acid. This also leads to the elimination of ion exchange sites [121]. Furthermore, as the solubility limit of the leached ions is surpassed, a secondary reaction, i.e., the precipitation of Ca and P ions occurs (Stage 4). The precipitated layer, along with the enhanced network connectivity at the glass surface, retards the glass dissolution [118]. In Stage 5, this initial layer acts as the substrate for further adsorption, and leads to the formation of an amorphous precipitated layer, which eventually crystallizes [120].

The CaP layer formed at the silica rich surface, due to the migration of Ca^{2+} and PO_4^{3-}, may be formed by the ions leaching into the solution, or by simply precipitating from the immersion media [112,133]. This layer later crystallizes to HA, which is similar to the mineral phase of bone, and is responsible for the bone-bonding properties of the bioactive SG [112,133]. Other than Ca^{2+} and PO_4^{3-}, other ions such as F^-, OH^- and CO_3^{2-} may also be incorporated into the crystalline phase [134]. The formation of HA layer upon immersion in aqueous solution is often perceived as a first sign of bioactivity. Consequently, 45S5, 13-93 and S53P4 received a lot of attention, due to their excellent clinical outcomes.

2.2.1.3 Bioactivity

In case of glasses, bioactivity is measured by their ability to form a bond with bone. Bioglass® has been the most widely researched bioactive glass, owing to its bone-bonding abilities [4]. The mechanisms of bioactivity and bone bonding of Bioglass® are relatively well researched and understood [3,135,136].

Several in-vivo studies [100,137,138] and clinical trials [139,140,149,150,141–148] successfully demonstrated the osteogenic properties of 45S5 glass. The reasons for osteogenic properties of bioactive SG have been investigated in detail with in-vitro experiments and human osteoblasts culture in glass extracts (glass dissolution products containing cell culture media) [6,151,160,152–159]. The dissolution products of SG, such as calcium ion and silicic acid were established to be favorable for osteoblastic differentiation [161–165]. The bioactivity of these glasses was found to be dictated by their dissolution rate and formation of a HCA layer, which in turn are dependent on the atomic structure and composition of the glass, as reviewed by Jones [166]. The initial in-vivo studies for 45S5 were done with monoliths in rat femurs, where the interfacial shear strength after 6 weeks of implantation was at least as high as the strength of the host bone [4,167]. Oonishi et al. quantitively compared the effectiveness of granules of 45S5 and hydroxyapatite, and gave rise to the “Oonishi model”, which involved drilling 6 mm wide defects into the femoral condyle of rabbits, and stopping bleeding before implanting the particles [168]. In that study, the use of 45S5 resulted in a 17 times higher rate of bone regeneration after 1 week, and twice as high after 24 weeks post-surgery than HA [168]. In another study, 45S5 was found to stimulate more bone growth in the jaw of Beagle dogs than HA [138]. PerioGlas® (45S5 particles in the range 90-710 µm) and Biogran® (45S5 particles in the range 300-355 µm) were found to initiate bone growth in rabbits as well, when tested in the Oonishi model [169]. Furthermore, putty-like materials based on bioactive glass particles, such as NovaBone® putty came into being as they are preferred by surgeons, due ease of handling during surgery. The NovaBone® putty was reported to be more effective for bone regeneration in sheep spine than the Novabone® particulate [170]. Later, Bonalive® based on another SG S53P4 was approved in Europe for orthopedic use as a bone graft substitute in 2006.

2.2.1.4 Limitations of bioactive silicate glasses

Despite the success of commercially available silicate bioactive glasses, they suffer from a few drawbacks. There is interest for development of porous scaffolds for tissue engineering or fiber for the reinforcement of fully resorbable implants [171,172]. Porous 3D

scaffolds of bioactive glass are obtained by sintering the glass particles, already formed into the desired geometry. Via sintering, the particles bond into a strong glass phase with an interconnected network of pores. In fiber drawing two techniques can be used. Either by pulling fibers from the glass melt or by drawing fibers from a cane. However, the thermal processing window of FDA approved bioactive glasses, which are fast dissolving, are low. This results in poor thermal processability into scaffolds and fibers. Crystallized porous scaffolds have poor mechanical properties [173] and fiber cannot be drawn. Furthermore, if the glass crystallizes during sintering, it typically leads to the formation of combeite crystalline phase ($Na_2O–2CaO–3SiO_2$), known to reduce bioactivity by inhibiting the rate of conversion to hydroxyaptatite (HA) [174]. While complete crystallization of glass particles results in a loss of bioactivity, partial crystallization gives rise to instability, due to the preferential degradation of the amorphous region [174]. Indeed, Ceravital® a glass-ceramic made from crystallized 45S5 doped with K_2O and MgO, bonded with bone [175] but eventually failed as an implant due to long term instability of crystal phase boundaries [176]. Another commercially used SG, 13-93, offsets some of the drawbacks of 45S5. It has a larger thermal processing window, which enables sintering of porous 3D scaffolds without crystallization. Furthermore, the in-vitro cell response was found to be at par with 45S5, when cells were cultured on glass bulk [177]. However, the degradation rate of 13-93, and subsequent conversion to HA was found to be slower than 45S5. Furthermore, in addition to the poor thermal processability of fast dissolving SG, they are also known to degrade incongruently in-vivo. This has proven undesirable, as another commercial SG S53P4, was found in the patient's body even 14 years after implantation [17]. These drawbacks of the SG can be attributed to the SG network and structure. The limitation of the silicate bioactive glasses led researchers to investigate new glass families as bioactive glasses.

2.2.2 Phosphate glasses

The interesting properties of PG have led to their use in a wide array of applications, such as solid state electrolytes, nuclear waste hosts and biomaterials. The versatility of PG as a material can be attributed to their structure [20,178–180]. PG are known to be completely biodegradable, degrade with a zero order rate, and the degradation can be tailored from weeks to years by varying the composition [18,181,182]. They are also known to possess a wide thermal processing window, which enables them to be drawn into fibers and sintered into scaffolds. The potential of phosphate glass fibers has been explored extensively for a wide array of applications [26,183–186].

2.2.2.1 Structure

The structure of simple PG has been reviewed in detail by Brow [187]. The building blocks of a PG are phosphate tetrahedra, described by the Q^n notation, where n is the number of bridging oxygen atoms. PG are mainly constituted by Q^1 (end unit), Q^2 (middle unit) and Q^3 (branching unit). Other than these, isolated orthophosphate groups, Q^0 may also exist. In the phosphate 3D network, the tetrahedra can attach to three neighbors at most, in contrast to the silicate tetrahedra, which can attach to four. Modifier metal oxides can be used to increase or decrease the network connectivity. Usually, when a modifier metal oxide is added to the composition, P-O-P bonds are broken to create NBOs, thereby changing Q^n units to Q^{n-1} units and depolymerizing the network. On the other hand, it is possible that the modifier metal ions can crosslink two non-bridging oxygen atoms, thus joining two phosphate chains. In such a case, an increase in the bond strength and chemical durability of the glass is observed.

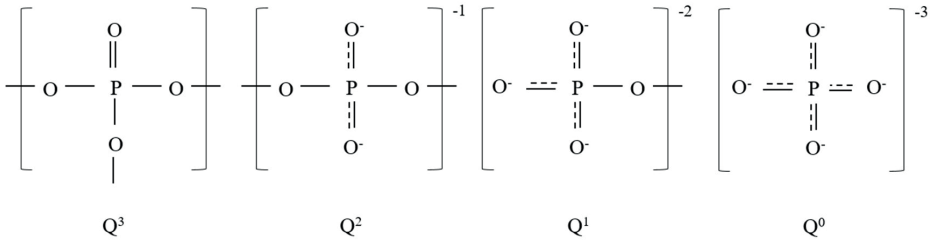

Figure 2.2 - Schematic representation of the different phosphate tetrahedra in the structure of a typical phosphate glass.

The average bond length of the P-O bond in the phosphate tetrahedral is around 1.54-1.57 Å, while that for bridging oxygen is around 1.61-1.64 Å. For NBOs, the P-O bond length decreases for decreasing n, i.e., $Q^3>Q^2>Q^1>Q^0$. Based on the composition, the structure of PG can range from:

(i) ultraphosphate glasses (P_2O_5 > 50 mol%) - cross linked network of Q^3 tetrahedra, connected via bridging oxygen atoms at the corner of the tetrahedra.

(ii) metaphosphate glasses ($P_2O_5 \approx 50$ mol%) - polymer like structure consisting of chains and rings of Q^2 tetrahedra. These chains and rings are further linked by ionic bonds between the modifier metal ions and the NBOs.

(iii) polyphosphate glasses (P_2O_5 < 50 mol%) – the networks are based on Q^2 chains, terminated by Q^1 tetrahedra.

The structure and properties of polyphosphate and metaphosphate glasses have been reviewed in detail in the past [188–190]. In this thesis, the focus is on metaphosphate glasses.

2.2.2.2 Dissolution mechanism

PG are known to dissolve at a faster rate than the bioactive SG, which led the researchers to focus more on the latter initially. However, from a biomedical perspective, the ability of the PG to dissolve completely in aqueous media is particularly advantageous. Furthermore, through modifying compositions, it is possible to tailor the rate of degradation to suit a wide range of applications [18]. As described previously for SG, the glass dissolution behavior depends on the reaction of glass network with H_2O, and the leaching of ions from glass matrix to the solution [191]. The initial stage of glass dissolution is the rapid ion exchange with the solution, breaking the metal – NBO bonds first. It is followed by an attack on the glass network, which results in an increasingly alkali depleted surface [18,191].

As is widely accepted [118,192,193], PG dissolve in aqueous media via the following interdependent steps:

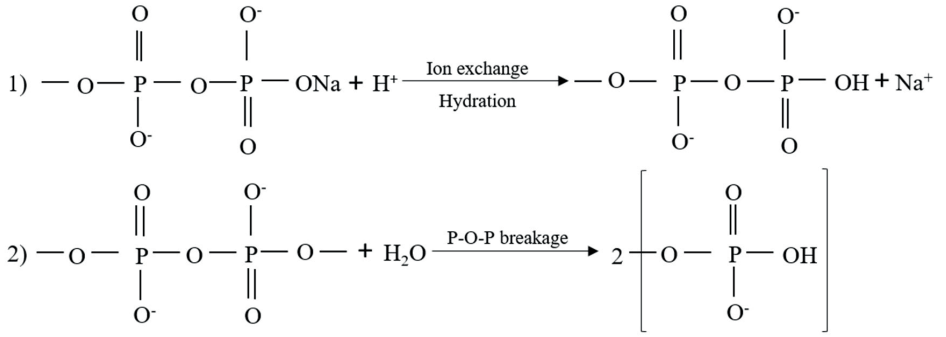

Figure 2.3 Typical dissolution reactions of a phosphate glass in aqueous media [194]

1) Hydration reaction – the Na^+ ion is exchanged with H^+ from the media, leading to the leaching of Na into the solution, and formation of a hydrated layer at the glass-water interface

2) Network breakage – rupture of P-O-P bonds in the hydrated layer due to attack of H^+ ions and water molecule, resulting in disassociation of phosphate chains, which are then released into the solution.

Regarding the rate of phosphate dissolution mechanism, Bunker et. al. suggested that the dominating reaction among the above, is the 1) ion exchange reaction [18]. They further divided the total dissolution process into two kinetic periods as per the profile of dissolved amounts, q vs time, t, into a decelerating dissolution period where $q \propto t^{1/2}$ and a uniform dissolution period, where $q \propto t$. Furthermore, the dissolution remains congruent throughout the process, and independent of the kinetic period [18]. Contrastingly, Liu et. al. proposed that 2) network breakage is the dominant reaction for another metaphosphate glass system [195]. According to them, the ion exchange reaction is only the precursor to the main network breakage step.

Thus, although the first step of dissolution is similar to SG, the later steps are different, leading to the difference in the dissolution mechanisms between PG and SG. On one hand, SG' surface becomes enriched in silica due to incongruent dissolution during the later stages, PG continue to dissolve by continuously releasing chains of phosphate groups into the solution. The dissolved silica species readily polymerize and/or repolymerize until there is little or no resemblance to the original glass, compared to the phosphate chains and rings, which are more stable aqueous media and hydrolyze very slowly [196].

2.2.2.3 Bioactivity

The properties of PG such as a tailorable degradation rate [18] and ability to be doped with ions of therapeutic value [23,197,198] are attractive from a biomedical perspective. These characteristics allow PG to be suitable for bone repair [198,199], neural repair [200], delivery of antimicrobial ions [184] or drugs [201]. Several studies have reported promising in-vitro and in-vivo results with PG, from a biomedical point of view [178,202–207]. As compared to the traditional silicate bioactive glasses, which are characterized by their ability to induce apatite formation at their surface in aqueous media, the apatite precipitation is much more complex on the typically fast dissolving PG [208]. Although PG containing 35-40 mol% of P_2O_5 do not exhibit HCA layer precipitation, high Ca and Na oxide content and high CaO/P_2O_5 ratio are thought to enable PG to show bioactivity [209]. As Si is absent in PG, the HCA formation cannot proceed via the same mechanism, and as readily on PG as on SG. However, apatite formation on a Ti-doped invert PG upon immersion in SBF for 10 days has been reported [208]. Addition of Ti is known to reduce the degradation rate of the glass and hydrated Ti has been shown to impact apatite formation [208]. Furthermore, Monem et al. reported another system of Ti doped PG, which facilitated bone growth in rabbit femur [210]. Another PG system P_2O_5 – CaO – K_2O – Na_2O exhibited bioactivity in SBF, attributed to the ion release from the glass

reduce the degradation rate of the glass and hydrated Ti has been shown to impact apatite formation [208]. Furthermore, Monem et al. reported another system of Ti doped PG, which facilitated bone growth in rabbit femur [210]. Another PG system P_2O_5 – CaO – K_2O – Na_2O exhibited bioactivity in SBF, attributed to the ion release from the glass [211]. Patel et al. reported the good cytocompatibility and cell adhesion proliferation on a near invert phosphate glass system containing Ca, Mg and Sr ions [212]. In another study, the influence of PG within the system CaO-Na_2O-P_2O_5 on soft and hard tissue were comprehensively investigated, and good cell attachment was reported for some of the compositions [202]. Furthermore, the viability and proliferation of osteoblast cells on PG has been reported in the past [202,213,214]. The studies concluded that there is indeed a strong correlation between the dissolution rate and cell response. During cell culture, there may occur loss in surface integrity of the glass due to being in contact with aqueous media, which affects the cell attachment and proliferation. PG have also been used as a coating on bioinert metals to enhance biological response at their surface [215].

Furthermore, the applications for phosphate glass fibers in hard and soft tissue engineering have been reviewed in detail by Lapa et al. [216]. Numerous articles have reported the advantages of using phosphate glass fibers in combination with bioresorbable polymers to obtain bone fixation devices possessing a similar modulus to that of the natural bone [217,218,227–230,219–226]. Bioresorbable screws, rods and nails have also been obtained from phosphate glass fibers based composites [26,226,231]. Additionally, phosphate glass fiber based 3D scaffolds have also been suggested in the past [213,232]. In soft tissue engineering, a particularly interesting application for phosphate glass fibers is in nerve regeneration [233–235]. The PGF provide directional guidance for the neurites to grow along the direction of the fiber axis, and it was demonstrated that this ability of the fibers is improved with a reduction in diameter [235,236].

2.3 Modifying glass properties

One of the major strengths of glasses as a biomaterial is that they can be tailored to suit a wide array of applications. For biomedical applications, arguably the most common route taken to attain specific properties (such as degradation rate and ion release rate), is to modify the glass composition by doping with metal oxides. However, it is worthwhile to note that seemingly small modifications to the composition may lead to significant

changes in the end properties of the glass. For instance, doping Bioglass® with 1-1.5 mol% Al_2O_3 lead to a significant reduction in its bioactivity [237], as the connectivity of the silica network is intrinsically connected to the glass' bioactivity [238–243]. Consequently, the effects of composition on the reactive properties of bioactive glasses has been reviewed in detail [244]. Furthermore, the impact of various elements on the glass's bioactivity has been reviewed in several PhD theses [245–247], while some others have focused on the impact of glass composition on their thermal properties in view of sintering or fiber drawing.

Other than changing the composition, it is also common to modify the glass' surface to suit different applications, where the surface chemistry is more important than the glass' properties itself. For instance, superhydrophobic and self-cleaning glass surfaces are highly desirable for solar cells [248] and solar buildings, and can be achieved by using a variety of techniques [249–252]. In the biomedical field, glass has been a popular substrate for protein chips, owing to its resistance to temperature and low noise in fluorescence signals [253–255]. Hence, several surface modification methods for protein immobilization at glass' surface have been reported in the literature [256–264]. In the following sections, the impact and benefits of doping glasses with metal ions and surface treatment methods from a biomedical perspective are discussed.

2.3.1 Doping with metal oxides

3D scaffolds in tissue engineering can be made from biodegradable polymers, ceramics or composites, and are usually loaded with therapeutic drugs, or therapeutic ions [265,266,275,267–274]. This is done in order to increase the functionality of the scaffold, by incorporating a drug-delivery function for therapeutic purposes [274,276]. For scaffolds made out of bioactive glasses, these metallic ions are a part of the glass composition, thus the glass acts as a drug delivery vehicle for releasing beneficial ions [165,277]. PG in particular, are promising as vehicles for delivery of therapeutic ions, as they dissolve congruently, thus potentially delivering ions in a sustained and controlled manner. For instance, Lakhkar et al. reported Ti and Sr doped PG for Sr ion delivery to the cells [197]. As PGF also dissolve congruently, apart from possessing good mechanical properties and promising for biosensing, Lapa et al. have reviewed their potential for therapeutic ion release [216]. However, for the purpose of this thesis, the focus is on Ag, Cu, Fe and Ce as dopants in PG. Ag and Cu are popular as dopants to instill antimicrobial properties in the glasses [184,278–280]. Fe has been shown to stabilize the glass network for efficient cell attachment and proliferation [26], and enhance the mitochondrial activity and gene expression of osteogenesis related genes [281]. Ce has also been

shown to stabilize the glass network [282], possess bacteriostatic properties, low toxicity [283] and mimics the fluorescence of natural teeth in dental ceramic [284]. In Table - 2.1 below, the biological functions of the metal ions contained in the PG and PGF in this thesis are discussed.

Table 2.1 The role and biological functions of the constituent ions of glasses under investigation in this thesis

Ion	Functions and Biological effects	Reference
Calcium	Primarily stored in bone (~99%). Forms hydroxyapatite with phosphate. Acts as an ionic messenger, and its movement in and out of cytoplasm signals cellular processes such as exocytosis of neurotransmitter for muscle contraction. Stimulates bone cell differentiation, osteoblast proliferation, bone metabolism and mineralization.	[161,162,292,163,285–291]
Strontium	Stored in skeleton by exchanging with Ca ion. Stimulates bone formation at low doses, whereas adversely affects bone mineralization at high doses. Increased osteoblast differentiation upregulates several osteogenic genes.	[293–296]
Copper	Stimulation of human endothelial cell proliferation, angiogenesis and promote formation of blood vessels. Accent the human mesenchymal stem cell proliferation and differentiation towards osteogenic lineage. Antibacterial action towards *Staphylococcus epidermis.*	[184,297–299]
Silver	Antibacterial in Ag^{+} ionic state. Inhibits replication by binding to microbial DNA and to sulfhydryl groups of bacteria enzymes.	[300,301,310,302–309]
Cerium	Osteogenic and a neuroprotective agent. Low toxicity and bactericidal.	[283,311,312]
Iron	Participates in redox reactions of metalloproteins, oxygen carrier proteins like hemoglobin and myoglobin.	[313,314]

2.3.2 Surface modification methods

In biomedical engineering, the surface of glasses are often treated to attune or improve them for specific applications. For instance, catheters are an indispensable tool in modern medical practice, yet are known to lead to infections and other surface related complications in patients. In their review, Neoh et al. elaborated on the several catheter related complications in patients and the surface treatment methods to tackle them [315]. For e.g., anti-adhesives and bactericidal coatings are often applied to the catheters, in order to repel/kill bacterial colonization at their surface. In case of bioactive glasses and glass composites, a common approach is to attach bioactive molecule at their surface to improve their functionality or biocompatibility. These bioactive molecules are often bounded to the glass surface, which is usually functionalized beforehand with an intermediary molecule like APTS (aminopropyltriethyloxysilane). APTS bonds to the surface of the bioactive glasses, as well as the biomolecule through the amine group. APTS grafting on SG and PG have been reported by Verne et al. [316] and Massera et al. [264].

In addition to facilitating the attachment of bioactive molecules, APTS is of particular interest for biomedical applications owing to its ability to interact with DNA [317]. APTS functionalization (or silanization) on glass' surface has been found useful for immobilization of proteins, antibodies as well as DNA arrays [318]. Post silanization, the effective immobilization of bone morphogenic protein 2 (BMP-2) and alkaline phosphatase enzyme was reported [316,319]. It is well regarded that when a biomaterial is exposed to biological media, an instantaneous adsorption of proteins occur at its surface. The protein adsorption leads to the formation of a provisional matrix, which in turn interacts with the approaching living cells. Thus, protein adsorption is indeed an important step in determining the effectiveness of cell attachment at a biomaterial's surface.

PG in general are known to dissolve faster than SG, and Salih et al. have shown that fast dissolving glasses inhibit cell growth and proliferation [320]. Indeed, when human gingival fibroblasts were cultured at the surface of the PG $50P_2O_5$+$10Na_2O$+20CaO+20SrO, referred to as Sr50, the cells were found to proliferate at a rate slower than the SG [321]. Furthermore, as PG dissolve with a congruent mechanism, leaching phosphate chains into the solutions, it leads to the loss of anchor points for cells/proteins at their surface. This is in contrast to SG, where the dissolution mechanism is incongruent, with the silica network remaining largely intact during dissolution. Thus, irrespective of the dissolution rate of PG, there is a need for appropriate surface modification methods, which can improve the cell attachment and proliferation at their surface, by countering the loss of anchor points for cells/proteins.

2.4 Glass fiber processing

There is growing demand for new biomaterials such has biomedical glass fibers, which can be used for applications like reinforcing composites [322,323], and biosensing [324]. Bioactive glass fibers are known to have suitable chemistry and morphology for mimicking the fibrous nature of tissues [26]. Phosphate glass fibers (PGF) are known to be completely bioresorbable and their potential in biomedical applications has been explored extensively [26,184,186,325]. PGF are commonly obtained by drawing from a high temperature melt, and the desirable fiber diameter is achieved by controlling the speed of the rotary drum on which the fibers are wound [326,327]. The wide thermal processing window of PG offers more flexibility in temperature adjustment for optimal viscosity of the melt [203], without risking crystallization which is known to reduce bioactivity [328]. Other than glass melts, fibers can also be drawn from preforms. The preform is heated until it softens and a drop is formed, which is then pulled and wound on a rotary drum. Nonetheless, it is important to note that when drawing fibers from melt, the difference in temperature between the melting and the endset of crystallization is of importance. While, with preforms, the difference between onset of crystallization and the glass transition temperature dictates the ease of fiber drawing.

2.4.1 Fibers for reinforcement

Traditional metal implants for load bearing applications are known to cause stress-shielding, which results in weakening of the bone and an increased probability of a recurring fracture [329]. This is due to the stiffness mismatch between the metallic implant and the surrounding bone, leading to the remodeling of bone according to the reduced stress it experiences in the presence of the implant. Thus, there is huge potential for resorbable implants, with better-matched mechanical properties and degradation rate to take over this role. Another intrinsic advantage of a completely bioresorbable implant is the negation of a second surgery for their removal. The traditional high modulus fibers that were considered for reinforcement, such as E-glass are highly durable in-vivo [1]. The use of natural fibers for reinforcement of composites has been reviewed in detail by [330][331], and they are known to be dimensionally unstable and have variable properties. In such a scenario, PGF are promising candidates, as they are bioresorbable, have good mechanical properties and depending on composition, the degradation products are typically non-toxic [202,332]. Their potential in soft tissue engineering has been acknowledged [203,326,327], as they can provide a template for muscle cells to grow along their

axis, and to form myotubes [203]. PGF also support the ingrowth of vasculature, thereby supporting soft tissue regeneration [327,333,334].

Apart from reinforcing the composites, PGF can be doped with metal ions for adding further functional features. Abou Neel et. al. reported the effectiveness of Cu doped PGF in eradicating *S. epidermis* due to the antimicrobial action of the Cu ion [184]. Ti and Fe containing core clad PGF were studied by Ahmed et. al., and the fibers were reported to maintain their tensile strength up to a few weeks upon immersion [185]. Other than reducing the degradation rate, Fe is also known to improve the strength properties of glass fibers [335]. It is well known that the tensile strength increases with a decrease in the glass fiber diameter in the range of 40-400 µm [336]. In literature, PGF within a diameter range of 15-25 µm have been reported with decent mechanical properties. These fibers exhibited a tensile strength and tensile modulus in the range of 370 – 1000 MPa, and 44 - 64 GPa respectively [26,27,230,234,337,338].

2.4.2 Biosensing

The aim of a device used for biosensing is to “produce a signal which is proportional to the concentration of a chemical or biochemical to which the biological element reacts” [339]. Gholamzadeh et al. [340] reviewed the capability of fiber optic sensor technology to sense physical, chemical or biological parameters (such as strain, temperature, pH) by modulating features (such as intensity, phase) of the light wave. Fiber optic sensors can be classified into intensity (amplitude), interferometric (i.e., phase or frequency) or a polarization sensor [340]. The sensors employed in biomedical sensing applications (or biosensors) are conventionally, intensity sensors, i.e., based on measuring the change in intensity or amplitude, or interferometric sensors, i.e., based on detecting change in phase or frequency [341].

Only few studies have attempted to relate the glass fiber reaction with the optical and biochemical response of a glass fiber. In one such study, Massera et al. explored the potential of PGF in tracking glass dissolution in-vivo [186]. Indeed, core-clad fibers are more desirable for guiding light waves than single core fibers. The light loss was measured from a sensing region created by removing the cladding for a part of the fiber’s length. Furthermore, for fibers meant for biosensing, it is useful to study the in-vitro degradation of fiber in terms of size and tensile strength. Ahmed et al. [185] reported that Fe and Ti doped core-clad PGF maintained their mechanical properties for ~4 weeks in-vitro.

Thus, PGF as a material are highly suited for biosensing, and are indeed promising for developing commercially available fully bioresorbable biosensors in the future.

3 Aims of the study

The bioactive SG form a Si-rich layer and eventually HA when in contact with aqueous media, which helps in bonding to bone. They are also osteoinductive, and have been used commercially for bone regeneration for several years. However, their commercial products are mainly based on granules, owing to their limited thermal processing window, which inhibits sintering and/or fiber drawing. Furthermore, the incongruent degradation mechanism of SG in-vivo lead to incomplete dissolution of the glass particles, increasing complications for both patients and surgeons alike. On the other hand, metaphosphate glasses are known to dissolve congruently, in a sustained manner and possess a wide thermal processing window for fiber drawing or powder sintering. However, they are set back by the poor cell attachment and proliferation at their surface, owing to the typically fast and/or congruent dissolution.

The overall aim of this study is to develop glasses with added functionality such as antimicrobial properties, which are suitable for fiber drawing and promote cell attachment and proliferation at their surface. The fibers drawn from these glasses should have decent mechanical properties to be used as reinforcements in composites, and can be used for biosensing.

To achieve these goals, the work undertaken here aims to answer the following questions:-

- While typical bioactive phosphate glasses are usually invert glasses, these glass systems are prone to crystallization and cannot be readily thermally processed. Can we develop metaphosphate glasses containing metal ions with

antimicrobial and/or optical properties of interest? What is the impact of metal ion doping on glass dissolution in aqueous solutions?

II Do these metal doped metaphosphate glasses possess favorable thermal properties for fiber drawing, i.e., can we draw fibers without significant crystallization?

III Do these glasses promote cell growth and proliferation at their surface? And if not can we enhance the biological response by tailoring the glass composition or by applying optimized surface treatments?

IV Can the produced fibers be used for more advanced application like biosensing? Would these fibers also possess mechanical properties granting their use as potential reinforcement in composites?

4 Materials and Methods

4.1 Bulk glass

4.1.1 Glass melting

Prior to preparing the phosphate and borophosphate glasses, $Ca(PO_3)_2$ and $Sr(PO_3)_2$ were made using $CaCO_3$, $SrCO_3$ and $NH_4H_2PO_4$. Each carbonate was mixed with $NH_4H_2PO_4$ in separate batches, and heated to 250°C to remove the NH_3 and H_2O, then to 650°C and 850°C to remove the CO_2. A constant heating rate of 1°C/min was employed throughout the heating cycle, and the batch was kept at each temperature step for 12 hours. Then, the glass batch was prepared using $Ca(PO_3)_2$, $Sr(PO_3)_2$, $Na(PO_3)$, Ag_2SO_4/CuO/CeO_2/Fe_2O_3 for the glasses in Publication I and II. For the borophosphate glasses in Publication III, B_2O_3, $CaCO_3$ and $SrCO_3$ were also used in preparing the glass batch (for borophosphate glasses only). The batches were heated at 10°C/min to 1100°C and kept there for 30 min in a silica crucible. Then, the molten batch was cast into a brass mold and annealed at T_g - 40°C for 5 hours to relieve the internal stresses. As an exception, in Publication I, the Ag doping was done using Ag_2O, and 1 wt% Na_2SO_4 was added to the batch to avoid reducing the silver oxide to metallic silver. To obtain glass discs, the glass rod obtained was cut into 2 mm thick discs with a Low Speed Diamond Wheel Saw, Model 650, South Bay Technology (San Clemente, CA, USA). The glass discs were then polished to the same surface smoothness using grit #320, #500, #800, #2400 and #4000. For obtaining glass powder, the glass rods were crushed and sieved to specific particle size ranges. The bioactive SG S53P4 and 13-93, used as control in the Unpublished manuscript were prepared using analytical grade SiO_2, $CaCO_3$, MgO,

K_2CO_3, Na_2CO_3 and $(CaHPO_4).2H_2O$ as raw materials. The glass melting temperature was based on the previous melting protocols described in [13,342].

The nominal compositions of the PG in Publication I-II and IV, and the borophosphate glasses in Publication III are reported in Table 4.1.

Table 4.1 Nominal composition of the phosphate and borophosphate glasses

Glass code	Composition (mol %)								
	P_2O_5	CaO	SrO	Na_2O	Ag_2O	CuO	Fe_2O_3	CeO_2	B_2O_3
Sr50	50	20	20	10	-	-	-	-	-
Ag-1	49.5	19.8	19.8	9.9	1	-	-	-	-
Ag-2	49	19.6	19.6	9.8	2	-	-	-	-
Ag-3	48.5	19.4	19.4	9.7	3	-	-	-	-
Ag-5	47.5	19	19	9.5	5	-	-	-	-
Cu-1	49.5	19.8	19.8	9.9	-	1	-	-	-
Cu-2	49	19.6	19.6	9.8	-	2	-	-	-
Cu-3	48.5	19.4	19.4	9.7	-	3	-	-	-
Cu-4	48	19.2	19.2	9.6	-	4	-	-	-
Cu-5	47.5	19	19	9.5	-	5	-	-	-
Fe-1	49.5	19.8	19.8	9.9	-	-	1	-	-
Fe-2	49	19.6	19.6	9.8	-	-	2	-	-
Fe-3	48.5	19.4	19.4	9.7	-	-	3	-	-
Ce-1	49.5	19.8	19.8	9.9	-	-	-	1	-
Sr50-B2.5	47.5	20	20	10	-	-	-	-	2.5
Ag1- B2.5	47.025	19.8	19.8	9.9	1	-	-	-	2.475
Cu2- B2.5	46.55	19.6	19.6	9.8	-	2	-	-	2.45
Ce2- B2.5	46.55	19.6	19.6	9.8	-	-	-	2	2.45

4.1.2 Physical properties

The density of the glasses in Publication I-II was measured using Archimedes principle with an accuracy of ±0.02 g/cm^3. A polished glass sample was used for the measurement, and ethanol was used as the immersion liquid. The molar volume, V_m, of the glasses was then calculated using their molar weight and the measured density.

4.1.3 Thermal properties

Differential Thermal Analysis (DTA, NETZCH Jupiter F1, Selb, Germany) of all the glasses in Publication I-III was performed at a heating rate of 10°C/min, in a Pt crucible, under 50 ml/min flow of N_2. The T_g (glass transition temperature), T_x (onset of crystallization temperature) and T_c (crystallization temperature) were obtained from the thermograms. T_g was calculated as the inflection point of the endotherm obtained by taking the first derivate of the DTA curve. The T_x was determined as the onset of the crystallization peak and T_c as the maxima of the exotherm. All the values were obtained with an accuracy of ±3°C.

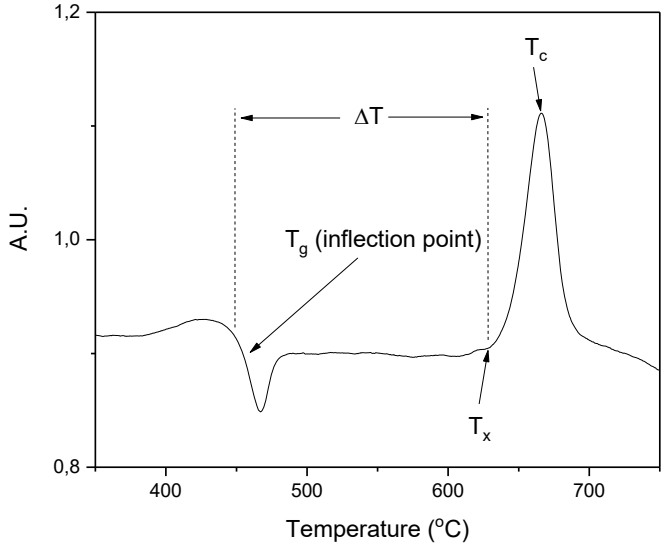

Figure 4.1 Example of a DTA exotherm depicting the characteristic temperatures T_g, T_x and T_c of a glass

4.1.4 FTIR Analyses

In Publication I-III, the glass particles before and after immersion were analyzed with a PerkinElmer Spectrum One FTIR Spectrophotometer (Waltham, Massachusetts, USA) in attenuated total reflectance (ATR) mode. All the spectra were recorded in the 600–1800 cm^{-1} range, corrected for Fresnel losses and normalized to the band having maximum intensity. All the spectra are obtained as an average of 8 scans with a resolution of 1 cm^{-1}.

4.1.5 Optical properties

The UV-Vis absorption spectra of all the glasses in Publication I-II was recorded using UV-3600 Plus UV-VIS-NIR Spectrophotometer Shimadzu. The measurement was done in the range of 200-1600 nm at room temperature, on an optically polished 2mm thick glass sample.

4.1.6 *In-vitro* dissolution

For the dissolution tests in Publication I-III, glass powders were obtained within a particle size range of 125-250 µm. 75 mg of the glass powder was immersed in 50 ml of TRIS buffer/SBF solution, and placed in an incubating shaker HT Infors Multitron (Bottmingen, Germany) at 37°C, 100 rpm to obtain a laminar flow [343]. Thus, the ICG TC04 methodology was followed, as described in detail by Macon et. al. [343]. The tests were conducted up to 42 days in TRIS buffer solution, and 21 days in SBF. SBF was prepared using the protocol described by Kokubo et. al. with the pH adjusted to 7.40 at 37°C [344]. The pH of the immersion media was measured using a pH ion analyzer Mettler Toledo SevenMultiMeter (Columbus, Ohio, USA), with an accuracy of ±0.02. The pH of the blanks (immersion media which does not contain glass powder) remained constant throughout the course of immersion, indicating that the immersion media were stable during the length of the study.

Post immersion, the glass particles were filtered out from the immersion media for further analysis, washed in acetone and dried overnight to terminate any surface reactions. The immersion media was also recovered, diluted with distilled water containing 10% 1M HNO_3 by volume, and stored at +4°C. The concentrations of B (249.678 nm), Ca (317.933 nm), Sr (460.733 nm), P (214.914 nm), Na (589.592 nm), Ag (328.068 nm), Cu (327.393 nm) and Ce (413.764 nm) in these solutions were obtained with an Inductively-coupled plasma – Optical emission spectrometer (Agilent Technologies 5110 ICP-OES,

Santa Clara, California, USA). The accuracy of the measurement was estimated at ±5% of the obtained values, except when the deviation between the triplicates was higher than 5%.

4.1.7 Imaging and elementary analysis

In Publication I-III, scanning electron microscopy (SEM), was performed for high resolution imaging of the sample' surfaces, using a JEOL JSM 7100F apparatus (Pressure 10^{-4} Pa, accelerator voltage 20 kV). For chemical microanalysis of the surface, Energy Dispersive X-Ray Spectroscopy (EDS SDD X-Max 80 mm^2 Oxford Instruments AZtecEnergy) was used in conjunction with SEM. EDS is capable of identifying elements heavier than Be with a spatial resolution better than 1μm^3, corresponding to a spot size of 1 μm^2, with an accuracy of ±1%.

In Publication IV, SEM was performed on the fiber's cross section post fracture, with Zeiss ULTRAplus SEM. Additionally, optical microscope Olympus BH2-UMA was used to confirm the deposition of a surface layer as a result of immersion in TRIS buffer solution. Furthermore, the optical microscope was also used for obtaining the fiber's diameter, pre and post immersion. In unpublished manuscript V, SEM (Leo 1530 Gemini from Zeiss, Oberkochen, Germany) and EDXA (Vantage, Thermo Electron Corporation, Waltham, Massachusetts, USA) were used to evidence the precipitation of a surface layer on the glass particles immersed in SBF and TRIS buffer solution.

4.1.8 Antimicrobial tests

In Publication II, the antimicrobial properties of Cu and Ag doped PG were investigated, along with the bioactive SG S53P4 as a reference. Glass powders within particle size range of <125 µm and 125-250 µm were obtained by crushing and sieving. The particles were heat sterilized at 180°C for 45 min, allowed to cool down to room temperature, and then pre-incubated in 0.5 ml physiological saline solution (0.85% NaCl). Then, the bacterial suspension was added to obtain the two different concentrations, 400 and 1200 mg glass particles/ml at room temperature for 48 h. Staphylococcus epidermidis ATCC 35984 was grown on Brain Heart Infusion agar supplemented with 0.5% Yeast extract at 37°C overnight. Then, one colony was transferred to Tryptic Soy Broth and incubated at 37°C until mid-exponential phase, corresponding to OD_{600nm} =0.8–0.9. Then, the bacteria were harvested by centrifugation (2500 rpm, 10 min) and re-suspended in fresh Tryptic Soy Broth to obtain a bacterial concentration of 2.2×10^8 CFU/ml. 0.5 ml of bacterial suspension was then added and cultured on each of the glasses, for 24h, 37°C, before

counting the colony forming units. The experiments were repeated thrice. The control contained only the physiological saline solution and bacterial suspension. One way ANOVA and Tukey test were used to obtain the mean CFU/ml for (1) various glass composition at a fixed concentration, and (2) same glass composition at 400 and 1200 mg/ml. All the obtained values were found to be statistically different at the 0.05 level. Furthermore, all the values were also statistically different to the control.

4.2 Surface modification

4.2.1 Preparation of buffer solution

In the Unpublished Manuscript, the basic buffer solution was prepared using TRIS base, while the neutral buffer solution was prepared with TRIS base and TRIS HCl. The acidic buffer solution was prepared using citric acid – sodium citrate. The solutions were filtered using 0.2 µm filter paper and autoclaved before being used. All the solutions had an ionic concentration of 10mM.

4.2.2 Washing and silanization

In the Unpublished Manuscript, for the washing step, the glass discs were immersed in acid/neutral/base buffer solutions for 6h at room temperature. The washed discs were then dried in a laminar hood at room temperature. Post washing, silanization of the glass surface was carried out by following the protocol discussed in [264]. The steps involved in washing and silanization are presented in the Table 4.2 below. The glass discs washed in the acid, neutral and base buffer solutions are referred to as WA/WN/WB and after silanization, as WAS/WNS/WBS respectively.

Table 4.2 Steps involved in the washing and silanization of glass discs (Unpublished Manuscript)

Washing in buffer solution	
Steps	**Description**
Washing in buffer solution	Glass discs immersed in the acid/neutral/basic buffer solution for 6h at room temperature (Post wash, the discs are referred to as WA/WN/WB depending on the buffer solution used for washing)
Silanization	
Steps	**Description**
Pre-wash	For 5 min in acetone (95 vol.%) in a sonicator
	3 × 5 min in double distilled water in ultrasonic bath
Silanization	Washed glass discs are immersed in 150 ml of a solution containing 95 vol.% of ethanol and 35µL of APTS (1 mmol/L), for 6 h, at RT
Drying	At 100°C to consolidate the bonding between the silane and glass surface
Post wash	3 × ethanol in an ultrasonic bath to remove any excess APTS sticking to the glass disc
Final step	Drying for 1 h at 100°C
	Post silanization, the discs are referred to as WAS/WNS/WBS depending on the buffer solution used to wash them beforehand

4.2.3 Contact angle measurements

In the Unpublished Manuscript, the static contact angle was measured on the untreated and treated samples (washed and washed+silanized) with sessile droplet method on Attension Theta contact angle meter (Biolin Scientific, Gothenburg, Sweden). A 2-3 µl droplet of the buffer solution was placed on the surface of the glass discs, and the droplet was imaged with a high speed camera. The contact angle of both sides of the droplet was recorded using the software Attension Theta (Biolin Scientific, Gothenburg, Sweden). This measurement was repeated thrice on different glass discs, and the values are reported here as mean ± standard deviation.

4.2.4 Zeta potential

In the Unpublished Manuscript, zeta potential on the glass disc's surface was obtained using an electrokinetic analyzer (SurPASS, Anton Paar) equipped with an adjustable glass cell at a fixed pH of 7.40. For the measurement, 0.001 M KCl was employed as the electrolyte and 0.05M HCl and 0.05M NaOH for the pH titration.

4.2.5 Protein adsorption and confocal microscopy

In the Unpublished Manuscript, before imaging the glass discs with confocal microscope Zeiss LSM 780 (Carl-Zeiss, Jena, Germany) and Nikon A1R+ (Tokyo, Japan), fluorescently labelled albumin and fibronectin were adsorbed at their surface. Fluorescent dye (Alexa Fluor™ 488 NHS Ester, Invitrogen, Thermo Fisher Scientific, Massachusetts, USA) was used for labelling the proteins, 1.04 dyes/protein for bovine serum albumin/BSA (Sigma-Aldrich, Missouri, USA) and 8.07 dyes/protein for fibronectin (purified from human plasma using gelatin column by Protein Dynamics Group – BioMediTech, Tampere University) respectively.

The proteins were diluted to a protein solution concentration of 10 µg/ml, using the buffer solutions from the previous washing step. Polystyrene (PS) uncoated 6-well plates were used to perform the protein grafting. A pair of 120 µm thick polydimethylsiloxane (PDMS) strips were placed on the well plate, to provide sufficient area (~80-90 mm^2) for the protein drop to reside under the glass disc, as well as spread uniformly across the disc's surface. The contact time was kept to 30 min and the volume of the protein drop was 20 µl. Then, the glass discs were washed with PBS 1X (2ml) thrice for 2 minutes with an orbital shaker at 250 rpm, to remove any excess protein from the surface. Finally, the discs were washed by dipping in distilled water and immediately mounted on glass slides

with 10 µl of ProLong™ Diamond Antifade Mountant, Invitrogen™, Thermo Fisher Scientific (Waltham, Massachusetts, USA). Finally, the mounted samples were covered and placed in dark to cure, for 24h before imaging.

4.3 Cell Culture Tests

4.3.1 Preparation of extracts

Glass powders within the particle size range of 500 – 1000 µm were obtained by crushing and sieving for preparing the extracts. The powders were disinfected by first washing with deionized water, then twice in 70% ethanol for 10 min, and then dried for 2 h at room temperature. Post disinfection, the powders were immersed in the extraction medium for 24 h, prepared from Dulbecco's Modified Eagle Medium/Ham's Nutrient Mixture F-12 (DMEM/F-12 1:1; Life Technologies, Gibco, Carlsbad, CA, USA), which was supplemented with 1% antibiotics (100 U/ml penicillin and 0.1 mg/ml streptomycin; Lonza, Bio-Whittaker, Verviers, Belgium) and 1% L-glutamine (GlutaMAX I; Life Technologies, Gibco). For all the compositions, the ratio of glass to extraction medium was kept at 87.5 mg/ml, similar to [345]. The extraction media was then filtered out using a sterile filter (0.45 µm), and human serum (Biowest, Nuaillé, France) was added to a concentration of 5%. This medium containing the glass ions leached from the powders over 24 h was referred to as Basic Medium (BM) extract, and was stored at +4°C. The control had the same composition, except no glass particles were immersed in it, and is called BM. Every 2 weeks, fresh extracts were prepared, and no precipitation was evidenced throughout the course of the cell culture experiments. Diluted extracts were obtained by mixing 1 part glass extract with 9 parts BM for the 1:10 diluted extract, and with 99 parts BM for the 1:100 diluted extract.

4.3.2 Adipose stem cell isolation, expansion and culture

The study was carried out in accordance with the Ethics Committee of the Pirkanmaa Hospital District, Tampere, Finland (R15161). The hASC were obtained from the subcutaneous white abdominal adipose tissue samples with a written informed consent of the donors. The donors were two women, aged 28 and 62 years.

The hASC were isolated using the protocol described earlier in [346,347]. Then, the hASC were maintained in T75 Polystyrene flasks (Nunc, Roskilde, Denmark) in BM. Post the primary cell culture, surface marker expression of hASC was examined by flow cytometry (fluorescence-activated cell sorting; FACS, FACSAria®; BD Biosciences, Erembodegem, Belgium)[348].The hASC used in this study, had a strong expression of CD73, CD90 and CD105, and negative or very low (<7%) expression of CD3, CD11a, CD14, CD19, CD34, CD45, CD54, CD80, CD86 and HLA-DR. Furthermore, the cells used were in passage 1 (i.e. were subcultured only once after the isolation from adipose tissue).

The cell viability and proliferation analyses were conducted in 24-well plates (Nunc) with plating density ~4200 cells/cm^2 and in 48-well plates (Nunc) with plating density ~8400 cells/cm^2, respectively. The media was replaced with the extract media 24 h after the plating and was marked as day 0 of culture. The cells were fed with fresh extract media twice a week, while the old media was collected and frozen for Lactate Dehydrogenase (LDH) analysis. Control samples were grown in BM.

The cells from both the donors were cultured separately, and the results presented in this study, i.e., Live/Dead, CyQUANT and LDH were performed for both the donors at the same respective time points. As the cells from both the donors behaved similarly with respect to time in culture and across the various glass compositions, the CyQUANT and LDH results were combined.

4.3.3 Cell viability and proliferation

The cell viability was measured qualitatively at day 3, 7 and 14 (referred to as D-3, 7, 14 respectively) using Live/Dead staining (Invitrogen, Life Technologies), as defined in [346]. The cells were incubated in a working solution containing 0.25 µM EthD-1 (staining dead cells red) and 0.5 µM Calcein-AM (staining live cells green) for 30 min. The cells were imaged immediately afterwards, using a fluorescence microscope (IX51, Olympus, Tokyo, Japan) equipped with a fluorescence unit and a camera DP30BMW.

4.3.4 Cytotoxicity assessment

Lactate Dehydrogenase (LDH) Assay Kit (Calorimetric) from Abcam (Cambridge, UK) was used to evaluate the cytotoxicity of the glass extracts at D-3, 7 and 14, using manufacturer's instructions. 20 µl of the previously collected cell media was pipetted in duplicates, supplemented with 30 µl/well of LDH assay buffer. 50 µl/well of working solution

was then added immediately prior to the analysis, and the absorbance at 450 nm at 20 min was measured after adding the working solution. All the values were normalized to the number of cells (obtained from CyQUANT measurements).

4.3.5 Statistical analyses

SPSS Statistics version 25 (IBM, Armonk, NY, USA) was used to perform statistical analyses. The CyQUANT and LDH results are presented as mean and standard deviation (SD). The number of biological replicates was n=6 (3 per cell line) for CyQUANT and n=4 (2 per cell line) for LDH, with 3 measurements/condition for each analysis. The significance of the impact of diluted and undiluted glass extracts was assessed with Mann-Whitney test. The Mann Whitney test is a non-parametric test which evaluates the difference between non-normally distributed data samples. Furthermore, to control the familywise error-rate, Bonferroni corrections were made based on the number of meaningful comparisons. For both the CyQUANT and LDH analyses, the number of meaningful comparisons was 39. The results were considered to be statistically different when the adjusted p-value after Bonferroni corrections was <0.05.

4.4 Glass fibers

4.4.1 Core preforms

The core preforms having the composition Sr50 and Ce-1 (Table 4.1) were obtained by melting batches of 45g using analytical grade chemicals. The chemicals and glass melting protocols are described earlier in the section "**2.1.1** Glass melting".

4.4.2 Core-clad preforms

The core-clad preform, with core being Ce-1 and clad being Sr50, was obtained using a homemade rotational caster. First, the clad composition was poured in a pre-heated brass mold (350°C), which is spun at 1000 rpm for 10 s, resulting in the formation of a hollow cylinder in the mold. Then, the core composition was poured slowly inside the hollow cylinder (cladding). The obtained core-clad preform was then annealed in the same way as the core preforms. The process was optimized in the same way as in [349], to guarantee a constant $Ø_{clad}$/ $Ø_{core}$ before and after fiber drawing. The addition of 1 mol%

of CeO_2 to the glass composition did not result in a significant change in the thermal expansion coefficient, and all the processed core-clad preforms were free from cracks and other defects.

4.4.3 Fiber drawing

For fiber drawing, the “rod” method was employed in a specially designed single zone drawing tower furnace. The temperature profiles of the tower were accurately mapped in advance, to prevent nucleation or crystallization, and the dwell times in the zones were controlled before and during the drawing. The thermal profiles for different setting temperatures were performed by using a thermocouple attached to the preform motion cane. After the furnace stabilized to the set temperature, the thermocouple was gradually lowered into it, while the thermocouple temperature and position were registered in the meantime, as presented in Figure 4.2. All the fibers were obtained at a drawing temperature of 645°C under a laminar He flow of 2.5 l/min. This temperature corresponded to a set temperature of 770°C (Fig-1). The high thermal conductivity of He aided in minimizing the dwell time before drop formation and during drawing. K_{He} = 33.63 × 10^{-5} cal·$sec^{-1}cm^{-1}°C^{-1}$, K_{Ar} = 4.06 × 10^{-5} cal·$sec^{-1}cm^{-1}°C^{-1}$, K_{air} = 5.68 × 10^{-5} cal·$sec^{-1}cm^{-1}°C^{-1}$ [350]. The drawing temperature was calculated based on the T_g and the thermal profile of the furnace. To obtain the fibers, the glass rod was placed into the furnace and the temperature was gradually increased until the formation of a drop. During drawing, the temperature was adjusted corresponding to the readings of the tension measurement gauge. The fiber was fixed on a rotary drum, and the fiber diameter and drawing tension were optimized by a computer system based on the LabView software.

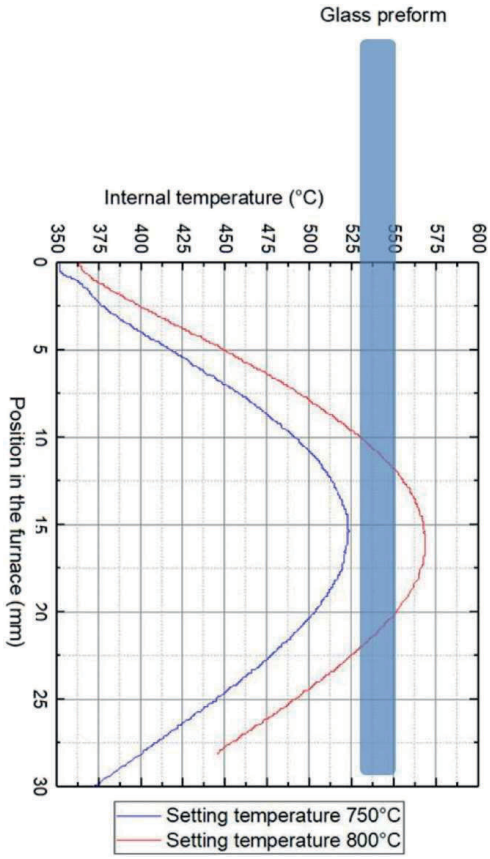

Figure 4.2. Thermal profiles of the drawing tower furnace. The zero mm position corresponds to the top of the heating element.

4.4.4 Refractive index measurements

2 mm thick bulk glass samples of core and cladding compositions were used for the refractive index measurements. Either faces of these samples were polished beforehand with SiC polishing paper (600, 800, 1200, 2400 and 4000 grit). The refractive index was measured using a fully automated Metricon, model 210 prism coupled refractometer, at 1060 nm.

4.4.5 Immersion tests

Immersion tests were performed by entirely immersing 10 fibers of length 15 cm each in 50 ml of TRIS buffer solution for up to 6 weeks. The media was not refreshed at any moment during the course of immersion. The same equipment and parameters were used for carrying out the immersion tests as for the glass powders in section **2.1.6** in-vitro dissolution.

4.4.6 Mechanical testing

The mechanical tests were performed, in tension (static), on the core and core-clad fibers before and after immersion in TRIS buffer solution. Post immersion, the core and core-clad fibers were collected, rinsed with acetone and dried in air overnight in an incubator at 37°C. The fibers were stored in a desiccator before testing. The measurements were carried out at ambient temperature with an Instron 4411 Materials Testing Machine, with a grip distance of 50 mm, load cell of 500 N and a crosshead speed of 30 mm/min. The metallic grips were padded with a rubber mat to avoid slipping of the fibers, and inflicting damage on the fibers during the measurements. The tensile strength and Young's modulus were calculated for 10 test fibers, and presented as mean ±standard deviation. Despite the low number of specimens, the Weibull modulus was calculated as reported in [15,351].

4.4.7 Light loss

The optical losses from the fibers were measured with the cut back technique. The signal from the FTIR spectrometer transmitted through a long piece of fiber (L_1) was measured (I_1) using a nitrogen cooled InSb detector. Then, without disturbing the input end, the fiber was cleaved and the output fiber signal was recorded (I_2). Using the signals I_1 and I_2, the cut length L_1 - L_2, the losses were calculated with the following equation:

$$Losses\ \left(\frac{dB}{m}\right) = \frac{10}{L_1 - L_2} \times \log\left(\frac{I_2}{I_1}\right)$$

The measurement was repeated several times to improve the accuracy.

The light transmission as a function of immersion time was obtained in the wavelength range of 200 -1000 nm. One end of a 50 cm long fiber was connected to a light source and the other to a spectrometer. The fibers were cleaved and coupled using a Thorlabs FC connector (Newton, New Jersey, USA). The position of the lamp was adjusted in

order to maximize the light intensity at the fiber output. A sensing region in the fiber was created beforehand by etching away the cladding of a portion of the fiber (5 cm) by immersing in 1M phosphoric acid. The sensing region of the fiber was immersed in TRIS buffer solution. For illumination and collecting the light, a broadband white light source (Edmund BDS130) and a Thorlabs Compact Spectrometer CCS200 were used respectively. The time period for light accumulation was set to 7.5 ms, to maximize the signal, and the light intensity at 680 nm was tracked as a function of immersion time. The signal obtained before immersion was normalized to 1, and the other intensities as reported relative to it. The TRIS solution was replaced with fresh TRIS solution every week, to avoid significant evaporation of the solution. As evaporation would increase the surface area to volume of the solution ratio, it may lead to a change in the dissolution rate.

5 Results

5.1 Characterization of new phosphate glasses

In Publication I-II, new doped and undoped PG were introduced. The glasses belonged to the general composition $[x(M_nO_m)+(100-x)(0.5P_2O_5+0.2CaO+0.2SrO+0.1Na_2O)]$ where M_nO_n (dopant metal oxides) were Ag_2SO_4, CuO or Fe_2O_3, and x (dopant concentration) $\in \{1, 2, 3, 4, 5\}$. The thermal, physical, structural and in-vitro dissolution properties of these glasses were obtained, and the results are presented below.

5.1.1 Physical properties

Density and molar volume of the glasses under investigation are presented in Figure 5.1 as a function of dopant concentration, x. For Ag doped glasses (Figure 5.1 a), the density increased almost linearly with an increase in x, while the molar volume remained constant, within the accuracy of measurement. In case of Cu-doped glasses (Figure 5.1 b), the density remained constant, whereas the molar volume decreased with an increase in x. For the Fe doped glasses (Figure 5.1 c), the density and molar volume were found to be independent of x.

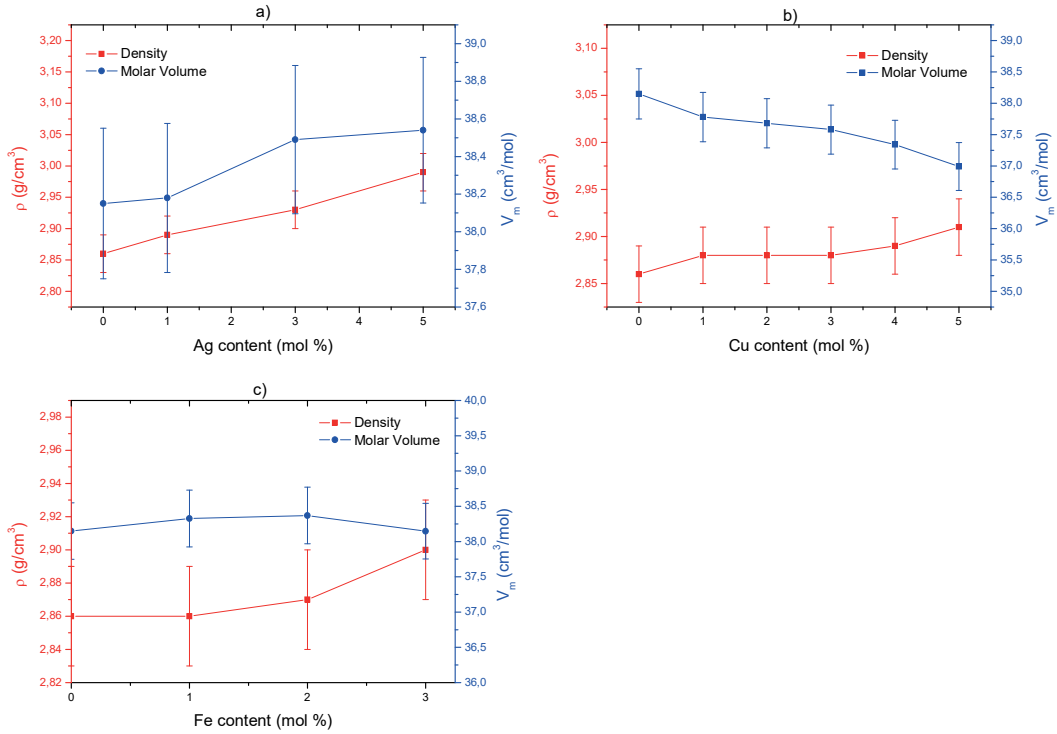

Figure 5.1 Density and molar volume of a) Ag, b) Cu and c) Fe glasses as a function of dopant concentration (Publication I and II)

5.1.2 Thermal properties

The thermal features, such as the glass transition temperature (T_g), onset of crystallization temperature (T_x) and the thermal processing window ($\Delta T = T_x - T_g$) of the glasses under investigation are presented in Figure 5.2 a), b) and c). With an increase in x for Ag glasses (Figure 5.2 a), T_g decreases, whereas T_x exhibits a maxima at x =2 mol%, and ΔT at x=2 and 3 mol%. For the Cu glasses (Figure 5.2 b), while T_g appears to remain constant regardless of x, T_x exhibits a steep increase when 1 mol% of CuO is doped into the glass. With further increasing the copper content, no significant change in T_x is measured. The steep increase in T_x for Cu-1 lead to an increase in the ΔT, which then remained constant with further increase in x. In case of the Fe glasses (Figure 5.2 c), the T_g and T_x are found to increase with an increase in x, whereas ΔT remains constant with

respect to x. All the doped glasses, at the exception of the Fe glasses, exhibit a ΔT > 120ºC.

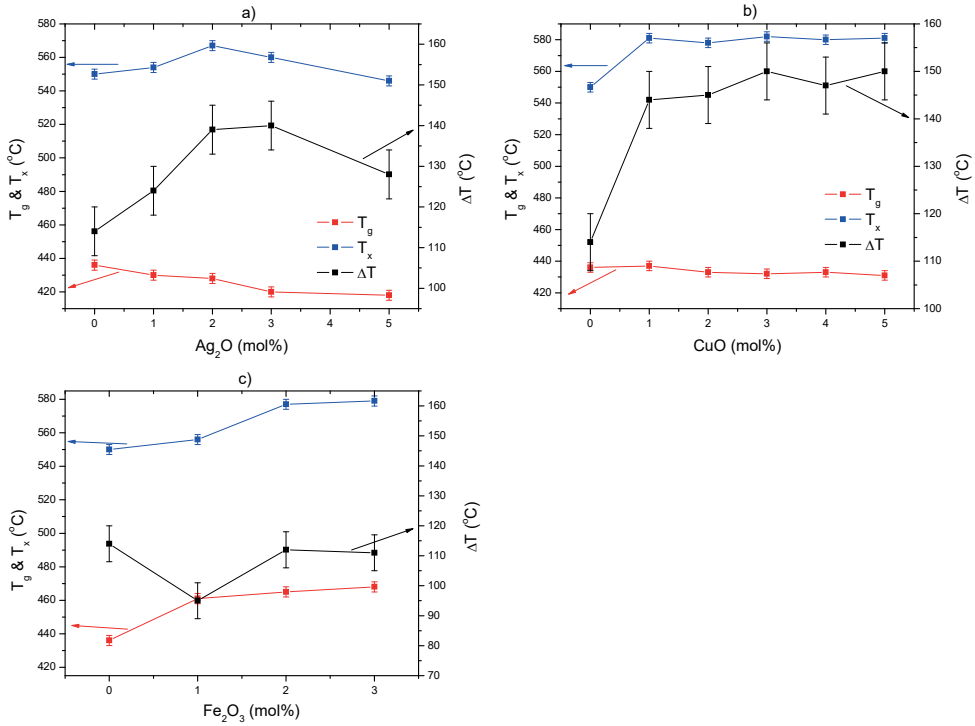

Figure 5.2 T_g, T_x and ΔT of a) Ag, b) Cu and c) Fe glasses as a function of dopant concentration (Publication I and II)

5.1.3 Structural properties

The FTIR-ATR and Raman spectra of the glasses under investigation are presented in Figure 5.3 and Figure 5.4 respectively, as a function of x. Additionally, the attributions for all the FTIR-ATR and Raman bands are illustrated in Table 5.1. All the spectra were normalized to the band having maximum intensity, at ~880 cm^{-1}. The bands at 1260, 1085, 880, 775 and 718 cm^{-1} and two shoulders at ~1154 and 980 cm^{-1} can be observed in all the spectra, as typically seen in the case of metaphosphate glasses [25,282]. With an increase in x, a slight decrease can be observed in the band intensity at 1260 cm^{-1} for all the glasses. Furthermore, for the Cu and Fe glasses, a decrease in intensity of the

band within the range 700-800 cm^{-1} can be evidenced with increasing x. The other bands/shoulders' position and intensity were found to be independent of x.

All the Raman spectra were normalized to the band with maximum intensity, at 1175 cm^{-1}. The spectra exhibit four bands and one shoulder, all attributed to the metaphosphate glass structure. With an increase in x, all the glasses presented an increase in intensity of the band at ~695 and 1020 cm^{-1}, and the shoulder at 1090 cm^{-1}. The band at 1260 cm^{-1} remained unchanged in the case of Ag and Cu glasses, whereas the intensity was found to increase in the Fe doped glasses with an increase in x.

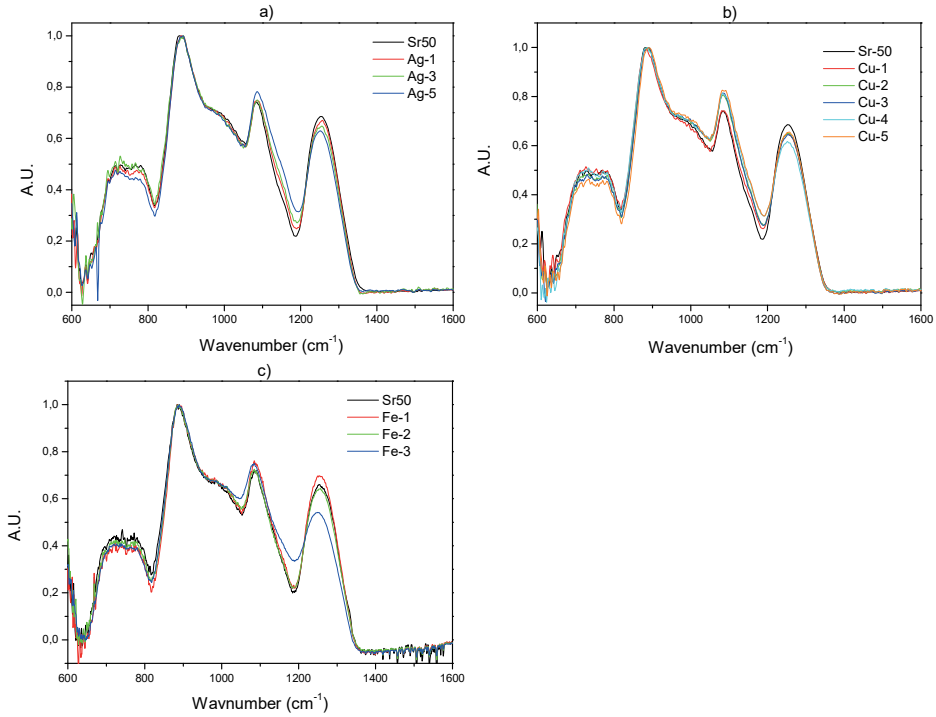

Figure 5.3 FTIR–ATR spectra of the a) Ag, b) Cu and c) Fe glasses (Publication I and II)

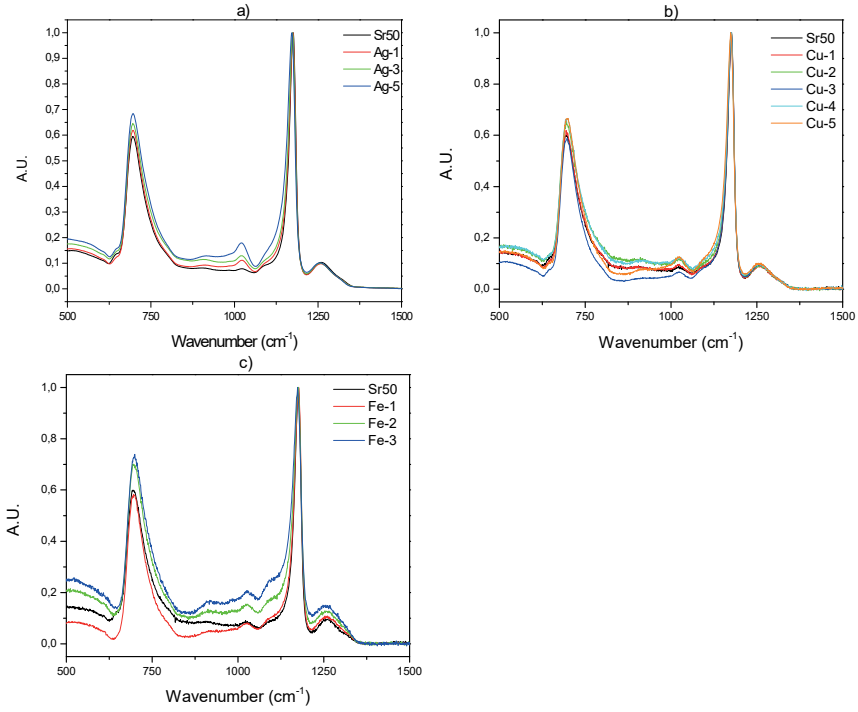

Figure 5.4 Raman spectra of the a) Ag, b) Cu and c) Fe glasses (Publication I and II)

Table 5.1 FTIR-ATR and Raman bands attribution

FTIR-ATR		
Wavenumber (cm^{-1})	Attribution	Reference
718-775	ν_s P-O-P in metaphosphate	[352]
880	ν_s P-O-P in Q^2	[353,354]
980	ν_s PO_3^{2-} in Q^1	[354–356]
1085	ν_{as} PO_3^{2-} in Q^1. PO_2 in Q^2	[352]
1154	ν_s PO_2^- in Q^2	[354–356]
1260	ν_{as} PO_2^- in Q^2	[354–356]
Raman		
695	P-O-P in chains	[352,357,358]
1020	ν_s NBO in Q^1	[352,357,358]
1090	Terminal oxygen bond	[352,357,358]
1175	ν_s PO_2 chains	[352,357,358]
1250	ν_{as} PO_2 chains	[352,357,358]
1320	P=O	[352,357,358]

5.1.4 Optical properties

The UV-Vis absorption spectra of the Ag, Cu and Fe glasses are presented in Figure 5.5 a), b) and c) respectively. No absorption bands were observed in the case of Ag glasses. On the other hand, Cu glasses presented a band at 850 nm, and Fe glasses presented a band at ~1020 nm and a shoulder at ~450 nm. With an increase in x, the optical band gap shifted to higher wavelengths in all the Figures, and the intensity of the absorption bands observed in Cu and Fe glasses increased in intensity with x.

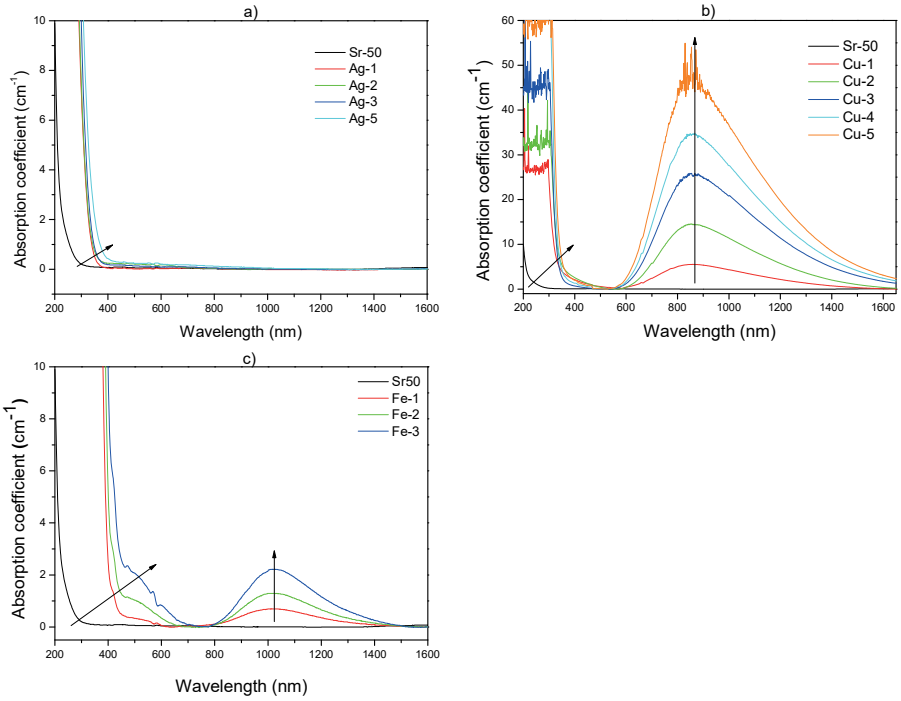

Figure 5.5 UV-Vis spectra of the a) Ag, b) Cu and c) Fe glasses (Publication I and II)

5.1.5 *In-vitro* dissolution characteristics

The impact of doping on the dissolution characteristics of the glasses was assessed by immersing the glass powders in TRIS buffer solution up to 42 days.

5.1.5.1 Change in pH

The pH of the TRIS buffer solutions before and after immersion were recorded at 37±0.2°C (Figure 5.6 a), b) and c)), to evidence the change in pH due to immersion. For the Ag and Cu glasses, a clear decrease in the pH with an increase in immersion time, as well as x can be evidenced. However, Cu-5 exhibited less change in pH than the glasses with lower Cu content. While for the Fe glasses, the pH of the solutions remained constant over time and with x.

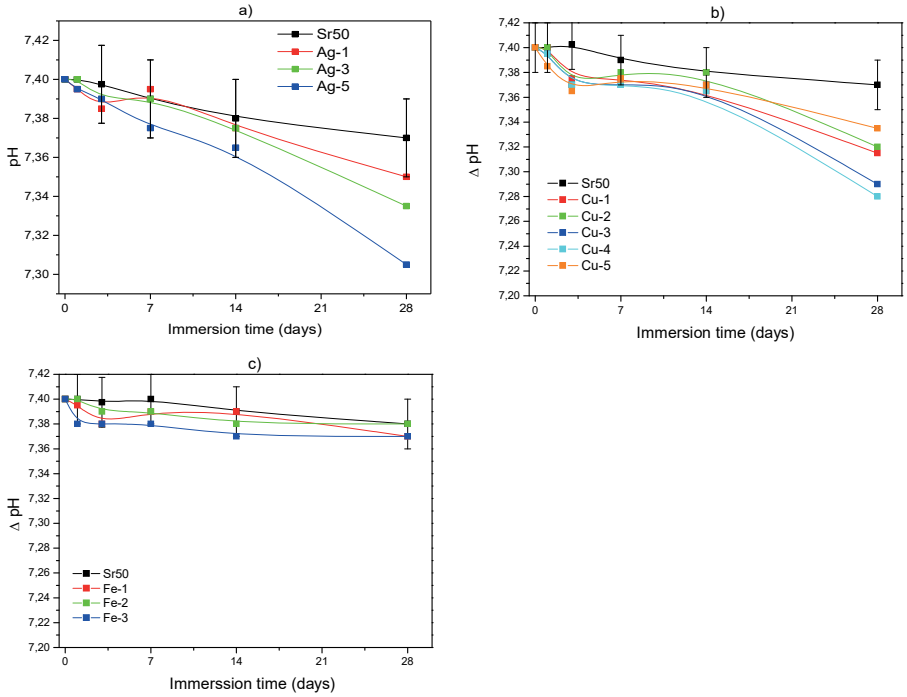

Figure 5.6 pH as a function of immersion time of the a) Ag, b) Cu and c) Fe glasses (Publication I and II)

5.1.5.2 Ion release

The ion release behavior of the glasses was assessed with ICP-OES analysis, and the results are presented in Figure 5.7, 5.8 and 5.9 for Ag, Cu and Fe glasses respectively. With an increase in Ag_2O concentration, an increase in the release of all the ions was observed, despite the initial lower P, Ca, Na and Sr content in the base glass due to the Ag doping. Furthermore, the concentration of Ca, Sr, Na and P were found to increase

linearly up to 7 days, after which it remained constant until 28 days, except for the Ag5 glass. In the case of the Ag5, while Ca, Sr and P seem to saturate, the release of Na remain linear for the whole duration of the immersion. Ag ions in the solution could not be quantified due to a high signal to noise ratio.

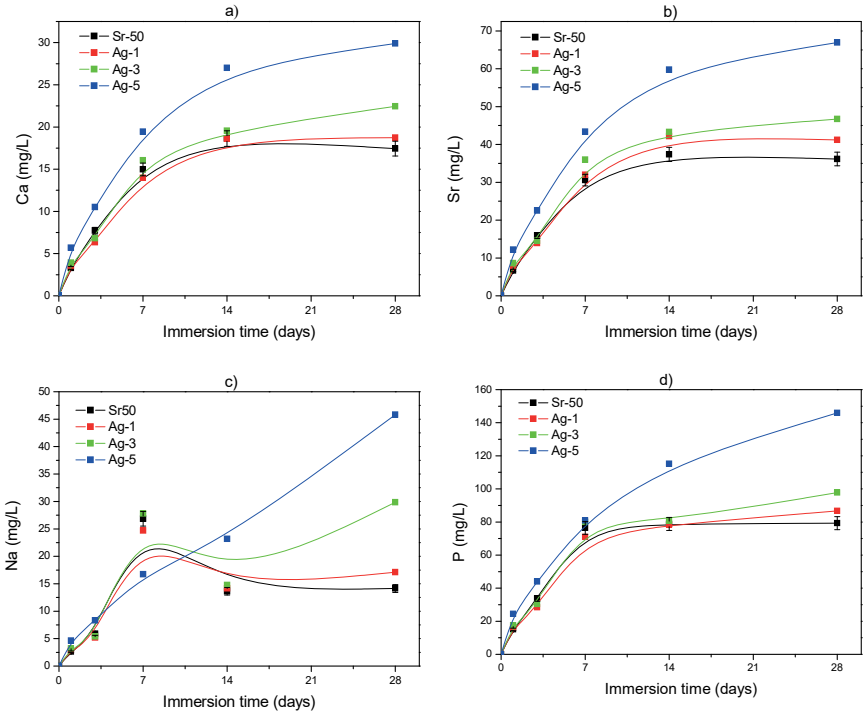

Figure 5.7 Concentration of a) Ca, b) Sr, c) Na and d) P ions in TRIS buffer solution as a function of immersion time for Ag glasses (Publication I)

For the Cu glasses as well (Figure 5.8), the ion concentrations were found to increase with an increase in the dopant concentration, except Cu-5, which exhibited a lower ion release than Cu-4. Furthermore, the ion release was found to be linear up to 7 days, after which it saturated. The release of Cu from these glasses could be evidenced, and was found to be almost linear up to 28 days.

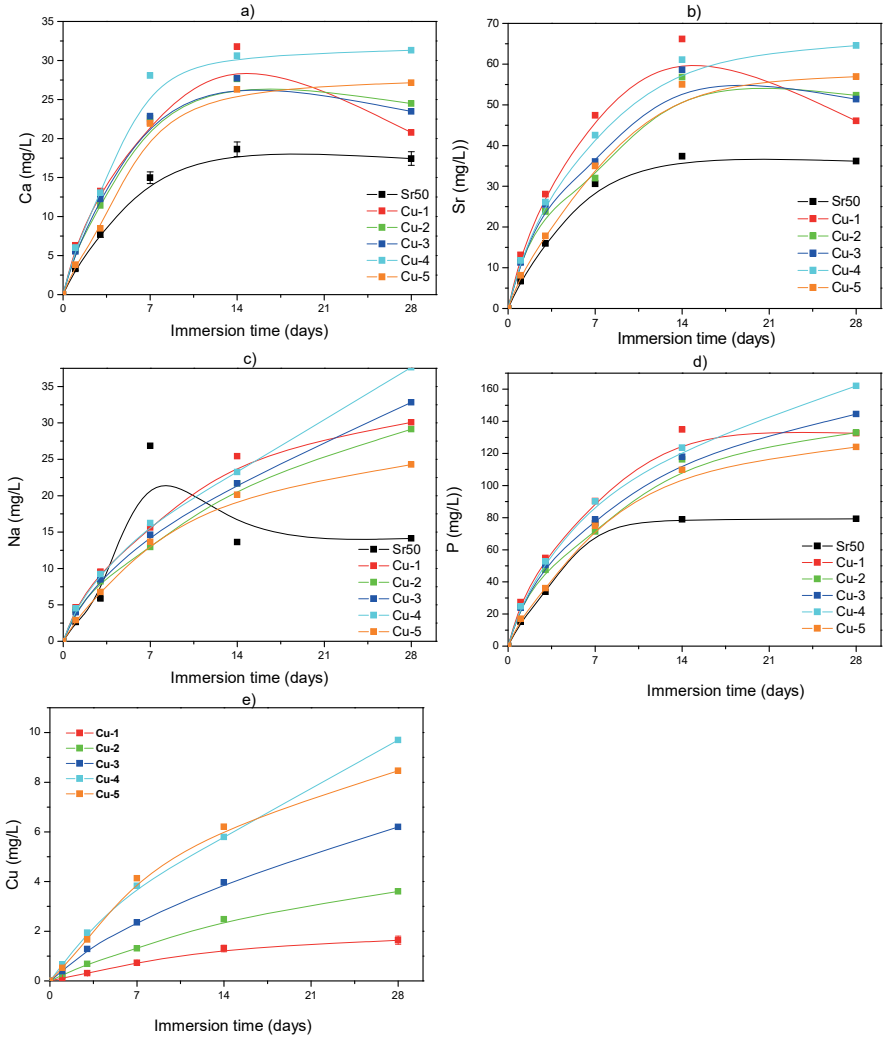

Figure 5.8 Concentration of a) Ca, b) Sr, c) Na d) P and e) Cu ions in TRIS buffer solution as a function of immersion time for Cu glasses (Publication II)

In Figure 5.9, all the Fe glasses presented a lower ion release than the reference Sr50, and an increase in Fe_2O_3 concentration was found to lower the ion release. All the ions were released almost linearly over the 28 days of immersion. Similar to the Ag ions, Fe release could not be evidenced due to a high signal to noise ratio.

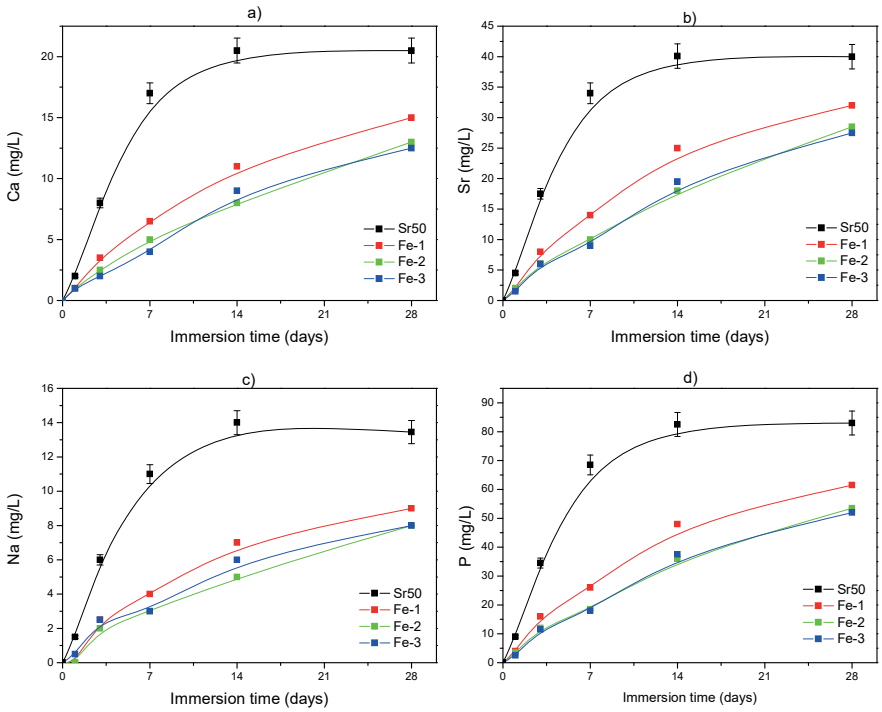

Figure 5.9 Concentration of a) Ca, b) Sr, c) Na and d) P ions in TRIS buffer solution as a function of immersion time for Fe glasses (Publication II)

5.1.5.3 Change in structure

The FTIR-ATR spectra of the reference Sr50, Ag-5, Cu-5 and Fe-3 are presented as a function of immersion time in Figure 5.10 a), b), c) and d) respectively. All the glasses depicted a drop in the intensity and shift of the bands at 775 and 1260 cm^{-1} to lower wavenumber. The highest band at 890 cm^{-1} shifted to lower wavenumber for all the glasses. The band at 1085 cm^{-1} decreased in intensity for Sr50, whereas for Ag glasses it decreased until 14 days, then increased and shifted to higher wavenumber. For Cu-5, it increased in intensity and shifted to higher wavenumber. For all the glasses except Sr50, appearance of new bands was observed at 988 and 1030 cm^{-1}.

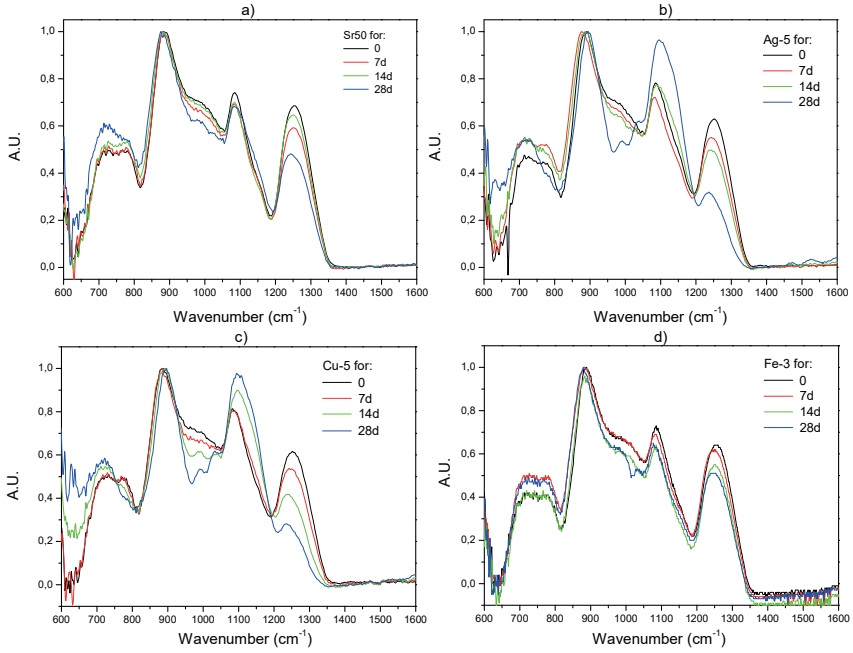

Figure 5.10 FTIR–ATR spectra of the a) Sr50, b) Ag, c) Cu and d) Fe glasses as a function of immersion time in TRIS buffer solution (Publication I and II)

5.1.5.4 Precipitation of a surface layer

The pre and post immersion SEM images of Sr50, Ag-5 and Cu-5 are depicted in Figure 5.11. For immersion up to 7 days, no surface layer could be observed on any of the glasses. After 14 days, a surface layer appeared at the surface of Ag-5 and Cu-5. However, no surface layer was observed on Sr50 and Fe-3 even after 28 days of immersion.

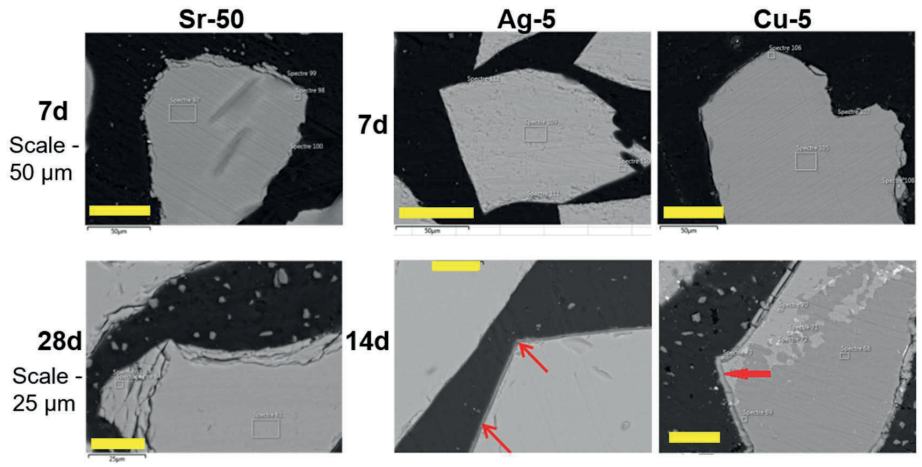

Figure 5.11 SEM images of Sr50 after 7 and 28 days of immersion, and Ag-5 and Cu-5 after 7 and 14 days of immersion. Scales on the images in the rows above and below correspond to 50 µm and 25µm respectively (Publication I and II)

5.1.6 Antimicrobial properties

Figure 5.12 illustrates the antimicrobial properties of Sr50, Ag-2, Ag-5, Cu-2 and Cu-5 glass powders, with two different particle size ranges 125-250 µm and <125 µm. For both the particle size ranges, the tests were performed at 400 and 1200 mg/ml glass concentrations. For the 125-250 µm range, well known SG S53P4 was also included in the study as a reference. The control contained only the culture medium with bacteria. The y-axis represents, on a logarithmic scale, the number of bacteria surviving in the solutions containing the glass powders. Thus, a low CFU value is indicative of a high antimicrobial effect. In the 125-250 µm size range, S53P4 presented a slight increase in bacterial count as compare to the control. Among PG, Sr50 and Cu glasses depicted a slightly lower CFU than S53P4, whereas the reduction in CFU was much higher in the Ag glasses. With an increase in glass concentration, the CFU values were lower for all the glasses.

For the smaller particle size range <125 µm, all the PG presented a significantly lower CFU than the control. The CFU values were found to further reduce with an increase in glass concentration from 400 to 1200 mg/ml. The Cu glasses exhibited a lower CFU than the Sr50, and a higher x was also found to reduce the bacterial count. However, with the Ag glasses, complete eradication of the bacteria was observed irrespective of the glass or dopant concentration.

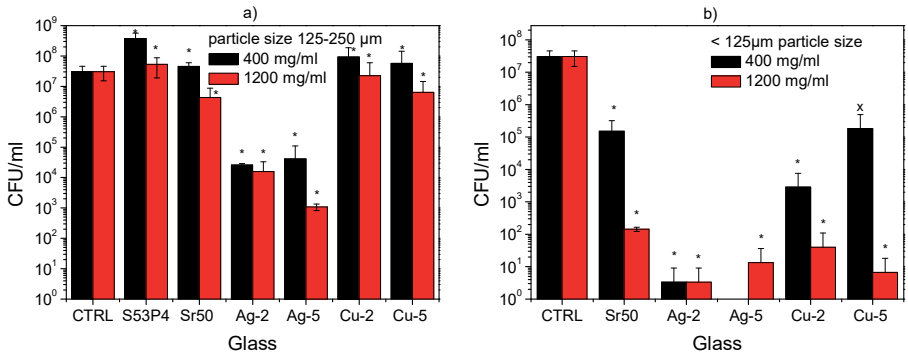

Figure 5.12 S. epidermidis growth as a function of glass concentration, for particle sizes a) 125–250 µm and b) >125 µm. *Values significantly different ($p < 0.05$) from control and Sr50; X Value only significantly different ($P<0.05$) from control (Publication II)

5.2 Preliminary cell culture tests

5.2.1 Cell culture on glass discs

hASC and fibroblasts were cultured on the Sr50 glass discs up to 14 days. Live/dead staining was performed at D-2, 7 and 14 to assess their viability on the glass' surface (Figure 5.13) and in glass extracts (Figure 5.14), relative to the control, which was the cell culture well plate bottom. As expected with such cells, at the bottom of the well plate (control) an increasing amount of green fluorescence can be seen with increasing the culture time. At the surface of the glass Sr50, very few live (green) cells were observed on the glass discs at all the time points. Furthermore, the cells on glass discs appeared

round and small, in contrast to the elongated spindle shaped cells in control, irrespective of the cell type used (fibroblasts vs hASC).

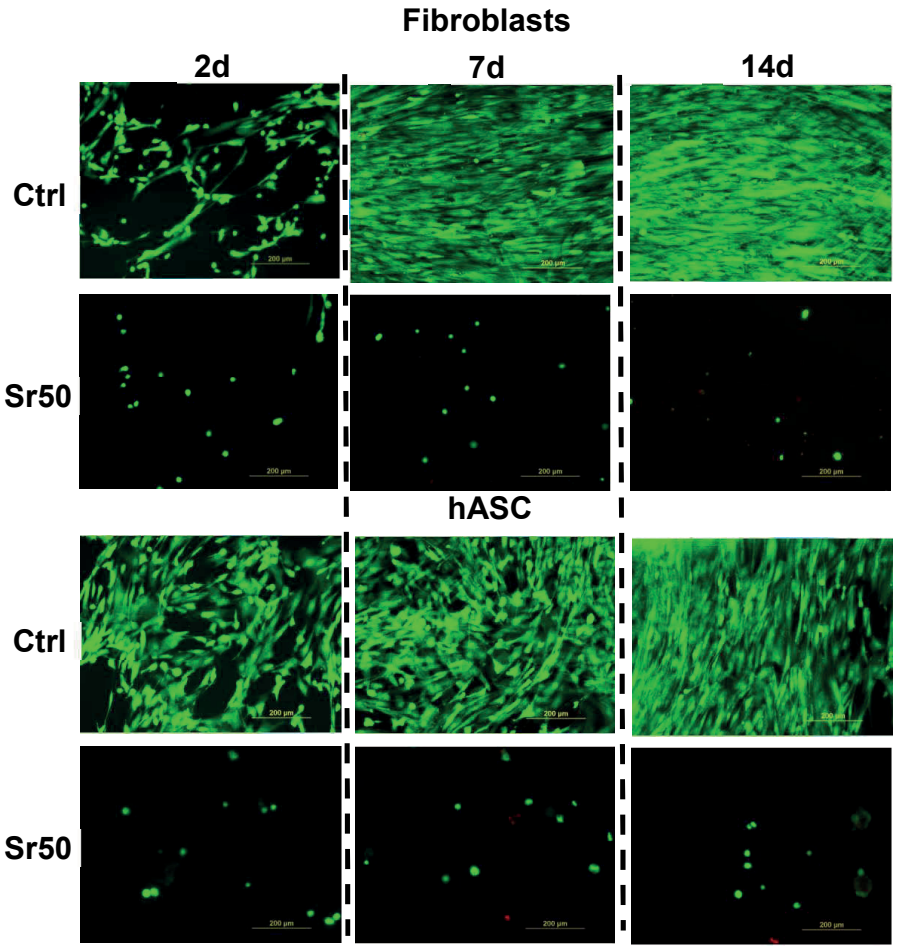

Figure 5.13 Live/dead staining images of the glass disc surface, at days 2, 7 and 14 of culture. The scale bar corresponds to 200 μm (unpublished results)

In Figure 5.14, live cells were observed at all the time points for both the control and Sr50 extract. For the control, the amount of cells appeared to increase from D-2 to D-7, and from D-7 to D-14 for both the cell types. For Sr50, the amount of fibroblasts increased from D-2 to D-7 and then remained constant from D-7 to D-14. It is worth mentioning that some red (dead) cells could be imaged at D7. The amount of hASC in Sr50 extract was found to increase from D-2 to D-7, and then decrease again at D-14. Overall, the amount

of cells were nearly identical in both control and Sr50 at all the time points, except for hASC in Sr50 extract at D-14 condition. In both the control and Sr50 extract, the cells were found to be elongated and spindle shaped.

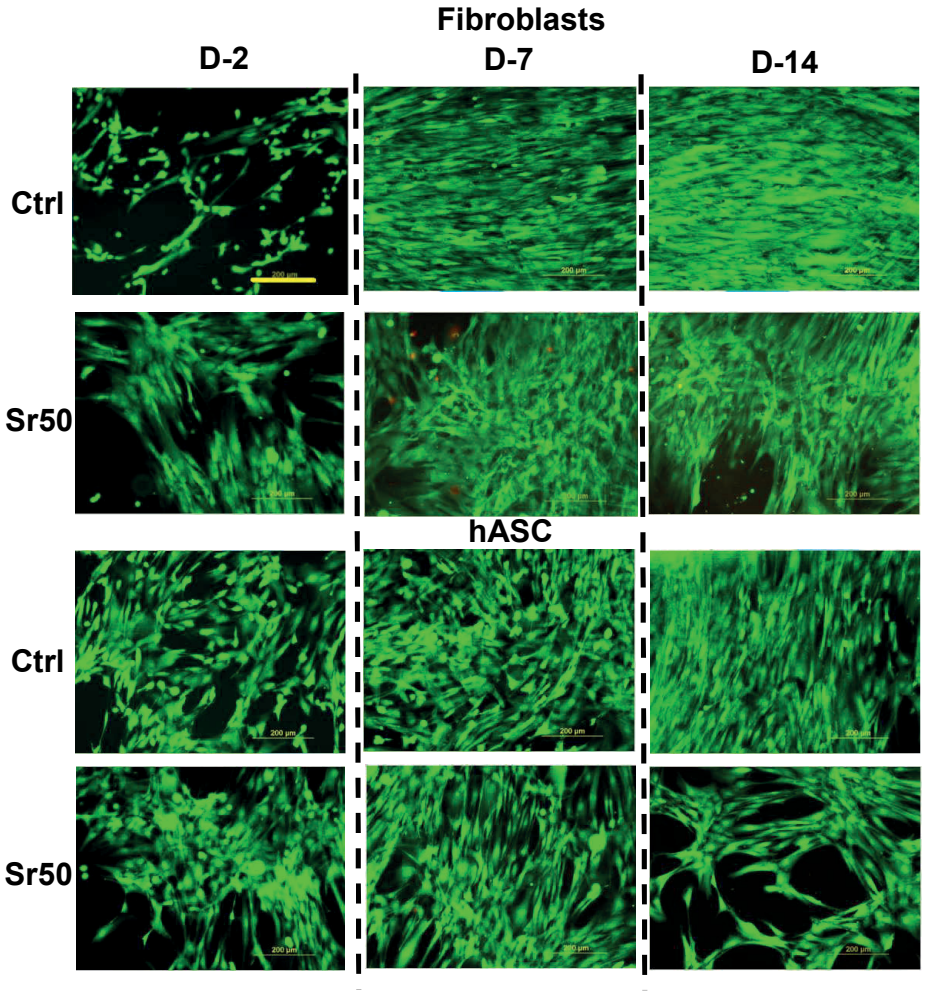

Figure 5.14 Live/dead staining images of the bottom of the well plate, at days 2, 7 and 14 of culture. The scale bar is shown in the control at D-2, and corresponds to 200 µm (unpublished results)

5.2.2 Cell culture in glass extracts

Cell tests with hASC were conducted in the extracts of Sr50, Ag-2, Ag-5, Cu-2, Cu-5, Ce-2 and Ce-5, which were obtained by enriching the cell culture medium with glass dissolution products. Here it is important to note that the Fe glasses were replaced by Ce glasses. This is due to the reduction in thermal processing window up on doping with Fe. Instead, previously studied glasses containing Ce, developed in the group, were chosen to replace Fe glasses for further investigations. The Ce glasses depicted a wider thermal processing window while maintaining a slow dissolution rate, and promising in-vitro dissolution properties in [282]. Figure 5.15 presents the live dead images of the bottom of the plate, at D-3 and 7 of the culture. At D-3, a high amount of live cells may be observed in all the conditions except Ag-5 and Cu-5. However, at D-7, almost no live cells could be observed in Ag-2 and Cu-5. In case of Sr50, Ag-2 and Ce-5, an increase

in the amount of cells were observed, and for the rest of the extracts, it remained constant or decreased.

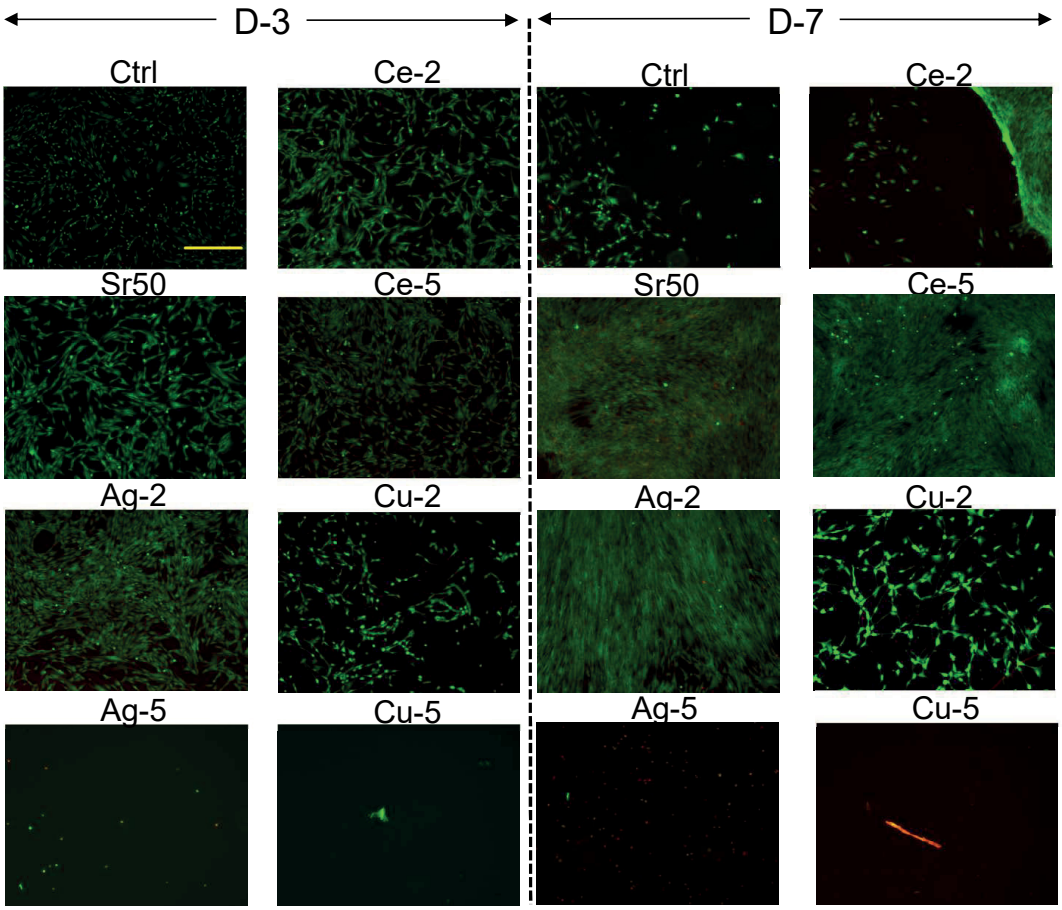

Figure 5.15 Live/dead staining images of the bottom of well plate, at D-3 and 7 of culture. The scale bar is shown in the control at D-3 condition, and corresponds to 500 μm (unpublished results)

Figure 5.16 depicts the CyQUANT analysis results of the extracts under investigation, at D-7 and 14 of the culture. In case of the control and Ce-5, and increase in the number of cells with time in culture may be observed. For Sr50 and Ce-2 the amount of cells was significantly higher but remained constant for longer culture time. The amount of cells upon exposure to the Ag-2, Ag-5, Cu-2 and Cu-5, was very low. Nearly no cells were evidenced at either time point.

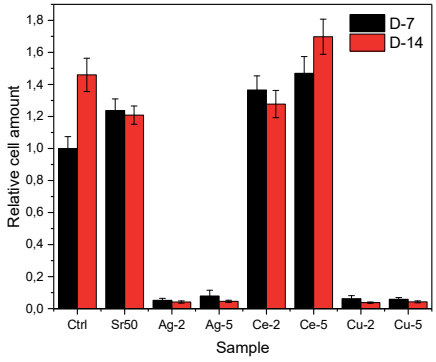

Figure 5.16 The proliferation of hASC cultured in the glass extract media analyzed with CyQUANT Cell Proliferation Assay kit at 7 and 14 days of culture. All the values presented are relative to the control at D-7 (unpublished results)

5.3 Improving cell attachment on phosphate glasses

In this study (Unpublished manuscript), PG from Publication I-II were studied in terms of their ability to adsorb proteins at their surface, relative to the commercially available silicate bioactive glasses 13-93 and S53P4. In order to improve the protein adsorption, the glasses were treated by washing in acidic, neutral and basic buffer solution, followed by silanization. The adsorption of albumin and fibronectin on the glass surfaces was evidenced with confocal microscopy, with a view to assess the impact of washing in different buffer solutions as well as silanization. Furthermore, the glasses were characterized in terms of the impact of these surface modification steps on their surface structure and surface chemistry.

5.3.1 Impact on structure due to washing and silanization

As the glasses were exposed to aqueous media of varying pH, a change in the short range structure and surface charge of the glasses was expected. The FTIR-ATR spectra of the SG and PG in this study are presented in Figure 5.16 and 5.17 respectively, as a function of washing (WA, WN and WB) and then silanization (WAS, WNS, WBS). In Figure 5.16, the IR spectra of the untreated 13-93 and S53P4 exhibit three adsorption bands at 740, 870 and 992 cm^{-1}. All the spectra were normalized to the band at 870 cm^{-1}. Generally, these bands are assigned to Si-O-Si bending, Si-O-Si symmetrical stretching mode and Si-O-NBO vibration, respectively [359,360]. As seen in earlier studies, these spectra are typical of silicate bioactive glasses, mainly composed of Q^2 and Q^3 units [359–362]. The intensity and position of the bands are found, however, to vary depending on the type of buffer solution used for the washing. The spectra of the base washed (WB) sample remains largely unchanged for both the glass S53P4 and 13-93. Upon washing in neutral buffer solution (WN), new bands at 1045 cm^{-1} and 1236 cm^{-1} appeared for both glass composition. However, it is worth mentioning that the intensity of these bands, when compared to the band at 870 cm^{-1} are significantly higher in the case of S53P4. Finally, upon washing of the glass 13-93 in acid, the absorption band at 1045 cm^{-1} and 1236 cm^{-1} increased in intensity. In the case of WA S53P4, the band at 870 cm^{-1} almost completely disappeared, while a sharp band at 1032 cm^{-1} with shoulder

at 1240 cm^{-1} were clearly visible. On the other hand, the intensity and location of the bands remained unaffected by silanization.

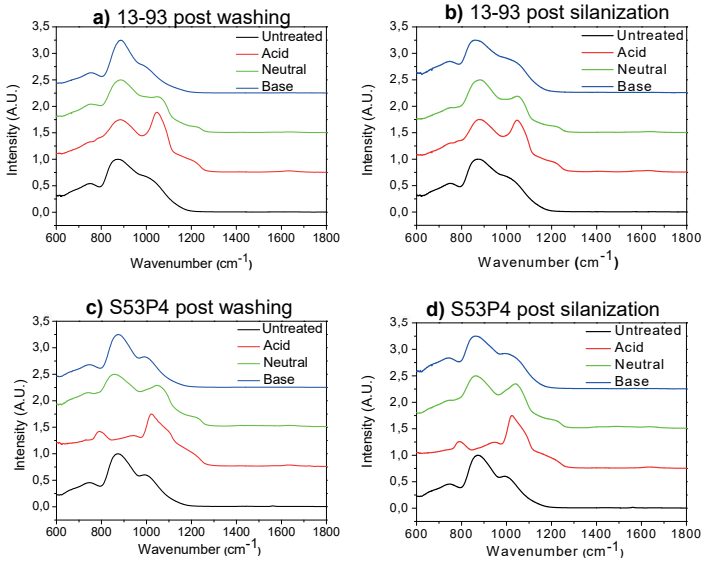

Figure 5.16 FTIR-ATR spectra of the SG a) 13-93 post washing, b) 13-93 post silanization, c) S53P4 post washing and d) S53P4 post washing (Unpublished Manuscript)

Figure 5.17 presents the FTIR-ATR spectra of the PG included in this study. The spectra of these glasses, prior to any surface treatment, exhibit absorption bands at 708, 782, 865, 1078 and 1234 cm^{-1}, and a shoulder at 980 cm^{-1}. All the spectra were normalized to the band having the maximum intensity at 865 cm^{-1}. All the bands could be attributed to a classical metaphosphate glass structure.

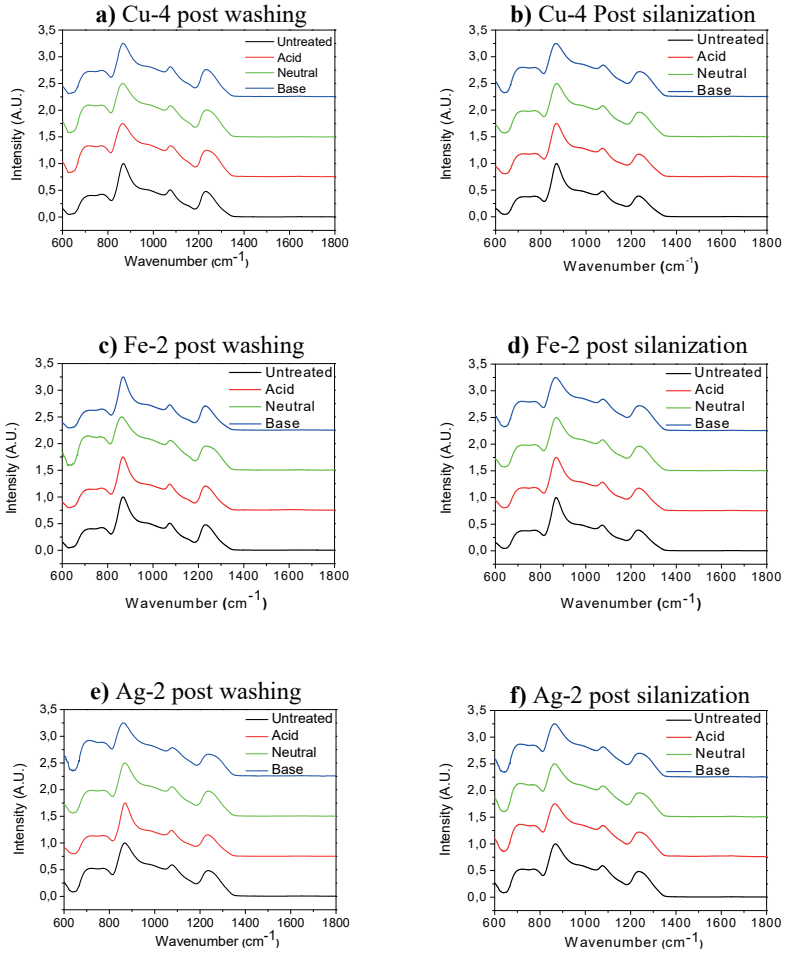

Figure 5.17 FTIR-ATR spectra of the PG a) Cu-4 post washing, b) Cu-4 post silanization, c) Fe-2 post washing, d) Fe-2 post silanization, e) Ag-2 post washing and f) Ag-2 post silanization (Unpublished Manuscript)

5.3.2 Impact on contact angle due to washing and silanization

Figure 5.18 presents the contact angle of a water droplet at the surface of the SG and PG, based on the pH of the buffer solution used for washing: a) acid, b) neutral and c) base. 13-93 had the highest contact angle among all the glasses of investigation. In the untreated condition, all the glasses presented a contact angle <20°, except 13-93, for which it was ~34±7 °C. In case of the SG, no change in the contact angle could be seen in the WA and WN conditions (Figure 5.18a and b respectively). However, for WB condition (Figure 5.18c), a drop in the contact angle of 13-93, and to a lower extent S53P4, can be observed. After silanization, an increase in the contact angle of both the SG was evidenced. On the other hand, for PG, the contact angle reduced upon washing, irrespective of the buffer solution used for washing. Upon silanization, the contact angle increased in the case of PG, to similar values than the SG.

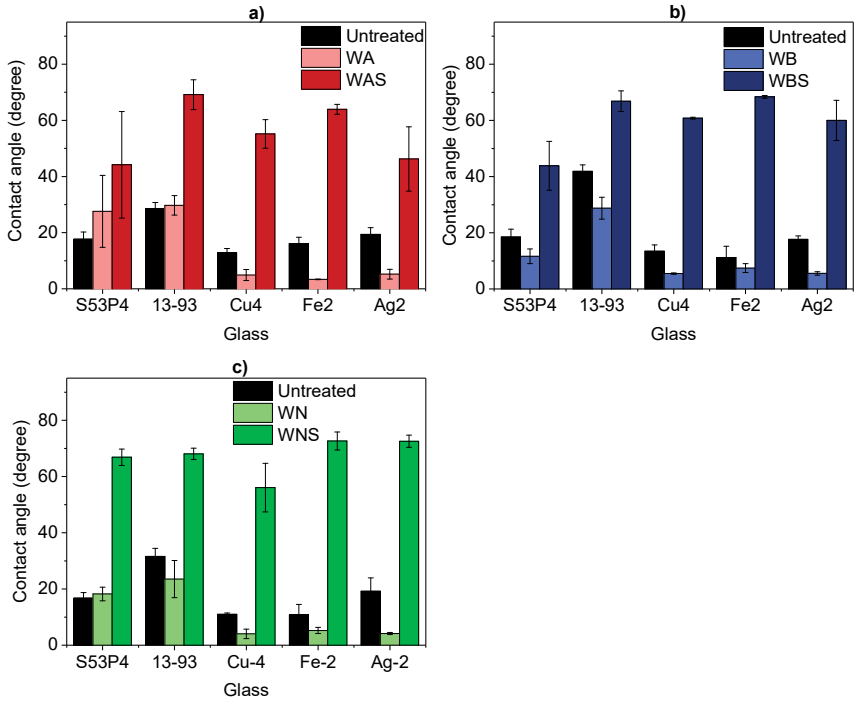

Figure 5.18 Contact angle of the SG and PG post washing and silanization, after a) Acidic buffer wash, b) Neutral buffer wash and c) Basic buffer wash (Unpublished Manuscript)

5.3.3 Impact on surface charge due to washing and silanization

Figure 5.19 depicts the variation of zeta potential (at pH 7.4) at the surface of the S53P4 and Ag-2 glass discs, taken as examples, as a function of washing in different buffers and post silanization. Initially, the zeta potential was similar for both the glasses. Upon washing, no change in the zeta potential In the case of S53P4 could be observed. However, post silanization, the zeta potential dropped for all the conditions compared to the only washed samples, with a minima for WAS. In the case of PG, while there was no change in the zeta potential upon WN, there was a significant increase in the zeta potential of Ag-2 upon WA and WB. Post silanization, a drop in the zeta potential was witnessed in the WAS condition, whereas it remained constant for the WBS and WNS conditions.

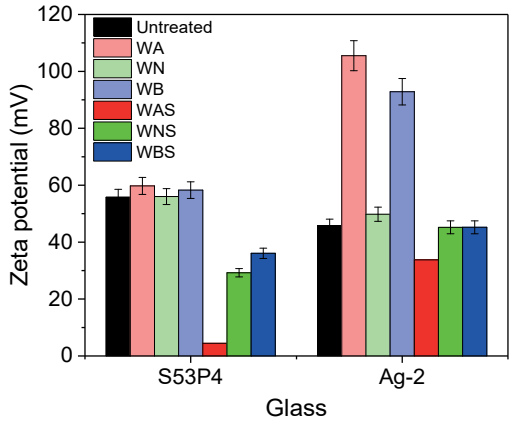

Figure 5.19 Zeta potential of S53P4 and Ag-2 post washing and silanization, as a function of different conditions (Unpublished Manuscript)

5.3.4 Impact on protein adsorption due to washing and silanization

Model proteins, i.e. fluorescently labelled fibronectin and albumin, were deposited at the surface of the untreated, washed in various buffer solutions and washed+silanized glass discs. Confocal fluorescence microscopy was utilized to evidence the adsorption of proteins. Figure 5.20 presents the confocal microscopy image of the glasses surface onto which albumin was adsorbed as a function of the surface treatment employed. It is worth mentioning that all green fluorescence on the images can be assigned to the fluorescently labelled proteins, as no glass surfaces (regardless of the surface treatment) showed any auto-fluorescence. From all glasses composition, only the glass S53P4 (SG)

exhibited visible green fluorescence, whereas the surfaces of all the other glasses appeared dark visually. All treated surfaces (washed and silanized) led to protein adsorption as indicated by the green fluorescence in the images. Clearly, for all the SG, the washing in acid and silanization lead to a more intense green fluorescence. Furthermore, on the SG, while the fluorescence appeared uniform across the WAS samples, the WBS and WBS samples exhibited patterns on their surface, indicative of the presence of clusters at the surface. In case of PG, while all treatments seemed to improve the adsorption of proteins, it is difficult to conclude which surface treatment lead to the highest degree of protein adsorption based only on visual examination..

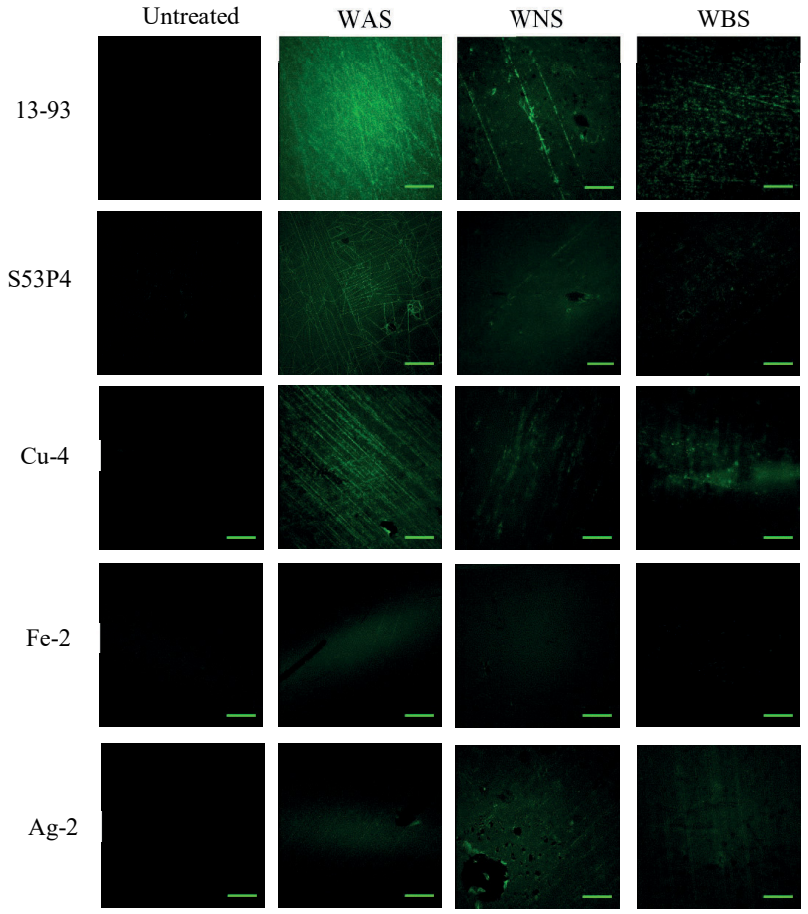

Figure-5.20 Albumin at the glass surface under different wash conditions. Scale bar represents 100 µm (Unpublished Manuscript)

Figure 5.21 presents the confocal microscopy image of the glasses surface onto which fibronectin was adsorbed as a function of the surface treatment employed. Similar to the test with albumin, both S53P4 and 13-93 exhibited green fluorescence at the surface of the untreated surface. While 13-93 presented the highest fluorescence in the WBS condition, S53P4 presented the highest fluorescence in the WNS condition. Interestingly, S53P4 in the WAS condition presented a surface replete with unusual topological patterns. All the PG also depicted protein adsorption upon washing+silanization, in contrast to no fluorescence in the untreated condition.

One should be aware that the surfaces in contact with albumin and fibronectin were imaged with different microscope. Therefore, while the intensity of materials coated with similar protein can be compared, materials exposed to different proteins cannot be compared.

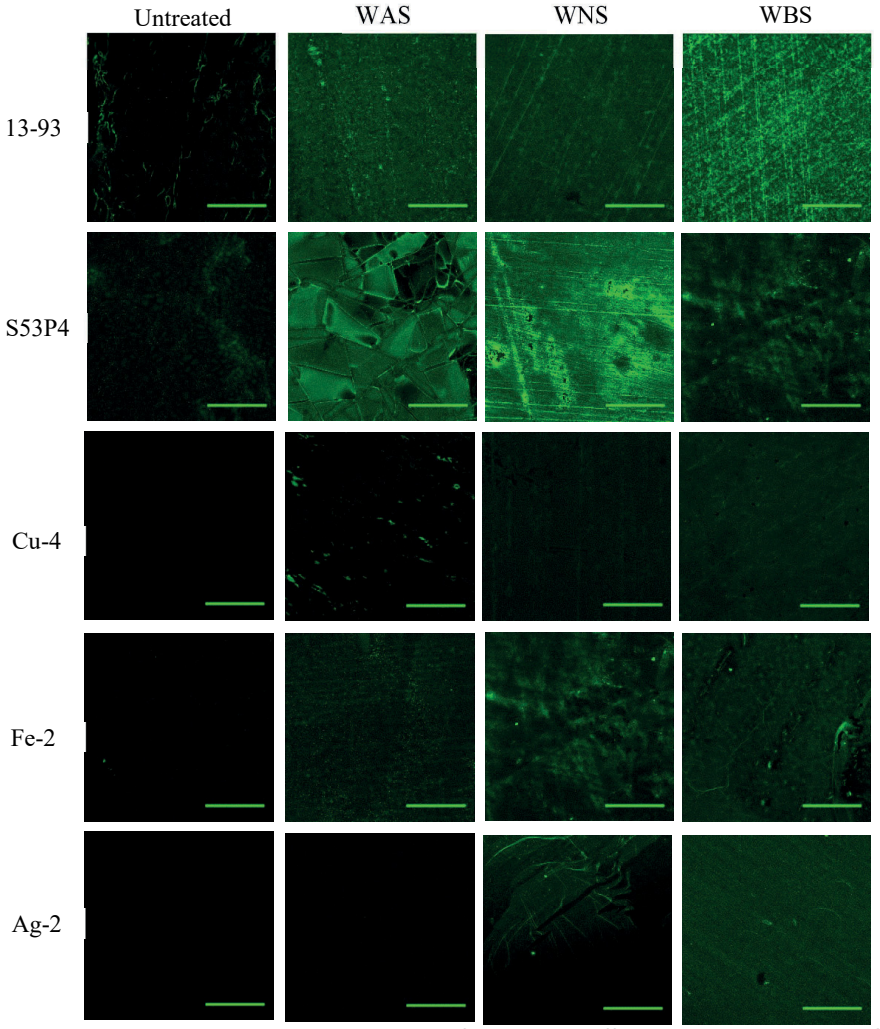

Figure 5.21 Fibronectin at the glass surface under different wash conditions. Scale bar represents 100 µm (Unpublished Manuscript)

5.3.5 Quantitative analysis of confocal microscopy images

Figure 5.22 a and b present the relative number of clusters (RNC) and the relative total fluorescence (RTF) observed on the glass discs, respectively, with albumin protein. Among the SG, S53P4 presented the highest RNC among all the samples in the untreated condition, and WAS 13-93 depicted the highest RNC overall. Furthermore, the highest RNC for S53P4 was observed in the WNS condition, while for 13-93, the maxima was observed for the WAS condition. For each of the phosphate glass, the highest RNC were observed for WAS Cu, WA Fe-2 and WNS Ag-2. S53P4 also presented the highest RTF in the untreated condition (Figure 5.22 b). Overall, across all the glasses, the maxima was observed in the WAS condition, barring Ag-2 where it appeared for the WNS condition, closely followed by the WBS condition. For both the SG, an improvement in the RTF was evidenced in the WA condition. For the PG, while the RTF remained nearly constant for the untreated, and all the washed conditions, it clearly increased upon silanization. It is worthwhile to observe that the PG presented nearly zero or very small RNC and RTF in the untreated condition, compared to the SG. Overall, even in the washed and washed + silanized conditions, Fe-2 presented the lowest RNC, while both Fe-2 and Ag-2 depicted the lowest RTF.

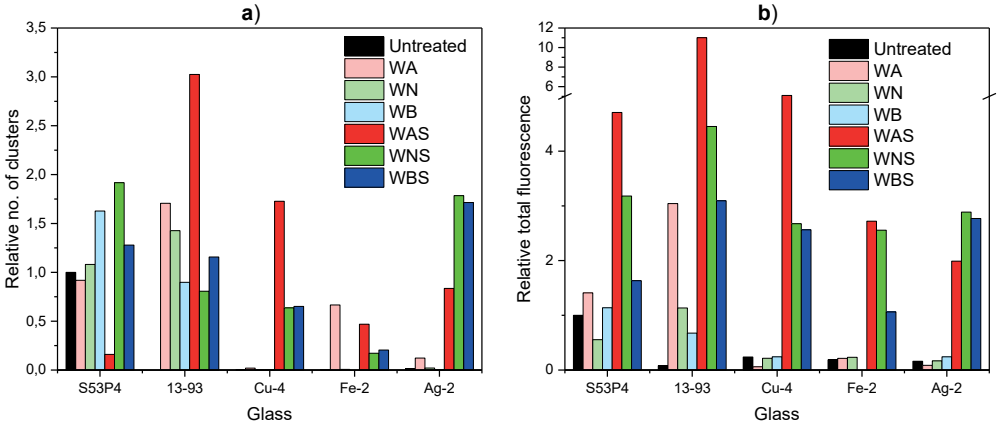

Figure 5.22 Albumin: a) Relative number of clusters and b) Relative total fluorescence of the untreated, washed and silanized silicate and phosphate glass discs. All the values presented are relative to that of the untreated S53P4 (Unpublished Manuscript)

The RNC and RTF for all the glasses under investigation, when tested with fibronectin, are presented in Figure 5.23 a and b respectively. Among all the untreated samples,

S53P4 presented the maximum value of RNC and RTF. Overall, 13-93 and Ag-2 presented the highest RNC for the silicate and PG respectively. Furthermore, for the SG, the RNC was found to increase upon washing in neutral buffer solution (WN), and it further increased for the WNS 13-93. Among the PG, the RNC in the untreated and all the washed conditions remained nearly zero, while it increased upon silanization. The maximum RNC was observed in the WBS condition for Cu-4 and Ag-2, while the maximum RNC for Fe-2 was in the WNS condition. Overall, Fe-2 presented the lowest RNC among all the glasses under investigation, even in the washed and washed+silanized conditions. In Figure 5.23 b, the SG present a much higher overall RTF than the PG. For the SG, very little improvement in RTF was observed upon washing, while upon silanization, the improvement was more marked. For the PG as well, while little or no increase in the RTF was seen due to washing, a much starker improvement was witnessed upon silanization. Furthermore, for each glass, the WBS condition presented the maxima in RTF for all the compositions, barring S53P4 where it was the WNS condition.

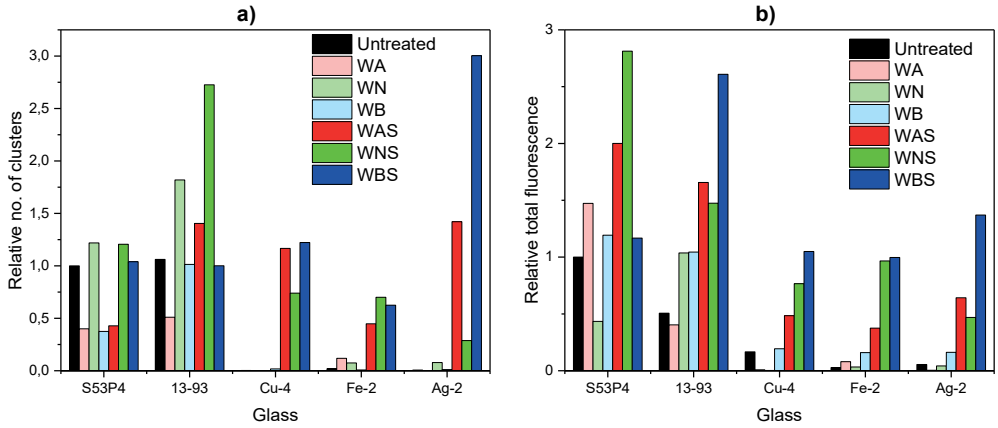

Figure 5.23 Fibronectin: a) Relative number of clusters and b) Relative total fluorescence of the untreated, washed and silanized silicate and phosphate glass discs. All the values presented are relative to that of the untreated S53P4 (Unpublished Manuscript)

5.3.6 Impact of protein adsorption and silanization on cell attachment

Figure 5.24 depicts the fluorescence images of stained cells (red dye for the focal adhesion points, green for the actin filaments and blue for the nuclei of the cells) for WBS and WBS+fibronectin decorated S53P4 and Sr50. It must be pointed that the images are not representative of the actual cell populations, as this was a qualitative analysis. The images at 20X depict the cells in both Sr50 and S53P4, with more observable red staining in the Sr50 samples than S53P4 samples in both the conditions, pointing to an increase in number of focal adhesion points. In the images at 60X, an increase in the red fluorescence can be seen in the WBS+fibronectin condition of Sr50, as compared to the WBS Sr50.

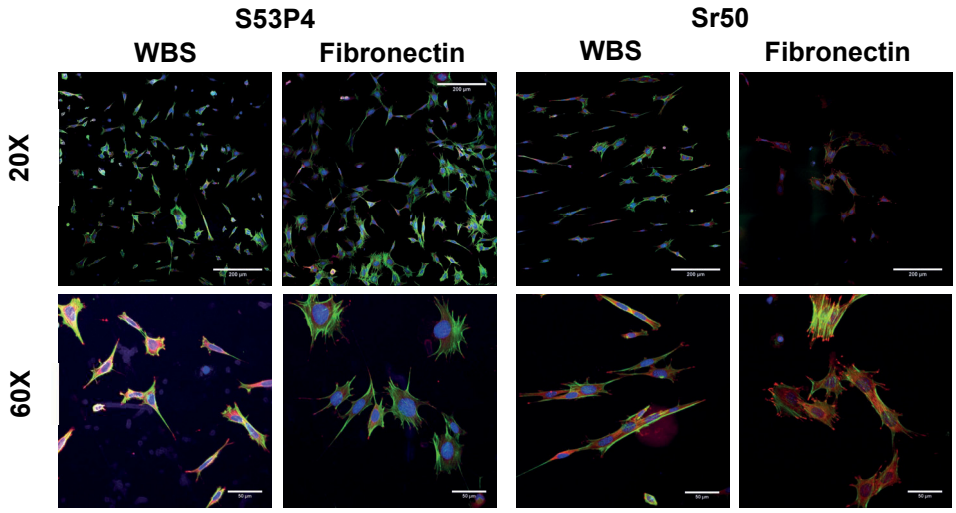

Figure 5.24 Fluorescence images of cells cultured on WBS and WBS+fibronectin decorated S53P4 and Sr50 samples. The red, green and blue dyes are representative of the focal adhesion points, actin filaments and nuclei of the cells respectively. The scale on the images at 20x (above) and 60X (below) correspond to 200 µm and 50 µm respectively (Unpublished Manuscript)

5.4 Characterization of new borophosphate glasses

To improve the cell response to the fast dissolving PG in Publication I and II, 2.5 mol% of P_2O_5 was replaced with B_2O_3. Subsequently, in the following study (Publication III), the impact of boron substitution on the new undoped reference Sr50-B2.5, Cu2-B2.5, Ce2-B2.5 and Ag1-B2.5 was analyzed in terms of the thermal and in-vitro dissolution properties. The doping was done such that the dopant metal ion concentration was 2 mol% for all the glasses. Cell response to the extracts of these glasses was also assessed, and the cytotoxicity of the extracts was measured.

5.4.1 Thermal properties

The thermal properties of the glasses under investigation are reported in Table 5.2. As compared to Sr50-B2.5, the glass transition temperature (T_g) remained unchanged for Ag1-B2.5 and Cu2-B2.5, while it increased slightly for Ce2-B2.5. Furthermore, Ag-1B2.5 depicted the same onset of crystallization (T_x) and crystallization peak (T_p) as Sr50B2.5, while they increased for Ce2-B2.5 and Cu2-B2.5. The thermal processing window ΔT, (where $\Delta T = T_x - T_g$) was found to be > 160^0C for all the glasses.

Table 5.2. Thermal properties of the investigated glasses (Publication III)

Glass	Glass transition temperature (T_g) (±3°C)	Onset of crystallization (T_x) (±3°C)	Crystallization temperature (T_c) (±3°C)	Thermal processing window ($\Delta T = T_x - T_p$) (±6°C)
Sr50-B2.5	450°C	616°C	660°C	166°C
Cu2-B2.5	448°C	630°C	671°C	182°C
Ce2-B2.5	463°C	627°C	665°C	163°C
Ag1-B2.5	452°C	617°C	659°C	165°C

5.4.2 In-vitro dissolution characteristics

The dissolution tests were conducted by immersing the glass particles in TRIS buffer solution and SBF up to 42 and 21 days respectively.

5.4.2.1 Change in pH

The change in pH of the TRIS buffer solution and SBF post immersion are presented in Figure 5.25 a) and b), respectively. Irrespective of the solution, no change in the pH was observed up to 21 days for all the glasses. At longer immersion times in TRIS, a small drop in the pH was recorded for Cu2-B2.5 and Ag1-B2.5 glasses, while the pH of the SBF solution remained unchanged even at longer immersion times.

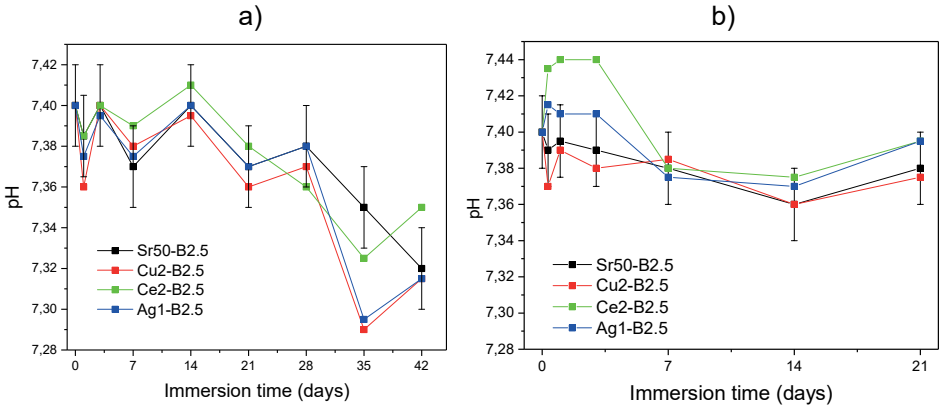

Figure 5.25 Change in pH of the a) TRIS buffer solution and b) SBF upon immersion of glass particles as a function of immersion time (Publication III)

5.4.2.2 Ion release

The ion concentration in TRIS buffer and SBF solutions used for immersion of these glasses were measured, to study their ion release behavior. To inspect the nature of dissolution, congruent or not, the fraction of ions (amount of ion released relative to the total amount of ion released into the solution in case of complete dissolution of the glass, based on the glass composition) released over time in the TRIS buffer solution from these glasses is presented in Figure 5.26. The fraction of ions dissolved at a given time point was calculated as the ratio of the actual ion concentration present, to the total ion concentration in case of complete dissolution of the glass particles. As expected the concentration in all ions increased with increasing immersion time. The fraction of Ca, Sr

and P at all time points for all the glasses was similar within the error of measurement. The fractions of B and Na released were slightly higher than the Ca, Sr and P ions, at immersion time points >21 days for all the glasses, with Na release being remarkably high for Ce2-B.2.5. Furthermore, at 42 days, Cu2-B2.5 exhibited the highest fraction of ions released among all the glasses.

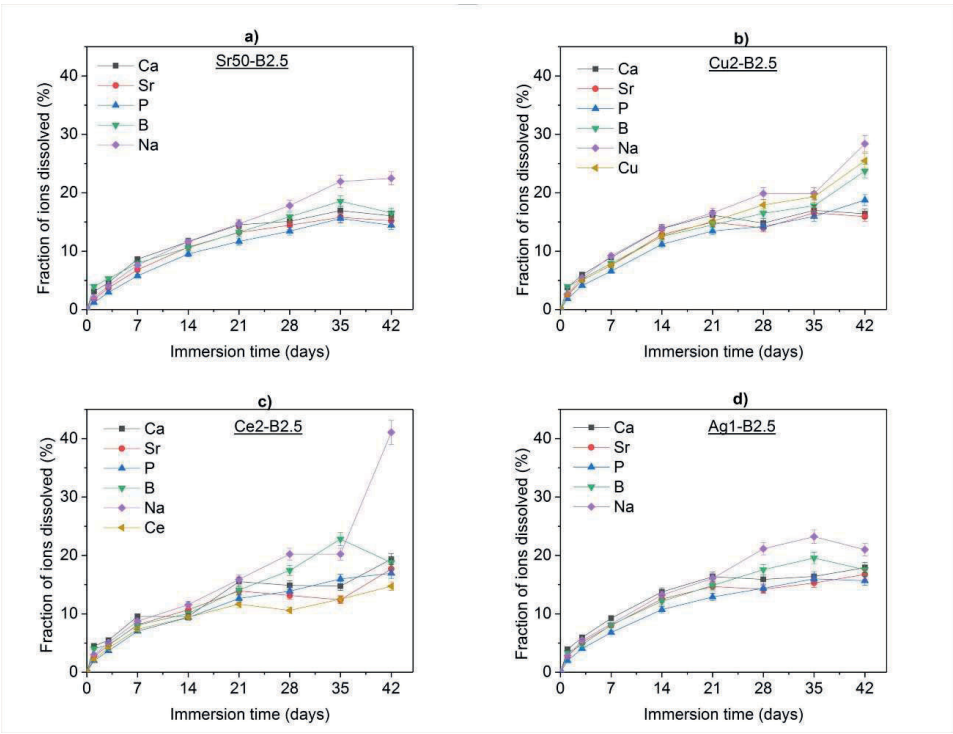

Figure 5.26 Fraction of the constituent ions leached into TRIS buffer solution after 42 days of immersion a) Sr50-B2.5, b) Cu2-B2.5, c) Ce2-B2.5, d) Ag1-B2.5 (Publication III)

The concentration of a) B, b) Ca, c) Sr, d) P and e) Cu released in SBF over time is depicted in Figure 5.27. The Ca concentration and release was found to be similar for all the glasses over time, within the accuracy of measurement. Overall, Ce2-B2.5 presented the lowest release of all the ions as compared to the other glasses. All the other glasses exhibited similar release of B, Sr and P ions into the SBF. Furthermore, a small decrease in the amount of Ca, Sr and P ions after 7 days could be observed. The release of Cu from Cu2-B2.5 was linear with respect to the immersion time, up to 7 days, and then saturated up to 21 days. The Ag and Ce ion release could not be evidenced in SBF.

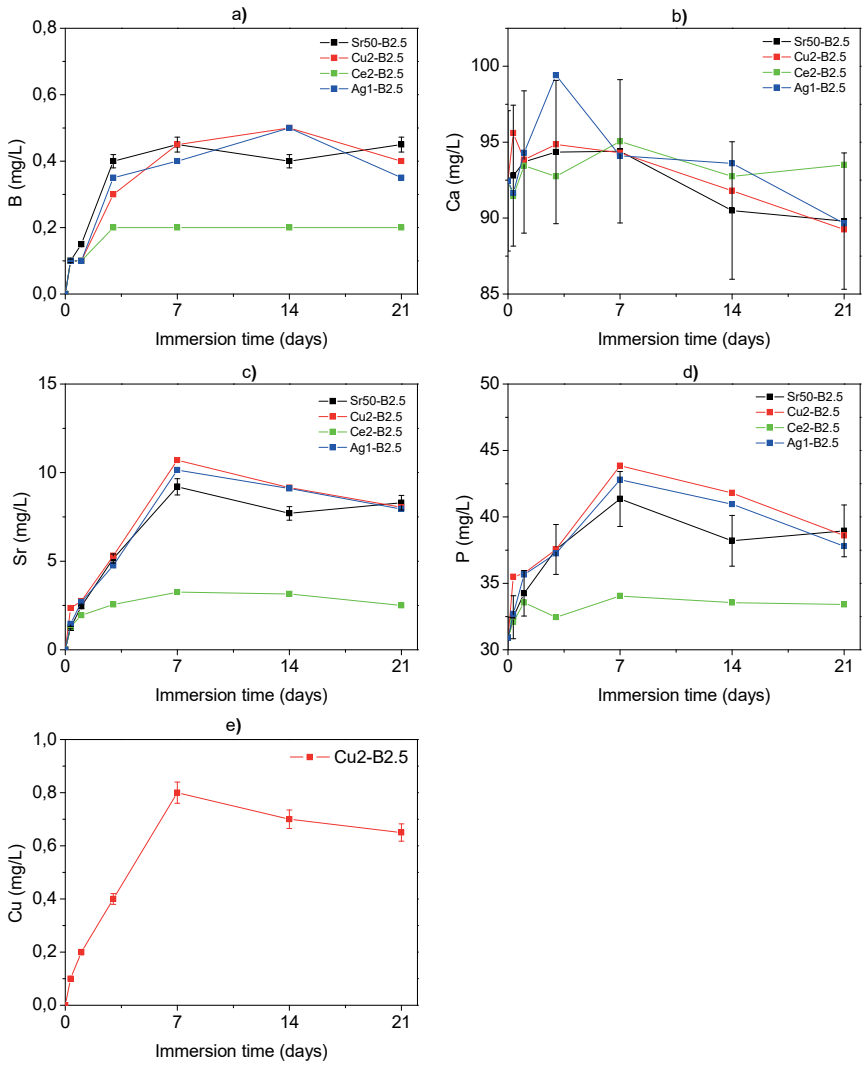

Figure 5.27 a) B, b) Ca, c) Sr, d) P and e) Cu concentration in SBF as a function of immersion time of the glass particles (Publication III)

5.4.2.3 Structural properties

Post immersion, the structural changes in the glasses were assessed as a function of immersion time in TRIS and SBF buffer solution. The changes observed due to immersion in TRIS buffer solution were identical to those observed in Publication I-II and [282],

and hence are not presented here. However, the IR spectra of the glasses post immersion in SBF are presented in Figure 5.28. The changes due to immersion were similar to those observed earlier in TRIS buffer solution (presented in 4.1.5 except Ce2-B2.5). New bands at 985 and 1050 cm^{-1} can be observed in the spectra of all the glasses except Ce2-B2.5. The overall changes to the spectra were also found to be smaller in case of Ce2-B2.5, as compared to other glasses.

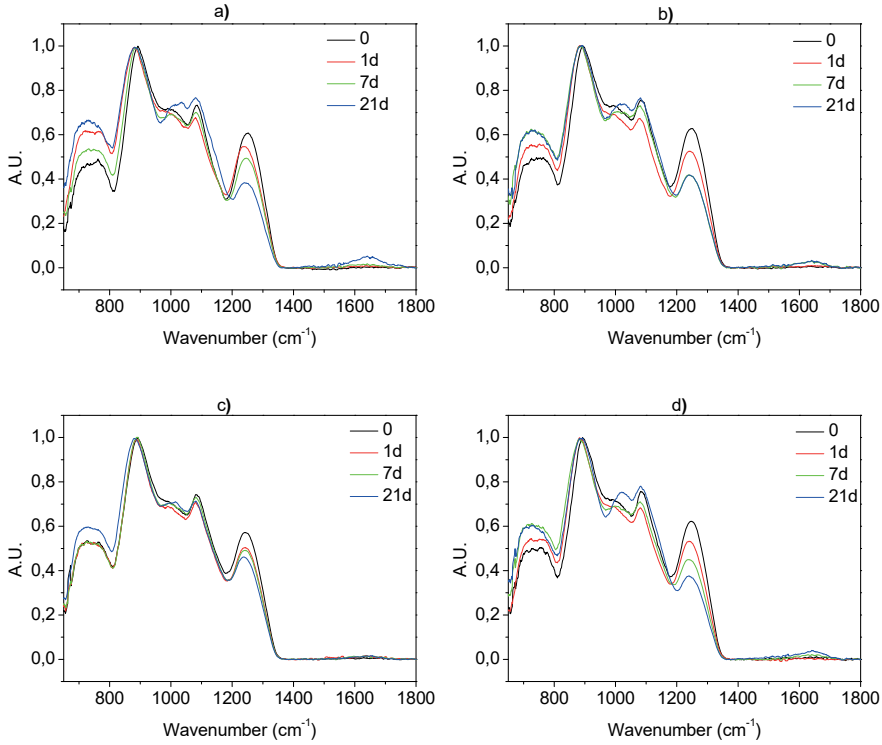

Figure 5.28 FTIR-ATR spectra of a) Sr50-B2.5, b) Cu2-B2.5, c) Ce2-B2.5 and d) Ag1-B2.5 as a function of immersion time in SBF (Publication III)

5.4.2.4 Surface analysis

Figure 5.29 depicts the SEM images of the glass particles post immersion for 42 days and 21 days in TRIS buffer solution and SBF, respectively. Prior to immersion the glass particles were found to be homogeneous in composition. The composition of the glass was measured by EDS. One should keep in mind that with EDS the boron concentration cannot be precisely measured. Therefore, only P, Ca, Na, Sr and the doped metal ions,

Ag, Cu and Ce were quantified and compared to the theoretical composition of the glass removing the Boron.

Post immersion in TRIS buffer solution for 42 days one can clearly see a reactive layer at the surface of the glasses Sr50-B2.5, Cu2-B2.5, Ce2-B2.5. The layer is very thin and seem to not be fully attached to the glass surface. The surface of the glass Ag2-B2.5, also seem to present some initial reactive layer. However the layer was not homogeneous and sparsely dispersed.

Upon immersion in SBF solution for 21 days, a reactive layer was seen only at the surface of the glasses Sr50-B2.5 and Cu2-B2.5, while no reactive layer was seen at the surface of the Ce2-B2.5 and Ag2-B2.5.

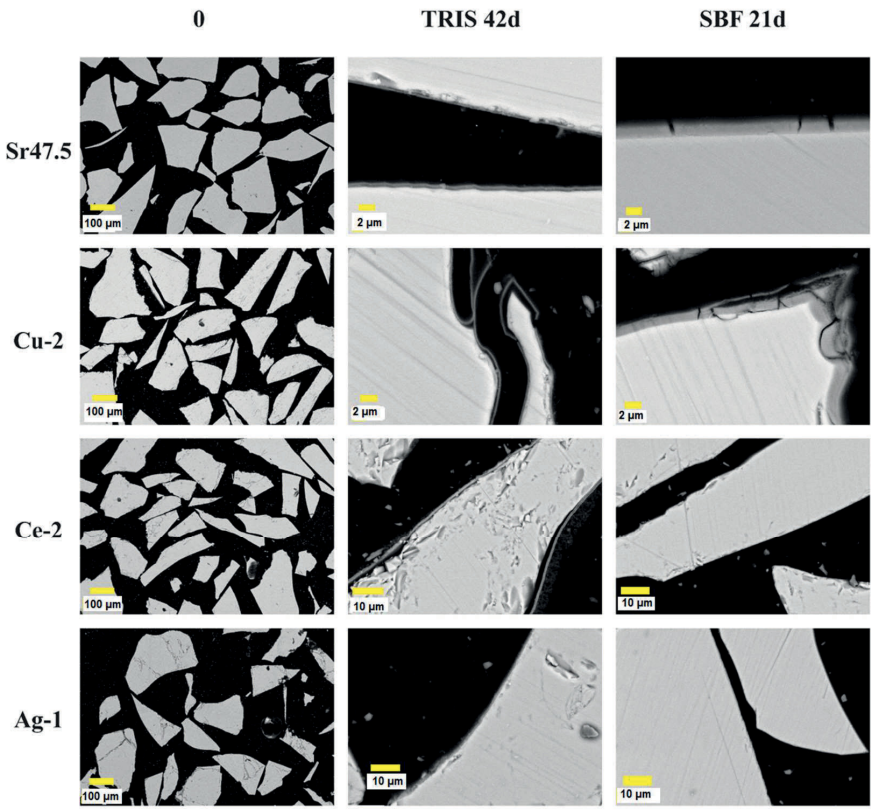

Figure 5.29 SEM images of the glass particles: before immersion and after immersion in TRIS and SBF solution for 42 and 21 days respectively (Publication III)

The EDX analysis of the surface layer is presented in Table 5.3. All the amounts were adjusted for the absence of B, as it could not be analyzed. The concentration of CaO was found to increase of all the glasses, and this increase was even greater at the surface of Sr50-B2.5 and Cu2-B2.5 immersed in SBF. On the other hand, the SrO concentration decreased at the surface of Sr50-B2.5 and Cu2-B2.5 in SBF. The P_2O_5 concentration dropped at the surface for all the glasses, apart from Ce2-B2.5 for both the immersion media. The reduction in P_2O_5 was starker in SBF than in TRIS. The Na concentration reduced rapidly at all the glass surfaces, with the largest decrease in case of Ce2-B2.5.

Table 5.3 Comparison of the surface layer composition with that of the bulk (in bracket) obtained by EDX analysis (Publication III)

After immersion in TRIS for 42 days							
	CaO (%)	**SrO (%)**	**P_2O_5 (%)**	**Na_2O (%)**	**Cu (%)**	**Ce (%)**	**Ag (%)**
Sr50-B2.5							
Surface	28.8	22.6	45.0	3.6	-	-	-
Bulk	(21.0)	(17.2)	(51,3)	(10.5)	-	-	-
Cu2-B2.5							
Surface	26.8	20.4	47.0	5.2	0.6	-	-
Bulk	(21.9)	(16.6)	(52.1)	(9.4)	(0)	-	-
Ce2-B2.5							
Surface	27.1±2.1	25.0	40.6±1.6	1.2	-	6.0	-
Bulk	(20.6)	(16.8)	(50.0)	(10.8)	-	(1.8)	-
Ag1-B2.5							
Surface	23.7	18.9	48.9	7.7	-	-	0.8
Bulk	(21.9)	(17.7)	(49.7)	(9.9)	-	-	(0.8)
After immersion in SBF for 21 days							
	CaO (%)	**SrO (%)**	**P_2O_5 (%)**	**Na_2O (%)**	**Cu (%)**	**Mg (%)**	
Sr50-B2.5							
Surface	39.6±1.8	9.7	42.0	4.2	-	4.5	
Bulk	(22.4)	(17.0)	(50.0)	(10.6)	-	0	
Cu2-B2.5							
Surface	45.2±6.5	6.4±3.4	39.2±3.1	3.1	0.5	5.6±1.6	
Bulk	(18.8)	(17.9)	(50.4)	(10.9)	(1.9)	0	

5.4.3 Cell growth and proliferation

The extracts of these glasses were used for culturing cells, to evaluate the cellular response to these glasses. The cell viability and proliferation were analyzed in the undiluted, 1:10 and 1:100 diluted extracts, to assess the optimal ion concentrations for cell survival and added functionality, potentially imparted by the dopant metal ions.

The ion concentration in the undiluted extracts were obtained with ICP-OES analysis, and are illustrated in Table 5.4. The ions concentrations were found to be highest for Cu-2, and lowest for Ce2-B2.5. The presence of Ag was also evidenced in the extracts, contrary to its absence in the TRIS buffer solution and SBF during in-vitro dissolution tests.

Table 5.4 Ion concentrations in the undiluted extract media of the glasses under investigation (mg/L) (Publication III)

	Ca	Sr	P	B	Cu	Ce	Ag
Extract Media	43±2	0	37±2	0	0	0	0
Sr50-B2.5	79±4	40±2	111±6	1±0.05	0	0	0
Cu2-B2.5	107±5	51±3	141±7	1±0.05	2±0.1	0	0
Ce2-B2.5	47±2	22±1	66±3	1±0.05	0	0	0
Ag1-B2.5	55±3	27±1	83±4	1±0.05	0	0	2±0.1

The viability of hASC was examined at 3, 7 and 14 days via live/dead staining in the undiluted, 1:10 and 1:100 diluted extracts (Figure 5.30). With this staining, large amount of live cells (green) were seen in all the conditions except the undiluted Cu2-B2.5 extract. Nearly no red cells could be observed in any condition. For some conditions, the amount of cells at D-14 appeared lower than at D-7. To quantify these observations, CyQUANT cell proliferation assay was performed at the same time points (Figure 5.31). Except undiluted Cu2-B2.5, the cell amount increased from D-3 to D-7 for all the extracts, and remained constant from D-7 to D-14. The undiluted Ag1-B2.5 extract presented a slightly lesser cell amount at all the time points than control, Sr50B2.5 and Ce2-B2.5, albeit much higher than the Cu2-B2.5. Among the 1:10 diluted samples, Ce2-B2.5 depicted the highest cell amount at D-14, and among the 1:100 diluted samples, the cell amount was

found to be independent of the composition, and improved as a function of time in culture for all the extracts.

Furthermore, the cytotoxicity of the undiluted and diluted extracts was evaluated with the LDH assay kit, and is presented in Figure 5.32. For the undiluted extracts, all the extracts exhibited comparable cytotoxicity, except Cu2-B2.5 which depicted the highest cytotoxicity at all the time points. Among the diluted extracts, the LDH values were at their peak at D-3, then dropped at D-7, and then rose again at D-14. At D-7, the 1:10 diluted Sr50B2.5 and Cu2-B2.5 extracts presented a slightly higher cytotoxicity than the control, whereas that of Ce2-B2.5 was slightly lower. Apart from these, all the diluted extracts presented similar cytotoxicity at a given time point, independent of the dopant metal ion.

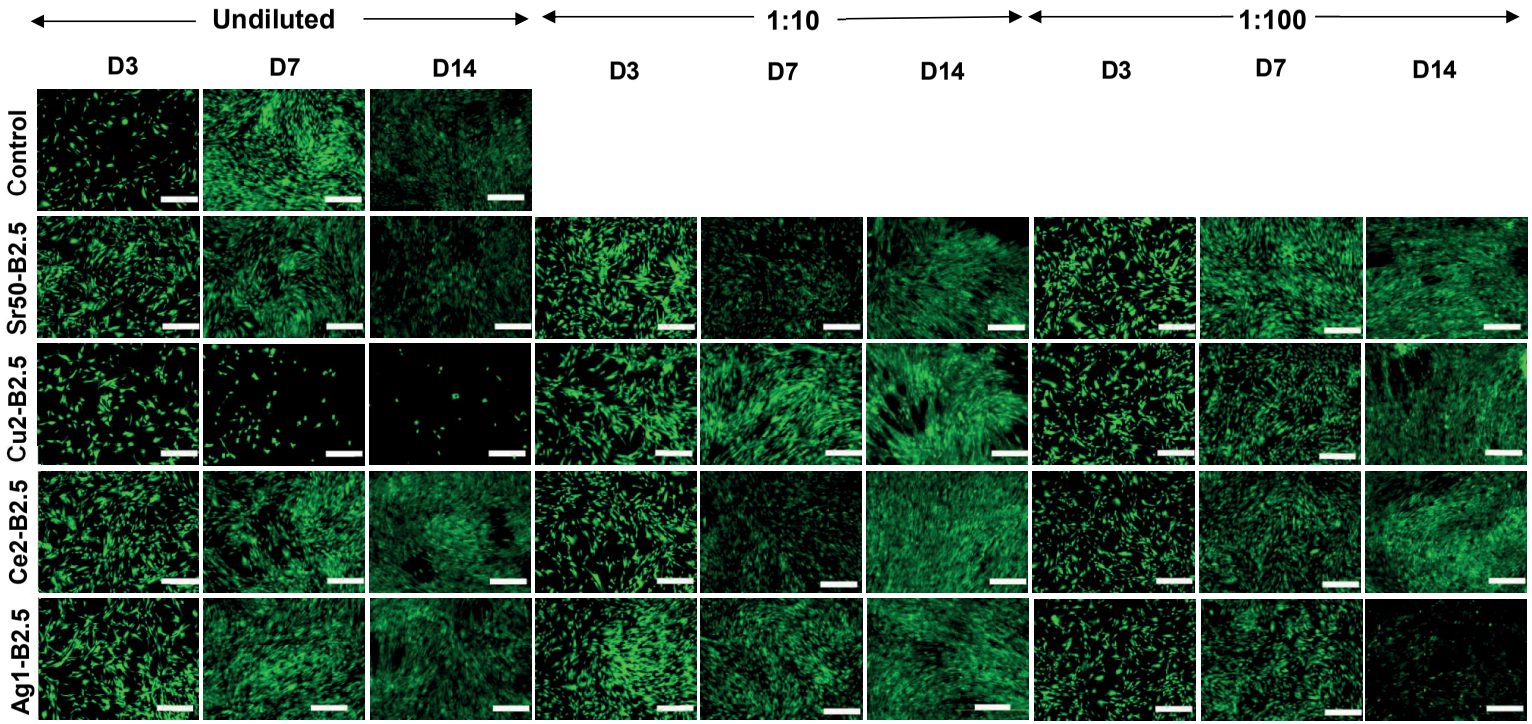

Figure 5.30 Viability of hASC cultured on undiluted, 1:10 and 1:100 diluted glass extract media, analyzed by live/dead staining at 3, 7 and 14 days of culture. The scale bar corresponds to 500 µm (Publication III)

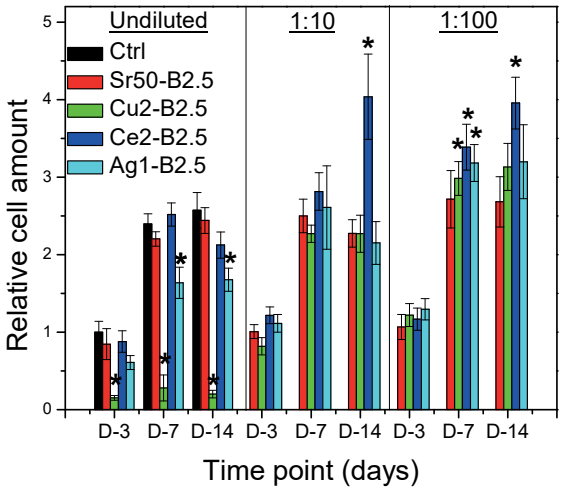

Figure 5.31 The proliferation of hASC cultured in a) undiluted, b) 1:10 diluted and c) 1:100 diluted glass extract media analyzed with CyQUANT Cell Proliferation Assay kit at 3, 7 and 14 days of culture. All the values presented are relative to the control at D-3. The level of significance is set at $p<0.05$. * implies that $p<0.05$ between the indicated extract and control (Ctrl) at the same time point (Publication III)

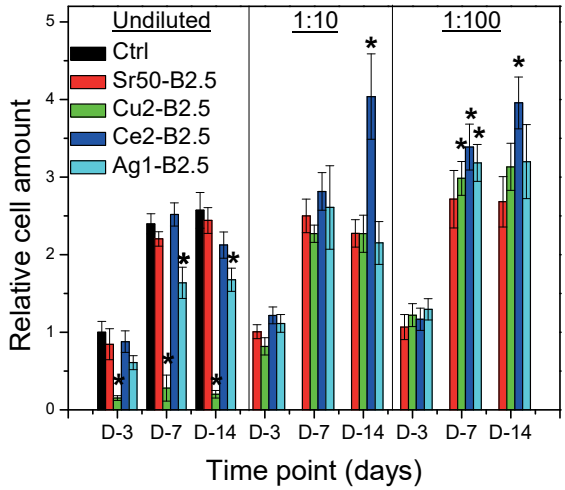

Figure 5.31 The proliferation of hASC cultured in a) undiluted, b) 1:10 diluted and c) 1:100 diluted glass extract media analyzed with CyQUANT Cell Proliferation Assay kit at 3, 7 and 14 days of culture. All the values presented are relative to the control at D-3. The level of significance is set at $p<0.05$. * implies that $p<0.05$ between the indicated extract and control (Ctrl) at the same time point (Publication III)

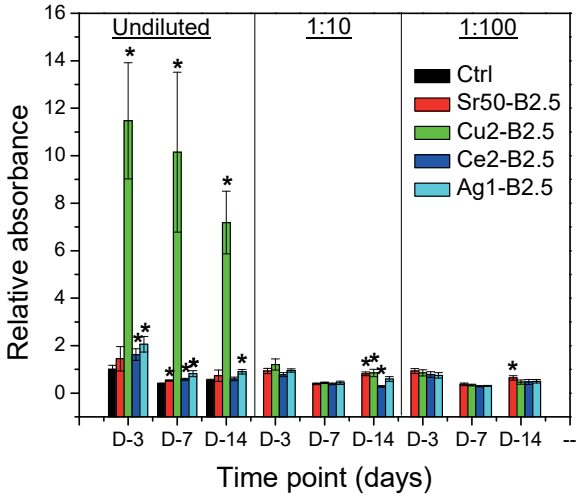

Figure 5.32. LDH activity in the a) undiluted, b) 1:10 diluted and c) 1:100 diluted glass extract media normalized with the corresponding CyQUANT assay values. The values are presented relative to the control at D-3. The level of significance is set at $p<0.05$. * implies that $p<0.05$ between the indicated extract and control (Ctrl) at the same time point (Publication III)

5.5 Phosphate glass fibers for biosensing

The potential of single core and core-clad PG fibers for biosensing was assessed in this study, Publication IV. The fibers were obtained from the Sr50 and Ce-1 compositions. Doping with Ce was found to increase the refractive index and resistance to dissolution of the Sr50 glass.

5.5.1 Single core and core-clad fibers

Single core fibers were drawn from the Sr50 and Ce-1 compositions, along with a core clad fiber with core as Ce-1 and clad as Sr50. The NA of the core clad fiber was 0.16,

similar to other fibers studied previously [363]. The cross section of the core-clad fiber is shown in Figure 5.33, where the core appeared brighter than the clad.

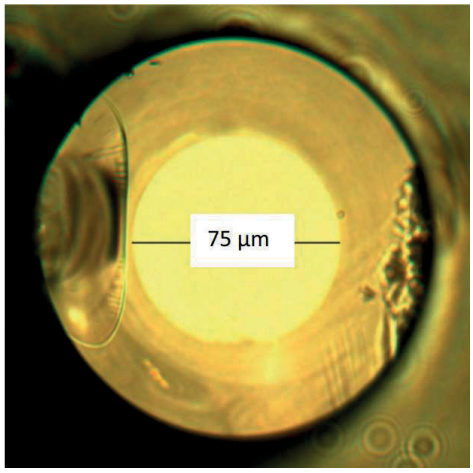

Figure 5.33 Optical microscope image of the core-clad fiber cross section (Publication IV)

5.5.2 Mechanical strength and origin of fracture

The variation in tensile strength, Young's modulus and Weibull modulus of single core and core-clad fibers as a function of immersion time in TRIS buffer solution are presented in Figure 5.34. In Figure 5.34 a), the tensile strength of Sr50 and Ce-1 core fibers were found to be similar ~550MPa, prior to immersion (t=0). However, the core-clad fiber exhibited a lower tensile strength at t=0 than the others. Upon immersion for 2 days, an increase in tensile strength can be observed for all the fibers. After 2 days and up to 6 weeks,, the tensile strength decreased for Sr50 core and the core-clad fibers. However, the core Ce-1 fibers maintained their tensile strength for 21 days, before the drop in tensile strength. Figure 5.34 b) illustrates the Young's modulus as a function of immersion time in TRIS for these fibers. Prior to immersion, the core-clad and core Sr50 fibers exhibited similar Young's modulus, while the Ce-1 fiber presented a higher Young's modulus. For all the fibers, the Young's modulus was found to increase initially, with core Sr50, core Ce-1 and core-clad fibers exhibiting a maxima at 7, 21 and 7 days respectively. In Figure 5.34 c), the Weibull modulus of the fibers is shown, as a function of immersion

time. Upon immersion, the Weibull modulus for all the fibers increased initially, and then dropped at the longer immersion times.

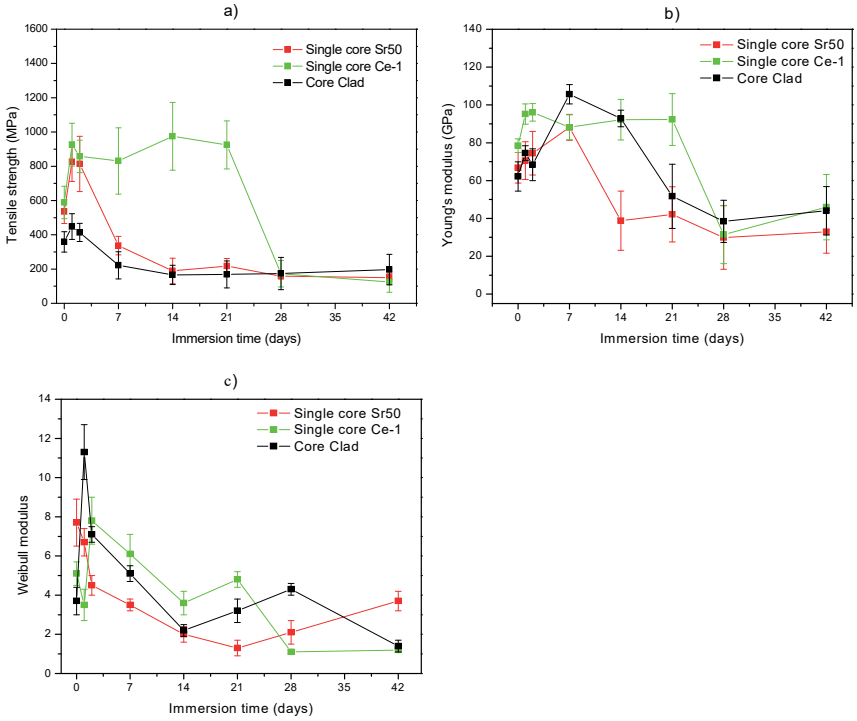

Figure 5.34 a) Tensile strength, b) Young's modulus and c) Weibull modulus of single core and core-clad fibers immersed for up to 42 days in TRIS buffer solution (Publication IV)

The core and core-clad fibers were imaged post fracture, and are presented in Figure 5.35 a) optical microscopy image of the core fiber Ce-1 and b) optical microscopy image of the core-clad fiber cross section, while post fracture, c) depicts the SEM micrographs of the core fiber and d) core-clad fiber cross section. In all the images, the origin of fracture is situated at the surface.

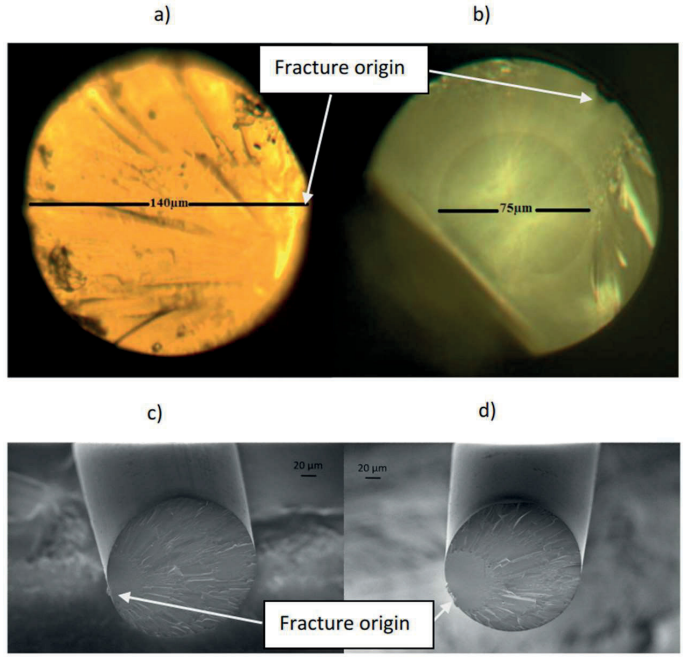

Figure 5.35 a), c) Optical microscope and SEM micrograph images of the cross section of single core (Ce-1) and b), d) core-clad fiber post tensile test (Publication IV)

5.5.3 Biosensing

A sensing region was created in the core-clad fiber, by etching away the cladding of a part of the length of the fiber, using 1M phosphoric acid. The change in diameter of the core-clad fiber as a function of immersion time in the acid is presented in Figure 5.36 a). The decrease in fiber diameter is almost linear with immersion time. The cross section of the fiber post etching for 13 h is presented in Figure 5.36 b). A very thin layer of cladding can be observed at this time point.

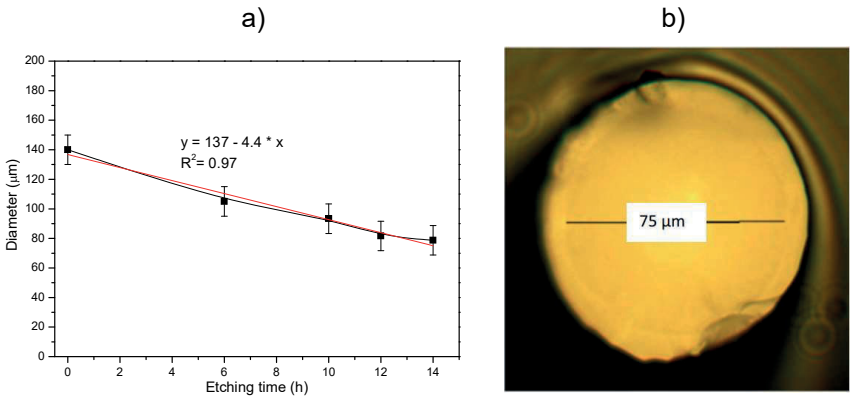

Figure 5.36 a) change in diameter of the core-clad fiber as a function of immersion time in 1M H_3PO_4 and b) cross section of the core-clad fiber after 13h of etching (Publication IV)

The tensile strength of the etched fiber was also assessed, and is presented in Figure 5.37 a). The Figure 5.37 b) presents the different regions in the fiber where the fracture occurred during the tensile test. Of the 10 tested fibers, four broke at the interface of the etched and un-etched region, four in the etched part, and two in the un-etched part of the fiber. The lowest tensile strength was observed for the fibers which broke in Region II. The fibers breaking in Region III were found to exhibit the highest tensile strength. Furthermore, the light transmission at 680 nm through the etched core clad fiber is presented as a function of immersion time in TRIS up to 42 days in Figure 5.38. The light transmitted was found to decrease progressively as a function of immersion time in TRIS.

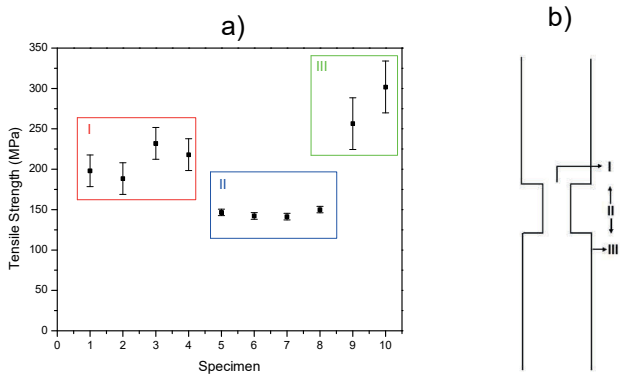

Figure 5.37 a) Tensile strength of etched fibers on the basis of the region where fracture occurs, b) the different regions of fracture in the etched fiber (Publication IV)

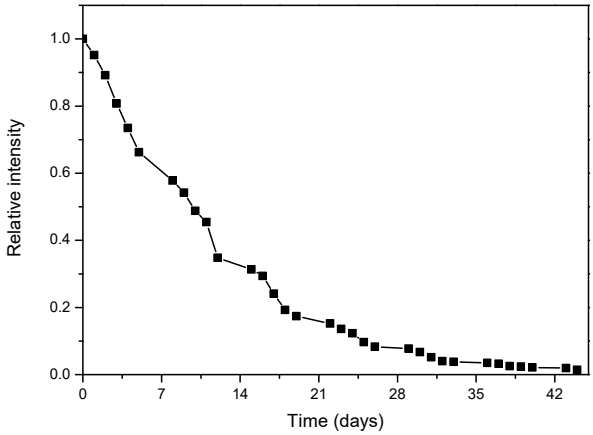

Figure 5.38 Relative intensity of the output light at 680nm through the core-clad fiber as a function of immersion time in TRIS (Publication IV)

In Figure 5.39 a), no surface layer on the etched portion of the core-clad fiber could be observed as a result of immersion in TRIS for 7 days. However, at 21 days (Figure 5.39 b)), a surface layer was evidenced, which grew thicker at 42 days of immersion (Figure 5.39c)).

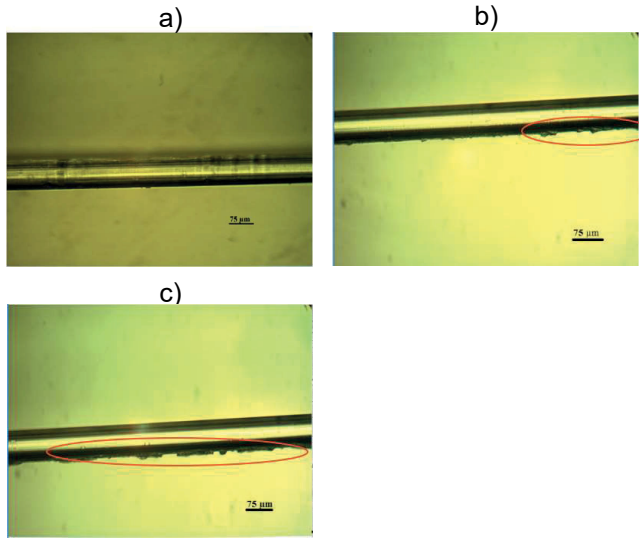

Figure 5.39 Microscope images of the etched part of the core-clad fibers immersed for a) 7 days, b) 21 days and c) 42 days in TRIS At 21 days, a surface layer starts to form (red circle) (Publication IV)

6 Discussion

6.1 Characterization of new phosphate glasses

In Publication I-II, new PG were introduced, with the general composition [x(MO)+(100-x)(0.5P_2O_5+0.2CaO+0.2SrO+0.1Na_2O)] where MO (dopant metal oxides) were Ag_2SO_4, CuO or Fe_2O_3, and x (dopant concentration) € {1, 2, 3, 4, 5}. These glasses were based on the glass with x=0, i.e., Sr50. The glass Sr50 was found to be a promising bioactive glass, possessing the slowest dissolution rate and the highest degree of thermal processability in the glass system 50P_2O_5 + 10Na_2O + (40-x)CaO + xSrO (mol%) [25].

Apart from potentially imparting added functionalities, the metal ions used for doping were chosen such that they affect the dissolution rate of the glass in different ways. While doping with Ag and Cu increased the dissolution rate of the glass, Fe was found to decrease the dissolution rate by increasing the network connectivity. In the following sections, the impact of doping on the physical, structural, thermal and in-vitro dissolution properties are described. Furthermore, the antimicrobial properties of the Ag and Cu doped glasses were investigated relative to those of the commercially available silicate SG S53P4.

6.1.1 Impact of doping on glass properties

For the Ag glasses, a rise in the density of the glass (Figure 5.1 a) with an increase in x could be observed, attributable to the higher mass of Ag as compared to the other modifier cations present in the glasses. However, the molar volume remained unchanged (Figure 5.1 a) within the error of measurement upon addition of Ag. This indicated that Ag entered the network as Ag^{+} in the glass network, which has a similar ionic radius to other modifier ions in the glasses, and occupies interstitial space in the network without expanding or contracting the structure. Furthermore, the absence of absorption bands in the UV-Vis spectra (Figure 5.5 a) of the Ag glasses confirmed that Ag has indeed entered the network as positively charged Ag ions, and no nanoparticles formed during the glass processing. For Cu glasses, a slight increase in density, coupled with a decrease in molar volume with increasing x (Figure 5.1 b) pointed to a contraction of the glass network. In the UV-Vis spectra of Cu glasses (Figure 5.5 b), the absorption band at 850 nm increased in intensity with an increase in x, indicating that Cu entered the network mainly as Cu^{2+}, in agreement with [364]. Furthermore, the shift of the band gap to higher wavenumbers can be assigned to the increase in non-bridging oxygen and/or the presence of Cu^{+}. In contrast to the Ag and Cu glasses, the density and molar volume of the Fe glasses (Figure 5.1 c) were found to be independent of x, indicating that the ions entered the glass network without affecting the network connectivity or compaction. Based on the UV-Vis spectra, Fe entered the glass network as Fe^{3+} and Fe^{2+} ions, corresponding to the observable bands at ~450 and 1020 nm respectively, whose intensity increased with an increase in x.

The thermal properties of these glasses were also measured as a function of x (Figure 5 a, b and c). For the Ag glasses, the T_g decreased with an increase in x, while the T_p and ΔT exhibited a maxima at x=2 and 3 mol%. The reduction in T_g can be ascribed to the lower cationic field strength value (Z/r^2) of Ag (0.6) as compared to the other cations present in the glasses, i.e. Sr (1.56), Ca (2.04) and Na (1.06). For Cu glasses, the addition of even 1 mol% of Cu lead to the creation of weak bonds, as observed from the decrease in T_g. Additionally, an increase in ΔT, which is representative of glass' resistance to crystallization, was observed with doping 1 mol% of Cu. However, with further addition of Cu, the ΔT remained constant. In the case of Fe glasses, an increase in T_g with an increase in x is observed, indicating that Fe ions increase the bond strength in PG. This has indeed been observed earlier in a study by Ahmed et al. [26].

The impact of doping on the structure of the glasses under investigation was studied with FTIR-ATR and Raman spectroscopy. In the FTIR-ATR spectra of Ag and Cu glasses

(Figure 5.3 a and b), the band at 1260 cm^{-1} decreased with an increase in x, confirming the reduction in network connectivity and an increase in the amount of Q^1 units. The same deductions were made from the analysis of the Raman spectra (Figure 5.3 a and b). With an increase in x, the shift of all the bands towards lower wavenumbers are indicative of the weakening of chemical bonds in the network. Furthermore, the depolymerization of the glass network with addition of Ag or Cu was corroborated by an increase in intensity of the band at 695 and 1020 cm^{-1}, coupled with the increase in intensity of the shoulder at 1090 cm^{-1}, indicative of an increase in Q^1 units and shortening of the phosphate chain. Indeed, the increase in intensity of the band at 1090 cm^{-1} and shift of the optical band gap pointed towards an increased number of non-bridging terminal oxygen atoms (NBO). This was anticipated, as due to doping, the overall phosphate content of the glasses decreased at the expense of modifier cations. In addition, the small shoulder at 1320 cm^{-1} related to P=O remained unaffected due to doping, confirming that the number of Q^3 units remained similar in all the glasses. However for the Fe glasses, significant changes in IR spectra were observed only when x increased from 2 to 3 (Figure 5.3 c). The slight shift and decrease in the intensity of the band at 1260 cm^{-1} represented the weakening of phosphate bond in the network with doping, as observed earlier in [365]. Fe glasses also presented more striking changes in the Raman spectra (Figure 5.4 c) as compared to the Ag and Cu glasses. In addition to the increase in intensity of the features at 695, 1020 cm^{-1} and 1090 cm^{-1} similar to the Ag and Cu glasses, the band at 1250 cm^{-1} also increased. This signaled that P-O-P bonds were broken, while P-O-Fe bonds were formed simultaneously, preventing further depolymerization of the phosphate network [365]. These changes in the Fe glass structure are in line with progressive increase in T_g and the shift in the optical band gap to higher wavelengths, with an increase in x, and are in agreement with [366].

6.1.2 Impact of doping on in-vitro dissolution characteristics

An increase in the durability of the Ag and Cu glasses towards aqueous media was expected, owing to the increase in Q^1 units in their network. However, upon immersion in TRIS buffer solution, they exhibited a marked decrease in the pH with an increase in x, as well as the immersion time, as compared to Sr50 (Figure 5.6 a and b). Furthermore, the TRIS buffer solutions recovered after immersion were analyzed with ICP-OES to understand the ion release behavior of these glasses. For both Ag and Cu glasses, the ion release curves of Ca, Sr, P and Na presented similar characteristics, with an almost linear release up to 7 days, and then saturation from 14 day onwards (Figure 5.7 and 5.8). The ion release curves of Sr50 also presented similar trends, however the overall

ion release was found to be lower than the Ag and Cu glasses. The saturation of the ion release curves may be credited to the TRIS solution becoming saturated with ions released from the glasses, which eventually lead to the precipitation of a surface layer. The release of Ag from the Ag glasses could not be evidenced from the ICP-OES analysis, owing to a high noise to signal ratio. However, a steady release of Cu over immersion time from the Cu glasses could be observed. The final Na concentration was found to be slightly higher than the other ions. Na is known to be among the first ions to leach into the solution [194].

The Ag-5 and Cu-5 glasses depicted similar changes in the IR spectra as a function of immersion (Figure 5.10 a and b). The progressive increase in the number of Q^1 units at the expense of Q^2 units indicated the initial stages of glass dissolution in PG [18,25]. The shift of the bands assigned to Q^2 units to lower wavenumbers suggested a weakening of their bond strengths. The disruption of phosphate chains continued up to the 28 days, the longest immersion time point in this study. Bunker et al., suggested that the glass dissolution is dictated by the rate of water diffusion into the surface of the PG [18]. When a phosphate chain is completely surrounded by OH groups, it is released into the solution. The appearance of new bands at ~980 and 1050 cm^{-1} marked the formation of a Ca-P layer partially substituted by Sr at the surface of the glass particles. The precipitation of the layer at 28 days could be evidenced in the SEM images of the glass particles after immersion in TRIS buffer solution (Figure 5.11). Furthermore, the EDX analysis confirmed the higher $\frac{Ca+Sr}{P}$ ratio of the surface layer, as compared to that of the bulk. For both the glasses, this ratio (accuracy of measurement = ±0.1) in the bulk was 0.4, while at the surface, the ratio was ~0.7 and 0. 6 for the Ag and Cu glasses, respectively. Furthermore, Na and Ag/Cu were absent from the surface layer, also explaining the slightly higher final Na concentration in TRIS buffer solution from the ICP-OES analysis.

Therefore, in summary, doping with Ag and Cu led to an increase in the dissolution rate, by weakening and depolymerizing the glass network. On the other hand, little or no change in the pH was recorded for the Fe glasses upon immersion (Figure 5.6 c). Furthermore, the ion release from the Fe glasses (Figure 5.9) was also found to be significantly lower than the Ag and Cu glasses, at all the immersion time points. In contrast to the Ag and Cu glasses, the ion release was found to be lower compared to the reference glass Sr50 as well. Indeed, the changes in the FTIR spectra due to immersion were also smaller in the case of Fe doped glasses (Figure 5.10 c). This could be attributed to the formation of P-O-Fe bonds, which prevented extensive depolymerization of the phosphate network upon immersion. Furthermore, even at the longest immersion time, no

surface layer could be observed on the Fe glasses, owing to the slow ion release and/or the layer being very thin and loosely bonded to the surface. Thus, relative to Sr50, doping with iron made the glasses highly resistant to dissolution in aqueous media, while doping with Cu and Ag led to the glasses becoming increasingly soluble in aqueous media.

The Cu and Ag ions are of particular interest for their antimicrobial nature [367,368]. Therefore, the antimicrobial properties of the Ag and Cu glasses with x=2 and 5, at two different particle size ranges 125-250 μm and <125 μm, and at two different dose levels (400 mg/ml and 1200 mg/ml) were evaluated, relative to the undoped Sr50 and S53P4 (a typical FDA approved silicate bioactive glass). The number of bacteria surviving in solutions containing the glass particles, is presented in a logarithmic scale in Figure 5.12 a and b. Therefore, a lower value of CFU represents a higher antimicrobial effect of the glass particles. For both the particle size ranges, all the PG depicted better antimicrobial properties than the S53P4. Irrespective of the particle size, the Ag glasses were found to be the most antimicrobial, with Ag-5 presenting the lowest CFU count at 1200 mg/ml concentration. Furthermore, for the smaller particle size range, Cu-2 and Cu-5 also depicted a reduction in CFU, with Cu-5 exhibiting complete bacterial eradication at 1200 mg/ml. Thus, Cu glasses with antimicrobial properties can also be obtained by tailoring the Cu concentration, particle size and dosage. It is known that S53P4 having particle size <45 μm completely eradicated a range of aerobic and anaerobic bacteria [369,370]. However, at particle size range 500-800 μm, S53P4 exhibited no antimicrobial properties [371]. The antimicrobial effects were credited to the rise in pH or to a high Na concentration, in [372]. As bigger particles have a lower surface area to volume ratio which leads to a lower ion release, the release of Na and the rise in pH could have been lower in this study, as the particle size of S53P4 was much larger. This could have led to the lack of antimicrobial action evidenced for S53P4 here.

Thus, in this study, the Ag and Cu glasses presented a faster dissolution rate in aqueous media than the reference Sr50. All glasses dissolved congruently in TRIS buffer solution. They also exhibited better antimicrobial properties than Sr50, and also the bioactive commercial SG S53P4. Therefore, it is interesting to check if these glasses support cell viability and proliferation, in which case they will be very promising for biomedical applications.

6.2 Preliminary cell culture tests

Cell culture tests were conducted on the Sr50 glass discs and extract, with fibroblasts and hASC. Irrespective of their type, cells were found to grow in control over time in culture, while very few live cells could be evidenced on the Sr50 disc's surface at all the time points (Figure 5.13). Furthermore, the round appearance of the cells on Sr50 disc's surface indicated that they are apoptotic. This indicated that cell viability on the Sr50 glass discs is extremely poor. Despite the poor cell attachment at the glasses surfaces, the cells seemed to grow and proliferate away from the glass which was seen as a sign of the biocompatibility. The lack of cell attachment was assigned to rapid surface degradation. Therefore, cell testing was also performed using extract supplemented DMEM (Figure 5.14). Cells were found to grow in the Sr50 extract, as well as the control. The amount of cells in the extract also appeared to grow from D-2 to D-7, while remaining constant from D-7 to D-14, similar to the control. Hence, it was concluded that the Sr50 extract, i.e., the dissolution products of Sr50 are not detrimental to cell growth and proliferation, while the Sr50 glass surface is inhibiting proper cell attachment.

A preliminary cell culture was also conducted with extracts of Sr50, and Ag, Cu and Ce doped glasses with x=2 and x=5 with hASC (Figure 5.15). In this study, the Ce glass previously studied in the research group were introduced, rather than the Fe glass, pertaining to their dissolution profiles. From the L/D images at D-3, cells were found to be viable in all the conditions except the Cu-5 and Ag-5 extracts. At D-7, the amount of cells remained constant or increased in all the conditions except Cu-5 and Ag-5, where nearly no live cells could be observed. From the cell proliferation results (Figure 5.16), the cell amount for the Ag and Cu glasses, irrespective of x, was almost zero at D-7 and D-14. On the other hand, the amount of cells increased over time for the control, and remained constant for Sr50, Ce-2 and Ce-5. Overall, Sr50 and the Ce glasses supported cell viability as much as or even better than the control.

6.3 Improving cell attachment on phosphate glasses

From the preliminary cell culture studies, all glass discs did not provide a suitable template for cell attachment and proliferation, most likely assigned to their rapid, layer-by-layer dissolution. Furthermore, the extract of Ag and Cu doped glasses was also found to be cytotoxic to hASC cells. Timelapse videos of the embryonic mouse fibroblasts,

cultured at the surface of the glasses, were recorded every 5 minutes for 24h (not included in the thesis). The videos demonstrated that the cells constantly attach and detach from the surface of PG before finally turning apoptotic. Contrastingly, the cells were found to attach, elongate and proliferate normally on the SG S53P4 which was used as a reference in this study. The inability of the cells to remain attached to the PG surface, and to proliferate confirmed that the congruent dissolution of PG inhibits proper cell attachment. As explained earlier, the dissolution of PG in aqueous media occurs via leaching of phosphate chains into the solutions. This must result in the loss of anchor points at the glass' surface, leading to cycles of attachment and detachment of cells at the glass' surface. Furthermore, it is well known that when a biomaterial is exposed to biological media, the first step is an immediate adsorption of proteins at its surface. Thus, as the cells approach the biomaterial, they interact with the provincial matrix of proteins at its surface, rather than the biomaterial surface itself. Therefore, in a bid to improve cell attachment at the surface of PG, it is of utmost importance to study the adsorption of proteins at their surface, relative to well-known silicate bioactive glasses. In this study, the effectiveness of surface modification methods involving tailoring the surface charge and silanization of the phosphate glass in Publication I-II their ability to adsorb proteins were assessed. Furthermore, the impact of enabling better protein adsorption on the glass's surface on their ability to support superior cell attachment was evidenced.

6.3.1 Impact on structure

In Figure 5.16, though the spectra of the WB glass discs remains unaffected, some changes are depicted by the spectra of the WN and WA samples. In the spectra of the untreated sample, bands can be observed at 740, 870 and 992 cm^{-1}. For the WN samples, the band at 740 cm^{-1} is found to reduce in intensity, and a new band at 790 cm^{-1} arises. Whereas, for the WA samples, the former is replaced completely by the latter. The new band at 790 cm^{-1} alongside the shoulder at 945 cm^{-1} correspond to the C-O vibration mode in carbonate (CO_3^{2-}) [373]. Additionally, the band at 870 cm^{-1} is found to shift to lower wavenumbers, and the new band at 1045 cm^{-1} is stronger in case of the acid washed samples than those base washed. The latter is attributed to P-O vibration mode from the formation of carbonated hydroxyapatite (HCA) [374]. The small shoulder at 1236 cm^{-1} may be assigned to the Si-O-Si symmetrical stretching, and indicates the formation of a silica-rich layer at the glass surface [342,375]. Overall, the changes due to washing are more pronounced in the WA samples. Due to silanization, no further shifting or appearance of new bands is observed in the spectra of these glasses. However, the broadening of the peaks of the WBS samples may be credited to the silane layer

deposition and/or the leaching of cations, thereby creating empty spaces in the glass network.

The FTIR spectra of the PG under investigation, i.e., Cu-4, Fe-2 and Ag-2 are presented in Figure 5.17. No changes due to washing or silanization can be observed, indicating that there is no change in the short-range structure at the surface of these glasses. This is owing to the fact that PG dissolve congruently in aqueous media, thereby surface structure remained unchanged [18].

6.3.2 Impact on contact angle

The impact of washing and silanization on the hydrophilicity of the glass surface was evidenced with contact angle measurements using a water drop (Figure 5.18). All the glass discs, even in the untreated conditions, presented a hydrophilic surface. In the untreated condition, 13-93 possessed the highest contact angle, due to the expected lower OH present at the surface of this glass. Compared to S53P4, 13-93 is known to be more resistant to dissolution [376]. Upon washing in the different buffer solutions, the contact angle of the SG remained constant within the accuracy of measurement, whereas that of the PG decreased. The increase in contact angle in PG is in agreement with earlier studies [264,316,319], which reported an increase in the exposure of OH groups at the phosphate glass surface upon dissolution in aqueous media, thus increasing its wettability. As described in [264], the grafting of an APTS layer can be detected via contact angle measurements. The same study further demonstrated that an increase in contact angle upon silanization is indicative of proper grafting of silane at the glass surface.

6.3.3 Impact on surface charge

Zeta potential was measured at the surface of S53P4 and Ag-2 (taken as example) as a function of the different treatments/conditions, to assess the impact of washing and silanization on the surface charge. An increase in the zeta potential is indicative of the increase in positive charge on the surface. Therefore, the overall drop in the zeta potential upon silanization for both the glasses can be attributed to the increase in the amount of OH^- groups at their surface. The drop in zeta potential of S53P4 in the WAS condition can be attributed to the precipitation of a crystalline HCA layer, similar to the observation made by Lu et.al. for the 45S5 glass [377]. This is in line with the FTIR results of S53P4 (Fig-5.19), where WA and WAS samples exhibit signs of significant HCA precipitation. On the other hand, Ag-2 depicted a sharp increase in zeta potential upon WA and WB.

Furthermore, the zeta potential remained relatively unchanged in the WNS and WBS conditions, with a slight decrease for WAS.

6.3.4 Impact on protein adsorption

Adsorption of the proteins albumin and fibronectin on the surface of untreated and washed+silanized glass discs was evidenced with confocal fluorescence microscopy (Figure 5.20 and 5.21 respectively). In Figure 5.20, no protein could be observed on the surface of the untreated glasses, irrespective of their composition, barring S53P4 which presented some weak fluorescence. Upon washing+silanization, varying degree of protein adsorption could be evidenced for the different glasses. However, the highest amount of protein for both the silicate and PG could be observed for the WAS condition (except Ag-2), with WAS 13-93 presenting the highest protein adsorption overall. Furthermore, irrespective of the wash, 13-93 seemed to depict the highest protein adsorption in silanized condition. This was expected as 13-93 is a well known bioactive glass [177,378,379], which has a much slower dissolution rate than S53P4 [376] and the fast dissolving PG. Therefore, it underwent the least degree of surface degradation upon incubation in the protein solution, and provided a much stable surface for the proteins to adsorb. However, it must be pointed out that the washed+silanized PG, also exhibited protein adsorption at their surface.

In Figure 5.21, both the SG presented some degree of protein adsorption in the untreated condition, as compared to the PG which depicted none, as can be expected. Furthermore, upon washing+silanization, an improvement in the protein adhesion on all the glasses was observed, with Cu-4 depicting the least amount of proteins overall. S53P4 in the WAS condition displayed clear signs of the precipitation of a crystalline layer, likely HCA [380], which is expected given its higher dissolution rate than 13-93, along with the low pH environment of the acidic wash accelerating the dissolution further compared to the other buffer solutions. Furthermore, for S53P4, significant surface degradation can also be observed in the WN condition, giving rise to the brightest fluorescence among all the fibronectin group of samples in all the conditions.

6.3.5 Quantitative analysis of confocal microscopy images

Quantitative analysis of the confocal microscopy images in Figure 5.20 and 5.21 were performed, in order to facilitate the comparison of the degree of protein adsorption on the different glass samples. The ability of the glasses to form clusters of proteins at their surface is represented by the relative number of clusters (RNC) at their surface, while

the overall ability of the glasses to be able to adsorb proteins at their surface is indicated by the relative total fluorescence (RTF). From the analysis of the albumin group of samples (Figure 5.22 a and b), a clear improvement in the RNC and RTF was observed for all the SG under investigation in the washing+silanization condition. Their inherent superiority over PG as bioactive glasses can indeed be evidenced in the fact that they depicted a better ability to form clusters as well adsorb more proteins overall even in the unsilanized conditions, whereas nearly no clusters or protein adsorption was observed on the PG before silanization. However, it is interesting to point out that improvement due to washing+silanization is much starker in case of the PG, as compared to the SG. Although their overall ability to form clusters and adsorb proteins initially was non-existent before treatment, with washing+silanization, their RNC and RTF increased substantially and were close to that exhibited by the commercial SG. Furthermore, no clear preference for a treatment condition could be observed pertaining to the RNC. However, a strong inclination towards the WAS condition could be observed for achieving maximum RTF (except for Ag-2, which shows a higher preference for the WBS and WNS conditions), which is more representative of the overall ability of the glasses to adsorb proteins, albumin in this case.

The image analysis results for the fibronectin group of samples are presented in Figure 5.23 a and b. In Figure 5.23 a, the SG depicted a marked improvement in the ability to form clusters in the neutral buffer wash conditions, which increased further upon silanization (WNS). Whereas among the PG, the WBS condition seemed to be the most adept at increasing the ability to form protein clusters at their surface in the WBS condition, except for Fe-2, where the WNS condition was slightly better than WBS. However, from Figure 5.23 b, a clear inclination towards the WBS treatment was observed for enhancing the overall protein adsorption, except for S53P4, for which it was the WNS condition. This is in-line with the observations for the IR spectra of S53P4, which presented a stronger rise in the new bands in WN condition, as compared to the 13-93, indicating that a much thicker layer of HCA was precipitated at its surface than 13-93. As the precipitation of a HCA layer is considered as a measure of the glass's ability to promote cell attachment and proliferation, it may have led to the higher protein adsorption evidenced for S53P4 as compared to 13-93 in the WNS condition. Furthermore, a highly crystalline layer precipitated on the S53P4's surface in the WAS condition which can be observed from its respective confocal microscopy image, which is also in agreement with the conclusion from the IR spectra (Figure 5.16 c and d). However, the layer precipitated in the WAS condition appeared to be breaking away from the surface, as compared to the WNS condition, where it seemed more uniform. This may explain the higher RTF observed in

the WNS condition than in the WAS condition, however, this is highly speculative, and further studies are needed to understand this phenomenon.

From the zeta potential results, it is known that the lowest degree of positive charge on S53P4 and Ag-2 was observed in the WAS condition. Furthermore, a sharp rise in the positive charge was witnessed for acid and base washed Ag-2 samples, and the base and neutral washed samples depicted a more positive charged surface among the silanized samples. From the image analysis results, the WAS and WBS conditions for the glasses depicted a clear preference for depositing albumin and fibronectin respectively. This is indicative of the preference of proteins for surfaces with a specific surface charge, i.e., more positive or negative. Hence, the surface of phosphate glasses can indeed be suitably modified by tailoring their surface charge to create affinity for a particular protein, and silanization to increase the overall ability to absorb proteins.

6.3.6 Impact of protein adsorption on cell proliferation

In Figure 5.24, for the 20X images, a higher number of focal adhesion points (red dye) for the cells may be observed in case of Sr50 than S53P4, across both the conditions. However, at 60X, a clear increase in the number of focal adhesion points for the cells can be seen in the WBS+fibronectin Sr50 sample, as compared to the only WBS Sr50. This is representative of the better cell attachment that can be achieved with a better coverage of protein at the phosphate glass's surface. However, in the case of S53P4, there is no marked difference in the red fluorescence in both the conditions.

Apart from the above tests, timelapse videos were obtained with the EVOS imaging system, which captured an image every 5 min for 24 hours of the discs in cell culture (not presented here). The cell attachment on the glasses S53P4, Sr50 and Ag-2 was observed in the untreated, WBS and WBS+fibronectin conditions. The untreated S53P4 presented decent cell attachment and proliferation in the untreated condition as well, which improved for the EBS and WBS+fibronectin conditions. On the other hand, cells cultured on the untreated Sr50 eventually turned apoptotic after repeatedly attaching and detaching from the surface. However, a clear improvement in the cell attachment and proliferation, as good as the treated S53P4 samples, was observed in the WBS and WBS+fibronectin conditions. This clearly showed that and improvement in the ability of a biomaterial of adsorbing proteins makes it a better substrates for proper cell attachment.

6.4 Characterization of new borophosphate glasses

Other than the glass discs, the glass extracts of the newly developed Ag and Cu doped PG were also found to be not suitable for cell growth and proliferation. However, the extract of the Ce doped PG were found to promote cell growth and proliferation even better than the control (cell culture medium). From Publication I-II and [282], it was known that in aqueous media, the Ce doped glasses were more stable than Sr50, while the Ag and Cu doped glasses were less stable than Sr50. As Ag and Cu doped PG are desirable from the point of view of antimicrobial properties, it would be of utmost interest to have Ag and Cu doped glasses which promote cell growth and proliferation. Therefore, an attempt to reduce the dissolution rate of these glasses was made, by introducing B into the PG network, by replacing 2.5 mol% of P_2O_5 with B_2O_3. In the past, the addition of B to PG network has been shown to improve the durability of the glass towards aqueous dissolution, without negatively impacting the thermal processability [28–32]. In Publication III, the in-vitro bioactivity of these new borophosphate glasses, the undoped reference Sr50-B2.5 with x= 0, and the Ag, Cu and Ce doped glasses with x=2 mol% were assessed. Furthermore, the cell response to the extracts obtained from these glasses was evaluated, along with the cytotoxicity of the extracts.

6.4.1 Thermal properties

All the new borophosphate glasses were found to depict a thermal processing window well over 100°C, irrespective of the dopant metal ion (Table 5.2). This was indicative of their high degree of thermal processability, with Cu2-B2.5 possessing the largest ΔT. Furthermore, the ΔT of these glasses were also found to be higher than their corresponding parent PG, which is attributed to the addition of B_2O_3 to the PG network at the expense of P_2O_5 [21,28–31].

6.4.2 In-vitro dissolution characteristics

As change in pH of the surrounding environment is known to impact cells, the pH of the TRIS buffer solution and SBF were measured as a function of immersion time (Figure 5.25 a and b). Upon immersion, none of the glasses presented a significant change in the pH of the immersion media up to 21 days. However, at longer immersion times in TRIS, a small decrease in the pH was recorded for the Cu2-B2.5 and Ag1-B2.5 glasses, owing to the high release of phosphorous ion, as is expected from dissolution of PG [25,203]. Still, a minor change in the pH should not affect the cells adversely. The small

decrease presented by Cu2-B2.5 and Ag1-B2.5 is consistent with their higher solubility than the undoped reference, as already reported earlier in Publication I-II. Indeed, the variation in pH was less pronounced for these glasses than their pure phosphate counterparts, indicative of their enhanced hydrolytic resistance [381,382].

ICP analysis was performed on the TRIS and SBF solutions recovered post immersion for obtaining the ion concentration in these solutions, with a view to evaluate the ion release behavior of these new glasses (Figure 5.26 and 5.27). In the as-prepared condition, TRIS solution is devoid of the ions present in the glasses, in contrast to SBF which contains Ca and P ions already prior to immersion. Therefore, the nature of dissolution of these glasses was evaluated by calculating the fraction of ions released in the TRIS solution with immersion time. Overall, a similar release of the constituent ions was observed up to 7 days for all the glasses, indicating the congruent nature of dissolution. Moreover, all the glasses presented a similar dissolution rate in TRIS. At longer immersion times, the ion release curve exhibited a parabolic nature, which may be indicative of the formation of a diffusion barrier. However, in SBF, Ce2-B2.5 demonstrated significantly lower ion release over immersion time, as compared to the others which behaved similarly within the error of measurement. This can be attributed to the higher resistance of Ce2-B2.5 towards aqueous dissolution, as reported in [282]. It must be pointed out that this difference in the behavior of Ce2-B2.5 in TRIS and SBF solutions may be due to the prompt precipitation of $CePO_4$ crystals when immersed in SBF, as observed for Ce doped SG earlier [283].

From the IR spectra of the glasses post immersion in SBF (Figure 5.28), similar changes were observed for all the compositions as a function of immersion time. With an increase in immersion time, the drop in intensity and shift towards lower wavenumbers (~14 cm^{-1}) of the band at 1260 cm^{-1} points to the progressive rise in Q^1 units at the expense of Q^2 units, owing to depolymerization of the PG network. The shift to lower wavenumbers of this band, corresponding to Q^2 units, is indicative of the weakening of their bond strengths. These alterations are typical of the early stages of glass dissolution [18,25]. For all the glasses, the new bands at 990 and 1032 cm^{-1} along with the increase in the shoulder at 1154 cm^{-1} suggest the precipitation of a Ca-P layer, partially substituted with Sr, as explained in Publication I and [383]. No new bands were observed for Ce2-B2.5, perhaps due to a delay in the precipitation of a surface layer, or detachment of the layer from glass surface. The overall changes to the Ce2-B2.5 spectra were also smaller as compared to the other glasses, owing to either the delayed precipitation of the reactive layer or formation of $CePO_4$ crystals.

The presence/absence of a reactive layer on the glass' surface post immersion was confirmed with SEM-EDS (Figure 5.29 and Table 5.3). A surface layer could be seen in all the conditions, except Ag1-B2.5 and Ce2-B2.5 in SBF. While, this is agreement with the conclusions from the IR spectra of Ce2-B2.5 glass, it is contradictory to the IR spectra of the Ag1-B2.5 glass. The Ag1-B2.5 spectra exhibited the formation of new bands upon immersion in SBF. This might be caused by a poor attachment of the surface layer, leading to detachment prior to the SEM analysis, or a surface layer forming only in limited areas. The EDS analysis further revealed the integration of Ce into the surface layer, as the Ce concentration increased at the surface compared to the nominal value. This is inline with the saturation of Ce concentration after immersion for 42 days in TRIS. This was also supported by an earlier study [283] which reported the formation of a mixed phase of Ce_2O_3-$CePO_4$ in the surface layer, upon dissolution of Ce containing phosphor-SG in SBF. This may inhibit the formation of a Ca-P reactive layer, and/or lead to a lower dissolution rate in SBF, which is not greatly affected in TRIS. The formation of the reactive layer in TRIS buffer solution is also in agreement with the ICP results. The higher release of B and Na as compared to Sr, Ca and P after 7 days, can be credited to the precipitation of a Sr substituted Ca-P layer.

Overall, these borophosphate glasses present a lower dissolution rate than their PG counterparts studied earlier in Publication I-II, which should have a positive impact on the cell viability.

6.4.3 Cell growth and proliferation

The undiluted glass extracts were analyzed with ICP to obtain the concentration of constituent ions (Table 5.4). Cu2-B2.5 and Ce2-B2.5 presented the highest and lowest amount of all the constituent ions respectively, indicating that it has the highest dissolution rate, while Ce2-B2.5 the lowest. In addition, Ag-1 presented a lower dissolution rate than the reference glass Sr50-B2.5.While the release of Cu was evidenced in the culture media, Ce was found to be absent. It is worth mentioning that DMEM contains a lower Ca^{2+} concentration and a higher HCO_3^- concentration than SBF. Furthermore, though TRIS, SBF and DMEM (major component of the cell culture media) are all buffered, they have different buffering capacities. Thus, expectedly, the glasses presented different ion release behavior in different media.

From the L/D results (Figure 5.30), cells were found to be viable in all the conditions, with no dead cells, except for the Cu2-B2.5 extract. Furthermore, for some of the samples, the number of cells at D-14 seemed lower compared to that at D-7, perhaps because of

the peeling off of the cell layer, which occurs at very high cell amounts. From the cell proliferation analysis (Figure 5.31), all the extracts depicted a rise in the cell amount from D-3 to D-7, except the undiluted Cu-2. The cell amounts remained unchanged from D-7 to D-14, which may be due to reaching 100% confluence at D-7. The low cell amounts observed for the Cu2-B2.5 extract may be credited to the high concentration of the dissolution products in the extract, and/or to the presence of Cu ion in the media. However, from the ICP analysis of the undiluted extracts (Table 5.4), it must be pointed out that 79 mg/L of Ca, 40 mg/L of Sr and 111 mg/L of P do not impact the cell proliferation negatively, which were the ion concentrations in the Sr50-B2.5 extract. Furthermore, for the Ag1-B2.5 glass extract, an increase in the cell number over culture time was recorded, despite the cell amounts remaining consistently lower than for the Sr50-B2.5 extract. This however, does not correlate to the Ca, Sr, P and B concentration in the extracts, which are lower for Ag1-B2.5 than Sr50-B2.5, and hence could be attributed to the Ag ions present in the solution. Among the 1:10 diluted extracts, the amount of cells increased as a function of time in culture, irrespective of the glass composition, with Ce-2 depicting the highest cell amount at D-14. This cannot be assigned to the Ce ion, as Ce was absent from the extract, perhaps due to precipitation of $CePO_4$ during extract preparation as discussed earlier. Finally, all the 1:100 diluted extracts depicted an increase in cell amount over time in culture, independent of the glass composition.

The cytotoxicity of these glass extracts was evaluated with LDH analysis (Figure 5.32). As LDH is released by dead cells, a higher LDH value correspond to higher cytotoxicity of the extract. Cu2-B2.5 presented the highest cytotoxicity among all the extracts at all the time points. Among the diluted extracts, all the extracts at a given dilution presented similar cytotoxicity at a given time point, owing to the lower metal ion concentrations present in them as compared to the undiluted ones. Additionally, the higher LDH value of diluted extracts at D-14 may be credited to the high cell amount at this time point.

Therefore, the glasses investigated in this study presented an improvement in cell response to their extracts, except the Cu2-B2.5 glass extract in undiluted form. The small addition of B did not compromise the thermal processability of the glass, and improved their resistance to aqueous dissolution without significantly impacting the nature of dissolution and the ion release behavior.

6.5 Phosphate glass fibers for biosensing

Single core and core-clad fibers were obtained from the Sr50 and Ce-1 compositions, for application in biosensing and for reinforcing composites. The potential of the core-clad fiber for biosensing was assessed in Publication IV by obtaining the light loss through the sensing region, which was immersed in TRIS buffer solution. The sensing region was created by etching away the clad for a part of the length of the core-clad fiber, using 1M phosphoric acid. The mechanical strength of the single core and core-clad fibers were obtained, as a function of immersion time in TRIS buffer solution. Furthermore, the mechanical strength of the etched core-clad fiber was also obtained.

The refractive index of the Ce-1 fiber was found to be higher than Sr50, hence the core-clad fiber was drawn with Ce-1 as the core and Sr50 as clad, to fulfill the condition for total internal reflection ($\eta_{core} < \eta_{clad}$). With a numerical aperture (NA) of 0.16, similar to some previously studied fibers [363], the fiber exhibited a bright core as compared to the clad (Figure 5.33). This confirmed proper guidance of light within the core of the fiber due to total internal reflection.

6.5.1 Mechanical strength upon immersion

Prior to immersion, both the single core fibers exhibited similar tensile strength, indicating that both the fibers contained similar amount of surface defects (Figure 5.34 a). On the other hand, the core-clad fiber depicted lower tensile strength than either of the single core fibers, which can be attributed to the core-clad fiber processing. For instance, stresses can arise from the mismatch of the coefficient of thermal expansion at the core-clad interface [384–386]. This is in agreement with Ahmed et al. [185], who studied core-clad PG fibers from compositions labeled P50Fe5 and P45Ti5, obtained via extrusion. These core-clad fibers presented a lower tensile strength than the single core fiber of P45Fe5 composition studied by Sharmin et al [387]. The origin of fracture in the fibers under investigation in this study was examined with optical microscopy and SEM (Figure 5.35 a, b, c and d). From the images a typical fiber fracture can be evidenced with the presence a mirror region and hackles. The origin of fracture is located at the surface of the Ce-1 fibers, and at the cladding surface for the core-clad fibers [388]. Indeed, all the core-clad fibers were found to break at the cladding interface, and not at the core-clad interface. This indicated that the low initial tensile strength of the core-clad fibers did not arise due to defects at the core-clad interface, but rather due to thermal stresses at the interface.

After immersion for 2 days in TRIS buffer solution, the tensile strength of all the fibers increased as also evidenced in [337], owing to the etching of the surface defects which leads to a decrease in the surface defect density of the fibers. At longer immersion time points, the tensile strength of the Sr50 fiber decreased, due to corrosion of the fiber [389]. On the other hand, the Ce-1 fiber's mechanical properties dropped only after 21 days in TRIS, credited to the reduced glass reactivity in aqueous media, owing to the presence of Ce in Sr50 glass network. Doping with Ce was shown to decrease the dissolution and delay the precipitation of a surface layer of the Sr50 glass, by Massera et al. [282]. The core-clad fibers depicted similar changes in tensile strength as the Sr50 fiber, over the course of immersion. Conversely, the initial increase in tensile strength up to 2 days of immersion was lower for the core-clad fibers compared to the single core Sr50 fiber. This may be attributed to the higher density of large defects at the core-clad fiber's surface, which were not efficiently etched. It is worth noting that all the fibers exhibited similar tensile strength after 42 days, ~150 MPa.

From Figure 5.36 b, the core-clad and the single core Sr50 fiber exhibited similar Young's modulus, whereas the single core Ce-1 fiber depicted a higher value. This is also attributed to the increase in network connectivity due to addition of Ce to the Sr50 glass network which may reduce the elasticity of the glass fibers [282]. In contrast to the fibers in [337,390], the fibers in this study presented an increase in Young's modulus initially, then decrease, upon immersion in TRIS buffer solution. For the Sr50 and core-clad fibers, the Young's modulus presented a maxima at 7 days, except for Ce-1 which exhibited its maxima at 21 days. A similar increase in the tensile modulus of the fibers post annealing was reported by [337], and was accredited to structural changes. It is also well regarded, that the mechanical properties of PG are a function of compositional parameters, i.e., dissociation energy and packing density, and the total bonding energy [391,392]. Although these glasses are considered to dissolve congruently, the fiber's surface undergoes depletion of alkaline and alkaline earth metals [264]. Thus, the decrease in the modulus was attributed to the pitting and local defect formation upon selective dissolution of areas with higher reactivity.

Weibull modulus of the fibers was evaluated, as immersion of fibers is known to impact the probability of early fracture, and thus the scatter in brittle fracture strength. A high value of Weibull modulus represents low scatter in brittle fracture strength, and hence a higher strength reproducibility. The initial rise in Weibull modulus of the core-clad and the single core Ce-1 fibers was expected (Figure 5.36 c), as the largest surface flaws

were etched away, reducing the possibility of a premature fracture of the fiber. This reciprocated in a decrease in the scatter in brittle fracture strength. The reduction in Weibull modulus at longer immersion times, signaled the rise in surface flaws, leading to fibers having lower tensile stress, hence early fracture, and a higher scatter in brittle fracture. It is also interesting to point out that the core-clad fibers exhibited lower Weibull modulus compared to the single core fibers, confirming the greater density of surface defects induce by the core-clad processing.

6.5.2 Etched fibers for biosensing

In an earlier study, the changes in the optical properties of a single core bioresorbable bioactive glass fiber upon immersion in SBF, could be correlated to its state of degradation [186]. In this study, the core-clad fiber was partly immersed in 1M phosphoric acid, to remove the cladding and reveal a sensing region. Upon immersion in phosphoric acid, a near linear reduction in the fiber diameter was evidenced, at a rate of 4.4µm/h (Figure 5.37 a and b). Thus, based on the thickness of the cladding, its complete removal was expected after 14.5 h of etching. Indeed, after 13 h of etching, only a very thin layer of cladding could be observed on the etched fiber. As etching was expected to impact the fiber's mechanical properties [393], the tensile strength of 10 etched core-clad fibers (etched for 14.5 h to completely remove the cladding) was evaluated. Interestingly, the fibers fractured in different regions, with average tensile strength of ~225 MPa, 150 MPa and 350 MPa for regions I, II and II respectively (Figure 5.38 a and b). Thus, etching of the fibers led to a drop in the fiber's mechanical properties, owing to a rise in flaw density, surface pits formation, a decrease in the fiber diameter and/or an increase in the size of surface flaws. While mild etching of the fibers due to dissolution in TRIS initially improved the mechanical properties, further etching reduced the mechanical properties owing to an increase in the fiber roughness, and/or precipitation of a reactive surface layer [393]. It is worth pointing out that the tensile strength of the etched fibers was similar to those immersed in TRIS for long immersion time. This indeed indicates that the surface roughness and surface flaws dictate the fiber's mechanical properties after significant etching.

Furthermore, the etched core-clad fibers were evaluated in terms of their potential for biosensing. This was accomplished by recording the light loss through the sensing region of these fibers, while it being immersed in TRIS buffer solution (Figure 5.39). The relative light intensity at 680 nm was found to progressively reduce with immersion time. Furthermore, etched fibers immersed for 7, 21 and 42 days were imaged to evidence the surface layer precipitation. The rapid initial drop in light intensity during the first 14 days was

assigned to the fast initial dissolution of the glass in TRIS buffer solution. At longer immersion time, a CaP reactive layer was observed at the fiber's surface, which grew thicker over time, leading to a further increase in the light loss, as also reported in [186].

Conclusions

The primary aims of this thesis were to (i) develop a new family of phosphate glasses which have added features such as antimicrobial properties, a high degree of thermal processability and are suitable for promoting cell growth and proliferation, and (ii) develop phosphate glass fibers which have potential applications in biosensing and have decent mechanical properties for use as reinforcements in composites.

Ag, Cu, Ce; Fe doped phosphate glasses were developed. The choice of the dopant was found to drastically impact the structure allowing to tailor the glasses in-vitro dissolution properties. The developed glasses were found to exhibit antimicrobial properties superior than for the typically available silicate bioactive glasses. All glasses possessed thermal properties enabling fiber drawing, not attainable with highly bioactive silicate glasses. However, initial cell culture revealed that cells did not attach to the glass surfaces. It was hypothesized that the poor cell attachment at the glass disc's surface is due to the congruent dissolution mechanism of phosphate glasses. Moreover, the glass extracts were also found unfavorable for cell survival, leading to another hypothesis that the glasses are too fast dissolving for supporting cell growth and proliferation. Hence, in order to develop phosphate bioactive glasses that could potentially replace silicate bioactive glasses, the thesis dealt with (i) ways to improve the phosphate glasses as substrates for optimal cell response, and (ii) developed and tested phosphate glass fibers for the targeted applications.

In a nutshell, the major results and conclusion obtained in this thesis were:

I. In Publication I-II, metaphosphate glasses doped with metallic ions Ag, Cu and Fe were manufactured, and tested in terms of their structural, thermal, physical, optical and in-vitro dissolution characteristics. The Ag and Cu doped glasses depicted additional functionality in the form of excellent antimicrobial properties, even better than the commercially available S53P4. Furthermore, the Ag and Cu doped glasses dissolved faster, while the Fe doped glasses dissolved at a much slower rate than the undoped reference glass.

II. The glasses in Publication I-II possessed favorable thermal characteristics for thermal processing such as fiber drawing and scaffold sintering, barring the Fe doped glasses. They were subsequently replaced by the previously studied Ce doped glasses in Publication III and IV, as they also possessed a slower dissolution rate than the undoped reference, but did not compromise on the thermal processability.

III. In the preliminary cell culture tests conducted with glass disc of the undoped reference glass, and in the glass extracts of the reference, and Ag, Cu and Ce doped glasses, the results showed cytotoxicity due to the fast dissolution rate of the metaphosphate glasses. However, these shortcomings were then addressed in the Unpublished manuscript and Publication III. In the former, a series of surface treatment methods were developed for improving protein adsorption at the surface of phosphate glass discs, which is known to be the crucial preceding step to cell attachment in-vivo. The commercial silicate bioactive glasses 13-93 and S53P4 were used as control. Following the surface treatments, a vast improvement was witnessed in the ability of phosphate glasses to adsorb proteins and attach cells at their surface, relative to that in the silicate glasses. It was shown that the phosphate glasses could promote nearly as good cell attachment at their surface as the commercial silicate glasses, upon suitable surface modifications.

In Publication III, new glasses with a reduced degradation rate were obtained, without compromising on the thermal processability, by the addition of 2.5 mol% of borate to the glass system, in place of phosphate. Consequently, the extracts of the newly obtained undoped reference, Ag, Cu and Ce doped glasses were found to support cell growth and proliferation nearly as good as or even better than the control, barring the undiluted Cu extract. Upon cytotoxicity measurements, the undiluted Cu extract indeed presented a much higher cytotoxicity as compared to the other extracts in the study. Additionally, it was demonstrated that at higher dilutions, all the glass extracts including that of the Cu doped glass, support cell growth and proliferation equally well or even better than the control.

In summary, by tailoring the composition, and using suitable surface treatment methods, phosphate glasses can definitely act as good substrates for cell growth and proliferation.

IV. Finally, in Publication IV, single core and core-clad glass fibers were obtained from the undoped reference and a Ce doped glass composition. All the fibers depicted good mechanical strength properties. Furthermore, the core-clad fiber was found to be very promising for biosensing applications, as it guided light effectively up to 4 weeks and maintained a tensile strength of ~150-200 MPa after 6 weeks in vitro.

Therefore, with this thesis, it was demonstrated that the dissolution rate of the phosphate glasses can be tailored by doping with suitable metallic ions, and added functionality such as antimicrobial properties may be imparted (Publication I-II). The phosphate glasses could indeed be made into good substrates for promoting cell attachment and proliferation, by tailoring the composition (Publication III) and by modifying their surface chemistry (Unpublished manuscript). Furthermore, the phosphate and borophosphate glasses investigated in this study possess excellent thermal processability (Publication I-III), and can be drawn into fibers with good mechanical properties and potential applications in biosensing (Publication IV). The results of the thesis open the path to new phosphate glasses for bone tissue engineering and/or biosensing.

Bibliography

[1] S. Ramakrishna, J. Mayer, E. Wintermantel, K.W. Leong, Biomedical applications of polymer-composite materials: a review, Compos. Sci. Technol. 61 (2001) 1189–1224. doi:10.1016/S0266-3538(00)00241-4.

[2] B. Ratner, A. Hoffman, F. Schoen, J. Lemons, Biomaterials Science: An Introduction to Materials in Medicine, I, Academic Press, 1997.

[3] L.L. Hench, Biomaterials: A forecast for the future, in: Biomaterials, 1998: pp. 1419–1423. doi:10.1016/S0142-9612(98)00133-1.

[4] L.L. Hench, R.J. Splinter, W.C. Allen, T.K. Greenlee, Bonding mechanisms at the interface of ceramic prosthetic materials, J. Biomed. Mater. Res. 5 (1971) 117–141. doi:10.1002/jbm.820050611.

[5] W. Cao, L.L. Hench, Bioactive materials, Ceram. Int. 22 (1996) 493–507. doi:10.1016/0272-8842(95)00126-3.

[6] L.L.L. Hench, J.M.M. Polak, I.D.D. Xynos, L.D.K.D.K. Buttery, Bioactive materials to control cell cycle, Mater. Res. Innov. 3 (2000) 313–323. doi:10.1007/s100190000055.

[7] M. Montazerian, E.D. Zanotto, A guided walk through Larry Hench's monumental discoveries, J. Mater. Sci. 52 (2017) 8695–8732. doi:10.1007/s10853-017-0804-4.

[8] O.H. Andersson, K. Karlsson, K. Kangasniemi, A. Yli-Urpo, Model for Physical Properties and Bioactivity of Phosphate Opal Glasses, Glas. Berichte. 61 (1988) 300–305.

[9] M. Waselau, M. Patrikoski, M. Juntunen, K. Kujala, M. Kääriäinen, H. Kuokkanen,

G.K. Sándor, O. Vapaavuori, R. Suuronen, B. Mannerström, B. von Rechenberg, S. Miettinen, Effects of bioactive glass S53P4 or beta-tricalcium phosphate and bone morphogenetic protein-2 and bone morphogenetic protein-7 on osteogenic differentiation of human adipose stem cells, J. Tissue Eng. 3 (2012) 1–14. doi:10.1177/2041731412467789.

[10] M. Bortolin, E. De Vecchi, C.L. Romano, M. Toscano, R. Mattina, L. Drago, Antibiofilm agents against mdr bacterial strains: Is bioactive glass bag-s53p4 also effective?, J. Antimicrob. Chemother. 71 (2016) 123–127. doi:10.1093/jac/dkv327.

[11] L. Drago, C. Vassena, S. Fenu, E. De Vecchi, V. Signori, R. De Francesco, C. Romanò, In vitro antibiofilm activity of bioactive glass S53P4, Future Microbiol. 9 (2014) 593–601. doi:10.2217/fmb.14.20.

[12] L. Drago, E. De Vecchi, M. Bortolin, M. Toscano, R. Mattina, C.L. Romanò, Antimicrobial activity and resistance selection of different bioglass S53P4 formulations against multidrug resistant strains, Future Microbiol. (2015). doi:10.2217/FMB.15.57.

[13] S. Fagerlund, J. Massera, M. Hupa, L. Hupa, T-T-T behaviour of bioactive glasses 1-98 and 13-93, J. Eur. Ceram. Soc. 32 (2012) 2731–2738. doi:10.1016/j.jeurceramsoc.2011.10.040.

[14] D. Groh, F. Döhler, D.S. Brauer, Bioactive glasses with improved processing. Part 1. Thermal properties, ion release and apatite formation, Acta Biomater. 10 (2014) 4465–4473. doi:10.1016/j.actbio.2014.05.019.

[15] E. Pirhonen, H. Niiranen, T. Niemelä, M. Brink, P. Törmälä, Manufacturing, mechanical characterization, and in vitro performance of bioactive glass 13-93 fibers, J. Biomed. Mater. Res. - Part B Appl. Biomater. 77 (2006) 227–233. doi:10.1002/jbm.b.30429.

[16] J. Massera, S. Fagerlund, L. Hupa, M. Hupa, Crystallization mechanism of the bioactive glasses, 45S5 and S53P4, J. Am. Ceram. Soc. 95 (2012) 607–613. doi:10.1111/j.1551-2916.2011.05012.x.

[17] N.C. Lindfors, I. Koski, J.T. Heikkilä, K. Mattila, A.J. Aho, A prospective randomized 14-year follow-up study of bioactive glass and autogenous bone as bone graft substitutes in benign bone tumors, J. Biomed. Mater. Res. - Part B Appl. Biomater. 94 (2010) 157–164. doi:10.1002/jbm.b.31636.

[18] B.C. Bunker, G.W. Arnold, J.A. Wilder, Phosphate glass dissolution in aqueous solutions, J. Non. Cryst. Solids. 64 (1984) 291–316. doi:10.1016/0022-3093(84)90184-4.

[19] C.W. Kim, C.S. Ray, D. Zhu, D.E. Day, D. Gombert, A. Aloy, A. Moguš-Milanković, M. Karabulut, Chemically durable iron phosphate glasses for vitrifying sodium bearing waste (SBW) using conventional and cold crucible induction melting

(CCIM) techniques, J. Nucl. Mater. 322 (2003) 152–164. doi:10.1016/S0022-3115(03)00325-8.

[20] D.E. Day, Z. Wu, C.S. Ray, P. Hrma, Chemically durable iron phosphate glass wasteforms, J. Non. Cryst. Solids. 241 (1998) 1–12. doi:10.1016/S0022-3093(98)00759-5.

[21] P.A. Bingham, R.J. Hand, O.M. Hannant, S.D. Forder, S.H. Kilcoyne, Effects of modifier additions on the thermal properties, chemical durability, oxidation state and structure of iron phosphate glasses, J. Non. Cryst. Solids. 355 (2009) 1526–1538. doi:10.1016/j.jnoncrysol.2009.03.008.

[22] I.W. Donald, B.L. Metcalfe, R.N.J. Taylor, The immobilization of high level radioactive wastes using ceramics and glasses, J. Mater. Sci. 32 (1997) 5851–5887. doi:10.1023/A:1018646507438.

[23] A. Kiani, N.J. Lakhkar, V. Salih, M.E. Smith, J. V. Hanna, R.J. Newport, D.M. Pickup, J.C. Knowles, Titanium-containing bioactive phosphate glasses, Philos. Trans. R. Soc. A Math. Phys. Eng. Sci. 370 (2012) 1352–1375. doi:10.1098/rsta.2011.0276.

[24] J. Clément, J.M. Manero, J.A. Planell, G. Avila, S. Martínez, Analysis of the structural changes of a phosphate glass during its dissolution in simulated body fluid, J. Mater. Sci. Mater. Med. 10 (1999) 729–732. doi:10.1023/A:1008927222081.

[25] J. Massera, L. Petit, T. Cardinal, J.J. Videau, M. Hupa, L. Hupa, Thermal properties and surface reactivity in simulated body fluid of new strontium ion-containing phosphate glasses, J. Mater. Sci. Mater. Med. 24 (2013) 1407–1416. doi:10.1007/s10856-013-4910-9.

[26] I. Ahmed, C.A. Collins, M.P. Lewis, I. Olsen, J.C. Knowles, Processing, characterisation and biocompatibility of iron-phosphate glass fibres for tissue engineering, Biomaterials. 25 (2004) 3223–3232. doi:10.1016/j.biomaterials.2003.10.013.

[27] X. Liu, D.M. Grant, A.J. Parsons, L.T. Harper, C.D. Rudd, I. Ahmed, Magnesium Coated Bioresorbable Phosphate Glass Fibres: Investigation of the Interface between Fibre and Polyester Matrices, Biomed Res. Int. 2013 (2013) 1–10. doi:10.1155/2013/735981.

[28] M. Karabulut, B. Yuce, O. Bozdogan, H. Ertap, G.M. Mammadov, Effect of boron addition on the structure and properties of iron phosphate glasses, J. Non. Cryst. Solids. 357 (2011) 1455–1462. doi:10.1016/j.jnoncrysol.2010.11.023.

[29] J. Massera, C. Claireaux, T. Lehtonen, J. Tuominen, L. Hupa, M. Hupa, Control of the thermal properties of slow bioresorbable glasses by boron addition, J. Non. Cryst. Solids. 357 (2011) 3623–3630. doi:10.1016/j.jnoncrysol.2011.06.037.

[30] T. Harada, H. In, H. Takebe, K. Morinaga, Effect of B2O3 Addition on the Thermal Stability of Barium Phosphate Glasses for Optical Fiber Devices, J. Am. Ceram. Soc. 87 (2004) 408–411. doi:10.1111/j.1551-2916.2004.00408.x.

[31] L. Koudelka, P. Mošner, Study of the structure and properties of Pb-Zn borophosphate glasses, J. Non. Cryst. Solids. 293 (2001) 635–641. doi:10.1016/S0022-3093(01)00765-7.

[32] P.A. Bingham, R.J. Hand, S.D. Forder, Doping of iron phosphate glasses with Al2O3, SiO2 or B2O3 for improved thermal stability, Mater. Res. Bull. 41 (2006) 1622–1630. doi:10.1016/j.materresbull.2006.02.029.

[33] R. Dimitriou, E. Jones, D. McGonagle, P. V Giannoudis, Bone regeneration: current concepts and future directions, BMC Med. 9 (2011) 66. doi:10.1186/1741-7015-9-66.

[34] E. Jimi, S. Hirata, K. Osawa, M. Terashita, C. Kitamura, H. Fukushima, The Current and Future Therapies of Bone Regeneration to Repair Bone Defects, Int. J. Dent. 2012 (2012) 1–7. doi:10.1155/2012/148261.

[35] H. Ghanbari, R. Vakili-Ghartavol, Bone Regeneration: Current Status and Future Prospects, in: A.R. Zorzi, J.B. de Miranda (Eds.), Adv. Tech. Bone Regen., InTech, 2016. doi:10.5772/63912.

[36] R. Spin-Neto, E. Marcantonio, E. Gotfredsen, A. Wenzel, Exploring CBCT-Based DICOM Files. A Systematic Review on the Properties of Images Used to Evaluate Maxillofacial Bone Grafts, J. Digit. Imaging. 24 (2011) 959–966. doi:10.1007/s10278-011-9377-y.

[37] J.A. Gruskay, B.A. Basques, D.D. Bohl, M.L. Webb, J.N. Grauer, Short-Term Adverse Events, Length of Stay, and Readmission After Iliac Crest Bone Graft for Spinal Fusion, Spine (Phila. Pa. 1976). 39 (2014) 1718–1724. doi:10.1097/BRS.0000000000000476.

[38] G.H. Westrich, D.S. Geller, M.J. O'Malley, J.T. Deland, D.L. Helfet, Anterior Iliac Crest Bone Graft Harvesting Using the Corticocancellous Reamer System, J. Orthop. Trauma. 15 (2001) 500–506. doi:10.1097/00005131-200109000-00007.

[39] T. A St John, A. R Vaccaro, A. P Sah, M. Schaefer, S. Berta, T. Albert, A. Hilibrand, Physical and monetary costs associated with autogenous bone graft harvesting, 2003.

[40] G. Kumar, B. Narayan, Morbidity at Bone Graft Donor Sites, in: Class. Pap. Orthop., Springer London, London, 2014: pp. 503–505. doi:10.1007/978-1-4471-5451-8_132.

[41] E. Ahlmann, M. Patzakis, N. Roidis, L. Shepherd, P. Holtom, Comparison of anterior and posterior iliac crest bone grafts in terms of harvest-site morbidity and

functional outcomes, 2002.

[42] C.G. Finkemeier, Bone-grafting and bone-graft substitutes., J. Bone Joint Surg. Am. 84-A (2002) 454–64. http://www.ncbi.nlm.nih.gov/pubmed/11886919.

[43] P. V. Giannoudis, H. Dinopoulos, E. Tsiridis, Bone substitutes: An update, Injury. 36 (2005) S20–S27. doi:10.1016/j.injury.2005.07.029.

[44] M. Saini, Implant biomaterials: A comprehensive review, World J. Clin. Cases. 3 (2015) 52. doi:10.12998/wjcc.v3.i1.52.

[45] N. Sykaras, A.M. Iacopino, V.A. Marker, R.G. Triplett, R.D. Woody, Implant materials, designs, and surface topographies: their effect on osseointegration. A literature review., Int. J. Oral Maxillofac. Implants. 15 (2000) 675–690. doi:10.1016/0167-4781(85)90057-0.

[46] S.B. Goodman, Wear particles, periprosthetic osteolysis and the immune system, Biomaterials. 28 (2007) 5044–5048. doi:10.1016/j.biomaterials.2007.06.035.

[47] I.D. Learmonth, C. Young, C. Rorabeck, The operation of the century: total hip replacement, Lancet. 370 (2007) 1508–1519. doi:10.1016/S0140-6736(07)60457-7.

[48] M.K.D. Benson, P.G. Goodwin, J. Brostoff, Metal sensitivity in patients with joint replacement arthroplasties, Br. Med. J. 4 (1975) 374–375. doi:10.1136/bmj.4.5993.374.

[49] U.E. Pazzaglial, L. Ceciliani, M.J. Wilkinson, C. Dell'Orboz, Involvement of metal particles in loosening of metal-plastic total hip prostheses, Arch. Orthop. Trauma. Surg. 104 (1985) 164–174. doi:10.1007/BF00454694.

[50] H.-G. Willert, M. Semlitsch, Reactions of the articular capsule to wear products of artificial joint prostheses, J. Biomed. Mater. Res. 11 (1977) 157–164. doi:10.1002/jbm.820110202.

[51] V.P. Nautiyal, A. Mittal, A. Agarwal, A. Pandey, Tissue response to titanium implant using scanning electron microscope, Natl. J. Maxillofac. Surg. 4 (2013) 7–12. doi:10.4103/0975-5950.117815.

[52] U. Dapunt, T. Giese, F. Lasitschka, J. Reinders, B. Lehner, J.P. Kretzer, V. Ewerbeck, G.M. Hansch, On the inflammatory response in metal-on-metal implants, J. Transl. Med. 12 (2014) 1–9. doi:10.1186/1479-5876-12-74.

[53] J.D. Bobyn, R. Thompson, L. Lim, J.A. Pura, K. Bobyn, M. Tanzer, Local Alendronic Acid Elution Increases Net Periimplant Bone Formation: A Micro-CT Analysis, Clin. Orthop. Relat. Res. 472 (2014) 687–694. doi:10.1007/s11999-013-3120-6.

[54] J.-W. Park, K.-B. Park, J.-Y. Suh, Effects of calcium ion incorporation on bone

healing of Ti6Al4V alloy implants in rabbit tibiae., Biomaterials. 28 (2007) 3306–13. doi:10.1016/j.biomaterials.2007.04.007.

[55] F. Yang, D. Yang, J. Tu, Q. Zheng, L. Cai, L. Wang, Strontium Enhances Osteogenic Differentiation of Mesenchymal Stem Cells and In Vivo Bone Formation by Activating Wnt/Catenin Signaling, Stem Cells. 29 (2011) 981–991. doi:10.1002/stem.646.

[56] K. Soballe, Hydroxyapatite ceramic coating for bone implant fixation. Mechanical and histological studies in dogs., Acta Orthop. Scand. Suppl. 255 (1993) 1–58. http://www.ncbi.nlm.nih.gov/pubmed/8237337.

[57] J. Toquet, R. Rohanizadeh, J. Guicheux, S. Couillaud, N. Passuti, G. Daculsi, D. Heymann, Osteogenic potential in vitro of human bone marrow cells cultured on macroporous biphasic calcium phosphate ceramic., J. Biomed. Mater. Res. 44 (1999) 98–108. http://www.ncbi.nlm.nih.gov/pubmed/10397909.

[58] H. Uludag, D. D'Augusta, R. Palmer, G. Timony, J. Wozney, Characterization of rhBMP-2 pharmacokinetics implanted with biomaterial carriers in the rat ectopic model., J. Biomed. Mater. Res. 46 (1999) 193–202. http://www.ncbi.nlm.nih.gov/pubmed/10379997.

[59] S. Rammelt, T. Illert, S. Bierbaum, D. Scharnweber, H. Zwipp, W. Schneiders, Coating of titanium implants with collagen, RGD peptide and chondroitin sulfate., Biomaterials. 27 (2006) 5561–71. doi:10.1016/j.biomaterials.2006.06.034.

[60] D.M. Ferris, G.D. Moodie, P.M. Dimond, C.W.D. Giorani, M.G. Ehlrich, R.F. Valentini, RGD-coated titanium implants stimulate increased bone formation in vivo, Biomaterials. 20 (1999) 2323–2331. doi:10.1016/S0142-9612(99)00161-1.

[61] B. Zhang, D. Myers, G. Wallace, M. Brandt, P. Choong, Bioactive Coatings for Orthopaedic Implants—Recent Trends in Development of Implant Coatings, Int. J. Mol. Sci. 15 (2014) 11878–11921. doi:10.3390/ijms150711878.

[62] B. Love, Metallic Biomaterials, in: Biomaterials, Elsevier, 2017: pp. 159–184. doi:10.1016/B978-0-12-809478-5.00007-9.

[63] M.A. Minnath, Metals and alloys for biomedical applications, in: Fundam. Biomater. Met., Elsevier, 2018: pp. 167–174. doi:10.1016/B978-0-08-102205-4.00007-6.

[64] H. Hermawan, D. Ramdan, J.R. P. Djuansjah, Metals for Biomedical Applications, in: Biomed. Eng. - From Theory to Appl., InTech, 2011. doi:10.5772/19033.

[65] K. Ohura, M. Bohner, P. Hardouin, J. Lema□tre, G. Pasquier, B. Flautre, Resorption of, and bone formation from, new beta-tricalcium phosphate-monocalcium phosphate cements: an in vivo study, J. Biomed. Mater. Res. 30 (1996) 193–200. doi:10.1002/(SICI)1097-4636(199602)30:2<193::AID-JBM9>3.0.CO;2-M.

[66] K. Kurashina, H. Kurita, Q. Wu, A. Ohtsuka, H. Kobayashi, Ectopic osteogenesis with biphasic ceramics of hydroxyapatite and tricalcium phosphate in rabbits, Biomaterials. 23 (2002) 407–412. doi:10.1016/S0142-9612(01)00119-3.

[67] M. Saito, H. Shimizu, M. Beppu, M. Takagi, The role of ß-tricalcium phosphate in vascularized periosteum, J. Orthop. Sci. 5 (2000) 275–282. doi:10.1007/s007760050163.

[68] S. Kotani, Y. Fujita, T. Kitsugi, T. Nakamura, T. Yamamuro, C. Ohtsuki, T. Kokubo, Bone bonding mechanism of beta-tricalcium phosphate, J. Biomed. Mater. Res. 25 (1991) 1303–1315. doi:10.1002/jbm.820251010.

[69] T. Suzuki, S. Kawamura, M. Toriyama, Y. Yokokawa, Y. Kawamoto, Y. Hakamatsuka, H. Irie, 5491082 Plasminogen activator covalently bonded to a porous body of beta-tricalcium phosphate, Biotechnol. Adv. 15 (1997) 171–172. doi:10.1016/S0734-9750(97)88227-4.

[70] P. Habibovic, C.M. van der Valk, C.A. van Blitterswijk, K. de Groot, G. Meijer, Influence of octacalcium phosphate coating on osteoinductive properties of biomaterials, J. Mater. Sci. Mater. Med. 15 (2004) 373–380. doi:10.1023/B:JMSM.0000021104.42685.9f.

[71] F. Barrère, C.M. van der Valk, R.A.J. Dalmeijer, G. Meijer, C.A. van Blitterswijk, K. de Groot, P. Layrolle, Osteogenecity of octacalcium phosphate coatings applied on porous metal implants, J. Biomed. Mater. Res. Part A. 66A (2003) 779–788. doi:10.1002/jbm.a.10454.

[72] L. Cheng, F. Ye, R. Yang, X. Lu, Y. Shi, L. Li, H. Fan, H. Bu, Osteoinduction of hydroxyapatite/β-tricalcium phosphate bioceramics in mice with a fractured fibula, Acta Biomater. 6 (2010) 1569–1574. doi:10.1016/j.actbio.2009.10.050.

[73] A.K. Gosain, P.A. Riordan, L. Song, M.T. Amarante, B. Kalantarian, P.G. Nagy, C.R. Wilson, J.M. Toth, B.L. McIntyre, A 1-Year Study of Osteoinduction in Hydroxyapatite-Derived Biomaterials in an Adult Sheep Model: Part II. Bioengineering Implants to Optimize Bone Replacement in Reconstruction of Cranial Defects, Plast. Reconstr. Surg. 114 (2004) 1155–1163. doi:10.1097/01.PRS.0000135852.45465.A9.

[74] D. Le Nihouannen, G. Daculsi, A. Saffarzadeh, O. Gauthier, S. Delplace, P. Pilet, P. Layrolle, Ectopic bone formation by microporous calcium phosphate ceramic particles in sheep muscles, Bone. 36 (2005) 1086–1093. doi:10.1016/j.bone.2005.02.017.

[75] U. Ripamonti, Osteoinduction in porous hydroxyapatite implanted in heterotopic sites of different animal models, Biomaterials. 17 (1996) 31–35. doi:10.1016/0142-9612(96)80752-6.

[76] P. Habibovic, U. Gbureck, C. Doillon, D. Bassett, C. Vanblitterswijk, J. Barralet,

Osteoconduction and osteoinduction of low-temperature 3D printed bioceramic implants, Biomaterials. 29 (2008) 944–953. doi:10.1016/j.biomaterials.2007.10.023.

[77] H. Yuan, Z. Yang, Y. Li, X. Zhang, J.D. De Bruijn, K. De Groot, Osteoinduction by calcium phosphate biomaterials, J. Mater. Sci. Mater. Med. 9 (1998) 723–726. doi:10.1023/A:1008950902047.

[78] C. Klein, K. de Groot, W. Chen, Y. Li, X. Zhang, Osseous substance formation induced in porous calcium phosphate ceramics in soft tissues, Biomaterials. 15 (1994) 31–34. doi:10.1016/0142-9612(94)90193-7.

[79] H. Yamasaki, H. Sakai, Osteogenic response to porous hydroxyapatite ceramics under the skin of dogs, Biomaterials. 13 (1992) 308–312. doi:10.1016/0142-9612(92)90054-R.

[80] R.Z. LeGeros, Calcium Phosphate-Based Osteoinductive Materials, Chem. Rev. 108 (2008) 4742–4753. doi:10.1021/cr800427g.

[81] R.Z. LeGeros, Properties of Osteoconductive Biomaterials: Calcium Phosphates, Clin. Orthop. Relat. Res. 395 (2002) 81–98. doi:10.1097/00003086-200202000-00009.

[82] C.P.A.T. Klein, A.A. Driessen, K. de Groot, A. van den Hooff, Biodegradation behavior of various calcium phosphate materials in bone tissue, J. Biomed. Mater. Res. 17 (1983) 769–784. doi:10.1002/jbm.820170505.

[83] K. de Groot, Clinical applications of calcium phosphate biomaterials: A review, Ceram. Int. 19 (1993) 363–366. doi:10.1016/0272-8842(93)90050-2.

[84] P. Ducheyne, S. Radin, L. King, The effect of calcium phosphate ceramic composition and structure onin vitro behavior. I. Dissolution, J. Biomed. Mater. Res. 27 (1993) 25–34. doi:10.1002/jbm.820270105.

[85] S.R. Radin, P. Ducheyne, The effect of calcium phosphate ceramic composition and structure on in vitro behavior. II. Precipitation., J. Biomed. Mater. Res. 27 (1993) 35–45. doi:10.1002/jbm.820270106.

[86] F.H. Lin, C.J. Liao, K.S. Chen, J.S. Sun, H.C. Liu, Degradation behaviour of a new bioceramic: Ca2P2O7 with addition of Na4P2O7.10H2O., Biomaterials. 18 (1997) 915–21. http://www.ncbi.nlm.nih.gov/pubmed/9199761.

[87] A.E. Porter, C.M. Botelho, M.A. Lopes, J.D. Santos, S.M. Best, W. Bonfield, Ultrastructural comparison of dissolution and apatite precipitation on hydroxyapatite and silicon-substituted hydroxyapatite in vitro and in vivo., J. Biomed. Mater. Res. A. 69 (2004) 670–9. doi:10.1002/jbm.a.30035.

[88] E.S. Thian, J. Huang, S.M. Best, Z.H. Barber, W. Bonfield, Novel silicon-doped

hydroxyapatite (Si-HA) for biomedical coatings: an in vitro study using acellular simulated body fluid., J. Biomed. Mater. Res. B. Appl. Biomater. 76 (2006) 326–33. doi:10.1002/jbm.b.30368.

[89] Y. Belmamouni, M. Bricha, J. Ferreira, K. El Mabrouk, Hydrothermal Synthesis of Si-doped Hydroxyapatite Nanopowders: Mechanical and Bioactivity Evaluation, Int. J. Appl. Ceram. Technol. 12 (2015) 329–340. doi:10.1111/ijac.12210.

[90] M. Wang, Developing bioactive composite materials for tissue replacement, Biomaterials. 24 (2003) 2133–2151. doi:10.1016/S0142-9612(03)00037-1.

[91] H. Liu, T.J. Webster, Nanomedicine for implants: A review of studies and necessary experimental tools, Biomaterials. 28 (2007) 354–369. doi:10.1016/j.biomaterials.2006.08.049.

[92] V. Beachley, X. Wen, Polymer nanofibrous structures: Fabrication, biofunctionalization, and cell interactions, Prog. Polym. Sci. 35 (2010) 868–892. doi:10.1016/j.progpolymsci.2010.03.003.

[93] G. Mendonça, D.B.S. Mendonça, F.J.L. Aragão, L.F. Cooper, Advancing dental implant surface technology – From micron- to nanotopography, Biomaterials. 29 (2008) 3822–3835. doi:10.1016/j.biomaterials.2008.05.012.

[94] M. Kohri, K. Miki, D.E. Waite, H. Nakajima, T. Okabe, In vitro stability of biphasic calcium phosphate ceramics., Biomaterials. 14 (1993) 299–304. http://www.ncbi.nlm.nih.gov/pubmed/8386558.

[95] W. den Hollander, P. Patka, C.P. Klein, G.A. Heidendal, Macroporous calcium phosphate ceramics for bone substitution: a tracer study on biodegradation with 45Ca tracer., Biomaterials. 12 (1991) 569–73. http://www.ncbi.nlm.nih.gov/pubmed/1772955.

[96] E.B. Nery, R.Z. LeGeros, K.L. Lynch, K. Lee, Tissue Response to Biphasic Calcium Phosphate Ceramic With Different Ratios of HA/βTCP in Periodontal Osseous Defects, J. Periodontol. 63 (1992) 729–735. doi:10.1902/jop.1992.63.9.729.

[97] P. Frayssinet, J.L. Trouillet, N. Rouquet, E. Azimus, A. Autefage, Osseointegration of macroporous calcium phosphate ceramics having a different chemical composition., Biomaterials. 14 (1993) 423–9. http://www.ncbi.nlm.nih.gov/pubmed/8507788.

[98] X. Yang, Z. Wang, Synthesis of biphasic ceramics of hydroxyapatite and β-tricalcium phosphate with controlled phase content and porosity, J. Mater. Chem. 8 (1998) 2233–2237. doi:10.1039/a802067a.

[99] N. Kivrak, A.C. Taş, Synthesis of Calcium Hydroxyapatite-Tricalcium Phosphate (HA-TCP) Composite Bioceramic Powders and Their Sintering Behavior, J. Am.

Ceram. Soc. 81 (2005) 2245–2252. doi:10.1111/j.1151-2916.1998.tb02618.x.

[100] J. Wilson, S.B. Low, Bioactive ceramics for periodontal treatment: Comparative studies in the patus monkey, J. Appl. Biomater. 3 (1992) 123–129. doi:10.1002/jab.770030208.

[101] L.L. Hench, J.K. West, Biological applications of bioactive glasses, Life Chem. Reports. 13 (1996) 187–241.

[102] L.L. Hench, Bioactive Ceramics: Theory and Clinical Applications, in: Ö.H. Andersson, A. Yli-Urpo (Eds.), Bioceramics, 7th ed., Elsevier, 1994: pp. 3–14. doi:10.1016/B978-0-08-042144-5.50005-4.

[103] L.L. Hench, D.L. Wheeler, D.C. Greenspan, Molecular Control of Bioactivity in Sol-Gel Glasses, J. Sol-Gel Sci. Technol. 9 (1998) 245–250. doi:10.1023/a:1008643303888.

[104] M. Hubert, C. Glass, B. V Solar, M. Hubert, A.J. Faber, On the structural role of boron in borosilicate glasses On the structural role of boron in borosilicate glasses, (2016).

[105] J. Ballato, H. Ebendorff-Heidepriem, J. Zhao, L. Petit, J. Troles, Glass and Process Development for the Next Generation of Optical Fibers: A Review, Fibers. 5 (2017) 11. doi:10.3390/fib5010011.

[106] J.I. Peterson, G.G. Vurek, Fiber-optic sensors for biomedical applications., Science. 224 (1984) 123–7. http://www.ncbi.nlm.nih.gov/pubmed/6422554.

[107] J. Keirsse, C. Boussard-Plédel, O. Loréal, O. Sire, B. Bureau, P. Leroyer, B. Turlin, J. Lucas, IR optical fiber sensor for biomedical applications, Vib. Spectrosc. 32 (2003) 23–32. doi:10.1016/S0924-2031(03)00044-4.

[108] S.K. Nandi, B. Kundu, S. Datta, Development and Applications of Varieties of Bioactive Glass Compositions in Dental Surgery, Third Generation Tissue Engineering, Orthopaedic Surgery and as Drug Delivery System, in: R. Pignatello (Ed.), Biomaterials, IntechOpen, Rijeka, 2011. doi:10.5772/24942.

[109] A. K. Varshneya, Fundamentals of Inorganic Glasses, Soc. Glas. Technol. Sheff. (2012). doi:10.1016/0022-3093(94)90112-0.

[110] J.E. Shelby, Introduction to Glass Science and Technology, 1999. doi:10.1524/zpch.1999.208.Part_1_2.292.

[111] A. Paul, Chemistry of Glasses, Springer Netherlands, Dordrecht, 1982. doi:10.1007/978-94-009-5918-7.

[112] L.L. Hench, Bioceramics: From Concept to Clinic, J. Am. Ceram. Soc. 74 (1991) 1487–1510. doi:10.1111/j.1151-2916.1991.tb07132.x.

[113] A. Helebrant, A. Jiricka, Modelling of glass corrosion under dynamic conditions, in: Fundam. Glas. Sci. Technol., 1997: pp. 80–87. doi:916305499X.

[114] C. Cailleteau, C. Weigel, A. Ledieu, P. Barboux, F. Devreux, On the effect of glass composition in the dissolution of glasses by water, J. Non. Cryst. Solids. 354 (2008) 117–123. doi:10.1016/j.jnoncrysol.2007.07.063.

[115] H. Scholze, Glass-water interactions, J. Non. Cryst. Solids. 102 (1988) 1–10. doi:10.1016/0022-3093(88)90105-6.

[116] W.H. Casey, Dynamics and durability, Nat. Mater. 7 (2008) 930–932. doi:10.1038/nmat2326.

[117] R. Conradt, Chemical Durability of Oxide Glasses in Aqueous Solutions: A Review, J. Am. Ceram. Soc. 91 (2008) 728–735. doi:10.1111/j.1551-2916.2007.02101.x.

[118] L.L. Hench, D.E. Clark, Physical chemistry of glass surfaces, J. Non. Cryst. Solids. 28 (1978) 83–105. doi:10.1016/0022-3093(78)90077-7.

[119] L.L. Hench, Characterization of glass corrosion and durability, J. Non. Cryst. Solids. 19 (1975) 27–39. doi:10.1016/0022-3093(75)90067-8.

[120] W.B. White, Theory of Corrosion of Glass and Ceramics, Corros. Glas. Ceram. Supercond. (1992) 2–28. doi:10.5121/ijassn.2015.5402.

[121] B.C. Bunker, Molecular mechanisms for corrosion of silica and silicate glasses, J. Non. Cryst. Solids. 179 (1994) 300–308. doi:10.1016/0022-3093(94)90708-0.

[122] R.W. Douglas, T.M.M. El-Shamy, Reactions of glasses with aqueous solutions, J. Am. Ceram. Soc. 50 (1967) 1–8. doi:10.1111/j.1151-2916.1967.tb14960.x.

[123] T.M. El-Shamy, R.W. Douglas, Kinetics of the reaction of water with glass, 1972.

[124] B.C. Bunker, G.W. Arnold, E.K. Beauchamp, D.E. Day, Mechanisms for alkali leaching in mized-Na-K silicate glasses, J. Non. Cryst. Solids. 58 (1983) 295–322. doi:10.1016/0022-3093(83)90031-5.

[125] L.L. Hench, Bioceramics, J. Am. Ceram. Soc. 81 (2005) 1705–1728. doi:10.1111/j.1151-2916.1998.tb02540.x.

[126] F.G.K. Baucke, III. Electrochemistry in Glasses and Melts. Glass electrodes: Why and how they function, Berichte Der Bunsengesellschaft Für Phys. Chemie. 100 (1996) 1466–1474. doi:10.1002/bbpc.19961000923.

[127] F.G.K. Baucke, The modern understanding of the glass electrode response, Fresenius. J. Anal. Chem. 349 (1994) 582–596. doi:10.1007/BF00323462.

[128] F.G.K. Baucke, The glass electrode — applied electrochemistry of glass surfaces, J. Non. Cryst. Solids. 73 (1985) 215–231. doi:10.1016/0022-3093(85)90348-5.

[129] A. Fick, Über Difusion, Ann. Phys. 94 (1855) 59--86.

[130] A. Fick, V. On liquid diffusion, London, Edinburgh, Dublin Philos. Mag. J. Sci. 10 (1855) 30–39. doi:10.1080/14786445508641925.

[131] A. Fick, On liquid diffusion, J. Memb. Sci. 100 (1995) 33–38. doi:10.1016/0376-7388(94)00230-V.

[132] R.K. Iler, The chemistry of silica, 1980. doi:10.1016/0160-9327(80)90074-5.

[133] L.L. Hench, G.P. LaTorre, Ö.H. Andersson, The Kinetics of Bioactive Ceramics Part III: Surface Reactions for Bioactive Glasses compared with an Inactive Glass, in: Bioceramics, Elsevier, 1991: pp. 155–162. doi:10.1016/B978-0-7506-0269-3.50025-6.

[134] J. Park, R.S. Lakes, Biomaterials, Springer New York, New York, NY, 2007. doi:10.1007/978-0-387-37880-0.

[135] W. Huang, D.E. Day, K. Kittiratanapiboon, M.N. Rahaman, Kinetics and mechanisms of the conversion of silicate (45S5), borate, and borosilicate glasses to hydroxyapatite in dilute phosphate solutions, J. Mater. Sci. Mater. Med. 17 (2006) 583–596. doi:10.1007/s10856-006-9220-z.

[136] W. Huang, M.N. Rahaman, D.E. Day, Y. Li, Mechanisms for converting bioactive silicate, borate, and borosilicate glasses to hydroxyapatite in dilute phosphate solution, Phys. Chem. Glas. Eur. J. Glas. Sci. Technol. Part B. 47 (2006) 647–658. doi:10.1017/S0022112010005914.

[137] A.E. Fetner, S.B. Low, J. Wilson, L.L. Hench, Histologic evaluation of Bioglass particulates in gingival tissue, J. Dent. Res. 66 (1987) 298–398.

[138] E.J. Schepers, P. Ducheyne, Bioactive glass particles of narrow size range for the treatment of oral bone defects: a 1-24 month experiment with several materials and particle sizes and size ranges., J. Oral Rehabil. 24 (1997) 171–81. http://www.ncbi.nlm.nih.gov/pubmed/9131472.

[139] S.B. Low, C.J. King, J. Krieger, An evaluation of bioactive ceramic in the treatment of periodontal osseous defects., Int. J. Periodontics Restorative Dent. 17 (1997) 358–67. http://www.ncbi.nlm.nih.gov/pubmed/9497726.

[140] T.B. Lovelace, J.T. Mellonig, R.M. Meffert, A.A. Jones, P. V. Nummikoski, D.L. Cochran, Clinical Evaluation of Bioactive Glass in the Treatment of Periodontal Osseous Defects in Humans, J. Periodontol. 69 (1998) 1027–1035. doi:10.1902/jop.1998.69.9.1027.

[141] E.S. Rosenberg, S.-C. Cho, N. Elian, Z.N. Jalbout, S. Froum, C.I. Evian, A comparison of characteristics of implant failure and survival in periodontally compromised and periodontally healthy patients: a clinical report., Int. J. Oral

Maxillofac. Implants. 19 (n.d.) 873–9. http://www.ncbi.nlm.nih.gov/pubmed/15623064.

[142] C.R. Anderegg, D.C. Alexander, M. Freidman, A bioactive glass particulate in the treatment of molar furcation invasions., J. Periodontol. 70 (1999) 384–7. doi:10.1902/jop.1999.70.4.384.

[143] R.A. Yukna, G.H. Evans, M.B. Aichelmann-Reidy, E.T. Mayer, Clinical comparison of bioactive glass bone replacement graft material and expanded polytetrafluoroethylene barrier membrane in treating human mandibular molar class II furcations., J. Periodontol. 72 (2001) 125–33. doi:10.1902/jop.2001.72.2.125.

[144] J.S. Park, J.J. Suh, S.H. Choi, I.S. Moon, K.S. Cho, C.K. Kim, J.K. Chai, Effects of pretreatment clinical parameters on bioactive glass implantation in intrabony periodontal defects., J. Periodontol. 72 (2001) 730–40. doi:10.1902/jop.2001.72.6.730.

[145] M.R. Norton, J. Wilson, Dental implants placed in extraction sites implanted with bioactive glass: human histology and clinical outcome., Int. J. Oral Maxillofac. Implants. 17 (n.d.) 249–57. http://www.ncbi.nlm.nih.gov/pubmed/11958408.

[146] A. Sculean, G. Barbé, G.C. Chiantella, N.B. Arweiler, M. Berakdar, M. Brecx, Clinical evaluation of an enamel matrix protein derivative combined with a bioactive glass for the treatment of intrabony periodontal defects in humans., J. Periodontol. 73 (2002) 401–8. doi:10.1902/jop.2002.73.4.401.

[147] R. Mengel, M. Soffner, L. Flores-de-Jacoby, Bioabsorbable membrane and bioactive glass in the treatment of intrabony defects in patients with generalized aggressive periodontitis: results of a 12-month clinical and radiological study., J. Periodontol. 74 (2003) 899–908. doi:10.1902/jop.2003.74.6.899.

[148] S.J. Froum, M.A. Weinberg, D. Tarnow, Comparison of bioactive glass synthetic bone graft particles and open debridement in the treatment of human periodontal defects. A clinical study., J. Periodontol. 69 (1998) 698–709. doi:10.1902/jop.1998.69.6.698.

[149] C.A. Shapoff, D.C. Alexander, A.E. Clark, Clinical use of a bioactive glass particulate in the treatment of human osseous defects., Compend. Contin. Educ. Dent. 18 (1997) 352–4, 356, 358 passim. http://www.ncbi.nlm.nih.gov/pubmed/9452543.

[150] J.S. Zamet, U.R. Darbar, G.S. Griffiths, J.S. Bulman, U. Brägger, W. Bürgin, H.N. Newman, Particulate bioglass as a grafting material in the treatment of periodontal intrabony defects., J. Clin. Periodontol. 24 (1997) 410–8. http://www.ncbi.nlm.nih.gov/pubmed/9205920.

[151] L.L. Hench, I. Thompson, Twenty-first century challenges for biomaterials., J. R.

Soc. Interface. 7 Suppl 4 (2010) S379-91. doi:10.1098/rsif.2010.0151.focus.

[152] J.E. Gough, J.R. Jones, L.L. Hench, Nodule formation and mineralisation of human primary osteoblasts cultured on a porous bioactive glass scaffold., Biomaterials. 25 (2004) 2039–46. http://www.ncbi.nlm.nih.gov/pubmed/14741618.

[153] E.A. Effah Kaufmann, P. Ducheyne, I.M. Shapiro, Evaluation of osteoblast response to porous bioactive glass (45S5) substrates by RT-PCR analysis., Tissue Eng. 6 (2000) 19–28. doi:10.1089/107632700320856.

[154] J.R. Jones, O. Tsigkou, E.E. Coates, M.M. Stevens, J.M. Polak, L.L. Hench, Extracellular matrix formation and mineralization on a phosphate-free porous bioactive glass scaffold using primary human osteoblast (HOB) cells., Biomaterials. 28 (2007) 1653–63. doi:10.1016/j.biomaterials.2006.11.022.

[155] M. Bosetti, M. Cannas, The effect of bioactive glasses on bone marrow stromal cells differentiation., Biomaterials. 26 (2005) 3873–9. doi:10.1016/j.biomaterials.2004.09.059.

[156] I.A. Silver, J. Deas, M. Erecińska, Interactions of bioactive glasses with osteoblasts in vitro: effects of 45S5 Bioglass, and 58S and 77S bioactive glasses on metabolism, intracellular ion concentrations and cell viability., Biomaterials. 22 (2001) 175–85. http://www.ncbi.nlm.nih.gov/pubmed/11101161.

[157] I.D. Xynos, A.J. Edgar, L.D. Buttery, L.L. Hench, J.M. Polak, Gene-expression profiling of human osteoblasts following treatment with the ionic products of Bioglass 45S5 dissolution., J. Biomed. Mater. Res. 55 (2001) 151–7. http://www.ncbi.nlm.nih.gov/pubmed/11255166.

[158] I.D. Xynos, A.J. Edgar, L.D. Buttery, L.L. Hench, J.M. Polak, Ionic products of bioactive glass dissolution increase proliferation of human osteoblasts and induce insulin-like growth factor II mRNA expression and protein synthesis., Biochem. Biophys. Res. Commun. 276 (2000) 461–5. doi:10.1006/bbrc.2000.3503.

[159] I.D. Xynos, M. V Hukkanen, J.J. Batten, L.D. Buttery, L.L. Hench, J.M. Polak, Bioglass 45S5 stimulates osteoblast turnover and enhances bone formation In vitro: implications and applications for bone tissue engineering., Calcif. Tissue Int. 67 (2000) 321–9. http://www.ncbi.nlm.nih.gov/pubmed/11000347.

[160] L.L. Hench, Genetic design of bioactive glass, J. Eur. Ceram. Soc. 29 (2009) 1257–1265. doi:10.1016/j.jeurceramsoc.2008.08.002.

[161] P.J. Marie, The calcium-sensing receptor in bone cells: a potential therapeutic target in osteoporosis., Bone. 46 (2010) 571–6. doi:10.1016/j.bone.2009.07.082.

[162] S. Maeno, Y. Niki, H. Matsumoto, H. Morioka, T. Yatabe, A. Funayama, Y. Toyama, T. Taguchi, J. Tanaka, The effect of calcium ion concentration on osteoblast viability, proliferation and differentiation in monolayer and 3D culture.,

Biomaterials. 26 (2005) 4847–4855. doi:10.1016/j.biomaterials.2005.01.006.

[163] P. Valerio, M.M. Pereira, A.M. Goes, M.F. Leite, Effects of extracellular calcium concentration on the glutamate release by bioactive glass (BG60S) preincubated osteoblasts., Biomed. Mater. 4 (2009) 045011. doi:10.1088/1748-6041/4/4/045011.

[164] D.M. Reffitt, N. Ogston, R. Jugdaohsingh, H.F.J. Cheung, B.A.J. Evans, R.P.H. Thompson, J.J. Powell, G.N. Hampson, Orthosilicic acid stimulates collagen type 1 synthesis and osteoblastic differentiation in human osteoblast-like cells in vitro., Bone. 32 (2003) 127–35. http://www.ncbi.nlm.nih.gov/pubmed/12633784.

[165] A. Hoppe, N.S. Güldal, A.R. Boccaccini, A review of the biological response to ionic dissolution products from bioactive glasses and glass-ceramics, Biomaterials. 32 (2011) 2757–2774. doi:10.1016/j.biomaterials.2011.01.004.

[166] J.R. Jones, Reprint of: Review of bioactive glass: From Hench to hybrids, Acta Biomater. 23 (2015) S53–S82. doi:10.1016/j.actbio.2015.07.019.

[167] L.L. Hench, C.G. Pantano, P.J. Buscemi, D.C. Greenspan, Analysis of bioglass fixation of hip prostheses., J. Biomed. Mater. Res. 11 (1977) 267–82. doi:10.1002/jbm.820110211.

[168] H. Oonishi, L.L. Hench, J. Wilson, F. Sugihara, E. Tsuji, M. Matsuura, S. Kin, T. Yamamoto, S. Mizokawa, Quantitative comparison of bone growth behavior in granules of Bioglass, A-W glass-ceramic, and hydroxyapatite., J. Biomed. Mater. Res. 51 (2000) 37–46. http://www.ncbi.nlm.nih.gov/pubmed/10813743.

[169] D.L. Wheeler, K.E. Stokes, R.G. Hoellrich, D.L. Chamberland, S.W. McLoughlin, Effect of bioactive glass particle size on osseous regeneration of cancellous defects., J. Biomed. Mater. Res. 41 (1998) 527–33. http://www.ncbi.nlm.nih.gov/pubmed/9697024.

[170] Z. Wang, B. Lu, L. Chen, J. Chang, Evaluation of an osteostimulative putty in the sheep spine., J. Mater. Sci. Mater. Med. 22 (2011) 185–91. doi:10.1007/s10856-010-4175-5.

[171] K.M.J. Aitasalo, J.M. Piitulainen, J. Rekola, P.K. Vallittu, Craniofacial bone reconstruction with bioactive fiber-reinforced composite implant, Head Neck. 36 (2014) 722–728. doi:10.1002/hed.23370.

[172] P.K. Vallittu, C. Sevelius, Resin-bonded, glass fiber-reinforced composite fixed partial dentures: A clinical study, J. Prosthet. Dent. 84 (2000) 413–418. doi:10.1067/mpr.2000.109782.

[173] Q.Z. Chen, I.D. Thompson, A.R. Boccaccini, 45S5 Bioglass®-derived glass-ceramic scaffolds for bone tissue engineering, Biomaterials. 27 (2006) 2414–2425. doi:10.1016/j.biomaterials.2005.11.025.

[174] O.P. Filho, G.P. LaTorre, L.L. Hench, O. Peitl Filho, G.P. LaTorre, L.L. Hench, Effect of crystallization on apatite-layer formation of bioactive glass 45S5., J. Biomed. Mater. Res. 30 (1996) 509–14. doi:10.1002/(SICI)1097-4636(199604)30:4<509::AID-JBM9>3.0.CO;2-T.

[175] U.M. Gross, V. Strunz, The anchoring of glass ceramics of different solubility in the femur of the rat, J. Biomed. Mater. Res. 14 (1980) 607–618. doi:10.1002/jbm.820140507.

[176] L.L. Hench, The story of Bioglass®, J. Mater. Sci. Mater. Med. 17 (2006) 967–978. doi:10.1007/s10856-006-0432-z.

[177] R.F. Brown, D.E. Day, T.E. Day, S. Jung, M.N. Rahaman, Q. Fu, Growth and differentiation of osteoblastic cells on 13-93 bioactive glass fibers and scaffolds, Acta Biomater. 4 (2008) 387–396. doi:10.1016/j.actbio.2007.07.006.

[178] J. Vogel, P. Wange, P. Hartmann, Phosphate Glasses and Glass-Ceramics for Medical Applications, Glas. Sci. Technol. Glas. Berichte. 70 (1997) 220–223.

[179] J. Fu, Fast Li+ion conduction in Li2O-(Al2O3Ga2O3)-TiO2-P2O5glass-ceramics, J. Mater. Sci. 33 (1998) 1549–1553. doi:10.1023/A:1017559619391.

[180] J.B.B. Bates, N.J.J. Dudney, G.R.R. Gruzalski, R.A.A. Zuhr, A. Choudhury, C.F.F. Luck, J.D.D. Robertson, Electrical properties of amorphous lithium electrolyte thin films, Solid State Ionics. 53–56 (1992) 647–654. doi:10.1016/0167-2738(92)90442-R.

[181] C.F. Drake, Continuous and pulsed delivery of bioactive materials using composite system based on inorganic glasses, in: Consult. Immunomodulation, 1985.

[182] C.F. Drake, W.M. Allen, The use of controlled-release glass for the controlled delivery of bioactive materials, Biochem. Soc. Trans. 13 (1985) 516 LP – 520. doi:10.1042/bst0130516.

[183] E.A. Abou Neel, I. Ahmed, J.J. Blaker, A. Bismarck, A.R. Boccaccini, M.P. Lewis, S.N. Nazhat, J.C. Knowles, Effect of iron on the surface, degradation and ion release properties of phosphate-based glass fibres, Acta Biomater. 1 (2005) 553–563. doi:10.1016/j.actbio.2005.05.001.

[184] E.A. Abou Neel, I. Ahmed, J. Pratten, S.N. Nazhat, J.C. Knowles, Characterisation of antibacterial copper releasing degradable phosphate glass fibres, Biomaterials. 26 (2005) 2247–2254. doi:10.1016/j.biomaterials.2004.07.024.

[185] I. Ahmed, S.S. Shaharuddin, N. Sharmin, D. Furniss, C. Rudd, Core/clad phosphate glass fibres containing iron and/or titanium, Biomed. Glas. 1 (2015) 20–30. doi:10.1515/bglass-2015-0004.

[186] J. Massera, I. Ahmed, L. Petit, V. Aallos, L. Hupa, Phosphate-based glass fiber vs. bulk glass: Change in fiber optical response to probe in vitro glass reactivity, Mater. Sci. Eng. C. 37 (2014) 251–257. doi:10.1016/j.msec.2014.01.021.

[187] R.K. Brow, Review: the structure of simple phosphate glasses, J. Non. Cryst. Solids. 263 (2000) 1–28. doi:10.1016/S0022-3093(99)00620-1.

[188] Y. Abe, Topics in Phosphorous Chemistry, in: M. Grayson, E.J. Griffith (Eds.), 11th ed., Wiley, 1983: p. 19.

[189] S.W. Martin, Review of the structures of phosphate glasses, Eur. J. Solid State Inorg. Chem. 28 (1991) 163–205.

[190] A.E.. Westman, Chapter 4, in: J.D. Mackenzie (Ed.), Mod. Asp. Vitr. State, Butterworths, London, 1960: p. 63.

[191] D. E. Clark, B. K. Zoitos, Corrosion of Glass, Ceramics and Ceramic Superconductors: Principles, Testing, Characterization and Applications, 1992.

[192] E. Fernández, F.J. Gil, M.P. Ginebra, F.C. Driessens, J. a Planell, S.M. Best, Calcium phosphate bone cements for clinical applications. Part I: solution chemistry., J. Mater. Sci. Mater. Med. 10 (1999) 169–176. doi:10.1023/A:1008937507714.

[193] J.O. Isard, A.R. Allnatt, P.J. Melling, Improved Model of Glass Dissolution, 1982.

[194] H. Gao, T. Tan, D. Wang, Dissolution mechanism and release kinetics of phosphate controlled release glasses in aqueous medium, J. Control. Release. 96 (2004) 29–36. doi:10.1016/j.jconrel.2003.12.031.

[195] Q.X. Liu, X.M. Chen, X. Li, The hydrolysis of Na2O _CaO_ 2P2O5 bioglass, J. Wuhan Univ. Technol. 18 (1996) 26–29.

[196] B.C. Sales, L.A. Boatner, J.O. Ramey, Chromatographic studies of the structures of amorphous phosphates: a review, J. Non. Cryst. Solids. 263 (2000) 155–166. doi:10.1016/S0022-3093(99)00644-4.

[197] N. Lakhkar, E.A. Abou Neel, V. Salih, J.C. Knowles, Titanium and strontium-doped phosphate glasses as vehicles for strontium ion delivery to cells, J. Biomater. Appl. 25 (2011) 877–893. doi:10.1177/0885328210362125.

[198] F. Foroutan, N.J. Walters, G.J. Owens, N.J. Mordan, H.-W. Kim, N.H. de Leeuw, J.C. Knowles, Sol-gel synthesis of quaternary (P2O5)55-(CaO)25-(Na2O)(20-x)-(TiO2) x bioresorbable glasses for bone tissue engineering applications (x = 0, 5, 10, or 15)., Biomed. Mater. 10 (2015) 045025. doi:10.1088/1748-6041/10/4/045025.

[199] M. Uo, M. Mizuno, Y. Kuboki, A. Makishima, F. Watari, Properties and cytotoxicity of water soluble Na2O-CaO-P2O5 glasses., Biomaterials. 19 (1998) 2277–84.

http://www.ncbi.nlm.nih.gov/pubmed/9884040.

[200] T. Gilchrist, M.A. Glasby, D.M. Healy, G. Kelly, D.V. Lenihan, K.L. McDowall, I.A. Miller, L.M. Myles, In vitro nerve repair — in vivo. The reconstruction of peripheral nerves by entubulation with biodegradeable glass tubes — a preliminary report, Br. J. Plast. Surg. 51 (1998) 231–237. doi:10.1054/bjps.1997.0243.

[201] D.M. Pickup, R.J. Newport, J.C. Knowles, Sol-gel phosphate-based glass for drug delivery applications., J. Biomater. Appl. 26 (2012) 613–22. doi:10.1177/0885328210380761.

[202] M. Bitar, V. Salih, V. Mudera, J.C. Knowles, M.P. Lewis, Soluble phosphate glasses: In vitro studies using human cells of hard and soft tissue origin, Biomaterials. 25 (2004) 2283–2292. doi:10.1016/j.biomaterials.2003.08.054.

[203] I. Ahmed, M. Lewis, I. Olsen, J.C. Knowles, Phosphate glasses for tissue engineering: Part 1. Processing and characterisation of a ternary-based P2O5-CaO-Na2O glass system, Biomaterials. 25 (2004) 491–499. doi:10.1016/S0142-9612(03)00546-5.

[204] K. Franks, V. Salih, J.C. Knowles, I. Olsen, The effect of MgO on the solubility behavior and cell proliferation in a quaternary soluble phosphate based glass system., J. Mater. Sci. Mater. Med. 13 (2002) 549–56. http://www.ncbi.nlm.nih.gov/pubmed/15348584.

[205] M. Navarro, M.-P. Ginebra, J.A. Planell, Cellular response to calcium phosphate glasses with controlled solubility., J. Biomed. Mater. Res. A. 67 (2003) 1009–15. doi:10.1002/jbm.a.20014.

[206] M. Navarro, M.-P. Ginebra, J. Clément, M. Salvador, A. Gloria, J.A. Planell, Physicochemical Degradation of Titania-Stabilized Soluble Phosphate Glasses for Medical Applications, J. Am. Ceram. Soc. 86 (2003) 1345–1352. doi:10.1111/j.1151-2916.2003.tb03474.x.

[207] D.S. Brauer, C. Rüssel, W. Li, S. Habelitz, Effect of degradation rates of resorbable phosphate invert glasses on in vitro osteoblast proliferation., J. Biomed. Mater. Res. A. 77 (2006) 213–9. doi:10.1002/jbm.a.30610.

[208] T. Kasuga, Y. Hosoi, M. Nogami, M. Niinomi, Apatite Formation on Calcium Phosphate Invert Glasses in Simulated Body Fluid, J. Am. Ceram. Soc. 84 (2004) 450–52. doi:10.1111/j.1151-2916.2001.tb00676.x.

[209] M.T. Islam, R.M. Felfel, E.A. Abou Neel, D.M. Grant, I. Ahmed, K.M.Z. Hossain, Bioactive calcium phosphate–based glasses and ceramics and their biomedical applications: A review, J. Tissue Eng. 8 (2017) 204173141771917. doi:10.1177/2041731417719170.

[210] A.S. Monem, H.A. ElBatal, E.M.A. Khalil, M.A. Azooz, Y.M. Hamdy, In vivo

behavior of bioactive phosphate glass-ceramics from the system P2O5–Na2O–CaO containing TiO2, J. Mater. Sci. Mater. Med. 19 (2008) 1097–1108. doi:10.1007/s10856-007-3044-3.

[211] A. Marikani, A. Maheswaran, M. Premanathan, L. Amalraj, Synthesis and characterization of calcium phosphate based bioactive quaternary P2O5–CaO–Na2O–K2O glasses, J. Non. Cryst. Solids. 354 (2008) 3929–3934. doi:10.1016/j.jnoncrysol.2008.05.005.

[212] U. Patel, L. Macri-Pellizzeri, K.M. Zakir Hossain, B.E. Scammell, D.M. Grant, C.A. Scotchford, A.C. Hannon, A.R. Kennedy, E.R. Barney, I. Ahmed, V. Sottile, In vitro cellular testing of strontium/calcium substituted phosphate glass discs and microspheres shows potential for bone regeneration, J. Tissue Eng. Regen. Med. 13 (2019) 396–405. doi:10.1002/term.2796.

[213] G. Novajra, N.G. Boetti, J. Lousteau, S. Fiorilli, D. Milanese, C. Vitale-Brovarone, Phosphate glass fibre scaffolds: Tailoring of the properties and enhancement of the bioactivity through mesoporous glass particles., Mater. Sci. Eng. C. Mater. Biol. Appl. 67 (2016) 570–580. doi:10.1016/j.msec.2016.05.048.

[214] K.L. Skelton, J. V. Glenn, S.A. Clarke, G. Georgiou, S.P. Valappil, J.C. Knowles, S.N. Nazhat, G.R. Jordan, Effect of ternary phosphate-based glass compositions on osteoblast and osteoblast-like proliferation, differentiation and death in vitro, Acta Biomater. 3 (2007) 563–572. doi:10.1016/j.actbio.2006.11.008.

[215] A.B. Edathazhe, H.D. Shashikala, Corrosion resistance and in-vitro bioactivity of BaO containing Na 2 O-CaO-P 2 O 5 phosphate glass-ceramic coating prepared on 316 L, duplex stainless steel 2205 and Ti6Al4V, Mater. Res. Express. 5 (2018) 035404. doi:10.1088/2053-1591/aab2f5.

[216] A. Lapa, M. Cresswell, P. Jackson, A.R. Boccaccini, Phosphate glass fibres with therapeutic ions release capability – a review, Adv. Appl. Ceram. 0 (2019) 1–14. doi:10.1080/17436753.2018.1564413.

[217] I. Ahmed, P.S. Cronin, E.A. Abou Neel, A.J. Parsons, J.C. Knowles, C.D. Rudd, Retention of mechanical properties and cytocompatibility of a phosphate-based glass fiber/polylactic acid composite., J. Biomed. Mater. Res. B. Appl. Biomater. 89 (2009) 18–27. doi:10.1002/jbm.b.31182.

[218] R.M. Felfel, I. Ahmed, A.J. Parsons, G. Palmer, V. Sottile, C.D. Rudd, Cytocompatibility, degradation, mechanical property retention and ion release profiles for phosphate glass fibre reinforced composite rods., Mater. Sci. Eng. C. Mater. Biol. Appl. 33 (2013) 1914–24. doi:10.1016/j.msec.2012.12.089.

[219] D.S. Brauer, C. Rüssel, S. Vogt, J. Weisser, M. Schnabelrauch, Degradable phosphate glass fiber reinforced polymer matrices: mechanical properties and cell response., J. Mater. Sci. Mater. Med. 19 (2008) 121–7. doi:10.1007/s10856-007-3147-x.

[220] I. Ahmed, I.A. Jones, A.J. Parsons, J. Bernard, J. Farmer, C.A. Scotchford, G.S. Walker, C.D. Rudd, Composites for bone repair: phosphate glass fibre reinforced PLA with varying fibre architecture, J. Mater. Sci. Mater. Med. 22 (2011) 1825–1834. doi:10.1007/s10856-011-4361-0.

[221] N. Han, I. Ahmed, A.J. Parsons, L. Harper, C.A. Scotchford, B.E. Scammell, C.D. Rudd, Influence of screw holes and gamma sterilization on properties of phosphate glass fiber-reinforced composite bone plates, J. Biomater. Appl. 27 (2013) 990–1002. doi:10.1177/0885328211431855.

[222] H.Y.L.S. Kobayashi, D.S. Brauer, C. Rüssel, Mechanical properties of a degradable phosphate glass fibre reinforced polymer composite for internal fracture fixation, Mater. Sci. Eng. C. 30 (2010) 1003–1007. doi:10.1016/j.msec.2010.04.017.

[223] P. Haque, I.A. Barker, A. Parsons, K.J. Thurecht, I. Ahmed, G.S. Walker, C.D. Rudd, D.J. Irvine, Influence of compatibilizing agent molecular structure on the mechanical properties of phosphate glass fiber-reinforced PLA composites, J. Polym. Sci. Part A Polym. Chem. 48 (2010) 3082–3094. doi:10.1002/pola.24086.

[224] P. Haque, A.J. Parsons, I.A. Barker, I. Ahmed, D.J. Irvine, G.S. Walker, C.D. Rudd, Interfacial properties of phosphate glass fibres/PLA composites: Effect of the end functionalities of oligomeric PLA coupling agents, Compos. Sci. Technol. 70 (2010) 1854–1860. doi:10.1016/j.compscitech.2010.06.012.

[225] M. Chen, A.J. Parsons, R.M. Felfel, C.D. Rudd, D.J. Irvine, I. Ahmed, In-situ polymerisation of fully bioresorbable polycaprolactone/phosphate glass fibre composites: In vitro degradation and mechanical properties, J. Mech. Behav. Biomed. Mater. 59 (2016) 78–89. doi:10.1016/j.jmbbm.2015.12.019.

[226] M.S. Mohammadi, I. Ahmed, N. Muja, S. Almeida, C.D. Rudd, M.N. Bureau, S.N. Nazhat, Effect of Si and Fe doping on calcium phosphate glass fibre reinforced polycaprolactone bone analogous composites., Acta Biomater. 8 (2012) 1616–26. doi:10.1016/j.actbio.2011.12.030.

[227] R.L. Prabhakar, S. Brocchini, J.C. Knowles, Effect of glass composition on the degradation properties and ion release characteristics of phosphate glass—polycaprolactone composites, Biomaterials. 26 (2005) 2209–2218. doi:10.1016/j.biomaterials.2004.07.016.

[228] I. Ahmed, A.J. Parsons, G. Palmer, J.C. Knowles, G.S. Walker, C.D. Rudd, Weight loss, ion release and initial mechanical properties of a binary calcium phosphate glass fibre/PCL composite, Acta Biomater. 4 (2008) 1307–1314. doi:10.1016/j.actbio.2008.03.018.

[229] L.V.J. Lassila, T. Nohrström, P.K. Vallittu, The influence of short-term water storage on the flexural properties of unidirectional glass fiber-reinforced composites., Biomaterials. 23 (2002) 2221–9.

http://www.ncbi.nlm.nih.gov/pubmed/11962663.

[230] R.M. Felfel, I. Ahmed, A.J. Parsons, L.T. Harper, C.D. Rudd, Initial mechanical properties of phosphate-glass fibre-reinforced rods for use as resorbable intramedullary nails, J. Mater. Sci. 47 (2012) 4884–4894. doi:10.1007/s10853-012-6355-9.

[231] R.M. Felfel, I. Ahmed, A.J. Parsons, C.D. Rudd, Bioresorbable screws reinforced with phosphate glass fibre: Manufacturing and mechanical property characterisation, J. Mech. Behav. Biomed. Mater. 17 (2013) 76–88. doi:10.1016/j.jmbbm.2012.08.001.

[232] K. Zheng, Z. Wu, J. Wei, C. R\Hussel, W. Liang, A.R. Boccaccini, Preparation and characterization of fibrous chitosan-glued phosphate glass fiber scaffolds for bone regeneration, J. Mater. Sci. Mater. Med. 26 (2015) 224. doi:10.1007/s10856-015-5554-8.

[233] Y.-P. Kim, G.-S. Lee, J.-W. Kim, M.S. Kim, H.-S. Ahn, J.-Y. Lim, H.-W. Kim, Y.-J. Son, J.C. Knowles, J.K. Hyun, Phosphate glass fibres promote neurite outgrowth and early regeneration in a peripheral nerve injury model, J. Tissue Eng. Regen. Med. 9 (2015) 236–246. doi:10.1002/term.1626.

[234] A.J. Parsons, I. Ahmed, P. Haque, B. Fitzpatrick, M.I.K. Niazi, G.S. Walker, C.D. Rudd, Phosphate Glass Fibre Composites for Bone Repair, J. Bionic Eng. 6 (2009) 318–323. doi:10.1016/S1672-6529(08)60132-8.

[235] N.-Y. Joo, J.C. Knowles, G.-S. Lee, J.-W. Kim, H.-W. Kim, Y.-J. Son, J.K. Hyun, Effects of phosphate glass fiber-collagen scaffolds on functional recovery of completely transected rat spinal cords., Acta Biomater. 8 (2012) 1802–12. doi:10.1016/j.actbio.2012.01.026.

[236] C. Vitale-Brovarone, G. Novajra, J. Lousteau, D. Milanese, S. Raimondo, M. Fornaro, Phosphate glass fibres and their role in neuronal polarization and axonal growth direction, Acta Biomater. 8 (2012) 1125–1136. doi:10.1016/j.actbio.2011.11.018.

[237] O.H. Andersson, G. Liu, K.H. Karlsson, L. Niemi, J. Miettinen, J. Juhanoja, In vivo behaviour of glasses in the SiO2-Na2O-CaO-P2O5-Al2O3-B2O3 system, J. Mater. Sci. Mater. Med. 1 (1990) 219–227. doi:10.1007/BF00701080.

[238] R. Hill, An alternative view of the degradation of bioglass, J. Mater. Sci. Lett. 15 (1996) 1122–1125. doi:10.1007/BF00539955.

[239] Z. Strnad, Role of the glass phase in bioactive glass-ceramics, Biomaterials. 13 (1992) 317–321. doi:10.1016/0142-9612(92)90056-T.

[240] R.D. Rawlings, Composition dependence of the bioactivity of glasses, J. Mater. Sci. Lett. 11 (1992) 1340–1343. doi:10.1007/BF00729356.

[241] K.H. Karlsson, H. Ylänen, H. Aro, Porous bone implants, Ceram. Int. 26 (2000) 897–900. doi:10.1016/S0272-8842(00)00033-X.

[242] R.G. Hill, D.S. Brauer, Predicting the bioactivity of glasses using the network connectivity or split network models, J. Non. Cryst. Solids. 357 (2011) 3884–3887. doi:10.1016/j.jnoncrysol.2011.07.025.

[243] M. Edén, The split network analysis for exploring composition-structure correlations in multi-component glasses: I. Rationalizing bioactivity-composition trends of bioglasses, J. Non. Cryst. Solids. 357 (2011) 1595–1602. doi:10.1016/j.jnoncrysol.2010.11.098.

[244] L. Hupa, Melt-derived bioactive glasses, in: Bioact. Glas., Elsevier, 2011: pp. 3–28. doi:10.1533/9780857093318.1.3.

[245] M. Brink, Bioactive glasses with a large working range, Åbo Akademi, 1997.

[246] D. Zhang, In vitro Characterization of Bioactive Glass, Åbo Akademi, 2008.

[247] H. Ylänen, Bone Ingrowth into Porous Bodies Made by Sintering Bioactive Glass Microspheres, Åbo Akademi, 2000.

[248] R. Blossey, Self-cleaning surfaces — virtual realities, Nat. Mater. 2 (2003) 301–306. doi:10.1038/nmat856.

[249] A. Venkateswara Rao, S.S. Latthe, D.Y. Nadargi, H. Hirashima, V. Ganesan, Preparation of MTMS based transparent superhydrophobic silica films by sol–gel method, J. Colloid Interface Sci. 332 (2009) 484–490. doi:10.1016/j.jcis.2009.01.012.

[250] Y. Xiu, D.W. Hess, C.P. Wong, UV and thermally stable superhydrophobic coatings from sol-gel processing, J. Colloid Interface Sci. 326 (2008) 465–470. doi:10.1016/j.jcis.2008.06.042.

[251] Q.F. Xu, J.N. Wang, I.H. Smith, K.D. Sanderson, Superhydrophobic and transparent coatings based on removable polymeric spheres, J. Mater. Chem. 19 (2009) 655–660. doi:10.1039/B812659C.

[252] H.M. Shang, Y. Wang, S.J. Limmer, T.P. Chou, K. Takahashi, G.Z. Cao, Optically transparent superhydrophobic silica-based films, Thin Solid Films. 472 (2005) 37–43. doi:10.1016/j.tsf.2004.06.087.

[253] C.M. Halliwell, A.E.G. Cass, A Factorial Analysis of Silanization Conditions for the Immobilization of Oligonucleotides on Glass Surfaces, Anal. Chem. 73 (2001) 2476–2483. doi:10.1021/ac0010633.

[254] S. Jaffar, K.T. Nam, A. Khademhosseini, J. Xing, R.S. Langer, A.M. Belcher, Layer-by-layer surface modification and patterned electrostatic deposition of quantum dots, Nano Lett. 4 (2004) 1421–1425. doi:10.1021/nl0493287.

[255] V.G. Cheung, M. Morley, F. Aguilar, A. Massimi, R. Kucherlapati, G. Childs, Making and reading microarrays, Nat. Genet. 21 (1999) 15–19. doi:10.1038/4439.

[256] W.H. Robinson, C. DiGennaro, W. Hueber, B.B. Haab, M. Kamachi, E.J. Dean, S. Fournel, D. Fong, M.C. Genovese, H.E.N. De Vegvar, K. Skriner, D.L. Hirschberg, R.I. Morris, S. Muller, G.J. Pruijn, W.J. van Venrooij, J.S. Smolen, P.O. Brown, L. Steinman, P.J. Utz, Autoantigen microarrays for multiplex characterization of autoantibody responses, Nat. Med. 8 (2002) 295–301. doi:10.1038/nm0302-295.

[257] J.C. Miller, H. Zhou, J. Kwekel, R. Cavallo, J. Burke, E.B. Butler, B.S. Teh, B.B. Haab, Antibody microarray profiling of human prostate cancer sera: Antibody screening and identification of potential biomarkers, Proteomics. 3 (2003) 56–63. doi:10.1002/pmic.200390009.

[258] J.B. Delehanty, F.S. Ligler, A Microarray Immunoassay for Simultaneous Detection of Proteins and Bacteria, Anal. Chem. 74 (2002) 5681–5687. doi:10.1021/ac025631l.

[259] M.-L. Lesaicherre, R.Y.P. Lue, G.Y.J. Chen, Q. Zhu, S.Q. Yao, Intein-Mediated Biotinylation of Proteins and Its Application in a Protein Microarray, J. Am. Chem. Soc. 124 (2002) 8768–8769. doi:10.1021/ja0265963.

[260] B.T. Houseman, J.H. Huh, S.J. Kron, M. Mrksich, Peptide chips for the quantitative evaluation of protein kinase activity, Nat. Biotechnol. 20 (2002) 270–274. doi:10.1038/nbt0302-270.

[261] R. Benters, C.M. Niemeyer, D. Wöhrle, Dendrimer-Activated Solid Supports for Nucleic Acid and Protein Microarrays, ChemBioChem. 2 (2001) 686–694. doi:10.1002/1439-7633(20010903)2:9<686::AID-CBIC686>3.0.CO;2-S.

[262] S. Nock, J.A. Spudich, P. Wagner, Reversible, site-specific immobilization of polyarginine-tagged fusion proteins on mica surfaces, FEBS Lett. 414 (1997) 233–238. doi:10.1016/S0014-5793(97)01040-5.

[263] L.R. Paborsky, K.E. Dunn, C.S. Gibbs, J.P. Dougherty, A Nickel Chelate Microtiter Plate Assay for Six Histidine-Containing Proteins, Anal. Biochem. 234 (1996) 60–65. doi:10.1006/abio.1996.0050.

[264] J. Massera, A. Mishra, S. Guastella, S. Ferraris, E. Verné, Surface functionalization of phosphate-based bioactive glasses with 3-aminopropyltriethoxysilane (APTS), Biomed. Glas. 2 (2016) 51–62. doi:10.1515/bglass-2016-0007.

[265] M. Sokolsky-Papkov, K. Agashi, A. Olaye, K. Shakesheff, A.J. Domb, Polymer carriers for drug delivery in tissue engineering, Adv. Drug Deliv. Rev. 59 (2007) 187–206. doi:10.1016/j.addr.2007.04.001.

[266] W.J.E.M. Habraken, J.G.C. Wolke, J.A. Jansen, Ceramic composites as matrices

and scaffolds for drug delivery in tissue engineering, Adv. Drug Deliv. Rev. 59 (2007) 234–248. doi:10.1016/j.addr.2007.03.011.

[267] J.K. Tessmar, A.M. Göpferich, Matrices and scaffolds for protein delivery in tissue engineering, Adv. Drug Deliv. Rev. 59 (2007) 274–291. doi:10.1016/j.addr.2007.03.020.

[268] L. De Laporte, L.D. Shea, Matrices and scaffolds for DNA delivery in tissue engineering, Adv. Drug Deliv. Rev. 59 (2007) 292–307. doi:10.1016/j.addr.2007.03.017.

[269] E.K. Moioli, P.A. Clark, X. Xin, S. Lal, J.J. Mao, Matrices and scaffolds for drug delivery in dental, oral and craniofacial tissue engineering, Adv. Drug Deliv. Rev. 59 (2007) 308–324. doi:10.1016/j.addr.2007.03.019.

[270] S.M. Willerth, S.E. Sakiyama-Elbert, Approaches to neural tissue engineering using scaffolds for drug delivery, Adv. Drug Deliv. Rev. 59 (2007) 325–338. doi:10.1016/j.addr.2007.03.014.

[271] S.-H. Lee, H. Shin, Matrices and scaffolds for delivery of bioactive molecules in bone and cartilage tissue engineering, Adv. Drug Deliv. Rev. 59 (2007) 339–359. doi:10.1016/j.addr.2007.03.016.

[272] G. Zhang, L.J. Suggs, Matrices and scaffolds for drug delivery in vascular tissue engineering, Adv. Drug Deliv. Rev. 59 (2007) 360–373. doi:10.1016/j.addr.2007.03.018.

[273] V. Mouriño, J.P. Cattalini, A.R. Boccaccini, Metallic ions as therapeutic agents in tissue engineering scaffolds: An overview of their biological applications and strategies for new developments, J. R. Soc. Interface. 9 (2012) 401–419. doi:10.1098/rsif.2011.0611.

[274] V. Mouriño, A.R. Boccaccini, Bone tissue engineering therapeutics: controlled drug delivery in three-dimensional scaffolds, J. R. Soc. Interface. 7 (2010) 209–227. doi:10.1098/rsif.2009.0379.

[275] V. Mouriño, P. Newby, F. Pishbin, J.P. Cattalini, S. Lucangioli, A.R. Boccaccini, Physicochemical, biological and drug-release properties of gallium crosslinked alginate/nanoparticulate bioactive glass composite films, Soft Matter. 7 (2011) 6705. doi:10.1039/c1sm05331k.

[276] B. Baroli, From natural bone grafts to tissue engineering therapeutics: Brainstorming on pharmaceutical formulative requirements and challenges, J. Pharm. Sci. 98 (2009) 1317–1375. doi:10.1002/jps.21528.

[277] P. Habibovic, J.E. Barralet, Bioinorganics and biomaterials: Bone repair, Acta Biomater. 7 (2011) 3013–3026. doi:10.1016/j.actbio.2011.03.027.

[278] I. Ahmed, D. Ready, M. Wilson, J.C. Knowles, Antimicrobial effect of silver-doped phosphate-based glasses, J. Biomed. Mater. Res. Part A. 79 (2006) 618–626. doi:10.1002/jbm.a.

[279] I. Ahmed, E.A. Abou Neel, S.P. Valappil, S.N. Nazhat, D.M. Pickup, D. Carta, D.L. Carroll, R.J. Newport, M.E. Smith, J.C. Knowles, The structure and properties of silver-doped phosphate-based glasses, J. Mater. Sci. 42 (2007) 9827–9835. doi:10.1007/s10853-007-2008-9.

[280] S.P. Valappil, D.M. Pickup, D.L. Carroll, C.K. Hope, J. Pratten, R.J. Newport, M.E. Smith, M. Wilson, J.C. Knowles, Effect of silver content on the structure and antibacterial activity of silver-doped phosphate-based glasses, Antimicrob. Agents Chemother. 51 (2007) 4453–4461. doi:10.1128/AAC.00605-07.

[281] C. Wu, W. Fan, Y. Zhu, M. Gelinsky, J. Chang, G. Cuniberti, V. Albrecht, T. Friis, Y. Xiao, Multifunctional magnetic mesoporous bioactive glass scaffolds with a hierarchical pore structure, Acta Biomater. 7 (2011) 3563–3572. doi:10.1016/j.actbio.2011.06.028.

[282] J. Massera, M. Vassallo-Breillot, B. Törngren, B. Glorieux, L. Hupa, Effect of CeO2 doping on thermal, optical, structural and in vitro properties of a phosphate based bioactive glass, J. Non. Cryst. Solids. 402 (2014) 28–35. doi:10.1016/j.jnoncrysol.2014.05.006.

[283] C. Leonelli, G. Lusvardi, G. Malavasi, L.Ã. Menabue, M. Tonelli, Synthesis and characterization of cerium doped glasses and in vitro evaluation of bioactivity.pdf, J. Non. Cryst. Solids. 316 (2003) 198–216.

[284] J.L. Rygel, C.G. Pantano, Synthesis and properties of cerium aluminosilicophosphate glasses, J. Non. Cryst. Solids. 355 (2009) 2622–2629. doi:10.1016/j.jnoncrysol.2009.09.004.

[285] E. Gentleman, Y.C. Fredholm, G. Jell, N. Lotfibakhshaiesh, M.D. O'Donnell, R.G. Hill, M.M. Stevens, The effects of strontium-substituted bioactive glasses on osteoblasts and osteoclasts in vitro., Biomaterials. 31 (2010) 3949–56. doi:10.1016/j.biomaterials.2010.01.121.

[286] J. Isaac, J. Nohra, J. Lao, E. Jallot, J.-M. Nedelec, A. Berdal, J.-M. Sautier, Effects of strontium-doped bioactive glass on the differentiation of cultured osteogenic cells, Eur. Cells Mater. 21 (2011) 130–143. doi:10.22203/eCM.v021a11.

[287] K.L. Lankford, P.C. Letouraneau, Evidence that calcium may control neurite outgrowth by regulating the stability of actin filaments, J. Cell Biol. 109 (1989) 1229–1243. doi:10.1083/jcb.109.3.1229.

[288] S.R. Bolsover, Calcium signalling in growth cone migration, Cell Calcium. 37 (2005) 395–402. doi:10.1016/j.ceca.2005.01.007.

[289] S. Konur, A. Ghosh, Calcium Signaling and the Control of Dendritic Development, Neuron. 46 (2005) 401–405. doi:10.1016/j.neuron.2005.04.022.

[290] S. Bunting, L. Di Silvio, S. Deb, S. Hall, Bioresorbable glass fibres facilitate peripheral nerve regeneration., J. Hand Surg. Br. 30 (2005) 242–7. doi:10.1016/j.jhsb.2004.11.003.

[291] H. Zhou, J. Wei, X. Wu, J. Shi, C. Liu, J. Jia, C. Dai, Q. Gan, The bio-functional role of calcium in mesoporous silica xerogels on the responses of osteoblasts in vitro, J. Mater. Sci. Mater. Med. 21 (2010) 2175–2185. doi:10.1007/s10856-010-4083-8.

[292] E. Hinoi, T. Takarada, Y. Yoneda, Glutamate Signaling System in Bone, J. Pharmacol. Sci. 94 (2004) 215–220. doi:10.1254/jphs.94.215.

[293] L.-L. Zhu, S. Zaidi, Y. Peng, H. Zhou, B.S. Moonga, A. Blesius, I. Dupin-Roger, M. Zaidi, L. Sun, Induction of a program gene expression during osteoblast differentiation with strontium ranelate, Biochem. Biophys. Res. Commun. 355 (2007) 307–311. doi:10.1016/j.bbrc.2007.01.120.

[294] G. Boivin, P. Deloffre, B. Perrat, G. Panczer, M. Boudeulle, Y. Mauras, P. Allain, Y. Tsouderos, P.J. Meunier, Strontium distribution and interactions with bone mineral in monkey iliac bone after strontium salt (S12911) administration, J. Bone Miner. Res. 11 (2009) 1302–1311. doi:10.1002/jbmr.5650110915.

[295] S.. Dahl, P. Allain, P.. Marie, Y. Mauras, G. Boivin, P. Ammann, Y. Tsouderos, P.. Delmas, C. Christiansen, Incorporation and distribution of strontium in bone, Bone. 28 (2001) 446–453. doi:10.1016/S8756-3282(01)00419-7.

[296] M.D. Grynpas, E. Hamilton, R. Cheung, Y. Tsouderos, P. Deloffre, M. Hott, P.J. Marie, Strontium increases vertebral bone volume in rats at a low dose that does not induce detectable mineralization defect, Bone. 18 (1996) 253–259. doi:10.1016/8756-3282(95)00484-X.

[297] G. Hu, Copper stimulates proliferation of human endothelial cells under culture, J. Cell. Biochem. 69 (1998) 326–335. doi:10.1002/(SICI)1097-4644(19980601)69:3<326::AID-JCB10>3.0.CO;2-A.

[298] J.P. Rodríguez, S. Ríos, M. González, Modulation of the proliferation and differentiation of human mesenchymal stem cells by copper, J. Cell. Biochem. 85 (2002) 92–100. doi:10.1002/jcb.10111.

[299] H. Xie, Y.J. Kang, Role of copper in angiogenesis and its medicinal implications., Curr. Med. Chem. 16 (2009) 1304–14. http://www.ncbi.nlm.nih.gov/pubmed/19355887.

[300] W. Chen, Y. Liu, H.. Courtney, M. Bettenga, C.M. Agrawal, J.D. Bumgardner, J.L. Ong, In vitro anti-bacterial and biological properties of magnetron co-sputtered

silver-containing hydroxyapatite coating, Biomaterials. 27 (2006) 5512–5517. doi:10.1016/j.biomaterials.2006.07.003.

[301] D. Westenberg, Fighting infections with glass, in: 100th Gen. Meet. Am. Soc. Microbiol., John Wiley & Sons Ltd., Los Angeles, 2000.

[302] M.A. Wassall, M. Santin, C. Isalberti, M. Cannas, S.P. Denyer, Adhesion of bacteria to stainless steel and silver-coated orthopedic external fixation pins, J. Biomed. Mater. Res. 36 (1997) 325–330. doi:10.1002/(SICI)1097-4636(19970905)36:3<325::AID-JBM7>3.0.CO;2-G.

[303] K. Yoshida, M. Tanagawa, M. Atsuta, Characterization and inhibitory effect of antibacterial dental resin composites incorporating silver-supported materials, J. Biomed. Mater. Res. 47 (1999) 516–522. doi:10.1002/(SICI)1097-4636(19991215)47:4<516::AID-JBM7>3.0.CO;2-E.

[304] L. Stanislawski, X. Daniau, A. Lautie, M. Goldberg, Factors responsible for pulp cell cytotoxicity induced by resin-modified glass ionomer cements, J. Biomed. Mater. Res. 48 (1999) 277–288. doi:10.1002/(SICI)1097-4636(1999)48:3<277::AID-JBM11>3.0.CO;2-T.

[305] A. Masse, A. Bruno, M. Bosetti, A. Biasibetti, M. Cannas, P. Gallinaro, Prevention of pin track infection in external fixation with silver coated pins: Clinical and microbiological results, J. Biomed. Mater. Res. 53 (2000) 600–604. doi:10.1002/1097-4636(200009)53:5<600::AID-JBM21>3.0.CO;2-D.

[306] H. Kumon, H. Hashimoto, M. Nishimura, K. Monden, N. Ono, Catheter-associated urinary tract infections: impact of catheter materials on their management, Int. J. Antimicrob. Agents. 17 (2001) 311–316. doi:10.1016/S0924-8579(00)00360-5.

[307] C.N. Kraft, M. Hansis, S. Arens, M.D. Menger, B. Vollmar, Striated muscle microvascular response to silver implants: A comparativein vivo study with titanium and stainless steel, J. Biomed. Mater. Res. 49 (2000) 192–199. doi:10.1002/(SICI)1097-4636(200002)49:2<192::AID-JBM6>3.0.CO;2-C.

[308] Q.L. Feng, J. Wu, G.Q. Chen, F.Z. Cui, T.N. Kim, J.O. Kim, A mechanistic study of the antibacterial effect of silver ions onEscherichia coli andStaphylococcus aureus, J. Biomed. Mater. Res. 52 (2000) 662–668. doi:10.1002/1097-4636(20001215)52:4<662::AID-JBM10>3.0.CO;2-3.

[309] S.S. Djokić, Behavior of Silver in Physiological Solutions, J. Electrochem. Soc. 145 (1998) 1426. doi:10.1149/1.1838499.

[310] E.M. Hetrick, M.H. Schoenfisch, Reducing implant-related infections: active release strategies, Chem. Soc. Rev. 35 (2006) 780. doi:10.1039/b515219b.

[311] D. Schubert, R. Dargusch, J. Raitano, S.-W. Chan, Cerium and yttrium oxide nanoparticles are neuroprotective., Biochem. Biophys. Res. Commun. 342 (2006)

86–91. doi:10.1016/j.bbrc.2006.01.129.

[312] J. Zhang, C. Liu, Y. Li, J. Sun, P. Wang, K. Di, Y. Zhao, Effect of cerium ion on the proliferation, differentiation and mineralization function of primary mouse osteoblasts in vitro, J. Rare Earths. 28 (2010) 138–142. doi:10.1016/S1002-0721(09)60067-3.

[313] M. Nanami, T. Ookawara, Y. Otaki, K. Ito, R. Moriguchi, K. Miyagawa, Y. Hasuike, M. Izumi, H. Eguchi, K. Suzuki, T. Nakanishi, Tumor Necrosis Factor-α–Induced Iron Sequestration and Oxidative Stress in Human Endothelial Cells, Arterioscler. Thromb. Vasc. Biol. 25 (2005) 2495–2501. doi:10.1161/01.ATV.0000190610.63878.20.

[314] T.A. Rouault, How Mammals Acquire and Distribute Iron Needed for Oxygen-Based Metabolism, PLoS Biol. 1 (2003) e79. doi:10.1371/journal.pbio.0000079.

[315] K.G. Neoh, M. Li, E.T. Kang, E. Chiong, P.A. Tambyah, Surface modification strategies for combating catheter-related complications: recent advances and challenges, J. Mater. Chem. B. 5 (2017) 2045–2067. doi:10.1039/c6tb03280j.

[316] E. Verne, C. Vitale-Brovarone, E. Bui, C.L. Bianchi, A.R. Boccaccini, Surface functionalization of bioactive glasses, J. Biomed. Mater. Res. - Part A. 90 (2009) 981–992. doi:10.1002/jbm.a.32153.

[317] A. Carré, V. Lacarrière, W. Birch, Molecular interactions between DNA and an aminated glass substrate, J. Colloid Interface Sci. 260 (2003) 49–55. doi:10.1016/S0021-9797(02)00147-9.

[318] M. Qin, S. Hou, L.K. Wang, X.Z. Feng, R. Wang, Y.L. Yang, C. Wang, L. Yu, B. Shao, M.Q. Qiao, Two methods for glass surface modification and their application in protein immobilization, Colloids Surfaces B Biointerfaces. 60 (2007) 243–249. doi:10.1016/j.colsurfb.2007.06.018.

[319] E. Verné, S. Ferraris, C. Vitale-Brovarone, S. Spriano, C.L. Bianchi, A. Naldoni, M. Morra, C. Cassinelli, Alkaline phosphatase grafting on bioactive glasses and glass ceramics, Acta Biomater. 6 (2010) 229–240. doi:10.1016/j.actbio.2009.06.025.

[320] V. Salih, K. Franks, M. James, G.W. Hastings, J.C. Knowles, I. Olsen, Development of soluble glasses for biomedical use part II: The biological response of human osteoblast cell lines to phosphate-based soluble glasses, J. Mater. Sci. Mater. Med. 11 (2000) 615–620. doi:10.1023/A:1008901612674.

[321] J. Massera, A. Kokkari, T. Närhi, L. Hupa, The influence of SrO and CaO in silicate and phosphate bioactive glasses on human gingival fibroblasts, J. Mater. Sci. Mater. Med. 26 (2015). doi:10.1007/s10856-015-5528-x.

[322] M. Marcolongo, P. Ducheyne, W.C. LaCourse, Surface reaction layer formationin

vitro on a bioactive glass fiber/polymeric composite, J. Biomed. Mater. Res. 37 (1997) 440–448. doi:10.1002/(SICI)1097-4636(19971205)37:3<440::AID-JBM15>3.0.CO;2-F.

[323] E. Pirhonen, P. Törmälä, Coating of bioactive glass 13-93 fibres with biomedical polymers, J. Mater. Sci. 41 (2006) 2031–2036. doi:10.1007/s10853-006-4503-9.

[324] D.C. Clupper, M.M. Hall, J.E. Gough, L.L. Hench, No Title, in: Trans. Soc. Biomater., Tampa, Fl, 2002.

[325] R. Shah, A.C.M. Sinanan, J.C. Knowles, N.P. Hunt, M.P. Lewis, Craniofacial muscle engineering using a 3-dimensional phosphate glass fibre construct, Biomaterials. 26 (2005) 1497–1505. doi:10.1016/j.biomaterials.2004.04.049.

[326] J. Choueka, J.L. Charvet, H. Alexander, Y.H. Oh, G. Joseph, N.C. Blumenthal, W.C. LaCourse, Effect of annealing temperature on the degradation of reinforcing fibers for absorbable implants, J. Biomed. Mater. Res. 29 (1995) 1309–1315. doi:10.1002/jbm.820291102.

[327] M.A. De Diego, N.J. Coleman, L.L. Hench, Tensile properties of bioactive fibers for tissue engineering applications, J. Biomed. Mater. Res. 53 (2002) 199–203. doi:10.1002/(SICI)1097-4636(2000)53:3<199::AID-JBM2>3.0.CO;2-J.

[328] J. Massera, M. Mayran, J. Rocherullé, L. Hupa, Crystallization behavior of phosphate glasses and its impact on the glasses' bioactivity, J. Mater. Sci. 50 (2015) 3091–3102. doi:10.1007/s10853-015-8869-4.

[329] T.W. Bauer, J. Schils, The pathology of total joint arthroplasty. I. Mechanisms of implant fixation, Skeletal Radiol. 28 (1999) 483–497. doi:10.1007/s002560050541.

[330] G.B. Blinkova, S.A. Vakhidov, A.K. Islamov, I. Nuritdinov, K.A. Khaidarova, On the nature of yellow coloring in cerium-containing silica glasses, Glas. Phys. Chem. 20 (1994) 283–286.

[331] L. Mohammed, M.N.M. Ansari, G. Pua, M. Jawaid, M.S. Islam, A Review on Natural Fiber Reinforced Polymer Composite and Its Applications, Int. J. Polym. Sci. 2015 (2015) 1–15. doi:10.1155/2015/243947.

[332] A.J. Parsons, M. Evans, C.D. Rudd, C.A. Scotchford, Synthesis and degradation of sodium iron phosphate glasses and their in vitro cell response, J. Biomed. Mater. Res. - Part A. 71 (2004) 283–291. doi:10.1002/jbm.a.30161.

[333] R.Z. Domingues, A.E. Clark, A.B. Brennan, A sol-gel derived bioactive fibrous mesh, J. Biomed. Mater. Res. 55 (2001) 468–474. doi:10.1002/1097-4636(20010615)55:4<468::AID-JBM1038>3.0.CO;2-T.

[334] D.J. Mooney, C.L. Mazzoni, C. Breuer, K. McNamara, D. Hern, J.P. Vacanti, R. Langer, Stabilized polyglycolic acid fibre-based tubes for tissue engineering,

Biomater. Silver Jubil. Compend. 17 (2006) 129–138. doi:10.1016/B978-008045154-1.50017-4.

[335] S. Tanaka, T. Takigawa, S. Ichihara, T. Nakamura, Mechanical properties of the bioabsorbable polyglycolic acid–collagen nerve guide tube, Polym. Eng. Sci. 46 (2006) 1461–1467. doi:10.1002/pen.20600.

[336] O. Mazurin, M. Streltsina, T. Shvaiko–Shvaikovskaya, Physical Sciences Data 15. Series: Handbook of Glass Data Part A, Elsevier, New York, NY, 1983.

[337] S. Cozien-Cazuc, A.J. Parsons, G.S. Walker, I.A. Jones, C.D. Rudd, Effects of aqueous aging on the mechanical properties of P40Na20Ca16Mg24phosphate glass fibres, J. Mater. Sci. 43 (2008) 4834–4839. doi:10.1007/s10853-008-2698-7.

[338] N. Sharmin, A.J. Parsons, C.D. Rudd, I. Ahmed, Effect of boron oxide addition on fibre drawing, mechanical properties and dissolution behaviour of phosphate-based glass fibres with fixed 40, 45 and 50 mol% P<inf>2</inf>O<inf>5</inf>, J. Biomater. Appl. 29 (2014) 639–653. doi:10.1177/0885328214539824.

[339] M. Bosch, A. Sánchez, F. Rojas, C. Ojeda, Recent Development in Optical Fiber Biosensors, Sensors. 7 (2007) 797–859. doi:10.3390/s7060797.

[340] B. Gholamzadeh, H. Nabovati, Fiber Optic Sensors, Int. J. Electr. Comput. Energ. Electron. Commun. Eng. 2 (2008) 1107–1117. doi:10.1134/S0018143908070096.

[341] J. Dakin, B. Culshaw, Optical fiber sensors: Principles and components. Volume 1, Artech House, Boston, 1988.

[342] J. Massera, L. Hupa, M. Hupa, Influence of the partial substitution of CaO with MgO on the thermal properties and in vitro reactivity of the bioactive glass S53P4, J. Non. Cryst. Solids. 358 (2012) 2701–2707. doi:10.1016/J.JNONCRYSOL.2012.06.032.

[343] A.L.B. Maçon, T.B. Kim, E.M. Valliant, K. Goetschius, R.K. Brow, D.E. Day, A. Hoppe, A.R. Boccaccini, I.Y. Kim, C. Ohtsuki, T. Kokubo, A. Osaka, M. Vallet-Regí, D. Arcos, L. Fraile, A.J. Salinas, A. V. Teixeira, Y. Vueva, R.M. Almeida, M. Miola, C. Vitale-Brovarone, E. Verné, W. Höland, J.R. Jones, A unified in vitro evaluation for apatite-forming ability of bioactive glasses and their variants, J. Mater. Sci. Mater. Med. 26 (2015) 1–10. doi:10.1007/s10856-015-5403-9.

[344] T. Kokubo, H. Kushitani, S. Sakka, T. Kitsugi, T. Yamamuro, Solutions able to reproduce in vivo surface-structure changes in bioactive glass-ceramic A-W3, J. Biomed. Mater. Res. 24 (1990) 721–734. doi:10.1002/jbm.820240607.

[345] M. Ojansivu, S. Vanhatupa, L. Björkvik, H. Häkkänen, M. Kellomäki, R. Autio, J.A. Ihalainen, L. Hupa, S. Miettinen, Bioactive glass ions as strong enhancers of osteogenic differentiation in human adipose stem cells, Acta Biomater. 21 (2015)

190–203. doi:10.1016/j.actbio.2015.04.017.

[346] L. Tirkkonen, S. Haimi, S. Huttunen, J. Wolff, E. Pirhonen, G.K. Sándor, S. Miettinen, Osteogenic medium is superior to growth factors in differentiation of human adipose stem cells towards boneforming cells in 3D culture, Eur. Cells Mater. 25 (2012) 144–158. doi:10.22203/eCM.v025a10.

[347] P.A. Zuk, M. Zhu, H. Mizuno, J. Huang, J.W. Futrell, A.J. Katz, P. Benhaim, H.P. Lorenz, M.H. Hedrick, Multilineage Cells from Human Adipose Tissue: Implications for Cell-Based Therapies, Tissue Eng. 7 (2001) 211–228. doi:10.1089/107632701300062859.

[348] B. Lindroos, S. Boucher, L. Chase, H. Kuokkanen, H. Huhtala, R. Haataja, M. Vemuri, R. Suuronen, S. Miettinen, Serum-free, xeno-free culture media maintain the proliferation rate and multipotentiality of adipose stem cells in vitro, Cytotherapy. 11 (2009) 958–972. doi:10.3109/14653240903233081.

[349] J. Massera, A. Haldeman, J. Jackson, C. Rivero-Baleine, L. Petit, K. Richardson, Processing of tellurite-based glass with low OH content, J. Am. Ceram. Soc. 94 (2011) 130–136. doi:10.1111/j.1551-2916.2010.04031.x.

[350] M. Curie, A. Lepape, Conductibilité thermique des gaz rares, J. Phys. Le Radium. 2 (1931) 392–397. doi:10.1051/jphysrad:01931002012039200.

[351] E. Pirhonen, L. Moimas, M. Brink, Mechanical properties of bioactive glass 9-93 fibres, Acta Biomater. 2 (2006) 103–107. doi:10.1016/j.actbio.2005.08.008.

[352] S. Lee, A. Obata, T. Kasuga, Ion release from SrO-CaO-TiO2-P2O5 glasses in Tris buffer solution, J. Ceram. Soc. Jpn. 117 (2009) 935 – 938. doi:10.2109/jcersj2.117.935.

[353] P.Y. Shih, H.M. Shiu, Properties and structural investigations of UV-transmitting vitreous strontium zinc metaphosphate, Mater. Chem. Phys. 106 (2007) 222–226. doi:10.1016/j.matchemphys.2007.05.038.

[354] H. Gao, T. Tan, D. Wang, Effect of composition on the release kinetics of phosphate controlled release glasses in aqueous medium, J. Control. Release. 96 (2004) 21–28. doi:10.1016/j.jconrel.2003.12.030.

[355] Y.M. Moustafa, K. El-Egili, Infrared spectra of sodium phosphate glasses, J. Non. Cryst. Solids. 240 (1998) 144–153. doi:10.1016/S0022-3093(98)00711-X.

[356] E.A. Abou Neel, W. Chrzanowski, D.M. Pickup, L.A. O'Dell, N.J. Mordan, R.J. Newport, M.E. Smith, J.C. Knowles, Structure and properties of strontium-doped phosphate-based glasses, J. R. Soc. Interface. 6 (2009) 435 LP – 446. doi:10.1098/rsif.2008.0348.

[357] M.A. Karakassides, A. Saranti, I. Koutselas, Preparation and structural study of

binary phosphate glasses with high calcium and/or magnesium content, J. Non. Cryst. Solids. 347 (2004) 69–79. doi:10.1016/j.jnoncrysol.2004.08.111.

[358] A.G. Kalampounias, Short-time vibrational dynamics of metaphosphate glasses, J. Phys. Chem. Solids. 73 (2012) 148–153. doi:10.1016/j.jpcs.2011.11.014.

[359] J. Serra, P. González, S. Liste, C. Serra, S. Chiussi, B. León, M. Pérez-Amor, H.O. Ylänen, M. Hupa, FTIR and XPS studies of bioactive silica based glasses, J. Non. Cryst. Solids. 332 (2003) 20–27. doi:10.1016/j.jnoncrysol.2003.09.013.

[360] K.Á. Magyari, L. Baia, A. Vulpoi, S. Simon, O. Popescu, V. Simon, Bioactivity evolution of the surface functionalized bioactive glasses, J. Biomed. Mater. Res. - Part B Appl. Biomater. 103 (2015) 261–272. doi:10.1002/jbm.b.33203.

[361] V.C. Farmer, The Layer Silicates, in: Infrared Spectra Miner., Mineralogical Society of Great Britain and Ireland, Londan, 1974: pp. 331–363. doi:10.1180/mono-4.15.

[362] A.M.B. Silva, C.M. Queiroz, S. Agathopoulos, R.N. Correia, M.H.V. Fernandes, J.M. Oliveira, Structure of SiO2-MgO-Na2O glasses by FTIR, Raman and 29Si MAS NMR, J. Mol. Struct. 986 (2011) 16–21. doi:10.1016/j.molstruc.2010.11.023.

[363] J. Massera, A. Haldeman, D. Milanese, H. Gebavi, M. Ferraris, P. Foy, W. Hawkins, J. Ballato, R. Stolen, L. Petit, K. Richardson, Processing and characterization of core–clad tellurite glass preforms and fibers fabricated by rotational casting, Opt. Mater. (Amst). 32 (2010) 582–588. doi:10.1016/j.optmat.2009.12.003.

[364] B.-S. Bae, M.C. Weinberg, Optical absorption of copper phosphate glasses in the visible spectrum, J. Non. Cryst. Solids. 168 (1994) 223–231. doi:10.1016/0022-3093(94)90333-6.

[365] Y.M. Moustafa, H.Ã. Doweidar, I. Abbas, Structure and electric conduction of Fe 2 O 3 – P 2 O 5 glasses, 353 (2004) 82–91. doi:10.1016/j.physb.2004.09.004.

[366] B. Mehdikhani, G. Borhani, Optical spectroscopy of sodium silicate glasses prepared with nano- and micro-sized iron oxide particles, Process. Appl. Ceram. 7 (2013) 117–121. doi:10.2298/pac1303117m.

[367] Q.L. Feng, J. Wu, G.Q. Chen, F.Z. Cui, T.N. Kim, J.O. Kim, A mechanistic study of the antibacterial effect of silver ions on Escherichia coli and Staphylococcus aureus, J. Biomed. Mater. Res. 52 (2000) 662–668. doi:10.1002/1097-4636(20001215)52:4<662::AID-JBM10>3.0.CO;2-3.

[368] C. Espírito Santo, E.W. Lam, C.G. Elowsky, D. Quaranta, D.W. Domaille, C.J. Chang, G. Grass, Bacterial killing by dry metallic copper surfaces., Appl. Environ. Microbiol. 77 (2011) 794–802. doi:10.1128/AEM.01599-10.

[369] E. Munukka, O. Leppäranta, M. Korkeamäki, M. Vaahtio, T. Peltola, D. Zhang, L. Hupa, H. Ylänen, J.I. Salonen, M.K. Viljanen, E. Eerola, Bactericidal effects of bioactive glasses on clinically important aerobic bacteria, J. Mater. Sci. Mater. Med. 19 (2008) 27–32. doi:10.1007/s10856-007-3143-1.

[370] O. Leppäranta, M. Vaahtio, T. Peltola, D. Zhang, L. Hupa, M. Hupa, H. Ylänen, J.I. Salonen, M.K. Viljanen, E. Eerola, Antibacterial effect of bioactive glasses on clinically important anaerobic bacteria in vitro, J. Mater. Sci. Mater. Med. 19 (2008) 547–551. doi:10.1007/s10856-007-3018-5.

[371] D.C. Coraça-Huber, M. Fille, J. Hausdorfer, D. Putzer, M. Nogler, Efficacy of antibacterial bioactive glass S53P4 against S. aureus biofilms grown on titanium discs in vitro., J. Orthop. Res. 32 (2014) 175–7. doi:10.1002/jor.22463.

[372] D. Zhang, O. Leppäranta, E. Munukka, H. Ylänen, M.K. Viljanen, E. Eerola, M. Hupa, L. Hupa, Antibacterial effects and dissolution behavior of six bioactive glasses, J. Biomed. Mater. Res. - Part A. 93 (2010) 475–483. doi:10.1002/jbm.a.32564.

[373] E. Saiz, M. Goldman, J.M. Gomez-Vega, A.P. Tomsia, G.W. Marshall, S.J. Marshall, In vitro behavior of silicate glass coatings on Ti6Al4V, Biomaterials. 23 (2002) 3749–3756. doi:10.1016/S0142-9612(02)00109-6.

[374] J. Li, Y. Chen, Y. Yin, F. Yao, K. Yao, Modulation of nano-hydroxyapatite size via formation on chitosan-gelatin network film in situ, Biomaterials. 28 (2007) 781–790. doi:10.1016/j.biomaterials.2006.09.042.

[375] G.J. Brentrup, H.M.M. Moawad, L.F. Santos, R.M. Almeida, H. Jain, Structure of Na2O-CaO-P2O5-SiO2glass-ceramics with multimodal porosity, J. Am. Ceram. Soc. 92 (2009) 249–252. doi:10.1111/j.1551-2916.2008.02847.x.

[376] M. Ramalingam, P. Vallittu, U. Ripamonti, W.-J. Li, Tissue Engineering and Regenerative Medicine: A Nano Approach, CRC Press, 2013.

[377] H. H. Lu, S. R. Pollack, P. Ducheyne, Temporal zeta potential variations of 45S5 bioactive glass immersed in an electrolyte solution, J. Biomed. Mater. Res. 51 (2000) 80–87. doi:10.1002/(SICI)1097-4636(200007)51:13.0.CO;2-6.

[378] K. Puumanen, M. Kellomäki, V. Ritsilä, T. Böhling, P. Törmälä, T. Waris, N. Ashammakhi, A novel bioabsorbable composite membrane of Polyactive® 70/30 and bioactive glass number 13-93 in repair of experimental maxillary alveolar cleft defects, J. Biomed. Mater. Res. - Part B Appl. Biomater. 75 (2005) 25–33. doi:10.1002/jbm.b.30218.

[379] P. Ruuttila, H. Niiranen, M. Kellomäki, P. Törmälä, Y.T. Konttinen, M. Hukkanen, Characterization of human primary osteoblast response on bioactive glass (BaG 13-93) coated poly-L,DL-lactide (SR-PLA70) surface in vitro, J. Biomed. Mater. Res. - Part B Appl. Biomater. 78B (2006) 97–104. doi:10.1002/jbm.b.30460.

[380] J. Massera, L. Hupa, Influence of SrO substitution for CaO on the properties of bioactive glass S53P4., J. Mater. Sci. Mater. Med. 25 (2014) 657–68. doi:10.1007/s10856-013-5120-1.

[381] N. Sharmin, M.S. Hasan, A.J. Parsons, D. Furniss, C.A. Scotchford, I. Ahmed, C.D. Rudd, Effect of boron addition on the thermal, degradation, and cytocompatibility properties of phosphate-based glasses, Biomed Res. Int. 2013 (2013). doi:10.1155/2013/902427.

[382] J. Massera, Y. Shpotyuk, F. Sabatier, T. Jouan, C. Boussard-Plédel, C. Roiland, B. Bureau, L. Petit, N.G. Boetti, D. Milanese, L. Hupa, Processing and characterization of novel borophosphate glasses and fibers for medical applications, J. Non. Cryst. Solids. 425 (2015) 52–60. doi:10.1016/j.jnoncrysol.2015.05.028.

[383] NIST Chemistry WebBook, SRD 69, (n.d.). doi:10.18434/T4D303.

[384] G.W. Scherer, A.R. Cooper, Thermal Stresses in Clad-Glass Fibers, J. Am. Ceram. Soc. 63 (1980) 346–347. doi:10.1111/j.1151-2916.1980.tb10739.x.

[385] D.A. Krohn, A.R. Cooper, Strengthening of Glass Fibers: I, Cladding *, J. Am. Ceram. Soc. 52 (1969) 661–664. doi:10.1111/j.1151-2916.1969.tb16072.x.

[386] U.C. Paek, C.R. Kurkjian, Calculation of Cooling Rate and Induced Stresses in Drawing of Optical Fibers, J. Am. Ceram. Soc. 58 (1975) 330–335. doi:10.1111/j.1151-2916.1975.tb11490.x.

[387] N. Sharmin, C.D. Rudd, A.J. Parsons, I. Ahmed, Structure, viscosity and fibre drawing properties of phosphate-based glasses: effect of boron and iron oxide addition, J. Mater. Sci. 51 (2016) 7523–7535. doi:10.1007/s10853-016-0032-3.

[388] P.K. Gupta, Fractography of Fiberglass, in: R.C. Bradt, R.E. Tressler (Eds.), Fractography Glas., Springer US, Boston, MA, 1994: pp. 185–206. doi:10.1007/978-1-4899-1325-8_6.

[389] R. Colquhoun, K.E. Tanner, Mechanical behaviour of degradable phosphate glass fibres and composites - A review, Biomed. Mater. 11 (2015). doi:10.1088/1748-6041/11/1/014105.

[390] P. Haque, I. Ahmed, A. Parsons, R. Felfel, G. Walker, C. Rudd, Degradation properties and microstructural analysis of 40P2O5–24MgO–16CaO–16Na2O–4Fe2O3 phosphate glass fibres, J. Non. Cryst. Solids. 375 (2013) 99–109. doi:10.1016/j.jnoncrysol.2013.05.008.

[391] L.G. Baikova, V.P. Pukh, Y.K. Fedorov, A.B. Sinani, L. V Tikhonova, M.F. Kireenko, Mechanical properties of phosphate glasses as a function of the total bonding energy per unit volume of glass, Glas. Phys. Chem. 34 (2008) 126–131. doi:10.1134/S1087659608020028.

[392] S. Inaba, S. Fujino, K. Morinaga, Young's Modulus and Compositional Parameters of Oxide Glasses, J. Am. Ceram. Soc. 82 (2004) 3501–3507. doi:10.1111/j.1151-2916.1999.tb02272.x.

[393] C.R. Kurkjian, M.J. Matthewson, J.M. Rooney, Effects of heat treatment and HF etching on the strength of silica lightguides, in: H.G. Limberger, M.J. Matthewson (Eds.), 2004: p. 223. doi:10.1117/12.548411.

Publications

PUBLICATION I

Ag-doped phosphate bioactive glasses: Thermal, structural and in-vitro dissolution properties

A. Mishra, J. Rocherulle, J. Massera

Biomedical Glasses 2 (1) (2016) 38–48

https://doi.org/10.1515/bglass-2016-0005

Research Article Open Access

A. Mishra, J. Rocherullé, and J. Massera*

Ag-doped phosphate bioactive glasses: thermal, structural and *in-vitro* dissolution properties

DOI 10.1515/bglass-2016-0005
Received Feb 01, 2016; revised May 14, 2016; accepted Jun 04, 2016

Abstract: Ag doped-bioactive phosphate glasses were processed by traditional melt quenching technique with the concentration of Ag_2O ranging from 0 to 5 mol%. The Ag doping led to the depolymerization of the phosphate network which is accompanied by a decrease in the glass transition temperature. The processing window represented by ΔT ($\Delta T=T_x-T_g$) exhibited a maximum for glasses containing 2-3 mol% of Ag_2O. An increase in Ag content induced an increase in the glass dissolution rate. The precipitation of a Sr-CaP layer at the surface of the glass particulates was found to occur at shorter immersion time for the Ag containing glasses. The congruent dissolution and wide processing window of these Ag containing glasses may be of great interest for scaffold manufacturing from sintering of glass powders with antimicrobial properties.

1 Introduction

Since the discovery of the bioactive glass 45S5 (Bioglass®) by L.L. Hench [1] and S53P4 by Andersson *et al.* [2], much work has focused on tailoring the silicate bioactive glass composition to enable fiber drawing or powder sintering [3–5]. Studies show that typical silicate bioactive glasses have a crystallization kinetics that not only inhibits shaping at medium to high temperature but also reduce the glass's bioactivity [3, 6].

Phosphate bioactive glasses (PBGs) arise as a potential substitute to the typical silicate glasses. The chemical resistance of phosphate glasses can be tailored to suit different applications. The time required for complete degradation can be adjusted from hours to years [7]. PBG demonstrate bioactivity and are promising materials for use in bone repair and reconstruction [8]. Furthermore PBG are known to possess thermal properties showing wider processing window as evidenced by the large number of bioactive phosphate fibers studied in the past years [9, 10].

Glasses within the $50P_2O_5$-$10Na_2O$-(40-x)CaO-xSrO composition exhibited a minimum in the dissolution when half of the CaO was replaced with SrO [11]. It was found that the dissolution rate is dependent on the glass structure and a reduction in the phosphate chain length leads to an increase in the chemical resistance. Furthermore, the proliferation and growth of gingival fibroblasts cells increased with increasing the SrO content. Whereas the SrO-free glass led to cell death within 24h, the CaO-free glass showed a cell count similar to the one measured at the surface of the glass S53P4 used as reference [12]. This is partially attributed to the decrease in initial dissolution rate when SrO is introduced in place of CaO in the glass. The effect of strontium ions both in the media and in the reactive layer also play an important role as discussed in [12]. However, despite those promising results, these metaphosphate glasses present a rapid initial dissolution rate and late precipitation of a reactive layer disabling the cells to efficiently attach for the first 1-3 days of culture [12]. This is in agreement with Salih *et al.* who showed that fast dissolving glasses did not allow for proper cell proliferation [13].

Metal ions such as Silver (Ag), Copper (Cu) or Cobalt (Co) just to cite a few can be added to glasses in order to give them unique properties or modify the existing physical or chemical properties for clinical applications. These ions are known to exhibit antimicrobial properties for example [14–16]. Ag is a popular choice as a dopant for several biomedical devices owing to its low toxicity to human cells and effectiveness against many types of microbial growth, even at low concentrations [17]. Ag ions in the form of nitrate, oxide are commonly found in several healthcare

A. Mishra: Department of Electronics and Communications Engineering, Tampere University of Technology, Korkeakoulunkatu 3, FI-33720, Tampere, Finland
J. Rocherullé: Equipe Verres et Céramiques, UMR-CNRS 6226, Sciences Chimiques de Rennes, Université de Rennes I, F-35042 Rennes Cedex, France
***Corresponding Author: J. Massera:** Department of Electronics and Communications Engineering, Tampere University of Technology, Korkeakoulunkatu 3, FI-33720, Tampere, Finland; BioMediTech, University of Tampere and Tampere University of Technology, Biokatu 10/FI-33520 Tampere, Finland; Email: jonathan.massera@tut.fi

Table 1: Glasses nominal compositions.

Glass	P_2O_5 (mol%)	CaO (mol%)	SrO (mol%)	Na_2O (mol%)	Ag_2O (mol%)
x=0	50	20	20	10	0
x=1	49.5	19.8	19.8	9.9	1
x=2	49	19.6	19.6	9.8	2
x=3	48.5	19.4	19.4	9.7	3
x=5	47.5	19	19	9.5	5

products, for *e.g.*, Ag coated catheters, wound dressing for example [17]. Ag based ointments have long been used to treat wounds susceptible to bacterial infections [18]. When PBGs are doped with Ag, the metal atoms are assumed to be incorporated in the structure [19]. As opposed to silicate glasses, PBG are known to have, in general, a congruent dissolution. Thus the rate of release of Ag ions, which depends upon the dissolution of the glass itself, can then be controlled if the Ag ions are added in PBG. Ahmed *et al.* developed silver-doped phosphate bioactive glasses with substitution of Na_2O for Ag_2O up to 15 mol%. Maximum antimicrobial effect was found to occur in glasses with 1 to 5 mol% of Ag_2O [14]. The structure and properties of the silver-doped glasses were also studied by the authors [20]. More recently, the investigation of silver-doped phosphate glasses with antimicrobial properties were also investigated for glasses with 65 and 70 mol% of P_2O_5 [21]. In this study an increase in the antimicrobial effect was seen with increasing the Ag content while similar effect was found on Ag-free glasses when increasing the phosphate content. However, in these studies, the phosphate content was 50 mol% or greater. The fast dissolution rate of glass in the P_2O_5-CaO-Na_2O family, with P_2O_5 content greater that 50 mol%, was found to inhibit growth and bone antigen expression. On the other hand the glasses with slow solubility upregulated the proliferation of cells [13]. Based on the previous research on Sr-containing bioactive glasses it appears that despite a P_2O_5 content of 50% gingival fibroblast cells can attach and proliferate [12]. Thus it is of tremendous interest to study the impact of Ag doping on this glass composition and assess whether antimicrobial Ag-doped strontium containing phosphate glasses can be obtained.

In this paper we report on the effect of Ag doping on the thermal, structural and *in-vitro* dissolution properties of the phosphate bioactive glass previously studied in [12]. Ag_2O was introduced relative to the entire base glass as opposed to the typical isomorphic substitution. The reason for such doping was to maintain the same (Ca+Sr)/P ratio in the glass while lowering the phosphate content. The thermal properties as a function of Ag content were measured using a differential thermal analyzer (DTA). The structure was assessed by Fourier transformed infrared spectroscopy in attenuated total reflectance mode (FTIR-ATR). The dissolution test was performed in TRIS buffer solution in order to confirm the congruent dissolution of investigated glasses. The formation of a CaP layer at the surface of the glasses upon immersion in TRIS was evidenced by SEM/EDS and FTIR-ATR. Finally the ions released in solution were quantified using ion chromatography and ICP.

2 Materials and Methods

Glass preparation

Glasses with nominal composition $[(Ag_2O)_x\text{-}(0.5P_2O_5 \cdot 0.2CaO{\cdot}0.2SrO{\cdot}0.1Na_2O)_{100-x}]$ where x = 0, 1, 2, 3 and 5 mol% were prepared. The nominal compositions are reported in Table 1. The glasses were obtained by melting in a silica crucible in air. Analytical grade $CaCO_3$, $SrCO_3$, $NH_4H_2PO_4$, Ag_2O, $NaPO_3$ and Na_2SO_4 were used to prepare the batch. $Ca(PO_3)_2$ and $Sr(PO_3)_2$ were first prepared by heating $NH_4H_2PO_4$ and carbonates at 300°C during 2 hours to remove NH_3, H_2O and CO_2 then maintained 10 hours at 850°C and 750°C for the calcium and strontium samples, respectively. The batch was placed in a silica crucible and heated up to 1000 °C for 30 minutes. 1 wt% Na_2SO_4 was added to the batch to avoid the reduction of silver oxide into metallic silver. The melt was poured into a preheated brass mould and annealed at T_g+15°C for 30 minutes, then cooled down to Tg-50°C at 1 °C·min^{-1} and annealed during one hour to lower the internal stress. Finally, the furnace was turned off and the glass cooled to room temperature before removal. After melting, the glasses were analyzed with EDS and the composition was found to be in agreement with the nominal one, within the accuracy of the measurement (1.5 wt%). Despite the melting in silica crucible and the addition of Na_2SO_4, no Si or S were found in the analysis.

Physical properties

The density of the glasses was measured using Archimedes principle with an accuracy of ±0.02 g/cm^3. Ethanol was used as immersion liquid and the measurement was performed on a polished glass bulk. Molar volume of the glasses was calculated using their density and molecular weight. Young's modulus (E) was measured by the ultrasonic velocity technique. This technique is based on time-of-flight measurements using the pulse-echo technique [22] with ±2 GPa as the accuracy value. Vickers microhardness (Hv) was measured by the indentation technique using a Matsuzawa® Digital Microhardness Tester MXT 70 with a pyramid shaped diamond indenter. A load of 0.4905 N was applied for 5 s for all the measurements which were performed at room temperature on polished surfaces. The displacement rate was the same on loading and unloading. All the characteristics were averaged over measurements on 10 indentations per sample. The accuracy is considered as better than ±0.2 GPa.

Thermal properties

Differential Thermal Analysis (DTA, Netzch JUPITER F1) of all the glasses was carried out at a heating rate of 10 °C/min, in a Pt crucible and with a flow of 50 ml/min of N_2. The T_g (glass transition temperature), T_x (crystallization temperature) and T_p (crystallization temperature) were assessed from the obtained thermogram. T_g was determined as the inflection point of the endotherm obtained by taking first derivative of the DTA curve with an accuracy of 2 °C. The T_x was taken as the onset of the crystallization peak and T_p as the maxima of the exotherm. All measurements were obtained with an accuracy better than ±3°C

Structural Properties

The IR absorption spectra for all glass powders before and after immersion in TRIS were recorded with Perkin Elmer Spectrum One FTIR Spectrophotometer in Attenuated Total Reflectance (ATR) mode. All spectra were recorded in the range 600–1600 cm^{-1}, corrected for Fresnel losses and were normalized to the band with maximum intensity. Each spectrum is an average of 8 scans and has a resolution of 1 cm^{-1}.

Optical Properties

The UV-Vis absorption spectra for all the glasses were recorded in the range 200–1600 nm at room temperature using a UV-3600 Plus UV-VIS-NIR Spectrophotometer Shimadzu. The glass samples used for this measurement were 2 mm thick and optically polished.

In-vitro dissolution

The glasses were crushed and sieved to obtain powder with size ranging from 125 to 200 µm. These particles were immersed in TRIS buffer solution and placed in an incubating shaker HT Infors Multitron at 37°C, 100 rpm to obtain laminar flow mixing without moving the particles. The mass to volume ratio was kept constant at 75 mg of glass for 50 ml TRIS. Immersion test was conducted for up to 4 weeks. The pH of the solution was measured before and after immersion using pH ion analyzer Mettler Toledo SevenMultimeter with accuracy better than ±0.02. The pH of the solutions containing glass was compared to a TRIS blank sample. The pH of the blank solution was found to remain unchanged throughout the testing period. Post immersion, the glass powder was recovered, washed with acetone and dried for FTIR-ATR and SEM-EDS analysis. 10 ml of the TRIS solution containing glassy powder was diluted in 90ml of ultra-pure water for ICP-OES measurement Inductively coupled plasma - Optical emission spectrometer (ICP-OES; Optima 5300DV, Perkin Elmer) was employed to quantify the amount of P, Sr, Ca and Na ions found in the TRIS solution after glass immersion. The value obtained for each ions was compared to the value obtained for the blank samples (only TRIS). The TRIS samples used as blanks were analyzed to ensure that the concentration of P, Ca, Sr and Na was consistently 0, or under the detection limit, as no such ions should be present in TRIS buffer solutions.

Imaging and elementary analysis

Scanning electron microscopy (SEM), using a JEOL JSM 7100F apparatus, was used for high-resolution imaging of the sample surfaces (Pressure: 10^{-4} Pa, accelerator voltage: 20 kV). Energy Dispersive X-Ray Spectroscopy (EDS) was used as the chemical microanalysis technique used in conjunction with SEM. The associated detector (EDS SDD X-Max 80mm2 Oxford Instruments AZtecEnergy) allows one to identify what particular elements are and their relative atomic proportions. This powerful tool of the elemen-

Table 2: Thermal and mechanical properties.

Glass	T_g(±3°C)	T_x(±3°C)	T_p(±3°C)	$\Delta T=T_x-T_g$ (±6°C)	HV (±0.2GPa)	E (±2GPa)
x = 0	436	550	603	114	2.3	55
x = 1	430	554	583	124	2.2	56
x = 2	428	567	611	139	2.2	55
x = 3	420	560	597	140	2.2	55
x = 5	418	546	587	128	2.2	56

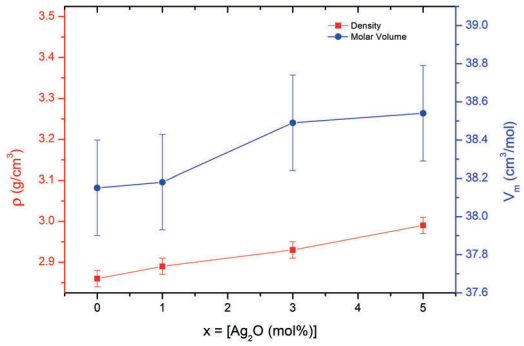

Figure 1: Density (ρ) and molar volume (V_m) of the investigated glasses.

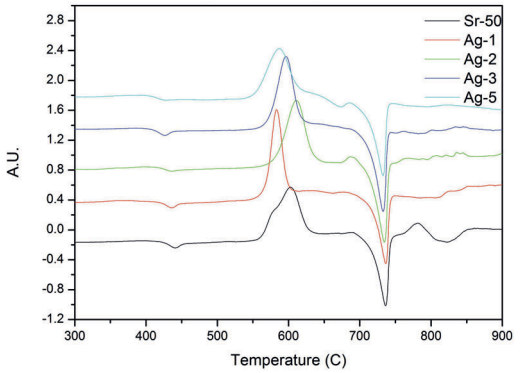

Figure 2: DTA thermogram of the investigated glasses.

tal analysis can identify elements heavier than Be with a spatial resolution better than 1 μm^3, corresponding to a smallest spot size of about 1 μm^2, and the accuracy is ±1% for polished bulk target in this case where pure standards are collected on site.

3 Results

The glasses of investigation with composition $[(Ag_2O)_x$-$(0.5P_2O_5 \cdot 0.2CaO{\cdot}0.2SrO{\cdot}0.1Na_2O)_{100-x}]$ where x = 0, 1, 2, 3 and 5 mol% were analyzed using EDS/SEM. All the compositions were found to be in agreement with the nominal one within the accuracy of the measurement. As already mentioned in the previous section, we assume that no Si was found despite using a silica crucible. Nevertheless, the Sr $L_{\alpha 1}$ EDX peak located at 1806 keV can mask the Si K peak at 1740 keV, however the low melting temperature (1000°C) and the short fining time used for the glass synthesis, allows to prevent the silica dissolution in phosphate melts, as stated in previous studies conducted on phosphate glasses which do not contain Sr and for which, the chemical compositions were checked by EDS [23, 24].

Figure 1 presents the density (ρ) and molar volume (V_m) of the investigated glass as a function of Ag_2O content. With an increase in Ag_2O, the density increases while the molar volume remains constant, within the accuracy of the measurements.

The thermal properties of the investigated glasses are reported in Table 2 and the DTA traces are shown in Figure 2. With an increase in Ag_2O, the glass transition temperature T_g decreases whereas T_x and T_p exhibit a maximum for the glass with x = 2 mol%. ΔT ($\Delta T=T_x-T_g$), which is a gauge of glass's resistance to crystallization, is also found to present a maximum for glasses with x = 2 and 3 mol%. It is interesting to note that the glass with x = 1 mol% possesses a sharper crystallization peak as compared to the other glasses under investigation. In addition, the Young's modulus and the Vickers microhardness were determined for all the glass samples. These values, summarized in Table 2, which do not exhibit any difference, when considering the accuracy of the measurements, are 55 GPa and 2.2 GPa for the Young's modulus and for the Vickers microhardness, respectively. The glass's structural properties were assessed using FTIR-ATR and Raman spectroscopy. The IR spectra of the glasses are shown in Figure 3a. All spectra were normalized to the band located

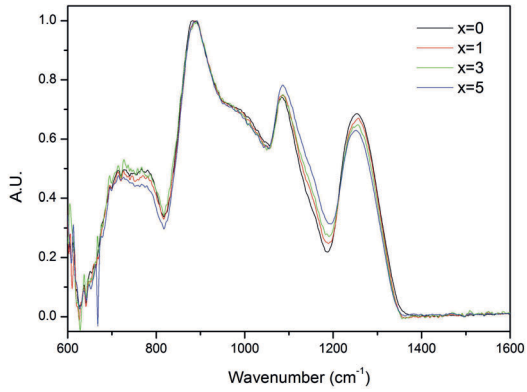

(a)

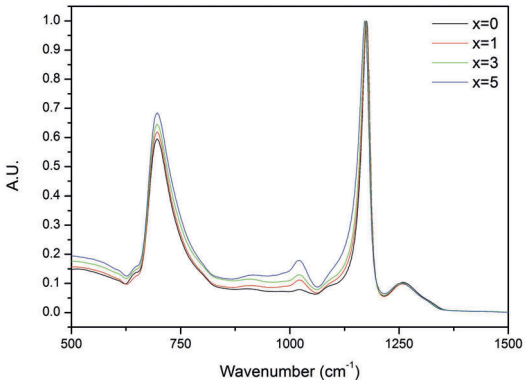

(b)

Figure 3: FTIR-ATR a) and Raman b) spectra of the investigated glasses.

at ~880 cm^{-1}. The spectra exhibit five absorption bands located around 1260, 1085, 880, 775 and 718 cm^{-1} and two shoulders at ~1154 and 980 cm^{-1}. With an increase in Ag_2O, all bands remained unchanged in terms of intensity and shape, except for the band at 1260 cm^{-1} which decreases in intensity.

Figure 3b presents the Raman spectra of the glasses. All spectra were normalized to the band with maximum intensity peaking at ~1175 cm^{-1}. The spectra exhibit four bands and one shoulder which are all characteristics of the metaphosphate network. With an increase in Ag_2O, all bands are found to shift to lower wavenumber. The bands at 695 and 1020 cm^{-1} as well as the shoulder at 1090 cm^{-1} are all found to increase in intensity as compared to the band at 1175 cm^{-1}.

Glass powder of each composition was immersed in TRIS solution for up to 672 hours. After 0, 24, 72, 168, 336

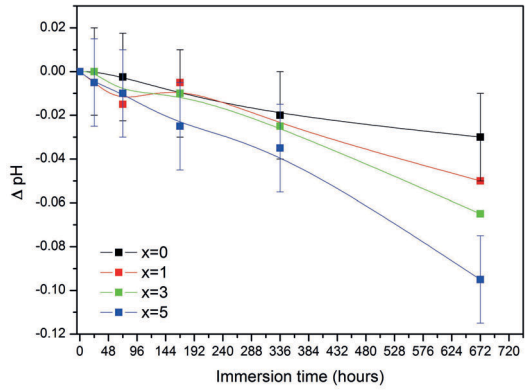

Figure 4: Change in pH as a function of immersion time.

and 672h of immersion, the particles were rinsed and dried for analyses using FTIR-ATR and EDS/SEM. The solution was diluted ten times for ion concentration analysis using ICP-OES.

At each immersion time, the pH of the solution was measured and the change in pH (as compared to the pH of the blank TRIS solution) is presented in Figure 4. As the immersion time increases, the pH of the solutions containing the newly prepared glasses decreased. One can notice that an increase in Ag_2O leads to a stronger decrease in the solution pH.

The ion concentration in solution was quantified using ICP-OES. The evolution over time of the Ca, Sr, Na, and P concentrations is presented in Figure 5a, b, c and d, respectively. With an increase of the immersion time, an increase in the Ca, Sr, Na and P concentration is seen. The release of ions is greater with an increase in Ag_2O. This increase is seen despite the decrease in these ions in the base glass (Table 1), due to the Ag doping.

The FTIR-ATR spectra of the glasses with silver content x = 0 a), x = 1 b), x = 3 c) x = 5 d) as a function of immersion time are presented in Figure 6. For immersion up to 72 h, no significant changes could be seen in the FTIR-ATR spectra of all investigated glasses. With an increase in immersion time, all glasses exhibit a decrease in intensity and shift to lower wavenumber of the bands located at 1260 and 775 cm^{-1}. The main band, at 890 cm^{-1}, is also found to shift to lower wavenumber. The band at 1085 cm^{-1}, is found to decrease in the glass with x = 0, whereas, for all Ag-containing samples the band decrease in intensity for immersion up to 336 h and then increases in intensity and shift to higher wavenumber for longer immersion time. All spectra for the Ag-containing glasses exhibit the appearance of new bands at 988 and 1030 cm^{-1}.

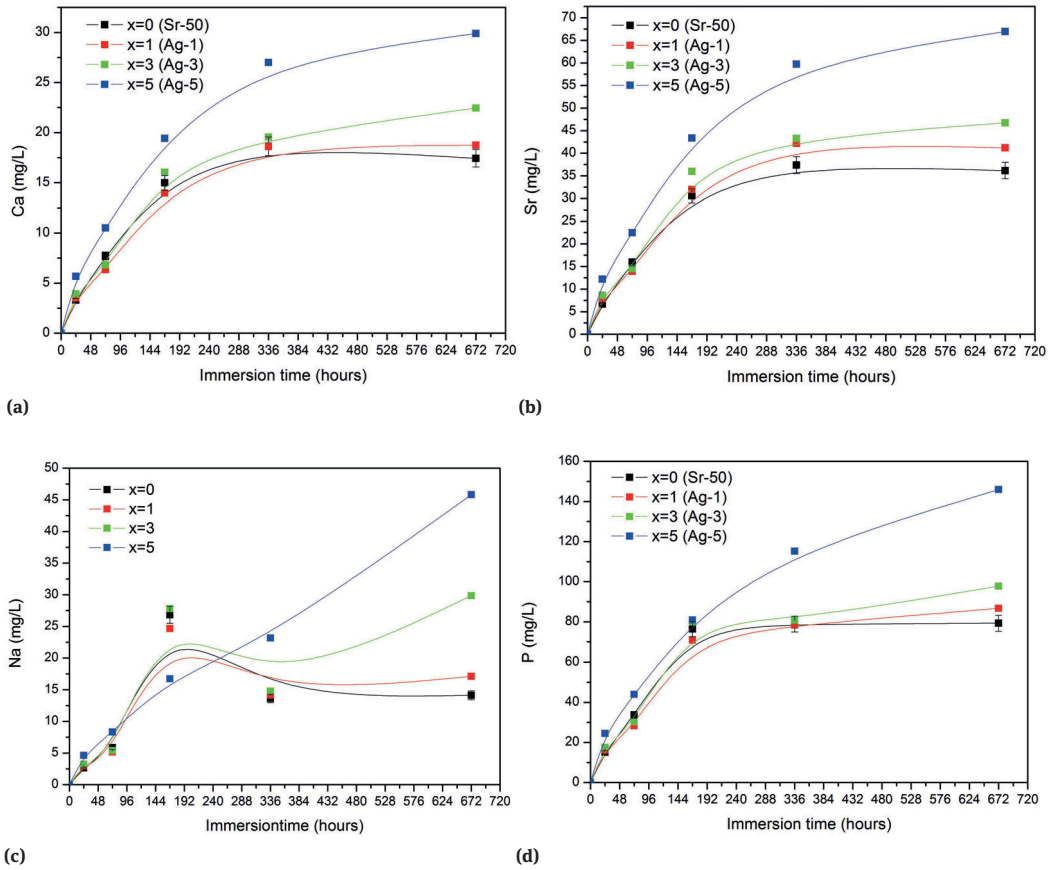

Figure 5: Ca a), Sr b), Na c) and P d) concentration in TRIS solution as a function of immersion time.

Comparison of the spectra for all glasses when immersed for 672 h is presented in Figure 6e. It is clearly seen that the rise of the peak at 1150 and the intensity of the new bands at 988 and 1030 cm^{-1} are higher with increasing Ag_2O.

The SEM images of the glasses with x = 0 after 672 h of immersion and of the glasses with x = 3 and 5 mol% after 336 h of immersion are presented in Figure 7a, 7b and 7c, respectively. At 168 h, no change in the glass surface composition could be evidenced by EDS analysis. After 672 h of immersion, no layer could be seen (or only sparsely) at the surface of the glass with x = 0, while a reactive layer could be seen at the surface of the Ag-containing glasses already after 336h of immersion. We noticed that its thickness grew thicker with increasing the immersion time. From SEM images the layer grew up to 5 µm for the glass with 5 mol% Ag_2O. EDS analysis revealed that this layer was rich in Ca and P and contained a significant amount of Sr. It appear clear that the layer thickness increases with increasing Ag_2O, whereas the layer composition was identical at the surface of all materials

4 Discussion

The aim of this research is to better understand the impact of Ag doping on the thermal, structural and dissolution of a phosphate bioactive glass.

Doping the glass Sr-50, which was found in the past to be a promising bioactive glass [11, 12], with Ag led to an increase in the density. This was expected as Ag has a larger mass than all the other elements present in the glass composition. However, the addition of Ag does not significantly change the molar volume indicating that the Ag acts

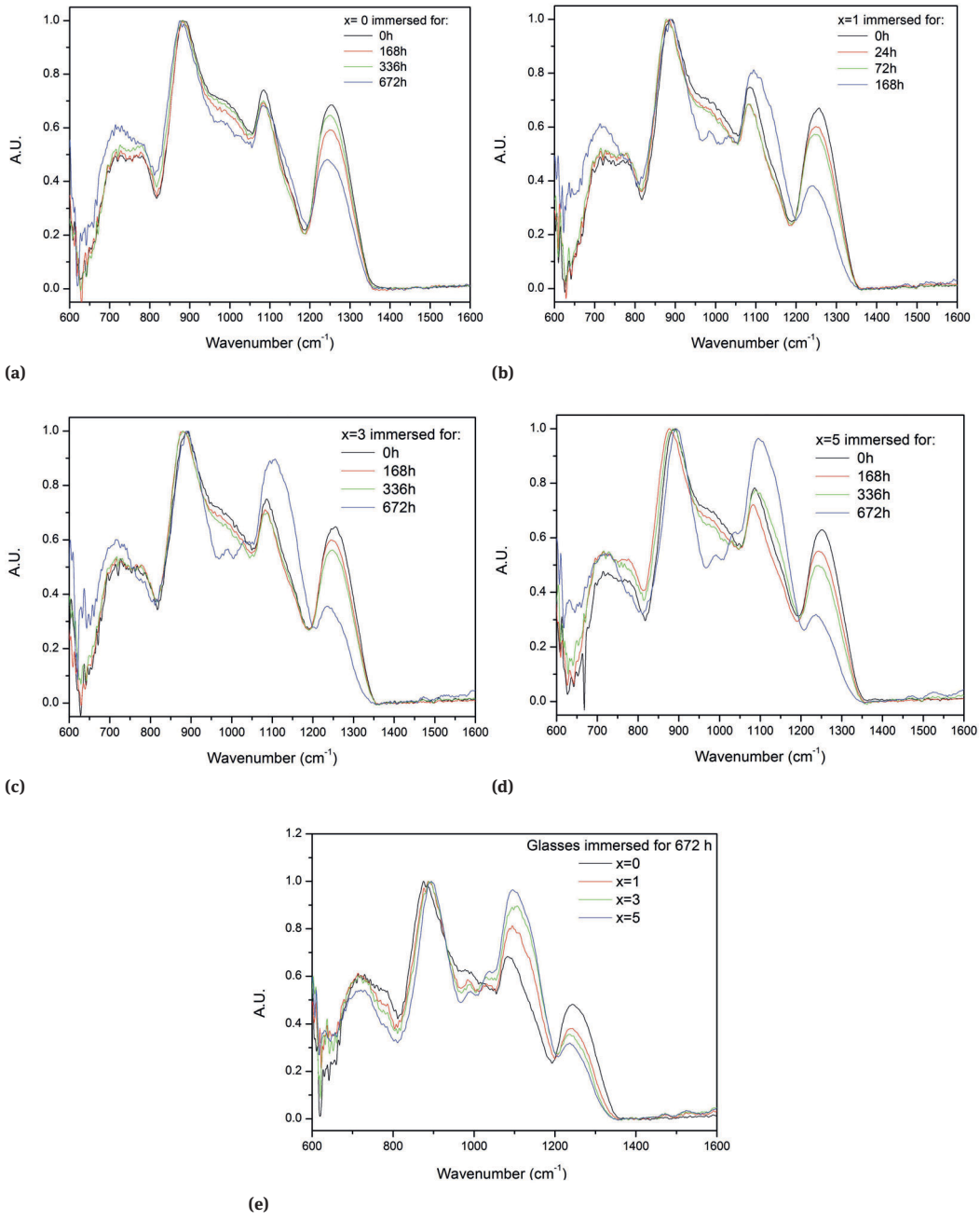

Figure 6: FTIR-ATR of the glass x = 0 a), x = 1 b), x = 3 c) and x = 5 d) as a function of immersion time and all glasses immersed for 672 h in TRIS e)

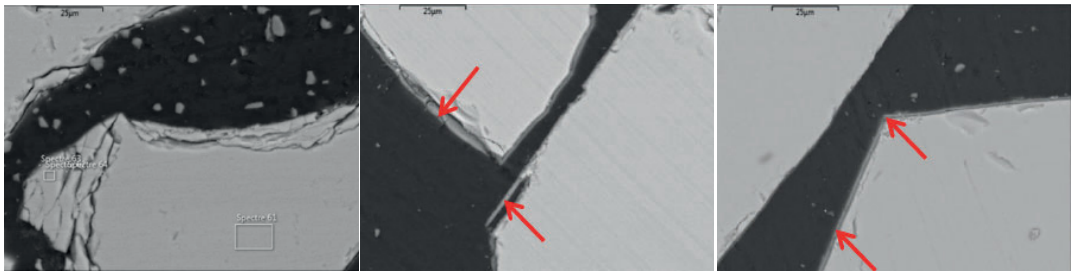

(a) (b) (c)

Figure 7: SEM images of the glasses with x = 0 after 672 h of immersion a) and of the glasses with x = 3 b) and 5 c) after 336 h of immersion.

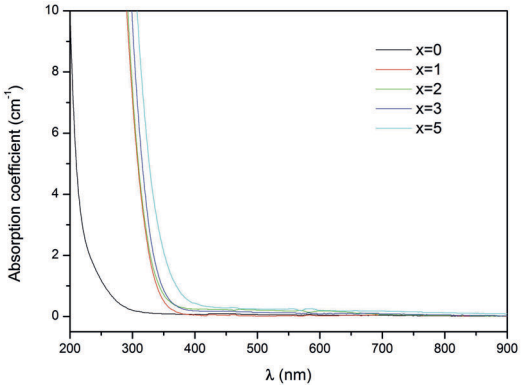

Figure 8: UV-Vis absorption spectra of the glasses of investigation.

as a monovalent cation in the phosphate vitreous network with a similar ionic radius and similar positions than the other modifiers in the network. However the redox activity of a glass melt is definitely a function of the composition and, at first sight, it is generally found that increasing basicity favors the upper oxidation state for most redox couples [25]. Compared to silicon oxide, phosphorus pentoxide is characterized by a lower value of the optical basicity, 0.45 and 0.33, respectively [26]. As a result, phosphate glasses favor the lowest stable oxidation state, *i.e.* Ag^0. To avoid the presence of metallic silver droplets, the use of sodium sulfate as an oxidizing agent was necessary. The dissolution of the sulfate in the melt leads to the oxidation of the metallic silver according to the following chemical reactions:

$$SO_4^{2-} \rightleftharpoons O^{2-} + SO_2 + \frac{1}{2}O_2$$

$$2Ag + \frac{1}{2}O_2 \rightleftharpoons 2Ag^+ + O^{2-}$$

It results the chemical balance:

$$2Ag^0 + SO_4^{2-} \rightleftharpoons 2O^{2-} + 2Ag^+ + SO_2$$

Furthermore, to confirm that the use of Na_2SO_4 prevents formation of Ag nanoparticles, the UV-Vis spectra of the glasses were recorded and are presented in Figure 8. The absence of absorption band in the visible which could be a characteristic of the presence of Ag nanoparticles confirms that all the Ag is present as positively charged ions in the glasses under investigation. This is of particular interest since Ag^+ ions have been found to possess antimicrobial properties [19, 27].

The thermal properties of these glasses were recorded. With an increase in Ag_2O, the T_g decreases whereas T_x, T_p and ΔT show a maximum for the glasses with 2 and 3 mol% of Ag_2O. More interestingly the crystallization peak of the glass containing 1 mol% of Ag_2O was narrower than that of the other glasses (Fig. 2). This can be attributed to the change in crystallization mechanism of the glass induced by the occurring of a small amount of silver particle during the reheating of the glass. It is well known that Ag can be used in glass as nucleating agent [28]. It is also rather common to see Ag^0 formation upon heat treatment in glassy thin films or bulk [29, 30]. The decrease in T_g when Ag_2O increases may be explained by the lower cationic field strength value (Z/r^2) of silver (0.6) when compared to the others modifiers cations, namely sodium (1.06), strontium (1.56) and calcium (2.04), the coordination number being considered as 6 for the calculation.

Contrary to the glass transition temperature which is strongly dependent of the cationic strength, it has been demonstrated that the mechanical properties clearly depend on physical quantities related to the compactness or the energy of cohesion of the vitreous network, such as those defined in [31]. The steadiness of the molar volume, whatever the silver oxide content, leads to the same compactness and of the microhardness values. Regarding the

Table 3: FTIR-ATR and Raman bands attribution.

FTIR-ATR		
Wavenumber (cm^{-1})	Attribution	Reference
718–775	ν_s P-O-P in metaphosphate	[38]
880	ν_{as} P-O-P in Q^2	[33, 34]
980	ν_s PO_3^{2-} in Q^1	[34–36]
1085	ν_{as} PO_3^{2-} in Q^1. PO_2 in Q^2	[38]
1154	ν_s PO_2^- in Q^2	[34–36]
1260	ν_{as} PO_2^- in Q^2	[34–36]
Raman		
695	P-O-P in chains	[38–40]
1020	ν_sNBO in Q^1	[38–40]
1090	Terminal oxygen bond	[38–40]
1175	ν_s PO_2 chains	[38–40]
1250	ν_{as} PO_2 chains	[38–40]
1320	P=O	[38–40]

Young's modulus, its variation, as a function of the glass composition, can be estimated with a good approximation from the following relation:

$$E = 2 \sum_i x_i G_i \sum_i x_i C_i$$

where G_i and C_i are the dissociation energy per unit volume and the compacity factor of the oxyde i with the molar content x_i, respectively. Details for the calculation of these physical quantities are given in [31]. Using thermodynamic data from [32], the calculation gives almost 56 GPa for both the parent glass and the one with the highest silver oxide content. As a consequence, a small amount of Ag_2O doesn't modify the mechanical properties of the parent glass.

All the absorption bands in the FTIR-ATR spectra (Fig. 3a) can be attributed to the phosphate glass network. The main band at ~880 cm^{-1} is attributed to P-O-P asymmetric stretching of bridging oxygen in Q^2 units (ν_{as} P-O-P Q^2) [33–35]. The shoulder centered at ~980 cm^{-1} and the band peaking at 1085 cm^{-1} correspond to the symmetric and asymmetric stretching vibration of PO_3^{2-} in Q^1 units, respectively [34–36]. The band at 1085 cm^{-1} can be attributed to an overlap between PO_3 Q^1 terminal group and PO_2 Q^2 groups in metaphosphate [37]. The shoulder at 1154 cm^{-1} and the absorption band at 1260 cm^{-1} correspond to symmetric and asymmetric vibration of PO_2^- in Q^2 units, respectively [34–36]. The absorption 3 band located at 718 and 775 cm^{-1} are characteristic of P-O-P symmetric stretching vibration in metaphosphate structure [38]. Only little change could be seen in the FTIR-ATR spectra when Ag_2O increases. The decrease in the absorption band located at 1260 cm^{-1} indicates a decrease in the network connectivity and an increasing amount of Q^1 units. This is further confirmed from the analysis of the Raman spectra of the glasses (Fig. 3b). The band at around 695 cm^{-1} corresponds to symmetric vibration P-O-P in metaphosphate type chains, the band at 1020 cm^{-1} to symmetric stretch mode of NBO in Q^1 units, and the ones at 1175 cm^{-1} and 1250 cm^{-1} to, respectively, symmetric and antisymmetric vibrations of PO_2 also in phosphate chains [38–40]. The shoulder at ~1090 cm^{-1} corresponds to motion of terminal oxygen bond vibration in phosphate chains [41]. The shift of all the bands toward lower wavenumber indicates a weakening of the chemical bonds in the network when Ag_2O is added in the network, due to a network depolymerization. The increase in intensity of the bands at 695 and 1020 cm^{-1} along with the increase in intensity of the shoulder at 1090 cm^{-1} further confirm the increase in Q^1 units and the shortening of the phosphate chain. This change in the glass structure induced by an increase in Ag_2O is in agreement with the shift of the optical band gap toward higher wavelength when Ag_2O increase (Fig. 8). The increase in the intensity of the shoulder at 1090 cm^{-1} along with the shift of the optical band gap indicates an increasing number of non-bridging terminal oxygens [42]. This is expected as the overall phosphate content decreases at the expense of the glass modifier elements [43]. Furthermore the small shoulder at 1320 cm^{-1} related to P=O remains unchanged indicating that the amount of Q^3 is similar in all investigated samples. A summary of the band attribution can be found in Table 3.

Typically an increase in Q^1 units leads to an increase in the glass chemical durability [7, 44]. However, in the studied glasses this seems not to be the case. As shown in Fig. 4, it is clear that the decrease in the solution pH is steeper with an increase in the Ag content. Furthermore, the ICP-OES results show that with increasing the immersion time, the Ca, Na, Sr and P are being released in solution. The increased dissolution rate with increasing Ag content is clearly seen from the higher content of each element in the solution. Except for Na, all the curves present a parabolic shape. It seems that the element release follows a $t^{1/2}$ law which is typical for a diffusion controlled process. However, the parabolic shape of the ion release could also come from the saturation of the solution with those ions leading to the precipitation of a reactive layer. The final Na concentration appears to be high, compared to the amount of the other ions, if a congruent dissolution is assumed [7]. Typically Na is the first element to leach out in solution upon dissolution of phosphate glasses. Furthermore, no Na is usually found in the reactive layer precipi-

Table 4: $(M^{I,II}/P)_{layer}$ / $(M^{I,II}/P)_{core}$ values with the corresponding standard deviations.

	Na/P	Ca/P	Sr/P
Parent glass	1.00	1.00	1.00
x=2-2w	0.24	1.59	1.46
	(0.03)	(0.07)	(0.10)
x=5-2w	0.32	1.31	1.25
	(0.03)	(0.09)	(0.09)

tating at the surface of bioactive glasses [11]. The Ag content was not quantified by ICP as the noise to signal ratio was too high to draw any clear conclusion.

The FTIR-ATR spectrum of the glasses was recorded at each immersion time point. From Fig. 6a, it is clear that at 168 h of immersion, structural modification occurs at the surface of the glasses. All glasses present a disruption of the Q^2 units with a subsequent increase of the Q^1 units. This is attributed to the first phase of phosphate bioactive glass reaction in physiological medium [7, 11]. The shift to lower wavenumber of the bands attributed to Q^2 units also confirms a weakening of the bonds strength for these structural units. The phosphate chains breakage is found to proceed up to the longest immersion time. In a first time, as explained by Bunker *et al.*, it appears that the glass dissolution is controlled by the rate at which the water diffuses at the surface of the glass. Once a full phosphate chain is surrounded by OH group it is released in solution [7]. This explains that ICP results reveal a perfect match between the ions released in solution and the ion concentration of the parent glass (congruent dissolution). At longer immersion time P-O-P bond breakage occurs as seen by the change in Q^2 to Q^1 ratio in the FTIR-ATR spectra. However, while the glass with x=0 only show the disruption of the phosphate chains at the surface of the particles (Fig. 6a), the spectra of all Ag-containing glasses (Fig. 6b–6d) present a sharp increase in Q^1 units and appearance of new bands at 988 and 1030 cm^{-1}, after 673 h of immersion. The new bands have been attributed to the formation of a CaP layer at the surface of the glass particles [11]. As shown in Fig. 6e, with an increase in Ag_2O the signal related to the CaP layer becomes stronger, as evidenced by the increasing intensity of the peaks at 988 and 1030 cm^{-1}. This might be attributed to the faster dissolution rate with increasing Ag_2O, which leads to faster saturation of the solution toward the reactive layer formation. The layer forming at the surface was analyzed via EDS/SEM. While the layer could be sparsely seen at the surface of the undoped glass (x = 0) even after the longest immersion time, the glasses with x = 3 and 5 mol% showed clear sign of CaP precipitation (as shown by the arrow in Fig.7b and 7c) already happening after 332 h of immersion. As the dissolution rate increases with Ag_2O, the layer thickness of the reactive layer was found to be thicker for the glass with higher Ag content. The EDS analysis confirmed that the layer was enriched in Ca and Sr, while Na was preferentially released in the solution. This is illustrated by the different ratios between the $M^{I,II}/P$ values obtained for the layer divided by those obtained for the core of the glass particles. These ratios are summarized in Table 4.

Furthermore, when comparing the EDS composition of all reactive layers, at the surface of all investigated glasses, a typical layer composition could be expressed as follow: 59±3%P, 24±4%Ca, 15±3%Sr, 1±1%Na, 0±1%Ag. Even more the layer was found of be free of Na and Ag. In addition, the average value of the (Ca+Sr)/P ratio for the layer is 0.7±0.1 and is higher than those of the parent glass (0.4). Based on this ratio, as well as the position of the new absorption bands appearing in the FTIR-ATR spectra one can assume that the layer forming is a Sr-substituted calcium-phosphate chemically close to the dibasic calcium phosphate, as seen previously [11]. Moreover, the layer composition was found to be independent of the Ag concentration. This can further explain the higher final level of Na in solution compared to the other ions. Ag appears to behave similarly as Na, *i.e.* it is not incorporated in the reactive layer and thus Ag is expected to leach out at a similar rate than Na. Such layer was found to promote the adhesion and proliferation of human gingival fibroblasts [12]. Furthermore, the controlled release of Ag as monovalent ions may be of interest for its antimicrobial properties.

5 Conclusion

The addition of Ag_2O in a phosphate bioactive glass, with composition $0.5P_2O_5{\cdot}0.2CaO{\cdot}0.2SrO{\cdot}0.1Na_2O$, leads to a glass with shorter phosphate chains and higher number of terminal non bridging oxygen, as evidenced by the increase in Q^1 units and the shift of the optical band gap towards higher wavelength. Adding up to 3 mol% of Ag_2O was also found to increase the processing window. Despite the decrease in the chain length, the decrease in network connectivity as evidenced by a progressive decrease in T_g when Ag_2O increases, leads to a glass more prone to react in aqueous solution. The formation of a Sr-substituted calcium phosphate layer was found to occur sooner in the Ag-containing glass due to the increased dissolution rate. However the layer composition was found to be indepen-

dent of the Ag content. Finally the Ag-containing glasses were found to dissolve in a congruent manner. Such materials could be employed for processing of implants with high surface area to volume ratio, with subsequent antimicrobial properties.

Acknowledgement: The authors would like to acknowledge the Academy of Finland for the financial support of JM through the Academy Research Fellow and Initial Research Cost.

References

[1] L.L. Hench, R.J. Splinter, W.C. Allen, T.K. Greenlee, J Biomed Mater Res Symp, 334 (1971), 117–141
[2] O.H. Andersson, K. H. Karlsson, K. Kangasniemi, A. Yli-Urpo, Glastechnische Berichte 61(10) (1988), 300–305
[3] S. Fagerlund, J. Massera, M. Hupa, L. Hupa, J Eur Ceram Soc 32 11(8) (2012), 2731–2738
[4] E. Pirhonen E, H. Niiranen, T. Niemelä, M. Brink P. Törmälä, J Biomed Mater Res B Appl Biomater 77(2) (2006), 227–33
[5] D. Groh, F. Döhler, D.S. Brauer, Acta Biomat., 10(10) (2014), 4465–4473
[6] J. Massera, S. Fagerlund, L. Hupa, M. Hupa, Journal of the American Ceramic Society, 95 (2012), 607–613
[7] B.C. Bunker, G.W. Arnold, J.A. Wilder, J. Non Crys Solids 64 (3) (1984), 291–316
[8] J. Clement, J.M. Manero, J.A. Planell, J Mater Sci: Mater Med 10 (1999), 729-32.
[9] I. Ahmed, M. Lewis, I. Olsen, J.C. Knowles, Biomaterials 25 (2004), 501–507
[10] J. Massera, Y. Shpotyuk, F. Sabatier, T. Jouan, C. B. Plédel, C. Roiland, B. Bureau, L. Petit, N.G. Boetti, D. Milanese, L. Hupa, J Non Crys Sol 425 (2015), 52–60
[11] J. Massera, L. Petit, T. Cardinal, J. J. Videau, M. Hupa, L. Hupa, J Mater Sci: Mater Med (24) (2013), 1407–1416
[12] J. Massera, A. Kokkari, T. Narhi, L. Hupa, J Mater Sci: Mater Med 26 (2015), 196
[13] V. Salih, K. Franks, M. James, W. Hastings, C. Knowles, I. Olsen, J Mater Sci: Mater Med 11 (2010) 615-620
[14] I Ahmed, D. Ready, M. Wilson, J.C. Knowles, Journal of Biomedical Research Part A, 79 (2006) 618–626
[15] C. Wu, Y. Zhou, M. Xu, P. Han, L. Chen, J. Chang, Y. Xiao, Biomaterials, 34 (2013) 422–433
[16] G. Poongodi, P. Anandan, R.M. Kumar, R. Jayavel, Spectrochimica Acta Part A: molecular and Biomolecular Spectroscopy, 148 (2015) 237–243.
[17] A.P. Adams, E.M. Santschi, M.A. Mellencamp, Vet. Surg. 28 (1999), 219–225
[18] H.S. Carr, T. Wlodkowski, H.S. Rosankranz: Silver sulfadiazine Che-mother 4 (1973), 585–587
[19] S. P. Valappil, D. M. Pickup, D. L. Carroll, C. K. Hope, J. Pratten, R. J. Newport, M. E. Smith, M. Wilson, J. C. Knowles, Antimicr Ag and Chemo 51 (12) (2007), 4453–4461.
[20] I. Ahmed, E.A. Abou-Neel, S.P. Valappil, S.N. Nazhat, D.M. Pickup, D. Carta, D.L. Caroll, R.J. Newport, M.E. Smith, J.C. Knowles, Journal of Materials Science, 42 (2007) 9827–9835
[21] A.A. Ahmed, A.A. Ali, Doaa A.R. Mahmoud, A.M. El-Fiqi, Solid State Sciences, 13 (2011) 981–992
[22] G. V. Blessing, ASTM STP 1045, Philadelphia, PA, USA (1990) 1045
[23] S. Chenu, J. Rocherullé, R. Lebullenger, O. Merdrignac, F. Cheviré, F. Tessier, H. Oudadesse, Journal of Non-Crystalline Solids 356 (2010) 87–92
[24] S. Chenu, R. Lebullenger, J. Rocherullé, Journal of Material Science, 45 (2010) 6505–6510
[25] C. Petitjean, P.J. Panteix, C. Rapin, M. Vilasi, R. Podor, Procedia Materials Science, 7 (2014) 101–110
[26] J.A. Duffy, J Non-Cry Sol 196 (1996), 145-50
[27] T. N. Kim, Q.L. Feng, J.O. Kim, J. Wu, H. Wang, G.C. Chen, F.Z. Cui, J Mater Sci Mater Med. 9(3): (1998) 129–134
[28] S.D. Stookey, Ind. Eng. Chem, 51 (1959), 805–808
[29] A.S. Kuznetsov, Ngo T. Cuong, V.K. Tikhomirov, M. Jivanescu, A. Stesmans, L.F. Chibotaru, J.J. Velázquez, V.D. Rodríguez, D. Kirilenko, G. Van Tendeloo, V.V. Moshchalkov, Opt Mat, 34 (2012), 616–621
[30] J. Massera, A. Martin, J. Choi, T. Anderson, L. Petit, M. Richardson, Y. Obeng, K. Richardson, J Phy Chem Sol, 71 (2010), 1634–1638
[31] J. Rocherullé, C. Ecolivet, M.Poulain, P. Verdier, Y. Laurent, J. of Non-Cryst. Solids 108 (1989) 187–193
[32] D.D. Wagman, W.H. Evans, V.B. Parker, I. Halow, R.H. Schumm, Selected values of chemical thermodynamic properties, NBS technical notes, 270, 3–9, 1981
[33] P.Y. Shih, H.M. Shiu, Mater Chem Phy 106: (2007), 222–226.
[34] H. GaO, T. Tan, D. Wang, J of Contr Rel 96: (2004), 21–28.
[35] Y.M. Moustafa, K. El-Egili, J Non-Crys Sol, 240: (1998), 144–153
[36] E.A. Abou Neel, W. Chrzanowski, D.M. Pickup, L.A. O'Deel, N.J. Mordan, R.J. Newport, M.E. Smith, J.C. Knowles, J Roy Soc Inter, 6: (2009), 435–446.
[37] D. Ilieva, B. Jivov, G. Bogachev, C. Petkov, I. Penkov, Y. Dimitriev, J Non-Crys Sol, 283 (2001), 195–202.
[38] S. Lee, A. Obata, T. Kasuga, J Cer Soc Jap, 117 (2009), 935–938
[39] M.A. Karakassides, A. Saranti, I. Koutselas, J Non-Crys Sol 347 (2004), 69–79.
[40] A.G. Kalampounias, J Phy Chem Sol, 73 (2012), 148–153.
[41] R. C. Lucacel, A.O. Hulpus, V. Simon, I. Ardelean, J Non-Crys Sol,355: (2009), 425–429.
[42] J. Massera, M. Vassallo-Breillot, B. Törngren, B. Glorieux, L. Hupa, J Non-Crys Sol, 402 (2014), 28–35
[43] R.K. Brow, Journal of Non Crystalline Solids, 263–264 (2000), 1–28
[44] J. Massera, K. Bourhis, L. Petit, T. Cardinal, L. Hupa, M. Hupa, Journal of Physics and Chemistry of Solids, 74 (2013) 121–127.

PUBLICATION II

Thermal, structural and in vitro dissolution of antimicrobial copper-doped and slow resorbable iron-doped phosphate glasses

A. Mishra, L. Petit, M. Pihl, M. Andersson, T. Salminen, J. Rocherullé, J. Massera

Journal of Material Science 52 (15) (2017) 8957–8972

https://doi.org/10.1007/s10853-017-0805-3

PUBLICATION III

In-vitro dissolution characteristics and human adipose stem cell response to novel borophosphate glasses

A. Mishra, M. Ojansivu, R. Autio, S. Vanhatupa, S. Miettinen, J. Massera

Journal of Biomedical Materials Research Part A 107 (9) (2019) 2099-2114

https://doi.org/10.1002/jbm.a.36722

Received: 17 January 2019 | Revised: 3 May 2019 | Accepted: 7 May 2019

DOI: 10.1002/jbm.a.36722

ORIGINAL ARTICLE

In-vitro dissolution characteristics and human adipose stem cell response to novel borophosphate glasses

Ayush Mishra[1] | Miina Ojansivu[2] | Reija Autio[3] | Sari Vanhatupa[2] | Susanna Miettinen[2,4] | Jonathan Massera[1]

[1]Laboratory of Biomaterials and Tissue Engineering, Faculty of Medicine and Health Technology and BioMediTech Institute, Tampere University, Tampere, Finland

[2]Adult Stem Cell Group, Faculty of Medicine and Health Technology and BioMediTech, Tampere University, Finland

[3]Faculty of Social Sciences and BioMediTech, Tampere University, Tampere, Finland

[4]Research, Development and Innovation Centre, Tampere University Hospital, Tampere, Finland

Correspondence
Ayush Mishra, Laboratory of Biomaterials and Tissue Engineering, Faculty of Medicine and Health Technology and BioMediTech Institute, Tampere University, Tampere, Finland.
Email: ayush.mishra@tuni.fi

Funding information
Buisness Finland; Competitive State Research Financing of the Expert Responsibility area of Tampere University Hospital; Suomen Akatemia; Academy of Finland

Abstract

The main drawbacks of traditional silicate bioactive glasses are their narrow hot forming domain and noncongruent dissolution. In this article, we report on new borophosphate glasses [$xM_nO_m + (100 - x)$ $(47.5P_2O_5 + 2.5B_2O_3 + 10Na_2O + 20CaO + 20SrO)$], M_nO_m being CuO, Ag_2O, and CeO_2, having high thermal processability, hence suitable for fiber drawing and sintering into scaffolds. Furthermore, the glasses dissolve congruently in simulated body fluid (SBF) and TRIS buffer solution, eventually leading to the precipitation of a reactive layer. Human adipose stem cells (hASC) were cultured in media enriched with glass extract at different dilutions, to investigate the optimal ion concentration for cell survival. Cells grew in all the extracts, except in the undiluted Cu-doped glass extract. At dilution 1:10, the lactate dehydrogenase (LDH) activity and cell proliferation were comparable to the control, while at 1:100, the cells proliferated faster than the control. Thus, the reference (undoped), Ag and Ce-doped glasses were found to be suitable for cell viability and proliferation. Cytotoxicity assessments using the LDH assay indeed revealed the high cytotoxicity of the Cu extract. This raises questions about the use of Cu in bioactive glasses and its optimal concentration as a dopant.

KEYWORDS
bioactive glass, borophosphate glass, cell proliferation, cytotoxicity, in-vitro dissolution

1 | INTRODUCTION

Due to the aging of our society, there is a growing need for novel bioactive materials that can be used as implants in the form of powders, scaffolds, fibers, and so on. Since the discovery of Bioglass® by Hench, Splinter, Allen, and Greenlee (1971), bioactive glasses have emerged as a promising candidate for biomedical applications. Understandably, most of the research on bioactive glasses since then has focused on silicate glasses, owing to their ability to promote cell growth, proliferation, and differentiation (Ojansivu et al., 2015; Ojansivu et al., 2018). Part of silicate glass bioactivity is assigned to their ability to precipitate a calcium phosphate (hydroxyapatite) reactive layer. This layer has the same composition and structure as the mineral phase of the bone, thereby enabling it to bond with the tissue. However, while the glass was expected to degrade over time and eventually disappear from the site of implantation, it was reported that the commercial bioactive silicate glass, S53P4, did not degrade completely in-vivo even 14 years post-surgery (Lindfors, Koski, Heikkilä, Mattila, & Aho, 2010). This phenomenon, coupled with the narrow thermal processing window of the FDA approved silicate glasses (Fagerlund, Massera, Hupa, & Hupa, 2012; Massera, Hupa, & Hupa, 2012), forced the researchers to look at alternatives. Phosphate glasses (PGs) are completely biodegradable and have a higher resistance to crystallization (Massera, Mayran, Rocherullé, & Hupa, 2015). Additionally, they have a congruent dissolution, and the degradation rate can be adjusted by varying the composition (Bunker, Arnold, & Wilder, 1984). PGs are known to have a good solubility toward metal ions enabling to dope the glass composition with ions having therapeutic relevance (Abou Neel, Ahmed, Pratten, Nazhat, &

Knowles, 2005; Mishra et al., 2017; Mishra, Rocherulle, & Massera, 2016; Mulligan, Wilson, & Knowles, 2003a; Mulligan, Wilson, & Knowles, 2003b). The sustained and congruent degradation of PGs enables to deliver those therapeutic metal ions in a controlled manner (Abou Neel et al., 2005). Consequently, the potential of Cu and Ag doped PGs, for example, has been explored extensively in view of their antimicrobial properties (Abou Neel et al., 2005; Ahmed, Ali, Mahmoud, & El-Fiqi, 2011; Ahmed, Ready, Wilson, & Knowles, 2006; Mulligan et al., 2003a; Mulligan et al., 2003b; Wu et al., 2013).

In light of the above facts and observations, new PGs within the composition $50P_2O_5 + 10Na_2O + (40 - x)CaO + xSrO$ (mol%) were investigated (Massera et al., 2013), and were found to support the attachment and proliferation of human gingival fibroblasts, except for the glass with $x = 0$, which possessed the fastest dissolution rate of all the glasses of investigation. The glass with $x = 20$ {$50P_2O_5 + 10Na_2O + 20CaO + 20SrO$ (mol%)}, labelled Sr50, had the slowest dissolution rate, and its dissolution products promoted proliferation of human gingival fibroblasts (Massera, Kokkari, Närhi, & Hupa, 2015). However, when compared with known silicate bioactive glasses, their fast initial degradation rate and late reactive layer precipitation led to poor cell attachment for the initial 1–3 days of culture. PGs with a fast degradation rate have been shown to have poor attachment and proliferation of human osteoblasts by Salih et al. (2000). Based on previous results, the glass Sr50 was further doped with Ag and Cu, and found to be promising in terms of thermal, dissolution, and antimicrobial properties (Mishra et al., 2016; Mishra et al., 2017). The doped glasses possessed a wide thermal processing window, a steady ion release in TRIS buffer solution, and effectively eradicated *Staphylococcus epidermidis* (*S. epidermis*). However, the dissolution rate was further increased by the presence of these metallic ions. When doped with Ce, the glasses were found to have a wider thermal processing window, a steady ion release, albeit a slower degradation rate than Sr50 (Massera, Vassallo-Breillot, Törngren, Glorieux, & Hupa, 2014). The fast degradation of the metal-doped PGs led to human adipose stem cell death in a preliminary cell culture experiment.

In response to the high degradation rate of the Ag and Cu doped Sr50 glasses, a new glass system with the composition $xM_nO_m + (100 - x)(47.5P_2O_5 + 2.5B_2O_3 + 10Na_2O + 20CaO + 20SrO)$ where $x = 1$ for Ag_2O, and 2 for CeO_2 and CuO, was developed in this study. This new glass system is derived from the Sr50 glass, where 2.5 mol% P_2O_5 is replaced with B_2O_3 to stabilize the glass network. Hence, the new glasses are expected to have a reduced degradation rate, while maintaining a high thermal processing window (Bingham, Hand, & Forder, 2006; Harada, In, Takebe, & Morinaga, 2004; Karabulut, Yuce, Bozdogan, Ertap, & Mammadov, 2011; Koudelka & Mošner, 2001; Massera et al., 2011). In this article, we investigate these glasses in terms of their thermal properties and in-vitro dissolution in TRIS and simulated body fluid (SBF). The Ca, Sr, and P-rich surface layer deposited at the surface of the glasses after immersion in TRIS buffer solution and SBF was evidenced with scanning electron microscopy-energy dispersive X-ray spectroscopy (SEM-EDS). Human adipose stem cells (hASC) were cultured up to 14 days in glass extracts obtained by enriching the culture media with the glass's dissolution by-products. The cytotoxicity of the extracts on hASC was assessed using quantitative lactate dehydrogenase (LDH) measurement. Live/dead staining and CyQUANT were performed at 3, 7, and 14 days to evaluate the influence of undiluted, 1:10 and 1:100 diluted extracts on cell viability and proliferation.

2 | MATERIALS AND METHODS

2.1 | Glass melting

Glasses within the composition $xM_nO_m + (100 - x)$ $(47.5P_2O_5 + 2.5B_2O_3 + 10Na_2O + 20CaO + 20SrO)$ (mol%) with $x = 0$ for Sr47.5, 1 for $M_nO_m = Ag_2SO_4$, and 2 for CuO and CeO_2 were prepared using a standard melting process in a silica crucible in air. x was chosen such that the number of metallic ions was constant across all doped borophosphate glasses.

To prepare the glass, a batch consisting of $Ca(PO_3)_2$, $Sr(PO_3)_2$, $Na(PO_3)$, $CaCO_3$, $SrCO_3$, H_3BO_3, and Ag_2SO_4/CuO/CeO_2 (depending on the composition to be melted) was prepared. All the chemicals used were analytical grade. Ag_2SO_4 was used in order to prevent the reduction of Ag ions to Ag^0. $Ca(PO_3)_2$ and $Sr(PO_3)_2$ were prepared beforehand using $CaCO_3$, $SrCO_3$, and $NH_4H_2PO_4$. The carbonates were mixed with $NH_4H_2PO_4$ in separate batches and heated to 250°C to remove the NH_3 and H_2O, then to 650 and 850°C to remove the CO_2. The heating rate was kept constant at 1°C/min throughout the process, and the batch was kept for 12 hr at each temperature step. The glass batches were heated at 10°C/min to 1,100°C and kept there for 30 min. The molten batch was cast into a brass mold and annealed at T_g −40°C for 5 hr to relieve the internal stresses. Post melting, EDS analysis of the glasses was performed. No Si from the silica crucible or S from the Ag_2SO_4 were evidenced in the glasses, within the accuracy of the measurement (1.5 mol%).

2.2 | Thermal properties

DTA thermograms of all the glasses were obtained using a SDTA, Netzsch Jupiter F1 (Selb, Germany). The glass powders were placed in Pt crucibles under 50 mL/min N_2 flow and heated at 10°C/min. The T_g (glass transition temperature) was determined as the inflection point of the first second order deviation in heat flow. The T_x (onset of crystallization temperature) and the T_p (crystallization temperature) were ascertained as the beginning and the maximum, respectively, of the exothermic peak. The accuracy of the temperatures obtained was estimated at ±3°C. The thermal processability window was calculated as $\Delta T = T_x - T_g$, as done earlier in (Ahmed, Shaharuddin, Sharmin, Furniss, & Rudd, 2015; Brauer, Brückner, Tylkowski, & Hupa, 2016; Fagerlund & Hupa, 2016; Massera, Ahmed, Petit, Aallos, & Hupa, 2014; Massera et al., 2010).

2.3 | In-vitro dissolution

Powders with particle size 125–250 μm were obtained by crushing and sieving. 75 mg of the glass powders were immersed in 50 mL of

TRIS buffer solution or SBF, and placed in an incubating shaker HT Infors Multitron (Bottmingen, Germany) at 37°C, 100 rpm to obtain a laminar flow, as proposed earlier (Maçon et al., 2015). In this study, the protocol used by Maçon et al. (2015) was followed, thereby the mass of glass to volume ratio was maintained constant. While it is known that the surface area to volume of solution ratio is more critical when studying glass dissolution, as in (Massera & Hupa, 2014), here the mass was maintained constant pertaining to the low variation in glass density with adding the dopant. The density of the glasses measured by the Archimedes principle were found to be 2.78 ± 0.02 g/cm^3 (Sr47.5), and 2.96 ± 0.02 g/cm^3 (for all the other glasses). The immersion tests were conducted for up to 42 days in TRIS and 21 days in SBF. The SBF was prepared using the protocol described by Kokubo, Kushitani, Sakka, Kitsugi, and Yamamuro (1990), with a pH adjusted to 7.40 at 37°C. The ion concentration of the SBF can be found in Table 1. The pH of the immersion media with and without ("blank") glass powders was measured using a pH ion analyzer Mettler Toledo SevenMultimeter (Columbus, OH) with an accuracy of ±0.02. The pH of the blanks was not found to change throughout the duration of the study, indicating that the immersion solution was stable across the length of the study. All samples were measured in triplicates and pH values are presented as average of the three values. If the deviation between the values was <0.02, then the accuracy of the measurement of the pH meter was used. If the deviation was >0.02 then the deviation between the triplicates was used.

Post immersion, 1 mL of the immersion media were recovered, and diluted with distilled water containing 10% 1 M HNO_3 by volume and stored at +4°C. These solutions were then analyzed with inductively-coupled plasma−−optical emission spectrometer (Agilent Technologies 5110 inductively coupled plasma-optical emission spectrometer (ICP-OES), Santa Clara, CA) to obtain the concentrations of Ca, Sr, P, Na, Ag, Cu, and Ce within the immersion solution. From the measured ion concentrations, the amount (in %) of each element dissolved from the glass was calculated. The accuracy of the measurement was estimated at ±5% of the ICP-OES values, except when the deviation between the triplicates was greater than 5%.

After recovering the media, the solution containing particles was filtered using filter paper with a pore size <5 μm. The particles were then washed with acetone, allowed to dry for 30 min in air, and then stored for further analysis in a desiccator.

TABLE 1 Ion concentrations in simulated body fluid (SBF; Kokubo et al., 1990)

Ion	Concentration in SBF (mM)
Na^+	142.0
K^+	5.0
$Mg2^+$	1.5
Ca^{2+}	2.5
Cl^-	148.8
HCO_3^-	4.2
HPO_4^{2-}	1.0
SO_4^{2-}	0.5

2.4 | Structural properties

The glass particles recovered post immersion were analyzed with a PerkinElmer Spectrum One FTIR Spectrophotometer (Waltham, MA) in attenuated total reflectance (ATR) mode. The IR spectra in the range of 650–1800 cm^{-1} were obtained and corrected for Fresnel losses. All the spectra were normalized to the band having maximum intensity. All the presented spectra have been obtained as an average of 8 scans and have a resolution of 1 cm^{-1}.

2.5 | SEM-EDS

SEM/EDXA (Leo 1530 Gemini from Zeiss, Oberkochen, Germany and EDXA from Vantage by Thermo Electron Corporation, Waltham, MA) was used to confirm the presence/absence of any surface layer precipitated on the glass particles due to immersion in SBF, and to analyze the composition of the layer as well as the bulk of the particle. The glass particles collected postimmersion were embedded in resin and polished to reveal the particles cross-section. The accuracy of the elemental analysis is ±1.5 mol%, based on the measurement of five areas in the samples (Table 2). The glass composition, postprocessing, was also checked with regards to the nominal composition. The B content within the glass was not quantified by EDS due to the system limitation. Therefore, the elemental composition obtained by EDS was compared to the nominal glass compositions as if B was not present. Sr content seemed to be slightly lower and P slightly higher than the expected content, most likely due to a Sr deficient $Sr(PO3)_2$. This was already reported in (Massera et al., 2013). Despite the use of silica crucible, no Si was found in the EDS analysis of the investigated glasses within the accuracy of the measurement.

2.6 | Preparation of PG extracts

Glass powders with size 500–1,000 μm were obtained by crushing and sieving, and were used to prepare the extracts. Disinfection of the powders was carried out by first washing with deionized water, then twice in 70% ethanol for 10 min, and subsequent drying for 2 hr at room temperature. The powders were then immersed for 24 hr at 37°C in the extraction medium prepared from Dulbecco's Modified Eagle Medium/Ham's Nutrient Mixture F-12 (DMEM/F-12 1:1; Life Technologies, Gibco, Carlsbad, CA), which was supplemented with 1% antibiotics (100 U/mL penicillin and 0.1 mg/mL streptomycin; Lonza, BioWhittaker, Verviers, Belgium) and 1% L-glutamine (GlutaMAX I; Life Technologies, Gibco). The extraction was conducted in the cell culture incubator at +37°C. The ratio of granules to the extraction medium was kept at 87.5 mg/mL for all compositions as reported in (Ojansivu et al., 2015). The extraction media was recovered via sterile filtering (0.45 μm), and human serum (Biowest, Nuaillé, France) was added to a concentration of 5%. This mixture containing glass ions released from the powders is referred to as Basic Medium (BM) extract, and was stored at +4°C. The control was prepared using the same recipe as above, but without immersing the glass particles, and is called BM. Fresh extracts were prepared every 2 weeks, and no precipitation

TABLE 2 Comparison of the surface layer composition with that of the bulk obtained by EDX analysis (all indicated values are in mol%)

After immersion in TRIS for 42 days							
	CaO (%)	SrO (%)	P_2O_5 (%)	Na_2O (%)	CuO (%)	CeO_2 (%)	Ag_2O (%)
Sr47.5							
Surface	28.8	22.6	45.0	3.6	-	-	-
Bulk	(21.0)	(17.2)	(51.3)	(10.5)	-	-	-
Cu-2							
Surface	26.8	20.4	47.0	5.2	0.6	-	-
Bulk	(21.9)	(16.6)	(52.1)	(9.4)	(0)	-	-
Ce-2							
Surface	27.1 ± 2.1	25.0	40.6 ± 1.6	1.2	-	6.0	-
Bulk	(20.6)	(16.8)	(50.0)	(10.8)	-	(1.8)	-
Ag-1							
Surface	23.7	18.9	48.9	7.7	-	-	0.8
Bulk	(21.9)	(17.7)	(49.7)	(9.9)	-	-	(0.8)

After immersion in SBF for 21 days						
	CaO (%)	SrO (%)	P_2O_5 (%)	Na_2O (%)	CuO (%)	MgO (%)
Sr47.5						
Surface	39.6 ± 1.8	9.7	42.0	4.2	-	4.5
Bulk	(22.4)	(17.0)	(50.0)	(10.6)	-	0
Cu-2						
Surface	45.2 ± 6.5	6.4 ± 3.4	39.2 ± 3.1	3.1	0.5	5.6 ± 1.6
Bulk	(18.8)	(17.9)	(50.4)	(10.9)	(1.9)	0

was observed during the course of the cell-culture experiments. Diluted extracts were prepared by mixing 1 part glass extract with 9 parts BM and 99 parts BM, for 1:10 and 1:100 diluted extracts, respectively.

2.7 | Adipose stem cell isolation, expansion, and culture

The study was carried out in accordance with the Ethics Committee of the Pirkanmaa Hospital District, Tampere, Finland (R15161). The hASC were isolated from subcutaneous white abdominal adipose tissue samples with a written informed consent of the donors. The donors were two women, aged 28 and 62 years.

The hASC were isolated using the protocol described in (Tirkkonen et al., 2012; Zuk et al., 2001). The hASC were then maintained in T75 Polystyrene flasks (Nunc, Roskilde, Denmark) in BM. After primary cell culture the surface marker expression of hASC was analyzed by flow cytometry (fluorescence-activated cell sorting; FACS, FACSAria®; BD Biosciences, Erembodegem, Belgium; Lindroos et al., 2009).The hASC used in this study, had a strong expression of CD73, CD90, and CD105, and negative or very low (<7%) expression of CD3, CD11a, CD14, CD19, CD34, CD45, CD54, CD80, CD86, and HLA-DR. In addition, the cells used were in passage 1 (i.e., were subcultured only once after the isolation from adipose tissue).

The cell viability and proliferation analyses were conducted in 24-well plates (Nunc) with plating density ~4,200 cells/cm^2 and in 48-well plates (Nunc) with plating density ~8,400 cells/cm^2, respectively. The media was changed to the extract media 24 hr after the plating and this was considered as the Day 0. The assay time points refer to the corresponding time after Day 0. Fresh extract media was given to the cells twice a week, and the old media was collected and frozen for LDH analysis. Control samples were grown in BM.

The cell culture for both the donors was done separately. All the analysis presented in this study, that is, Live/Dead, CyQUANT, and LDH were performed for both the donors at the same respective time points. As the cells from both the donors behaved similarly with respect to time in culture and across the various glass compositions, the CyQUANT and LDH results were combined.

2.8 | Cell viability

The cell viability was assessed qualitatively at Day 3, 7, and 14 (referred to as D-3, 7, 14, respectively) using live/dead staining (Invitrogen, Life Technologies), as described in Tirkkonen et al. (2012). The cells were incubated in a working solution containing 0.25 μM EthD-1 (staining dead cells red) and 0.5 μM Calcien-AM (staining live cells green) for 30 min. The cells were imaged immediately afterward, using a fluorescence microscope (IX51, Olympus, Tokyo, Japan) equipped with a fluorescence unit and a camera DP30BMW.

2.9 | Cell proliferation

Cell proliferation was determined at D-3, 7, and 14 by analyzing the DNA amount using CyQUANT Cell Proliferation Assay Kit (Invitrogen, Life Technologies), by following the manufacturers' protocol. At the

chosen time points, the cells were lysed with 0.1% Triton X-100 lysis buffer (Sigma-Aldrich) and then frozen (−70°C) to be analyzed at a later date. On the day of analysis, the plates were thawed at room temperature. Three parallel 20 μL samples of each lysate were pipetted to a 96 well plate (Nunc), and 180 μL of working solution prepared from CyQUANT GR dye and cell lysis buffer was added to each parallel. Victor 1420 Multilabel counter (Wallac, Turku, Finland) was used to measure the fluorescence at 480/520 nm.

2.10 | Cytotoxicity assessment

Lactate dehydrogenase (LDH) Assay Kit (Calorimetric) from Abcam (Cambridge, UK) was used to evaluate the cytotoxicity of the glass extracts at D-3, 7, and 14, using manufacturer's instructions. 20 μL of the previously collected cell media was pipetted in duplicates, supplemented with 30 μL/well of LDH assay buffer. Fifty micro liter per well of working solution was then added immediately prior to the analysis, and the absorbance at 450 nm at 20 min was measured after adding the working solution. All the values were normalized to the number of cells (obtained from CyQUANT measurements).

2.11 | Statistical analyses

SPSS Statistics version 25 (IBM, Armonk, NY) was used to perform statistical analyses. The CyQUANT and LDH results are presented as mean and standard deviation (SD). The number of biological replicates was $n = 6$ (3 per cell line) for CyQUANT and $n = 4$ (2 per cell line) for LDH, with three measurements done per condition for each analysis. The significance of the impact of diluted and undiluted glass extracts was assessed with Mann–Whitney test. The Mann–Whitney test is a nonparametric test which evaluates the difference between non-normally distributed data samples. Furthermore, to control the familywise error-rate, Bonferroni corrections were made based on the number of meaningful comparisons. For both the CyQUANT and LDH analyses, the number of meaningful comparisons was 39. The results were considered to be statistically different when the adjusted p-value after Bonferroni corrections was <0.05.

3 | RESULTS

In this study, the in-vitro dissolution characteristics of Cu, Ag, and Ce doped borophosphate glasses were obtained. Their thermal processability was also assessed as these glasses are intended to be used as fibers and/or scaffolds for biomedical applications. The biological response of hASC toward the extract obtained from these glasses was examined.

Post processing, a visual inspection of the glasses revealed that the Ag doped glass was transparent, while the Cu doped glass was blue and the Ce doped glass yellow. UV-Vis spectroscopy (not shown here) confirmed the absence of an absorption band for the Ag doped glass indicating that no or little Ag^0 formed during the processing of the glass, as in (Mishra et al., 2016). The UV-Vis spectra of the Cu doped glass revealed the presence of a broad absorption band at 850 nm correlated to Cu^{2+} ions as discussed in (Bae & Weinberg, 1994; Mishra et al., 2017). While the UV-Vis spectra of the Ce doped glass does not exhibit any absorption band, a strong shift of the absorption band gap, to higher wavelength was noticed, pertaining to the presence of Ce^{4+} ions leading to the yellow coloration as discussed in Blinkova, Vakhidov, Islamov, Nuritdinov, and Khaidarova (1994); Massera, Vassallo-Breillot, et al. (2014).

Their thermal properties are reported in Table 3. While no change in the glass transition temperature was recorded for the Ag and Cu doped glasses, Ce doping led to a slight increase in T_g. Furthermore, while the onset of crystallization (T_x) and crystallization peak (T_p) remained unchanged when doping the glass with Ag, doping with Ce and Cu led to an increase in both characteristic temperatures. All the glasses present a thermal processing window ($\Delta T = T_x - T_g$), $\Delta T > 100$°C. The DTA thermograms are presented as supplementary information Figure S1.

FTIR-ATR was performed on the glasses to evaluate the changes in the structure due to doping. Figure 1 exhibits the IR spectra of the

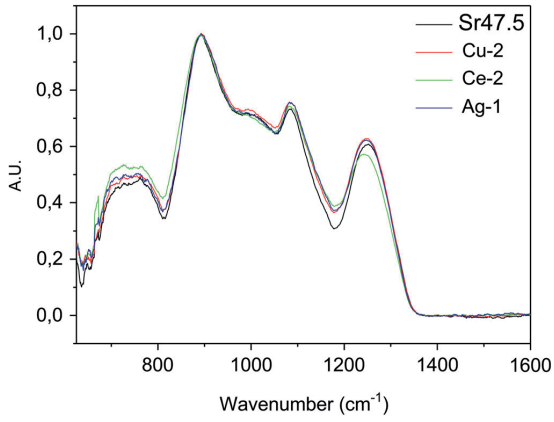

FIGURE 1 FTIR-ATR spectra of the glasses under investigation before immersion

TABLE 3 Thermal properties of the investigated glasses

Glass	Glass transition temperature (T_g) (±3°C)	Onset of crystallization (T_x) (±3°C)	Crystallization temperature (T_c) (±3°C)	Thermal processing window ($\Delta T = T_x - T_p$) (±6°C)
Sr47.5	450°C	616°C	660°C	166°C
Cu-2	448°C	630°C	671°C	182°C
Ce-2	463°C	627°C	665°C	163°C
Ag-1	452°C	617°C	659°C	165°C

glasses under investigation. All the spectra were normalized to the band at 890 cm^{-1}, which has the maximum intensity. Five absorption bands can be observed at 1260, 1085, 980, 890 cm^{-1} and a broad band in the 700–800 cm^{-1} region. All the bands can be attributed to the PG network. The band having the maximum intensity at 890 cm^{-1} is attributed to P–O–P asymmetric stretching in Q^2 units (ν_{as} P–O–P Q^2) (Gao, Tan, & Wang, 2004; Moustafa & El-Egili, 1998; Shih & Shiu, 2007). The bands at 980 and at 1085 cm^{-1} correspond to the symmetric and asymmetric stretching vibration of PO_3^{2-} in Q^1 units, respectively (Abou Neel et al., 2009; Gao et al., 2004; Moustafa & El-Egili, 1998). In addition, the band at 1085 cm^{-1} is attributed to the overlap between PO_3 Q^1 terminal group and PO_2 Q^2 groups in metaphosphate glass structure (Ilieva et al., 2001). The band at 1260 cm^{-1} relate to the symmetric and asymmetric vibration of PO_2^- in Q^2 units (Abou Neel et al., 2009; Gao et al., 2004; Moustafa & El-Egili, 1998). The broad absorption band located in the 700–800 cm^{-1} region corresponds to P–O–P symmetric stretching vibration in metaphosphate structure (Lee, Obata, & Kasuga, 2009). The spectra present little observable changes as a result of doping except for a small decrease in the absorption band at 1260 cm^{-1} in the case of the glass doped with Ce, while it slightly increased when doping with Cu and Ag. Furthermore, this band shifts from 1,250 cm^{-1} for the Sr47.5, Ag-1 and Cu-2 to 1,245 cm^{-1} for the Ce-2 glass.

The in-vitro dissolution properties of the glasses under investigation were evaluated prior to the cell culture tests. The glass particles were immersed in TRIS buffer solution from 1 to 42 days, and in SBF from 8 hr to 21 days. Figure 2 presents the change in pH, ΔpH, as a function of immersion time in TRIS buffer solution and SBF. For the first 21 days of immersion in either media, no change in pH were recorded within the accuracy of measurement. However, at longer immersion time in TRIS, a small decrease in pH was recorded for Cu-2 and Ag-1.

Figure 3 depicts the ion concentrations in the immersion solution as a function of immersion time in TRIS buffer solution. In Figure 3 (a) B, (b) Ca, (c) Sr, (d) P, (e) Na, all the immersion solutions show a similar ion concentration increase, throughout the duration of immersion. The initial ion release was fast and linear, then slowed down after the 7 day time point. In Figure 3f), the release of Ce from Ce-2 nearly saturated around the 14 day time point. A more steady release of Cu from Cu-2 can be observed in Figure 3g). To further understand the ion release behavior, the fraction of ions released from the glass into the TRIS buffer solution as a function of immersion time was calculated, relative to the total amount of ions which would be present in the solution if the glass particles dissolved completely (presented in Figure 4). The fraction of Ca, Sr, and P ions released at all the time points was similar within the error of measurement, for all the glasses. The B and Na ion release was slightly higher than the Ca, Sr, and P ions at the long immersion time points such as 28, 35, and 42 days. At 42 days, Cu-2 had the highest fraction of ions dissolved among the glasses under investigation. Exceptionally, after 42 days, Na release was highest in the case of the Ce-2.

In SBF (Figure 5), the Ca concentration and therefore release were similar within the error of measurement for all the glasses over time. Ce-2 exhibited a lower release of each ion (other than Ca), as compared to the other glasses. Sr47.5, Cu-2, and Ag-1 released similar amounts of B, Sr, and P ions in the solution. Additionally, a slight decline in the amount of Ca, Sr, and P ions, in solution, is evidenced after 7 days. The Cu ion release from the Cu-2 glass was linear up to the 7 day time point, and then saturated up to 21 days. Ag could not be quantified in the SBF or TRIS owing to a very high noise to signal ratio, and further investigation is needed to understand the underlying phenomenon of Ag release from PG in TRIS and SBF. Similarly, no Ce was quantified upon dissolution of the Ce-2 glass despite being evidenced upon dissolution in TRIS.

Figure 6a–d present the IR spectra of the Sr47.5, Cu-2, Ce-2, and Ag-1 glasses, respectively, as a function of immersion time in TRIS buffer solution. The changes in the spectra were similar for all the glasses. A decrease in the intensity and a shift toward lower wavenumbers of the band at 1,260 cm^{-1}, can be observed as a function of immersion time. In the case of the Ce and Ag doped glasses an increase in a shoulder located at 1,154 cm^{-1} and assigned to symmetric

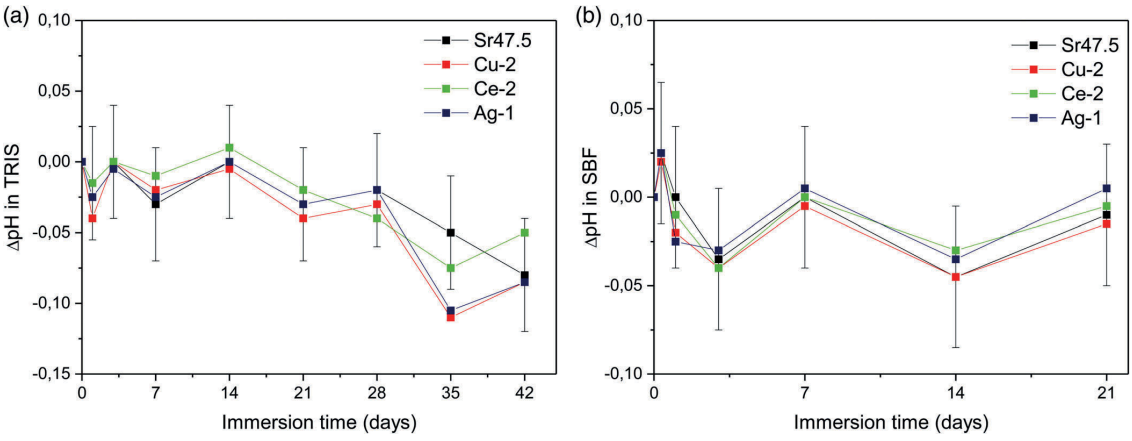

FIGURE 2 Change in pH of the (a) TRIS buffer solution and (b) SBF upon immersion of glass particles as a function of immersion time

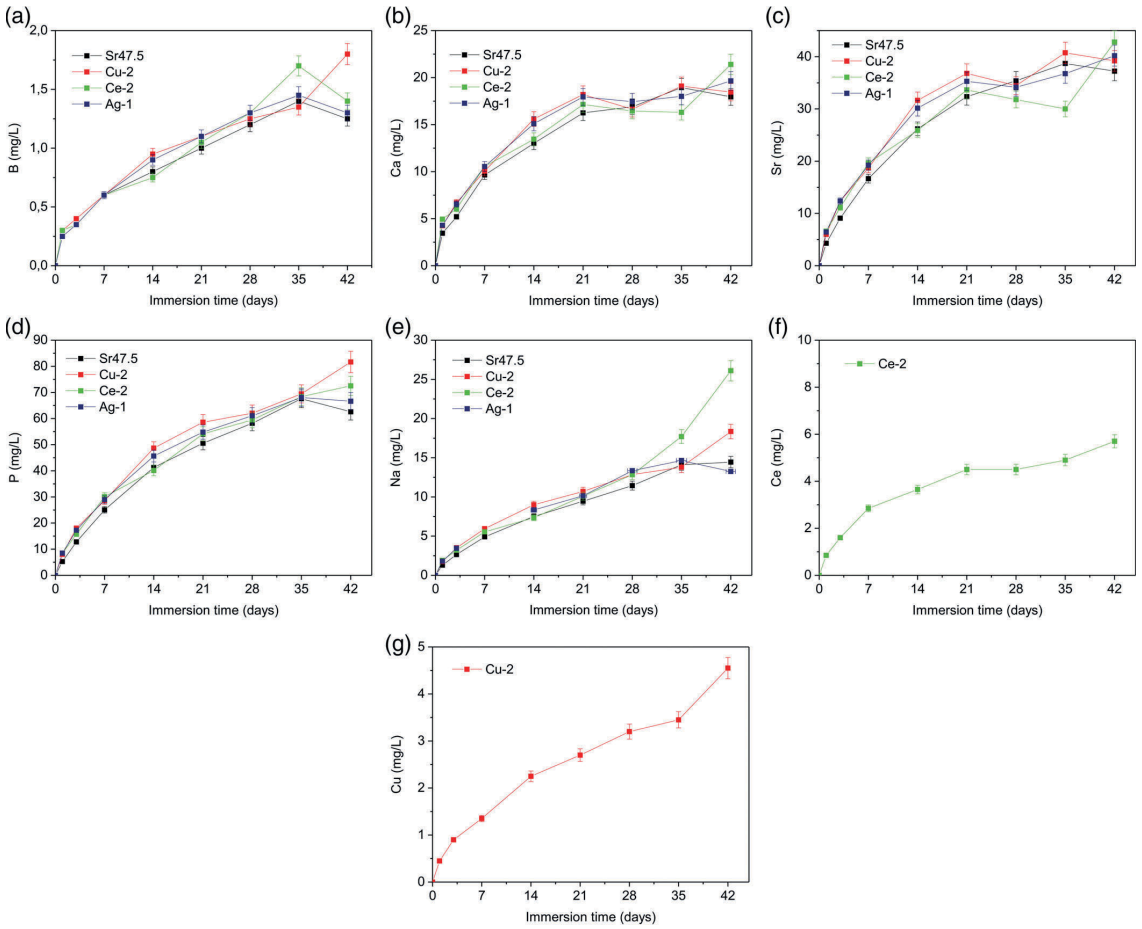

FIGURE 3 (a) B, (b) Ca, (c) Sr, (d) P, (e) Na, (f) Ce and (g) Cu concentration in TRIS buffer solution as a function of immersion time of the glass particles

vibration in PO_2^- in Q^2 units can be seen (Abou Neel et al., 2009; Gao et al., 2004). New bands appeared at 990 and 1,032 cm^{-1} for all the glasses. Figure 7a–d depict the IR spectra of the Sr47.5, Cu-2, Ce-2, and Ag-1 glasses, respectively, with respect to the immersion time in SBF. As in the case of immersion in TRIS buffer solution, similar changes in the spectra may be observed, except for the Ce-2 glass. Furthermore, in all Figures 6 and 7a,b,d, an absorption band in the 1,500–1,650 cm^{-1} region can be seen, typically assigned to OH vibration (Queiroz, Santos, Monteiro, & Prado da Silva, 2003). The only difference between the spectra recorded post TRIS immersion and post SBF immersion lay in the time required to evidence the appearance of the new bands.

The SEM images of the glass particles before and after immersion for 6 weeks (6 W) and 3 weeks (3 W) in TRIS and SBF, respectively, are presented in Figure 8. A surface layer can be observed in all the conditions except Ag-1 and Ce-2 in SBF. The composition of the observable surface layer and the bulk glass upon immersion in TRIS and SBF were obtained with EDX analysis, and are presented in Table 2. As B could not be analyzed with the EDX, all the concentrations presented have been corrected for the absence of B. The CaO concentration increased at the surface of all glasses. This increase is even greater at the surface of the Sr47.5 and Cu-2 immersed in SBF. The SrO content increased slightly at the surface, upon immersion in TRIS, except in the case of Ce-2. However, the Sr content decreased at the surface of the Sr47.5 and Cu-2 immersed in SBF. The P_2O_5 concentration decreased at the surface of all glasses, except Ce-2, irrespective of the immersion solution. It is noteworthy that the decline in the P_2O_5 concentration is more pronounced upon immersion in SBF. The Na concentration decreased at the surface of all the glasses, with the largest decrease in case of Ce-2.

To evaluate the cell response to these new glasses, hASC were cultured in glass extracts. The cell viability and proliferation of hASC were examined in glass extracts at different dilutions, to adjudge the optimal ion concentrations for both cell viability and added functionality, potentially imparted by the metal ions.

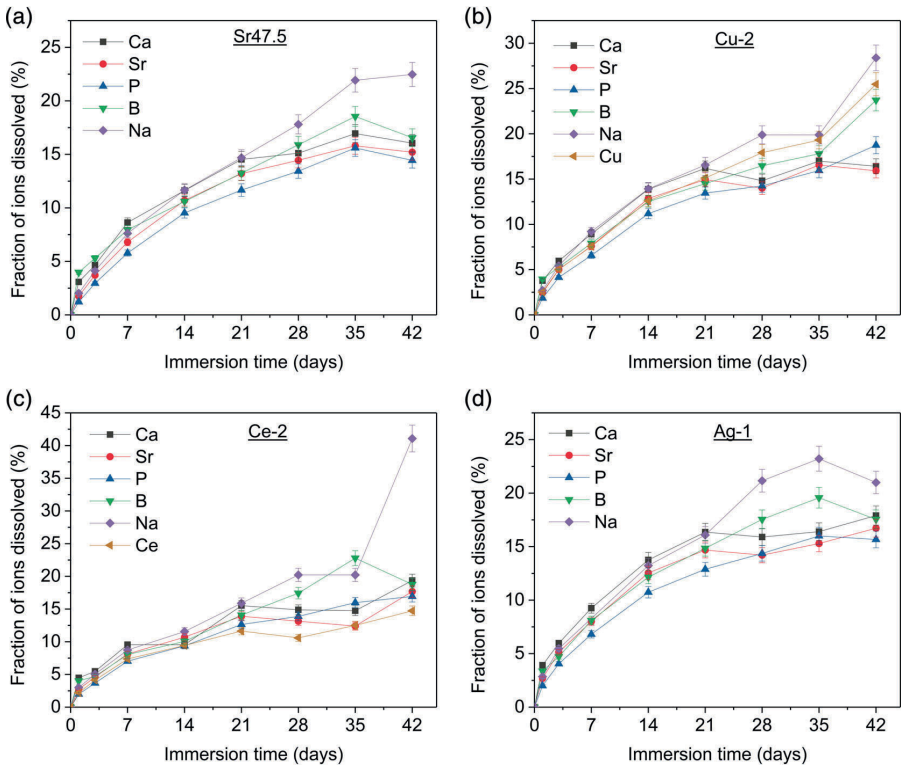

FIGURE 4 Fraction of the constituent ions leached into TRIS buffer solution after 42 days of immersion (a) Sr47.5, (b) cu-2, (c) Ce-2, (d) Ag-1

The undiluted extracts were analyzed with ICP-OES, and the ion concentrations obtained are presented in Table 4. Cu-2 exhibits the highest ion concentrations among all the glasses, while Ce-2 the lowest. Ag was also released in the extract media, contrary to its absence in the TRIS and SBF during in-vitro dissolution tests. The survival of hASC was evaluated at D-3, 7, and 14 (3, 7, and 14 days respectively) via live/dead staining in the undiluted, 1:10 diluted and 1:100 diluted glass extracts (Figure 9). Based on this staining, high amount of green (live) cells could be seen in all condition, except for the undiluted Cu-2 extract. Almost no red (dead) cells were observed in all other conditions. In some cases, the images at D-14 seemed to exhibit lower density of cells than D-7. To ascertain the above observations, CyQUANT cell proliferation assay was also performed at the same time points (Figure 10). For all the extracts except the undiluted Cu-2, the cell amount increased from D-3 to D-7 and remained constant from D-7 to D-14 with an increase in the time in culture. The undiluted Cu-2 extract presented a significantly lower cell amount at all the time points. The undiluted Ag-1 extract exhibited a slightly lower cell amount than the control, Sr47.5 and Ce-2 at all the time points, but much higher than the Cu-2. For the 1:10 dilution, Ce-2 presented the highest cell amount at D-14 and for the 1:100 dilutions, the cell amount was independent of the composition and increased over time in culture for all the extracts.

Consequently, LDH assay kit was used to quantitatively determine the cytotoxicity of the undiluted, 1:10 and 1:100 extracts. Figure 11 depicts the cytotoxicity of all the glass extracts, normalized to the cell amounts. Among the undiluted extracts, all the glasses exhibited similar cytotoxicity level at all the time points, except Cu-2 which had a consistently higher cytotoxicity than the other extracts and the control. For the 1:10 and 1:100 diluted extracts, the LDH values were highest at D-3, then decreased at D-7 and then increased again at D-14. At D-7, the 1:10 diluted Sr47.5 and Cu-2 extracts exhibited slightly higher cytotoxicity than the control, whereas Ce-2 a bit lower. Other than that, all the diluted extracts presented the same cytotoxicity level at a given time point, independent of the doped metal ion.

4 | DISCUSSION

The goal of this study was to develop new glasses doped with metal ions for added functionality, which possess a wide thermal processing window, and support cell viability and proliferation. From Table 3, all the glasses exhibit a thermal processing window (ΔT) well over 100°C, indicating their high degree of thermal processability. The glass doped with Cu appeared to have the wider hot forming domain of all processed glasses. Also, these glasses had a higher thermal processing window than those investigated earlier (Massera, Vassallo-Breillot,

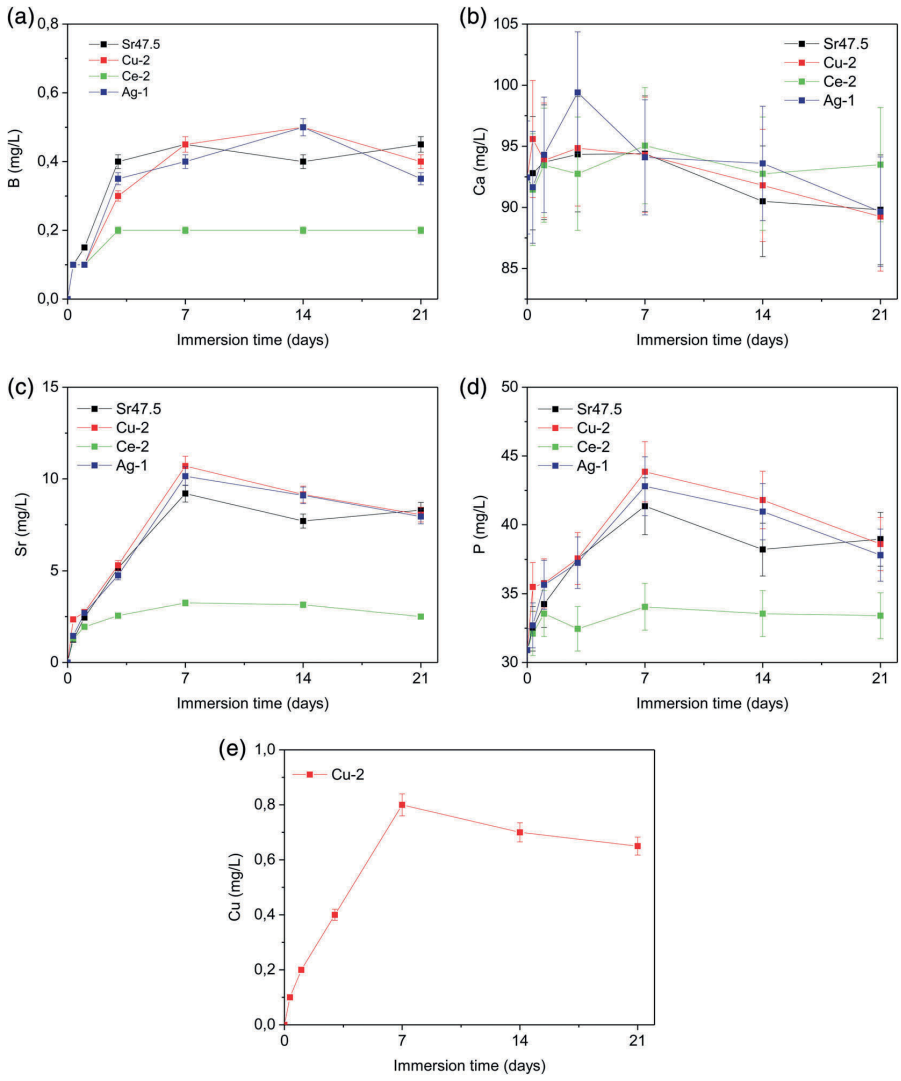

FIGURE 5 (a) B, (b) ca, (c) Sr, (d) P, and (e) Cu concentration in SBF as a function of immersion time of the glass particles

et al., 2014; Mishra et al., 2016, 2017), which may be attributed to partial substitution of P_2O_5 with B_2O_3. The improvement in the thermal processing window of PGs as a result of boron addition has been reported in the past (Bingham et al., 2006; Harada et al., 2004; Karabulut et al., 2011; Koudelka & Mošner, 2001; Massera et al., 2011).

In Figure 1, the IR spectra of the glasses before immersion are presented. The decrease in the 1,260 cm^{-1} band intensity and the shift to lower wavenumber, in the case of the Ce-2 samples, is attributable to a decrease in the network connectivity, weakening of the Q^2 units and an increase in the amount of Q^1 units. This is in agreement with structural changes reported on PGs by Massera, Vassallo-Breillot, et al. (2014). In contrast, the intensity of this band increased in the case of Ag-1 and Cu-2, indicating a decrease in the amount of Q^1 units, is in agreement with structural changes reported on Ag and Cu doped PGs (Mishra et al., 2016, 2017). While these findings are in agreement with previous studies on M_nO_m doped PGs, one should keep in mind that in this study boron was also introduced. The presence of boron will lead to BO_3 and BO_4 structural units, which in turn, will affect the phosphate structural units by either phosphate disproportionation and/or B–O–P linkages. A more thorough structural study would be required to fully grasp the changes in structure due to metal ion doping and will be the scope of future research.

The change in pH (ΔpH) of the TRIS buffer solution and SBF as a function of immersion time is presented in Figure 2a,b), respectively. In-vitro dissolution tests were performed in TRIS buffer solution, in order to judge the dissolution mechanism of the glasses of investigation, while

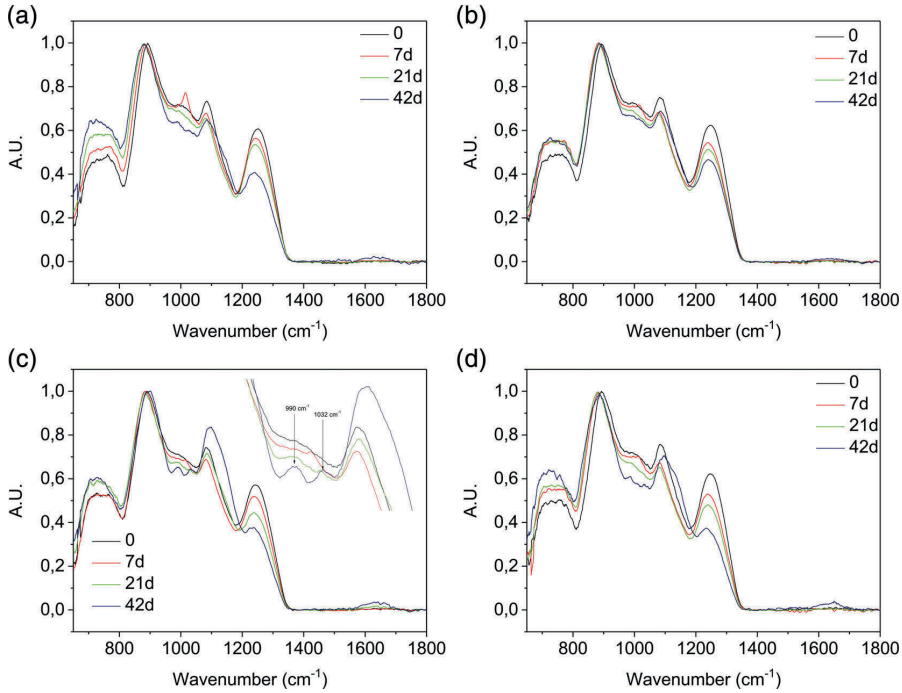

FIGURE 6 FTIR change in the structure of (a) Sr47.5, (b) Cu-2, (c) Ce-2, (d) Ag-1 as a function of immersion time in TRIS buffer solution

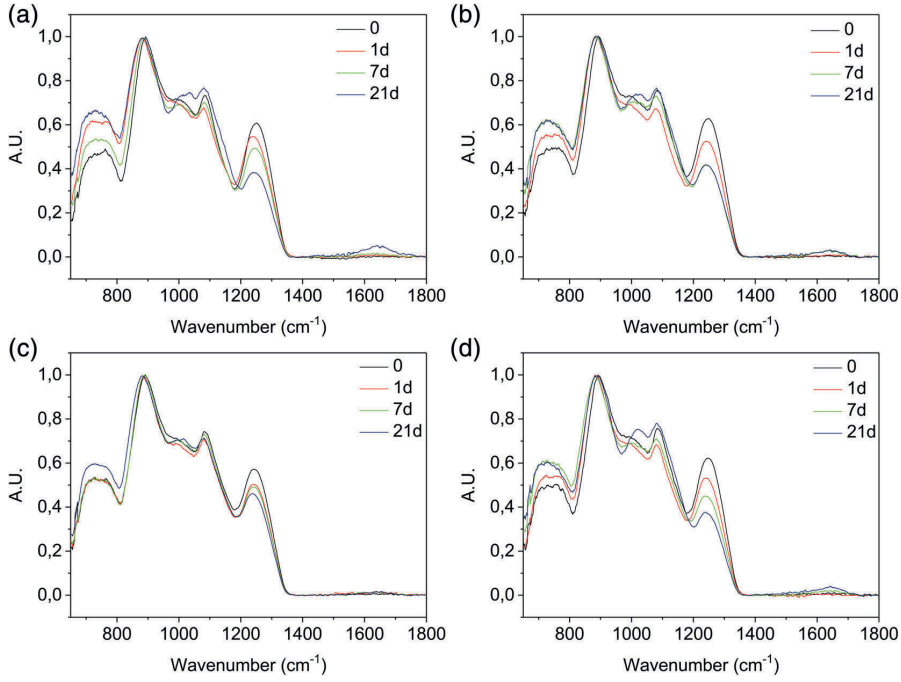

FIGURE 7 FTIR change in the structure of (a) Sr47.5, (b) Cu-2, (c) Ce-2, (d) Ag-1 as a function of immersion time in SBF

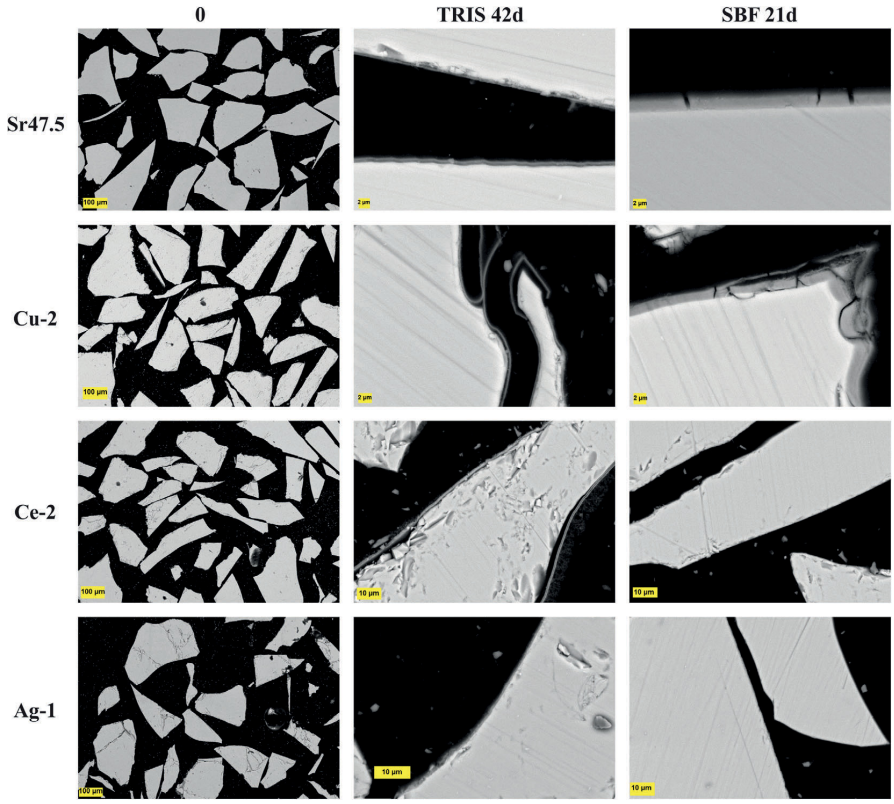

FIGURE 8 SEM images of the glass particles: Before immersion and after immersion in TRIS and SBF solution for 42 and 21 days, respectively

TABLE 4 Ion concentrations in the undiluted extract media of the glasses under investigation (mg/L)

	Ca	Sr	P	B	Cu	Ce	Ag
Extract media	43 ± 2	0	37 ± 2	0	0	0	0
Sr47.5	79 ± 4	40 ± 2	111 ± 6	1 ± 0.05	0	0	0
Cu-2	107 ± 5	51 ± 3	141 ± 7	1 ± 0.05	2 ± 0.1	0	0
Ce-2	47 ± 2	22 ± 1	66 ± 3	1 ± 0.05	0	0	0
Ag-1	55 ± 3	27 ± 1	83 ± 4	1 ± 0.05	0	0	2 ± 0.1

immersion in SBF was done to assess if a reactive layer would form due to super-saturation of the solution. The in-vitro dissolution also aimed at evaluating the change in the immersion solution pH which could later impact the cell viability. When immersed in TRIS and SBF, no significant change in the pH were observed for up to 21 days. Therefore, the solutions remained at a physiological pH. A small decrease in pH at longer immersion times for Cu-2 and Ag-1 in TRIS, was expected due to the high release of phosphorous ion (Ahmed, Lewis, Olsen, & Knowles, 2004; Massera et al., 2013), upon dissolution of PG. However, the change in pH remained minor and should not affect the cells adversely. The slightly lower pH recorded upon immersion (for over 21 days) of the Cu-2 and Ag-1 was consistent with their higher solubility, as already reported in (Mishra et al., 2016, 2017). However, the changes in pH were much less pronounced compared to the glasses investigated in (Massera, Vassallo-Breillot, et al., 2014; Mishra et al., 2016, 2017). This is attributed to the B_2O_3 substitution for P_2O_5, which leads to enhanced hydrolytic resistance (Massera et al., 2015; Sharmin et al., 2013).

The ICP analysis of the TRIS solutions recovered after immersion (Figure 3), revealed that all the glasses show similar ion release behavior overall. The ion release profiles in TRIS buffer solution are in agreement with previously reported data (Mishra et al., 2016, 2017). Figure 4 depicts the fraction of ions released from the glasses upon immersion in TRIS buffer solution. Overall, the glasses presented a congruent dissolution, as evidenced by the similar release of the constituent ions at least up to 7 days. Furthermore, the change in glass composition does not seem to significantly impact the glass dissolution rate. At longer

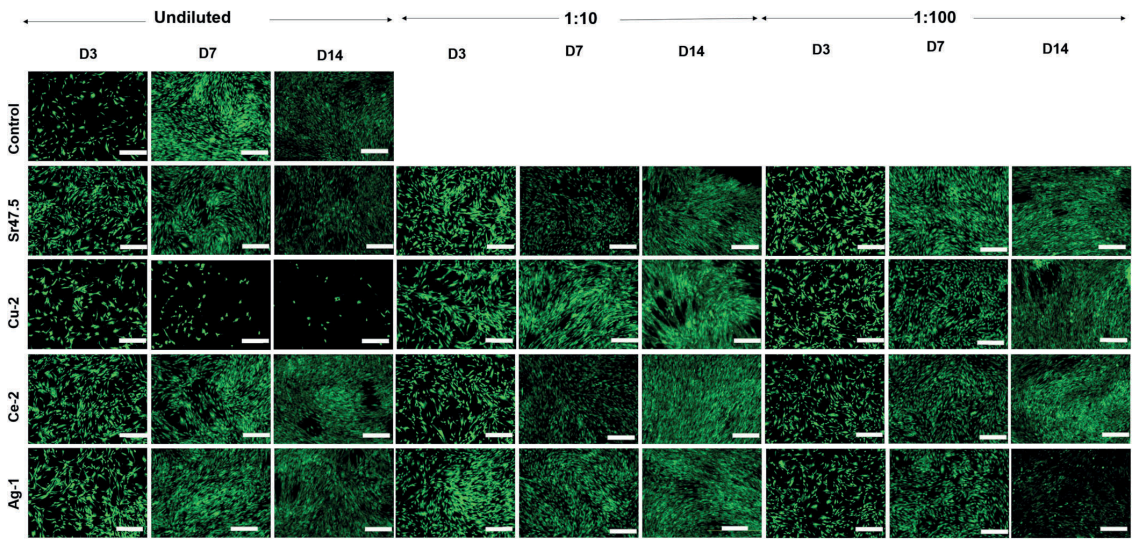

FIGURE 9 Viability of hASC cultured on undiluted, 1:10 and 1:100 diluted glass extract media, analyzed by live/dead staining at 3, 7, and 14 days of culture. The scale bar corresponds to 500 μm

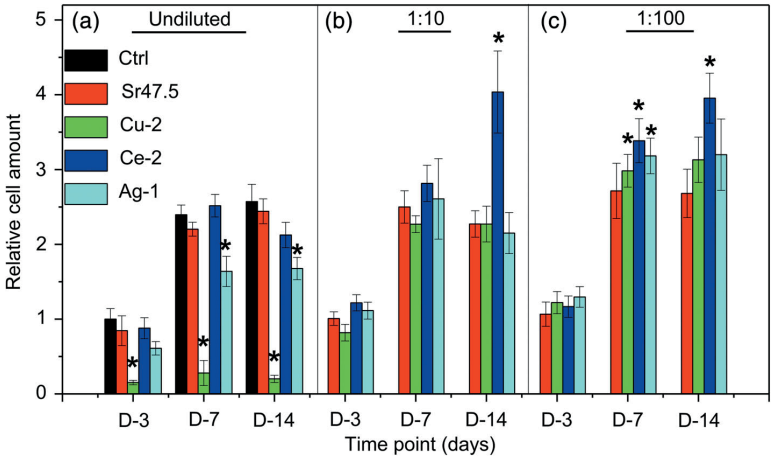

FIGURE 10 The proliferation of hASC cultured in (a) undiluted, (b) 1:10 diluted, and (c) 1:100 diluted glass extract media analyzed with CyQUANT cell proliferation assay kit at 3, 7, and 14 days of culture. All the values presented are relative to the control at D-3. The number of biological replicates was $n = 6$. The level of significance is set at $p < .05$. *implies that $p < .05$ between the indicated extract and control (Ctrl) at the same time point. The reported values correspond to the combined results from the two donors

immersion times, the release of the ions appeared to be parabolic which may imply the formation of a diffusion barrier.

From Figure 5, the different ion concentrations in SBF compared to TRIS, may be attributed to the significantly higher amount of ions present in the SBF. The SBF closely mimics the inorganic phase of the blood plasma, and provides a favorable model for evaluating a materials' bioactivity by measuring the materials' ability to induce apatite formation at its surface. As Ca is already present in SBF, it leads the solution to reach super-saturation at earlier time points compared to that in TRIS. Indeed, the decline in Ca, Sr, and P measured upon dissolution of PG for longer than 7 days in SBF is often assigned to the precipitation of a reactive layer (Massera et al., 2013; Mishra et al., 2016). The presence of Sr in Ca-P reactive layer has been discussed previously (Massera et al., 2013). However, one should keep in mind that the SBF solution is already thermodynamically prone to form apatite crystals (Bohner & Lemaitre, 2009). Furthermore, while all the glasses were found to release ions at similar speed upon immersion in TRIS (Figure 4), here the glass containing Ce demonstrated significantly lower ion release kinetics. This might be correlated to the higher hydrolytic resistance of the Ce doped PGs, as reported earlier (Massera, Vassallo-Breillot, et al., 2014). However, if the Ce would stabilize the glass network toward aqueous dissolution, similar trend would be seen upon immersion in TRIS and SBF. Therefore, it is also possible that Ce readily precipitated $CePO_4$ crystals as seen in Ce doped silicate glasses (Leonelli, Lusvardi, Malavasi, Menabue, & Tonelli, 2003).

In Figures 6 and 7, the IR spectra of all the glasses present similar changes as a function of immersion in TRIS and SBF, respectively. With an increase in immersion time, the decrease in the intensity and

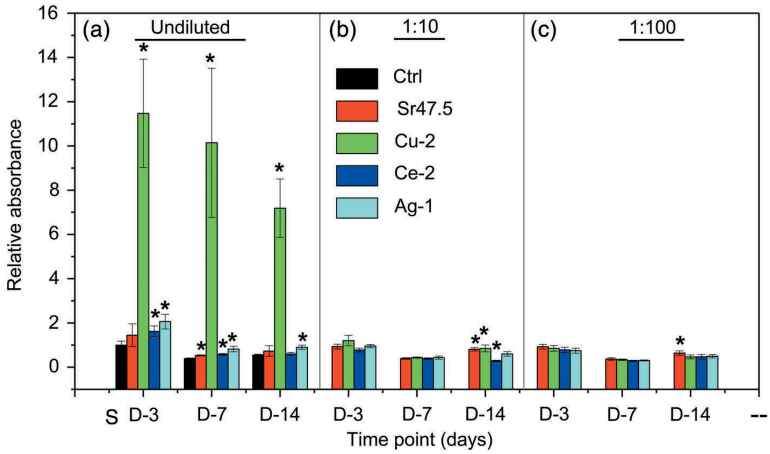

FIGURE 11 LDH activity in the (a) undiluted, (b) 1:10 diluted, and (c) 1:100 diluted glass extract media normalized with the corresponding CyQUANT assay values. The values are presented relative to the control at D-3. The number of biological replicates was $n = 4$. The level of significance is set at $p < .05$. *implies that $p < .05$ between the indicated extract and control (Ctrl) at the same time point. The reported values correspond to the combined results from the two donors

a shift toward lower wavenumbers (−14 cm^{-1}) of the band at 1260 cm^{-1}, indicates the progressive increase in the amount of Q^1 units at the expense of Q^2 units, due to de-polymerization of the phosphate network. The shift to lower wavenumbers of the band at 1260 cm^{-1}, attributed to Q^2 units, represents the weakening of their inherent bond strengths. These changes are characteristic of the early stages of glass dissolution (Bunker et al., 1984; Massera et al., 2013). The new bands at 990 and 1,032 cm^{-1} for all glasses along with the increase in the shoulder at 1154 cm^{-1} can be assigned to the precipitation of a Ca-P layer, as dicalcium phosphate dehydrate, possibly partially substituted with Sr, at their surface as explained in (Mishra et al., 2016; NIST, 2019). Ce-2, however, did not exhibit the appearance of new bands, indicating that the reactive layer precipitation was either delayed or a new form of reactive layer precipitated and did not attach to the glass surface. The overall changes to the spectra as a function of immersion time were also smaller for Ce-2 which could be supported by either the delayed formation the Ca-P reactive layer or the formation of $CePO_4$ crystals.

The formation of the reactive layer was further confirmed in Figure 8. A surface layer can be observed in all the conditions across both the immersion media, except Ag-1 and Ce-2 in SBF. This is in disagreement with the IR spectra of the Ag-1 glass after immersion for 21 days in SBF, which does show the formation of new bands. This may be due to poor attachment of the surface layer, leading to detachment before the SEM measurement or to a surface layer forming only in limited areas. However, the absence of the surface layer in case of Ce-2 in SBF is consistent with its IR spectra (Massera, Vassallo-Breillot, et al., 2014). From EDX analysis (Table 2) of the particles after immersion, it can be observed that Ce is incorporated in the surface layer, as the Ce concentration increases, compared to the nominal value. This explains the saturation in Ce concentration after immersion for 42 days in TRIS. In line with this observation, an earlier study (Leonelli et al., 2003) reported the formation of a mixed phase of Ce_2O_3-$CePO_4$ in the surface layer, upon dissolution of Ce containing phospho-silicate glasses in SBF, which might (a) limit the formation of a Ca-P reactive layer and (b) lead to a lower dissolution rate of this glass in SBF, while it is not greatly impacted in TRIS. The precipitation of the reactive layer in TRIS buffer solution is also in agreement with the ICP data (Figure 5). The higher release of B and Na than Sr, Ca, and P after 7 days can be attributed to the precipitation of the reactive layer. It should be mentioned, that in the case of Sr47.5 and Cu-2 the reactive layer is thicker upon immersion in SBF than in TRIS solution.

The new glasses, developed in this study, were found to possess a slower dissolution rate than their counterparts studied earlier in (Massera, Vassallo-Breillot, et al., 2014; Mishra et al., 2016, 2017). This should have a positive impact on the cell viability and proliferation.

Upon ICP analysis of the undiluted glass extracts (Table 4), Cu-2 presented the highest dissolution rate in the extract media as indicated by the high concentrations for all the constituent ions, and Ce-2 the lowest. Also, Ag-1 seemed to have a slower dissolution rate than the reference glass Sr47.5. Notably, the release of Ag may be observed in the extract media, which is probably due to a higher glass amount to media ratio than in the dissolution tests. The release of Cu was also evidenced, whereas Ce was not released into the extract media. It is worth noting here that DMEM, which is a major component of cell culture medium in this study, has a smaller Ca^{2+} concentration compared to SBF and a high concentration of HCO_3^- (Rohanová et al., 2014). Hence, the ion release profiles were expected to be different than in the SBF, justifying the need for quantifying ion release from glass when comparing data from different immersion media. Furthermore, while all three solution are, to some extend buffered, their buffering capacities are significantly different. This could also explain some of the discrepancy between the dissolution rate/mechanism evidenced here. Finally, from the Ce release point of view it appears that the glass dissolution/reaction is more closely related to the one seen in SBF rather than in TRIS buffer solution.

During cell culture with hASC, cell viability in different dilutions of glass extracts was ascertained at D-3, 7 and 14 with the help of live/dead (L/D) staining (Figure 9). Cells were found to be viable in all the conditions, with no observable dead cells, except for the undiluted Cu-2

extract. Some images at D-14 depict less cells than the ones at D-7, but this could be due to peeling-off of the cell layer owing to very high cell amounts. Furthermore, the morphology of the cells remained unchanged across the conditions and time points (Figure S2).

From cell proliferation analysis in Figure 10, other than undiluted Cu-2, all the extracts exhibit an increase in the cell amount from D-3 to D-7. The cell amounts remained constant from D-7 to D-14, perhaps due to reaching 100% confluence at D-7. The low cell amounts observed in the case of Cu-2 can be attributed to the high concentration of the dissolution products in the extract, and/or the presence of Cu ion in the media. However, it appears that release of up to 79 mg/L of Ca, 40 mg/L of Sr, and 111 mg/L of P do not negatively affect the cells behavior as seen by the ion concentration of the Sr47.5 glass extract (Table 4). In the case of the Ag-1 glass extract, despite an increase in the cell number as a function of culture time, a lower amount of cells than in the control, were recorded. This can hardly be attributable to the Ca, Sr, P, and B concentration which are lower than for the Sr47.5 glass extract, and therefore could be assigned to the presence of Ag ions in the solution. In 1:10 diluted glass extracts, the cell amount increased over time in culture for all the extracts, and Ce-2 exhibited the highest cell amount at D-14. However, this cannot be assigned to the Ce as no Ce was found in the extract, maybe due to the precipitation of $CePO_4$ during the extract preparation. Among the 1:100 diluted glass extracts, cell amounts increased over time in culture, and were also independent of the glass composition.

LDH is released from dead cells and, therefore, a higher LDH is indicative of higher cytotoxicity. Consequently, upon LDH analysis of the undiluted and diluted glass extracts, the undiluted Cu-2 exhibited a higher cytotoxicity than the other extracts at all the time points. Among the diluted extracts, all the extracts at the same dilution present similar cytotoxicity at a given time point, which was due to the lower metal ion concentrations in the diluted extracts as compared to the undiluted ones. Additionally, the increased LDH of diluted extracts at D-14 can be attributed to the high cell amount at this time point.

5 | CONCLUSION

In this article, we investigated the undoped and Ag, Cu, and Ce doped glasses within the system $xM_nO_m + (100 - x)$ $(47.5P_2O_5 + 2.5B_2O_3 + 10Na_2O + 20CaO + 20SrO)$ (mol%), to assess the impact of low metal ion doping on the in-vitro dissolution, thermal, and structural properties. The data can also be compared to previously reported glasses with similar doping within the phosphate matrix. These new glasses were found to have a wider thermal processing window compared to their predecessors. The in-vitro dissolution study in TRIS and SBF solution revealed that the choice of the immersion media used was of paramount importance. All glasses appeared to have similar dissolution kinetics in TRIS buffer solution with precipitation of a Ca-P reactive layer for the Ag and Cu doped glasses, and Ce containing Ca-P layer for the Ce doped glass. The Ce doped glasses had a lower dissolution rate in SBF compared to the other glasses. This was attributed to the precipitation of $CePO_4$ crystals in phosphorus rich solution. The change in dissolution mechanism and kinetics was further confirmed when preparing the extract. The Cu-2 glass leached more ions, while the Ag-1 leached out less ions than the reference glass. No Ce could be detected in the extract of the Ce-doped glass supporting the probable precipitation of $CePO_4$ crystals in solution with high P content.

In hASC culture up to 14 days, the undiluted and diluted extracts of these glasses were found to support cell viability and proliferation, except the undiluted Cu-2 extract. The Ag-doped extract, undiluted was found to be more cytotoxic than the control and the Sr47.5 and Ce-2 at 3 days of culture, but at the same level later on. The higher LDH activity could be due to the relatively higher ion concentrations in the extracts resulting from higher dissolution rate, or excess Cu ion concentration. Thus, despite the popularity of Cu as a dopant for bioactive glasses, the dopant concentration needs to be optimized for every glass system. On the other hand, the reference Sr47.5, Ag-1, and especially Ce-2 show great promise as biomaterials, and could pave way for new glasses and glass fibers for new biomedical applications. Ce doped glass fibers have been shown earlier to be antimicrobial, and are currently being researched by the authors for their potential in biosensing.

ACKNOWLEDGMENTS

The authors would like to acknowledge the support of Academy of Finland for the financial support of Dr. Jonathan Massera and Ayush Mishra through the Academy Research Fellow and Initial Research Cost. This study was partly supported by the Academy of Finland, Business Finland and Competitive State Research Financing of the Expert Responsibility area of Tampere University Hospital. The authors would also like to thank Anna-Maija Honkala and Sari Kalliokoski for the technical assistance.

CONFLICT OF INTEREST

There are no conflict to declare.

ORCID

Ayush Mishra https://orcid.org/0000-0002-2916-8427

REFERENCES

Abou Neel, E. A., Ahmed, I., Pratten, J., Nazhat, S. N., & Knowles, J. C. (2005). Characterisation of antibacterial copper releasing degradable phosphate glass fibres. *Biomaterials*, *26*, 2247–2254.

Abou Neel, E. A., Chrzanowski, W., Pickup, D. M., O'Dell, L. A., Mordan, N. J., Newport, R. J., … Knowles, J. C. (2009). Structure and properties of strontium-doped phosphate-based glasses. *Journal of the Royal Society Interface*, *6*, 435 LP–446 Retrieved from http://rsif.royalsocietypublishing.org/content/6/34/435.abstract

Ahmed, A. A., Ali, A. A., Mahmoud, D. A. R., & El-Fiqi, A. M. (2011). Study on the preparation and properties of silver-doped phosphate antibacterial glasses (part I). *Solid State Sci*. Elsevier Masson SAS, *13*,

981–992 Retrieved from https://doi.org/10.1016/j.solidstatesciences.2011.02.004

Ahmed, I., Lewis, M., Olsen, I., & Knowles, J. C. (2004). Phosphate glasses for tissue engineering: Part 2. Processing and characterisation of a ternary-based P2O5-CaO-Na2O glass fiber system. *Biomaterials*, *25*, 501–507.

Ahmed, I., Ready, D., Wilson, M., & Knowles, J. C. (2006). Antimicrobial effect of silver-doped phosphate-based glasses. *Journal of Biomedial Materials Research Part A*, *79*, 618–626.

Ahmed, I., Shaharuddin, S. S., Sharmin, N., Furniss, D., & Rudd, C. (2015). Core/clad phosphate glass fibres containing iron and/or titanium. *Biomedical Glasses*, *1*, 20–30.

Bae, B.-S., & Weinberg, M. C. (1994). Optical absorption of copper phosphate glasses in the visible spectrum. *Journal of Non-Crystalline Solids*, *168*, 223–231 Retrieved from https://linkinghub.elsevier.com/retrieve/pii/0022309394903336

Bingham, P. A., Hand, R. J., & Forder, S. D. (2006). Doping of iron phosphate glasses with Al2O3, SiO2 or B2O3 for improved thermal stability. *Materials Research Bulletin*, *41*, 1622–1630.

Blinkova, G. B., Vakhidov, S. A., Islamov, A. K., Nuritdinov, I., & Khaidarova, K. A. (1994). On the nature of yellow coloring in cerium-containing silica glasses. *Glass Physics and Chemistry*, *20*, 283–286.

Bohner, M., & Lemaitre, J. (2009). Can bioactivity be tested in vitro with SBF solution? *Biomaterials*, *30*, 2175–2179 Retrieved from http://www.ncbi.nlm.nih.gov/pubmed/19176246

Brauer, D. S., Brückner, R., Tylkowski, M., & Hupa, L. (2016). Sodium-free mixed alkali bioactive glasses. *Biomedical Glasses*, *2*, 99–110 Retrieved from https://www.degruyter.com/view/j/bglass.2016.2.issue-1/bglass-2016-0012/bglass-2016-0012.xml

Bunker, B. C., Arnold, G. W., & Wilder, J. A. (1984). Phosphate glass dissolution in aqueous solutions. *Journal of Non-Crystalline Solids*, *64*, 291–316.

Fagerlund, S., & Hupa, L. (2016). Chapter 1. Melt-derived bioactive silicate glasses. In A. R. Boccaccini, D. S. Brauer, & L. Hupa (Eds.), *Bioactive Glasses: Fundamentals, Technology, and Applications*. Cambridge: Royal Society of Chemistry Retrieved from http://ebook.rsc.org/?DOI=10.1039/9781782622017

Fagerlund, S., Massera, J., Hupa, M., & Hupa, L. (2012). T-T-T behaviour of bioactive glasses 1-98 and 13-93. *Journal of the European Ceramic Society*, *32*, 2731–2738.

Gao, H., Tan, T., & Wang, D. (2004). Effect of composition on the release kinetics of phosphate controlled release glasses in aqueous medium. *Journal of Controlled Release*, *96*, 21–28.

Harada, T., In, H., Takebe, H., & Morinaga, K. (2004). Effect of B2O3 addition on the thermal stability of barium phosphate glasses for optical fiber devices. *Journal of the American Ceramic Society*, *87*, 408–411.

Hench, L. L., Splinter, R. J., Allen, W. C., & Greenlee, T. K. (1971). Bonding mechanisms at the interface of ceramic prosthetic materials. *Journal of Biomedical Materials Research*, *5*, 117–141.

Ilieva, D., Jivov, B., Bogachev, G., Petkov, C., Penkov, I., & Dimitriev, Y. (2001). Infrared and Raman spectra of Ga2O3-P2O5glasses. *Journal of Non-Crystalline Solids*, *283*, 195–202.

Karabulut, M., Yuce, B., Bozdogan, O., Ertap, H., & Mammadov, G. M. (2011). Effect of boron addition on the structure and properties of iron phosphate glasses. *Journal of Non-Crystalline Solids*, *357*, 1455–1462 Retrieved from https://doi.org/10.1016/j.jnoncrysol.2010.11.023

Kokubo, T., Kushitani, H., Sakka, S., Kitsugi, T., & Yamamuro, T. (1990). Solutions able to reproduce in vivo surface-structure changes in bioactive glass-ceramic A-W3. *Journal of Biomedical Materials Research*, *24*, 721–734.

Koudelka, L., & Mošner, P. (2001). Study of the structure and properties of Pb-Zn borophosphate glasses. *Journal of Non-Crystalline Solids*, *293*, 635–641.

Lee, S., Obata, A., & Kasuga, T. (2009). Ion release from SrO-CaO-TiO2-P2O5 glasses in Tris buffer solution. *Journal of the Ceramic Society of Japan*, *117*, 935–938.

Leonelli, C., Lusvardi, G., Malavasi, G., Menabue, L. Ã., & Tonelli, M. (2003). Synthesis and characterization of cerium doped glasses and in vitro evaluation of bioactivity.Pdf. *Journal of Non-Crystalline Solids*, *316*, 198–216.

Lindfors, N. C., Koski, I., Heikkilä, J. T., Mattila, K., & Aho, A. J. (2010). A prospective randomized 14-year follow-up study of bioactive glass and autogenous bone as bone graft substitutes in benign bone tumors. *Journal of Biomedical Materials Research Part B*, *94*, 157–164.

Lindroos, B., Boucher, S., Chase, L., Kuokkanen, H., Huhtala, H., Haataja, R., … Miettinen, S. (2009). Serum-free, xeno-free culture media maintain the proliferation rate and multipotentiality of adipose stem cells in vitro. *Cytotherapy*, *11*, 958–972.

Maçon, A. L. B., Kim, T. B., Valliant, E. M., Goetschius, K., Brow, R. K., Day, D. E., … Jones, J. R. (2015). A unified in vitro evaluation for apatite-forming ability of bioactive glasses and their variants. *Journal of Materials Science. Materials in Medicine*, *26*, 1–10.

Massera, J., Ahmed, I., Petit, L., Aallos, V., & Hupa, L. (2014). Phosphate-based glass fiber vs. bulk glass: Change in fiber optical response to probe in vitro glass reactivity. *Materials Science and Engineering: C*, *37*, 251–257 Retrieved from https://linkinghub.elsevier.com/retrieve/pii/S0928493114000290

Massera, J., Claireaux, C., Lehtonen, T., Tuominen, J., Hupa, L., & Hupa, M. (2011). Control of the thermal properties of slow bioresorbable glasses by boron addition. *Journal of Non-Crystalline Solids*, *357*, 3623–3630 Retrieved from https://doi.org/10.1016/j.jnoncrysol.2011.06.037

Massera, J., Haldeman, A., Milanese, D., Gebavi, H., Ferraris, M., Foy, P., … Richardson, K. (2010). Processing and characterization of core-clad tellurite glass preforms and fibers fabricated by rotational casting. *Optical Materials*, *32*, 582–588 Retrieved from https://doi.org/10.1016/j.optmat.2009.12.003

Massera, J., & Hupa, L. (2014). Influence of SrO substitution for CaO on the properties of bioactive glass S53P4. *Journal of Materials Science. Materials in Medicine*, *25*, 657–668 Retrieved from http://www.ncbi.nlm.nih.gov/pubmed/24338267

Massera, J., Hupa, L., & Hupa, M. (2012). Influence of the partial substitution of CaO with MgO on the thermal properties and in vitro reactivity of the bioactive glass S53P4. *J Non Cryst Solids*. Elsevier B.V., *358*, 2701–2707 Retrieved from http://www.sciencedirect.com/science/article/pii/S0022309312003754

Massera, J., Kokkari, A., Närhi, T., & Hupa, L. (2015). The influence of SrO and CaO in silicate and phosphate bioactive glasses on human gingival fibroblasts. *Journal of Materials Science. Materials in Medicine*, *26*, 196.

Massera, J., Mayran, M., Rocherullé, J., & Hupa, L. (2015). Crystallization behavior of phosphate glasses and its impact on the glasses' bioactivity. *Journal of Materials Science*, *50*, 3091–3102 Retrieved from https://doi.org/10.1007/s10853-015-8869-4

Massera, J., Petit, L., Cardinal, T., Videau, J. J., Hupa, M., & Hupa, L. (2013). Thermal properties and surface reactivity in simulated body fluid of new strontium ion-containing phosphate glasses. *Journal of Materials Science. Materials in Medicine*, *24*, 1407–1416.

Massera, J., Shpotyuk, Y., Sabatier, F., Jouan, T., Boussard-Plédel, C., Roiland, C., … Hupa, L. (2015). Processing and characterization of novel borophosphate glasses and fibers for medical applications. *Journal of Non-Crystalline Solids*, *425*, 52–60 Retrieved from https://doi.org/10.1016/j.jnoncrysol.2015.05.028

Massera, J., Vassallo-Breillot, M., Törngren, B., Glorieux, B., & Hupa, L. (2014). Effect of CeO2 doping on thermal, optical, structural and in vitro properties of a phosphate based bioactive glass. *J Non Cryst Solids*. Elsevier B.V., *402*, 28–35 Retrieved from https://doi.org/10.1016/j.jnoncrysol.2014.05.006

Mishra, A., Petit, L., Pihl, M., Andersson, M., Salminen, T., Rocherullé, J., & Massera, J. (2017). Thermal, structural and in vitro dissolution of

antimicrobial copper-doped and slow resorbable iron-doped phosphate glasses. *Journal of Materials Science*, *52*, 8957–8972.

Mishra, A., Rocherulle, J., & Massera, J. (2016). Ag-doped phosphate bioactive glasses: Thermal, structural and in-vitro dissolution properties. *Biomedical Glasses*, *2*, 38–48.

Moustafa, Y. M., & El-Egili, K. (1998). Infrared spectra of sodium phosphate glasses. *Journal of Non-Crystalline Solids*, *240*, 144–153.

Mulligan, A. M., Wilson, M., & Knowles, J. C. (2003a). Effect of increasing silver content in phosphate-based glasses on biofilms of streptococcus sanguis. *Journal of Biomedical Materials Research Part A*, *67*, 401–412.

Mulligan, A. M., Wilson, M., & Knowles, J. C. (2003b). Effect of increasing copper content in phosphate-based glasses on biofilms of streptococcus sanguis. *Biomaterials*, *24*, 1797–1807.

NIST, NIST chemistry WebBook, SRD 69. 2019. Retrieved from https://webbook.nist.gov/cgi/cbook.cgi?ID=B6009796&Mask=80#IR-Spec

Ojansivu, M., Mishra, A., Vanhatupa, S., Juntunen, M., Larionova, A., Massera, J., & Miettinen, S. (2018). The effect of S53P4-based borosilicate glasses and glass dissolution products on the osteogenic commitment of human adipose stem cells. Boccaccini a editor. *PLoS One*, *13*, e0202740 Retrieved from https://dx.plos.org/10.1371/journal.pone.0202740

Ojansivu, M., Vanhatupa, S., Björkvik, L., Häkkänen, H., Kellomäki, M., Autio, R., … Miettinen, S. (2015). Bioactive glass ions as strong enhancers of osteogenic differentiation in human adipose stem cells. *Acta Biomaterialia*, *21*, 190–203 Retrieved from https://doi.org/10.1016/j.actbio.2015.04.017

Queiroz, A. C., Santos, J. D., Monteiro, F. J., & Prado da Silva, M. H. (2003). Dissolution studies of hydroxyapatite and glass-reinforced hydroxyapatite ceramics. *Materials Characterization*, *50*, 197–202 Retrieved from https://linkinghub.elsevier.com/retrieve/pii/S1044580303000925

Rohanová, D., Boccaccini, A. R., Horkavcová, D., Bozděchová, P., Bezdička, P., & Častorálová, M. (2014). Is non-buffered DMEM solution a suitable medium for in vitro bioactivity tests? *Journal of Materials Chemistry B*, *2*, 5068–5076.

Salih, V., Franks, K., James, M., Hastings, G. W., Knowles, J. C., & Olsen, I. (2000). Development of soluble glasses for biomedical use part II: The biological response of human osteoblast cell lines to phosphate-based soluble glasses. *Journal of Materials Science. Materials in Medicine*, *11*, 615–620.

Sharmin, N., Hasan, M. S., Parsons, A. J., Furniss, D., Scotchford, C. A., Ahmed, I., & Rudd, C. D. (2013). Effect of boron addition on the thermal, degradation, and cytocompatibility properties of phosphate-based glasses. *BioMed Research International*, *2013*, 1–12.

Shih, P. Y., & Shiu, H. M. (2007). Properties and structural investigations of UV-transmitting vitreous strontium zinc metaphosphate. *Materials Chemistry and Physics*, *106*, 222–226.

Tirkkonen, L., Haimi, S., Huttunen, S., Wolff, J., Pirhonen, E., Sándor, G. K., & Miettinen, S. (2012). Osteogenic medium is superior to growth factors in differentiation of human adipose stem cells towards boneforming cells in 3D culture. *European Cells & Materials*, *25*, 144–158.

Wu, C., Zhou, Y., Xu, M., Han, P., Chen, L., Chang, J., & Xiao, Y. (2013). Copper-containing mesoporous bioactive glass scaffolds with multifunctional properties of angiogenesis capacity, osteostimulation and antibacterial activity. *Biomaterials*, *34*, 422–433.

Zuk, P. A., Zhu, M., Mizuno, H., Huang, J., Futrell, J. W., Katz, A. J., … Hedrick, M. H. (2001). Multilineage cells from human adipose tissue: Implications for cell-based therapies. *Tissue Engineering*, *7*, 211–228.

SUPPORTING INFORMATION

Additional supporting information may be found online in the Supporting Information section at the end of this article.

How to cite this article: Mishra A, Ojansivu M, Autio R, Vanhatupa S, Miettinen S, Massera J. In-vitro dissolution characteristics and human adipose stem cell response to novel borophosphate glasses. *J Biomed Mater Res*. 2019;107A: 2099–2114. https://doi.org/10.1002/jbm.a.36722

PUBLICATION IV

Core-clad phosphate glass fibers for biosensing

A. Mishra, F. Désévédavy, L. Petit, F. Smektala, J. Massera

Journal of Material Science and Engineering C 96 (2019) 458–465

https://doi.org/10.1016/j.msec.2018.11.038

Materials Science & Engineering C 96 (2019) 458–465

Contents lists available at ScienceDirect

Materials Science & Engineering C

journal homepage: www.elsevier.com/locate/msec

Core-clad phosphate glass fibers for biosensing☆

A. Mishra[a], F. Désévédavy[b], L. Petit[c], F. Smektala[b], J. Massera[a,*]

[a] Faculty of Medicine and Health Technology, Tampere University, Korkeakoulunkatu 10, FI-33720 Tampere, Finland
[b] Laboratoire Interdisciplinaire Carnot de Bourgogne, UMR 6303 CNRS-Université de Bourgogne Franche-Comté, 9 Av. A. Savary, 21078 Dijon, France
[c] Laboratory of Photonics, Tampere University, Korkeakoulunkatu 10, FI-33720 Tampere, Finland

ABSTRACT

Recently, a phosphate glass with composition 20 CaO-20 SrO-10 Na_2O-50 P_2O_5 (mol%) was found to have good potential as a biomaterial and to possess thermal properties suitable for fiber drawing. This study opened the path towards the development of fully bioresorbable fibers promising for biosensing. In the past, this phosphate glass with CeO_2 was found to increase the refractive index and the glass stability. Therefore, a new SrO-containing glass was prepared with 1 mol% of CeO_2 and core fibers were drawn from it. A core-clad fiber was also processed, where the core was a Ce-doped glass and the clad undoped, to allow for total internal reflection. The mechanical properties of the core and core-clad fibers are discussed as a function of immersion time in TRIS-buffer solution. Finally, a sensing region was created, in the core-clad fiber, by etching the cladding using phosphoric acid. Then, the change in light transmission, upon immersion in TRIS-buffer solution, was quantified to assess the potential use of the novel core-clad fiber as a biosensor. Upon immersion in TRIS, the core-clad fiber was found to guide light effectively and to maintain a tensile strength of ~150–200 MPa up to 6 weeks in TRIS, clearly showing that this fiber has potential as a biosensing device.

1. Introduction

Phosphate glasses (PGs) have emerged as good alternatives to the traditional silicate glasses for biomedical applications. Silicate glasses have long been the popular choice as bioactive glasses among researchers, since the discovery of 45S5 by Hench et al. [1]. However, the processability of silicate glasses into scaffold, fibers etc. is hindered due to their crystallization kinetics [2,3]. Meanwhile, phosphate glasses have emerged as promising candidates as bioactive materials due to their unique properties: they are completely biodegradable, and their composition can be adjusted to attain desirable degradation rates (from weeks to years) [4]. Moreover, phosphate glasses possess excellent thermal properties enabling fiber drawing without adverse crystallization [4–7]. A detailed study of the potential use and benefits of PGs, in the medical field, can be found in [8].

Glass fibers have been researched extensively both in the medical and optical research fields. Degradable bioactive glass fibers can be used in composites to improve the mechanical properties of scaffolds and of other biomedical devices [9]. Similar to the bulk glasses, phosphate glass fibers have been found to be particularly suitable not only for bone repair and reconstruction but also in soft tissue engineering applications [10–14]. From an optics perspective, the potential of glass fibers as biosensors has been investigated in detail in [15]. Their potential in tracking glass dissolution is discussed in [16]. Additionally, phosphate fibers exhibit high transparency in the UV–Visible/Near infrared (UV–Vis/NIR) range, and their refractive index is comparable to the commercially available silicate glass fibers [17–19].

Glass with composition 50P_2O_5-20SrO-20CaO-10Na_2O (mol%), referred to as Sr50 has favorable degradation characteristics for potential use in biomedical applications as reported in [20]. When Sr50 is doped with CeO_2 (from 1 to 7 mol%), the glass network becomes more cross-linked and therefore more resistant to dissolution delaying the precipitation of a reactive surface layer [7]. The CeO_2 doping was done such that the (Ca + Sr)/P remained the same than in Sr50, thereby not affecting its ability to form a Ca-Sr-P layer at the surface. The resistance to crystallization, of these CeO_2 doped glasses, increased compared to the Sr50 [7]. Furthermore, the addition of CeO_2 leads to an increase in the refractive index, allowing the drawing of core-clad fiber from Sr50 (Clad) and a Ce-doped-Sr50 composition (core) having suitable Δn (where $\Delta n = n_{core} - n_{clad}$ is positive) for total internal reflection. In this study, core and core-clad preforms were drawn into fibers to determine their suitability for biosensing. Core fibers were drawn from the Sr50 glass and Ce-1 glass with the [0.99 (50P_2O_5-20SrO-20CaO-10Na_2O)–1CeO_2 (mol%)] composition, with a diameter of (140 ± 10) μm and (110 ± 10) μm respectively. For the core-clad fiber, Ce-1 glass was chosen as the core, and Sr50 as the cladding, and fibers were drawn with a diameter of (140 ± 10) μm from preform produced using a homemade rotational caster.

In this paper, we investigated the effect of in-vitro dissolution of the fibers on their mechanical and optical properties. In the core-clad

☆ This work will lay the base on using optical properties to probe protein and/or cell attachment at the surface of a fiber.

* Corresponding author.
E-mail address: jonathan.massera@tut.fi (J. Massera).

https://doi.org/10.1016/j.msec.2018.11.038
Received 16 January 2018; Received in revised form 14 November 2018; Accepted 24 November 2018
Available online 26 November 2018
0928-4931/

fibers, a sensing region was produced by selectively etching the cladding, revealing the core of the fiber. Then, light loss of the etched core-clad fibers was measured as a function of immersion time in TRIS. The mechanical properties of the etched core-clad fibers, were also ascertained. Additionally, the impact of immersion in TRIS buffer on the mechanical properties of the fibers was obtained.

2. Materials and methods

2.1. Preform preparation and fiber drawing

2.1.1. Core preforms

The core preforms with the composition [$50P_2O_5$-20SrO-20CaO-$10Na_2O$] (labeled as Sr50) and [0.99 ($50P_2O_5$-20SrO-20CaO-$10Na_2O$)–$1CeO_2$ (mol%)] (labeled as Ce-1) were prepared by melting batches of 45 g comprising of $Ca(PO_3)_2$, $Sr(PO_3)_2$, $NaPO_3$ (and CeO_2 for Ce-1 composition) at 1100 °C (heating rate 10 °C/min) for 30 min. Ca $(PO_3)_2$ and $Sr(PO_3)_2$ were prepared beforehand by heating $NH_4H_2PO_4$ with $CaCO_3$ and $SrCO_3$ respectively, in separate batches. The batch was heated to 250 °C for 12 h, then to 650 °C for 12 h and finally to 850 °C for 12 h at 1 °C·min^{-1} to remove CO_2, NH_3 and H_2O. After melting, the molten batch was cast into a 10 cm long pre-heated (350 °C) brass mold having a diameter of 12 mm, and annealed at 15 °C below their respective glass transition temperature for 15 h, to obtain a mechanically stable preform. Annealing was performed below T_g to decrease the risk of nuclei formation.

2.1.2. Core-clad preform

The core-clad preform, with core Ce-1 and clad Sr50, was prepared using a homemade rotational caster. The clad composition was first poured in a pre-heated brass mold (350 °C), which is then spun at 1000 rpm for 10 s. The spinning results in the formation of a hollow cylinder in the mold. Then the core composition is poured slowly inside the hollow cladding. The preform was then annealed similarly as for the core preforms. The process was optimized as in [21] to guarantee a constant $Ø_{clad}/Ø_{core}$, before and after drawing. The small CeO_2 addition to the glass composition did not lead to a significant change in thermal expansion coefficient and all the processed core-clad preforms were free of cracks or any defects.

2.1.3. Fiber drawing

Fibers were drawn using the “rod” method in a specially designed single zone drawing tower furnace. To prevent nucleation or crystallization, the temperature profiles of this furnace were precisely mapped beforehand, and the dwell time in the zones was controlled prior to and during the drawing. Thermal profiles for different setting temperatures were performed by means of a thermocouple attached to the preform motion cane. After waiting for the furnace to stabilize to the set temperature, the thermocouple was gradually moved down into the furnace. In the meantime the thermocouple temperature and position were registered, as presented in Fig. 1. The drawing temperature was 645 °C for all the fibers under an inert He gas laminar flow of 2.5 l·min^{-1}. This temperature corresponded to a set temperature of 770 °C (Fig. 1). The high thermal conductivity K_{He} of helium allowed to minimize the dwell time before drop formation and during drawing, K_{He} = $33{,}63.10^{-5}$ cal·sec^{-1}·cm^{-1}. $°C^{-1}$, K_{Ar} = $4{,}06.10^{-5}$ cal·sec^{-1}·cm^{-1}. $°C^{-1}$, K_{air} = $5.68.10^{-5}$ cal·sec^{-1}·cm^{-1}. $°C^{-1}$ [22]. The drawing temperature was determined based on the glass transition temperature (T_g) and the furnace thermal profile. The glass rod was placed into the furnace and the temperature gradually increased above T_g until the formation of a drop. During the drawing, the temperature was adjusted based on readings from the tension measurement gauge. The fiber was then fixed on a rotary drum, while the fiber diameter and drawing tension were controlled by a computer system based on LabView software.

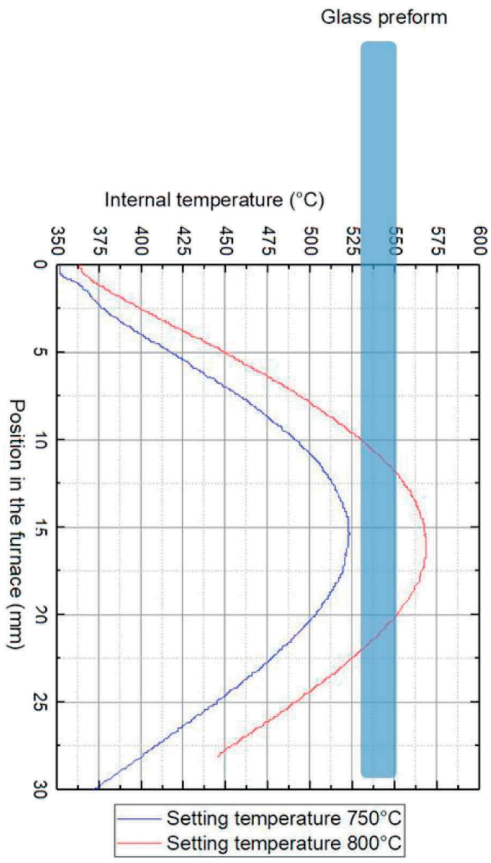

Fig. 1. thermal profiles of the drawing tower furnace. The zero mm position corresponds to the top of the heating element.

2.2. Optical properties

A fully automated Metricon, model 2010 prism coupled refractometer was used to measure the refractive index of 2 mm thick glass samples of bulk core and cladding glass samples at 1060 nm. The accuracy of the measurement was ± 0.0001. The samples were polished with SiC polishing paper (600, 800, 1200, 2400 and 4000 grit) on both faces.

2.3. Immersion tests

Immersion tests were carried out by immersing the fibers in TRIS buffer solution for up to 6 wks. For each immersion time point, 10 fibers of length 15 cm were entirely immersed in 50 ml of TRIS, and were placed in an incubating shaker HT Infors Multitron at 37 °C, 100 rpm to obtain laminar flow mixing without moving the fibers.

2.4. Mechanical testing

Mechanical tests were performed, in tension (static), on the core and core-clad fiber prior to and after immersion in TRIS. Post immersion, the core and core-clad fibers were carefully collected, rinsed with acetone and dried in air, overnight, in an incubator at 37 °C. The specimens were then maintained in desiccator before testing. Mechanical strength measurements were carried out at ambient temperature using

Instron 4411 Materials Testing Machine, with a grip distance of 50 mm, a load cell of 500 N, and a crosshead speed of 30 mm·min^{-1}. The grips were covered with a rubber mat to avoid slipping of the fiber during the test and damage caused by the metallic grips. The tensile strength and the Young's modulus were calculated as the mean of 10 test fibers. Despite the low number of specimens, the Weibull modulus was estimated as reported in [23–24].

2.5. Light loss

The fibers' optical losses were measured using the cut back technique. The signal from the FTIR spectrometer transmitted through a long piece of fiber (L_1) was recorded (I_1), using a nitrogen cooled InSb detector. Then, without moving the input end, the fiber was cut (cleaved) and the output fiber signal was recorded (I_2). From the measurement of the cut length corresponding to L_1-L_2, the signals I_1 and I_2, the losses were calculated by using the following equation:

$$\text{Losses(dB/m)} = \frac{10}{L_1 - L_2} \times \log\left(\frac{I_2}{I_1}\right).$$

The same measurement was repeated several times to increase accuracy.

The light transmission, as a function of immersion time, was measured in the wavelength range of 200–1000 nm. A 50 cm long fiber, was connected on one end to a light source and at the other end to a spectrometer. The fibers were cleaved and coupled using FC connector (Thorlabs). The lamp position was adjusted to maximize the light intensity at the fiber output. A 5 cm portion (sensing region) of the fiber was immersed in TRIS. For the illumination, a broadband white light source (Edmund BDS130) was used, and a ThorLabs Compact Spectrometer CCS200 was used for collecting the light. The light accumulation was set to 7.5 ms to maximize the signal. The light intensity recorded at 680 nm was tracked as a function of immersion time. The signal was normalized to 1 prior to immersion and only the relative intensity is reported. The TRIS solution was refreshed each week in order to avoid significant evaporation of the solution. Evaporation would increase the surface area to volume of the solution ratio, leading to a change in the dissolution rate.

2.6. Microscopy

The core-clad fibers were collected post mechanical tests for imaging. They were imaged along their length using optical microscope Olympus BH2-UMA to evidence the deposition of a surface layer after immersion in TRIS. The optical microscope was also used to measure the initial and post-immersion fiber diameter. The fibers cross-section, post fracture was also visualized using Zeiss ULTRAplus scanning electron microscope (SEM).

3. Results and discussion

To guide the light successfully, a core-clad fiber should be drawn using glasses with specific refractive index (n) to allow total internal reflection of the light: the n_{core} should be greater than n_{clad}. Here, the glasses under investigation were [50P_2O_5-20SrO-20CaO-10Na_2O] (labeled as Sr50) and [0.99 (50P_2O5-20SrO-20CaO-10Na_2O) – 1CeO_2 (mol %)] (labeled as Ce-1) with a refractive index at 1060 nm of 1.5261 and 1.5345, respectively. Core fibers were drawn from Sr50 and Ce-1 glasses with a diameter of (~140 ± 10) and (~110 ± 10) μm, respectively.

A core-clad fiber was drawn using Sr50 glass as the clad and the Ce-1 as the core, with a total diameter of (~140 ± 10) μm. This fiber had a numerical aperture NA of 0.16, which is similar to the NA of some of our earlier studied fibers [21]. The preparation of fiber with such large NA guarantees the proper light guiding through the core of the fiber, as confirmed by the optical image of the core-clad fiber cross-section, presented in Fig. 2. The step index difference between the core and the clad can be seen on the micrograph by the bright coloration of the core compared to that of the cladding [25]. The clad diameter was 140 μm as targeted, with a core diameter of 75 μm.

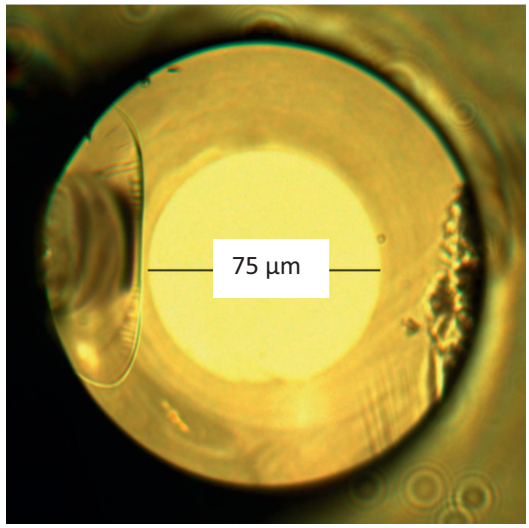

Fig. 2. Optical microscope image of the core-clad fiber cross section.

The attenuation spectra of the core fibers are shown in Fig. 3. The optical losses of the Sr50 and Ce-1 core fibers were around 20 and 10 dB/m, respectively. The lower optical losses in the Ce-1 fiber compared to that of Sr50 fiber was attributed to an increase in the network cross-linking due to the doping with CeO_2. Indeed, most of the phosphate glasses used as laser are within the metaphosphate structure and contain large amount of Al_2O_3. The aim of Al^{3+} ions in the glass is to increase the connectivity between the phosphate chains that in turn reduce the light loss [26]. The core-clad fiber was found to have similar light losses than the Ce-1 core fiber at 1.55 μm.

The core fibers (Sr50 and Ce-1) and the core-clad fiber were immersed in TRIS buffer solution for up to 42 days. The change in the fibers' mechanical properties (namely tensile strength, Young's modulus and Weibull modulus) as a function of days in TRIS are reported in Fig. 4. Prior to immersion (t = 0), the Sr50 and Ce-1 core fibers exhibit similar tensile strength at ~550 MPa indicating that the preform

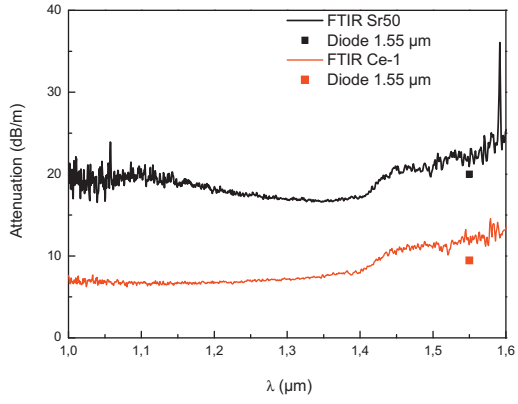

Fig. 3. Attenuation of the single core fibers, Sr50 and Ce-1.

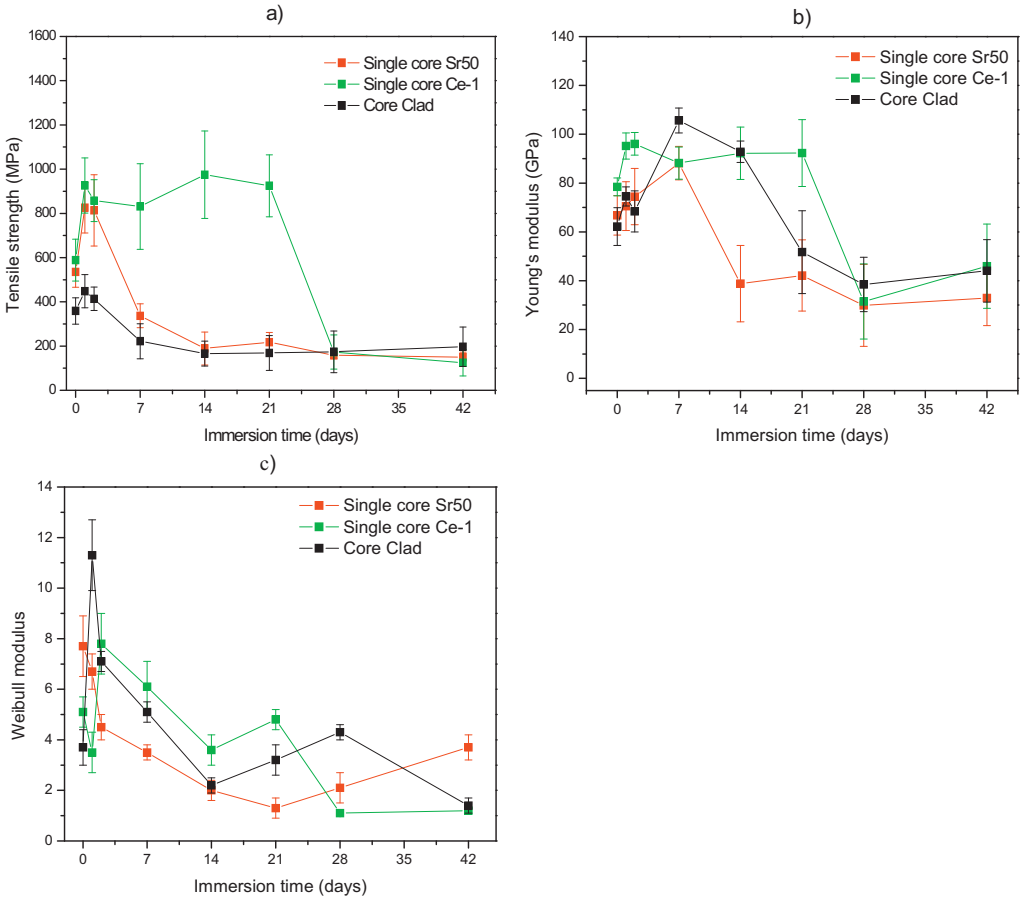

Fig. 4. a) Tensile strength, b) Young's modulus and c) Weibull modulus of single core and core-clad fibers immersed for up to 42 days in TRIS buffer solution.

processing and fiber drawing of these two glass compositions lead to similar density of surface defects (Fig. 4a). However, the core-clad fibers exhibit lower tensile strength compared to the core fibers. This can be attributed to the manufacturing process; for example, coefficient of thermal expansion mismatch between the core and the clad could cause a drop in the mechanical properties [27–29]. This is in agreement with [30]: Ahmed et al. reported on the processing of core-clad fibers obtained via extrusion. In their study, a glass with composition $50P_2O_5$-16CaO-$5Na_2O$-24MgO-$5Fe_2O_3$ (P50Fe5) was extruded together with a glass with composition $45P_2O_5$-16CaO-$10Na_2O$-24MgO-$5TiO_2$ (P45Ti5) to obtain fiber with 39–45 μm diameter. These core-clad fibers exhibited an average tensile strength of 302 ± 73 MPa and 236 ± 53 MPa when the glass P50Fe5 was used as clad (P45Ti5 as core) and core (P45Ti5 as clad) respectively. Sharmin et al. reported a tensile strength of ~526 ± 110 MPa for a fiber drawn from the P45Fe5 composition with diameter of ~20 μm [31]. This clearly indicated that the processing of core-clad fibers might negatively influence the mechanical properties of the fiber. The origin of the fibers' fracture was investigated using optical microscopy. The core and core-clad fibers were inspected and two examples of the cross-section of fibers are given in Fig. 5: (a) presents the optical microscope image of the core fiber (Ce-1) and (b) the core-clad fiber cross-section while (c) presents the SEM micrographs of the core fiber and (d) the core-clad fibers cross section post-fracture. From Fig. 5, one can see the surface fracture origin, the mirror and the hackles, as evidenced in [32]. Fig. 5b does not show the hackles as clearly as in Fig. 5a but can clearly be seen in Fig. 5d. In all cases, even for the core-clad fibers, the surface fracture origin was located at the cladding surface. No core-clad fibers were found to break at the core-clad interface. Therefore, the low mechanical properties of the core-clad fiber seen in Fig. 4, did not come from defects at the core-clad interface.

As seen in Fig. 4a, upon immersion for 2 days, an increase in tensile strength of all the fibers was observed. Such increase, upon immersion, was also evidenced in [33] and was due to the etching of the fiber surface, which reduced the amount of surface defects. At longer immersion time, a decrease in tensile strength of the Sr50 fiber was measured due to the corrosion of the fiber [34]. However, the tensile strength of the Ce-1 fiber started to decrease only after 21 days in TRIS. The delay in the decrease of the Ce-1 fiber's mechanical properties may be attributed to the presence of Ce in the Sr50 glass network, which was found to drastically reduce the glass reactivity in aqueous solution (both dissolution and precipitation of a reactive layer) as explained in [7]. The core-clad fiber exhibited similar changes in the mechanical properties than the Sr50 core fiber. However, the increase in tensile strength of the core-clad fiber during the first two days of immersion was lower compared to the Sr50 core fiber. This might be related to a high density of large defects at the core-clad fiber surface, which cannot be efficiently etched. It should be pointed out that all the fibers

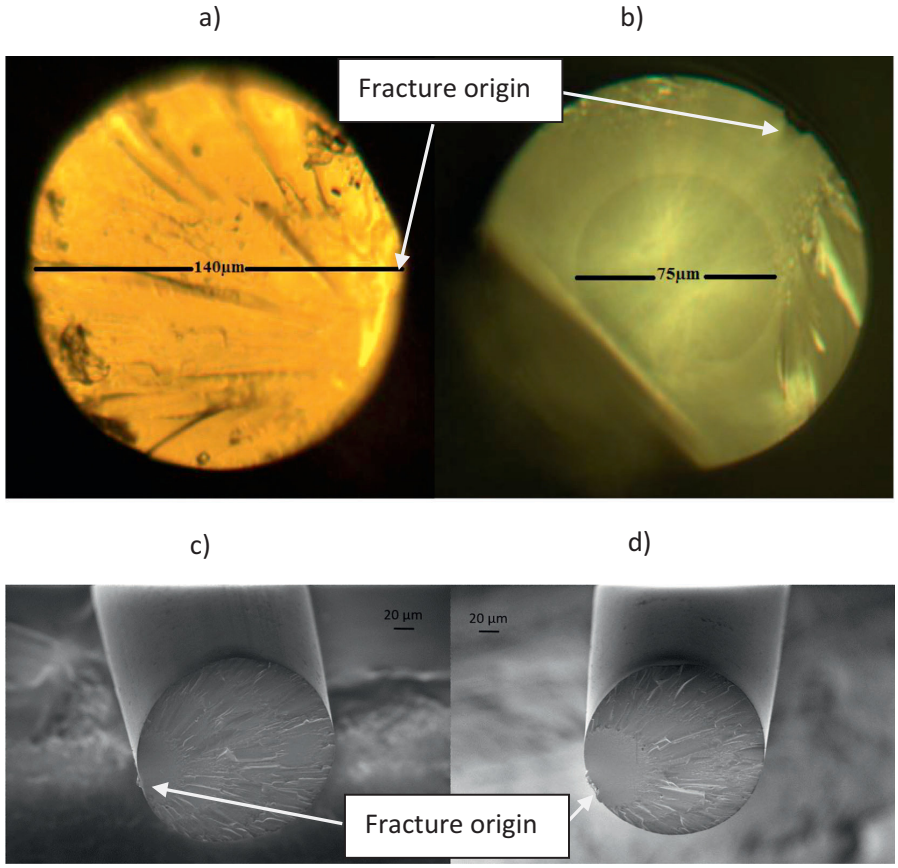

Fig. 5. Optical microscope and SEM micrograph image of the single core (Ce-1) a), c) and core-clad fiber b), d) cross section post tensile-test.

exhibited a similar tensile strength of about 150 MPa after 42 days in TRIS.

Fig. 4b presents the Young's modulus of the investigated fibers as a function of immersion time in TRIS. Initially (at t = 0), the core-clad and the Sr50 core fibers exhibit similar Young's modulus. The Ce-1 core fiber exhibits a larger Young's modulus probably due to the increase in network connectivity when adding CeO_2 in the glass network [7]. While the fibers in [33,35] were reported to maintain their Young's modulus, upon immersion in buffer solution, the investigated fibers exhibited a Young's modulus which increased initially and then decreased upon immersion in TRIS. Surprisingly, the Young's modulus of the fibers increased during the first few days in TRIS. The Young's modulus for Sr50 and the core-clad fibers exhibited a maximum after 7 days in TRIS while that of the Ce-1 fiber exhibited a maximum during 21 days in TRIS due to its slower reactivity. A similar increase in the tensile modulus post-annealing of the fibers was reported in [33] and was assigned to structural changes. It is also accepted that the mechanical properties of phosphate glasses are a function of compositional parameters (dissociation energy and packing density) and the total bonding energy [36–37]. Despite the dissolution of these glasses being considered as congruent, the surface of the fiber is expected to undergo alkaline and alkaline earth depletion as reported in [38]. The change in the fiber surface composition can lead to an initial increase in the Young's modulus. The drop in the modulus was then related to pitting and local defect formation upon selective dissolution of areas with higher reactivity.

Immersion of fibers is also known to affect the probability of early fracture and therefore the scatter in brittle fracture strength, as defined by the Weibull modulus [39]. Weibull modulus of the fibers as a function of immersion time is presented in Fig. 4c. A high modulus indicates low scatter in brittle fracture strength and, thus, a higher strength reproducibility. Both the core-clad and the Ce-1 fibers exhibited an initial rise in the Weibull modulus which then drops at longer immersion times in TRIS. The initial increase in the Weibull modulus was expected, as the etching of the fiber is expected to remove the largest surface flaws decreasing then the probability of a fiber to undergo premature breakage. This, in turn, reduces the scatter in brittle fracture strength. The decrease in the Weibull modulus of fibers immersed for longer immersion time indicated that the surface flaws started to increase, leading to fibers with early fracture (lower tensile stress) and higher scatter in brittle fracture.

In the past, it was demonstrated that the changes in the optical properties of a core bioresorbable bioactive glass fibers, upon immersion in SBF, could give information regarding the state of degradation [16]. To reveal a sensing region, the clad of the core-clad fiber was etched away. Etching was performed using 1 M phosphoric acid. Fig. 6 exhibits the reduction in diameter of the core-clad fiber as a function of etching time. The fiber diameter decreased almost linearly at a rate of 4.4 $\mu m \cdot h^{-1}$. Therefore, the clad was suspected to be completely etched away after 14.5 h. Fig. 7 presents the optical images of the cross-section of the partially etched fiber after 13 h of immersion in 1 M H_3PO_4, showing near complete removal of the clad.

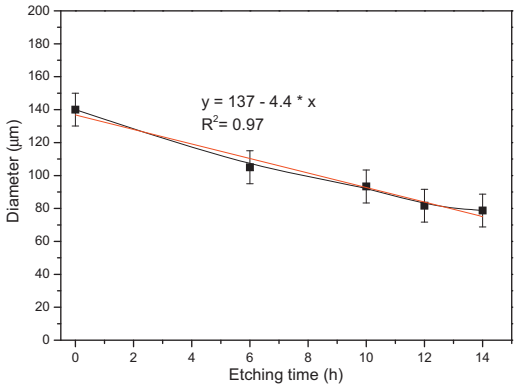

Fig. 6. Change in diameter of the core-clad fiber as a function of immersion time in 1 M H_3PO_4.

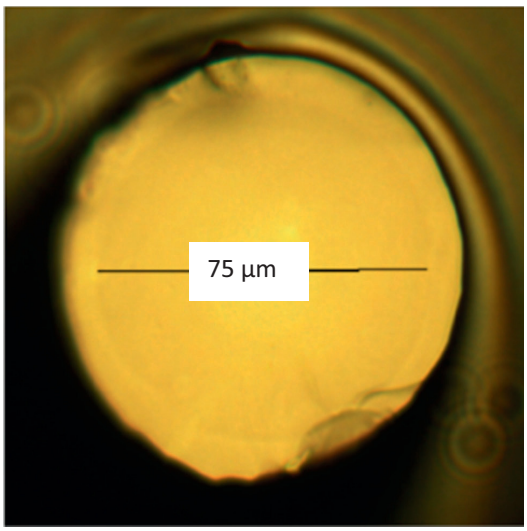

Fig. 7. Cross section of the core-clad fiber after 13 h of etching.

Etching of the fiber was suspected to have an effect on the fiber's mechanical properties as reported in [40]. Fig. 8a, depicts the tensile strength of 10 etched core-clad fibers (etching time was 14.5 h to fully remove the cladding). The fibers were not all fractured in the etched region. Fig. 8b presents a schematic of the location of the fracture origin. Out of the 10 fibers, four broke at the interface between the etched and un-etched region (Region I), four broke in the etched region (Region II) and two broke in the un-etched part (Region III). The average tensile strength was ~225 MPa, ~150 MPa and ~350 MPa, in Region I, II and III, respectively (Fig. 8a). This clearly shows that the etching of the fibers led to a decrease in the fiber mechanical properties due to an increase in flaw density, formation of surface pits, a decrease in the fiber diameter and/or an increase in the size of surface flaws. Indeed, mild etching, obtained using dissolution of the fiber in TRIS initially increased the mechanical properties (such as tensile or bending strength), while at longer dissolution time the mechanical properties decreased most likely due to an increase in the fiber roughness and/or due to the precipitation of a reactive calcium phosphate layer at the fibers' surface [40]. It is also interesting to point out that the low tensile strength of the etched fibers are similar to that of fibers immersed for

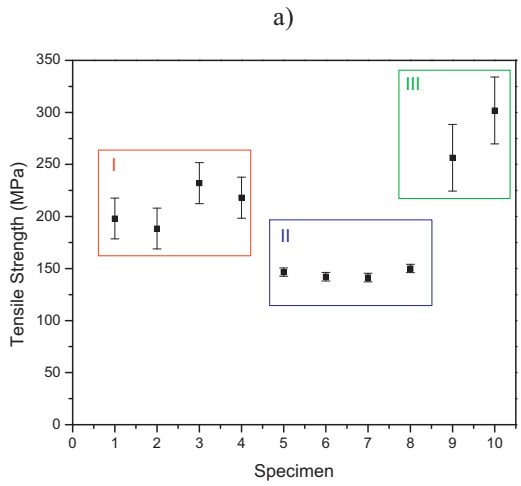

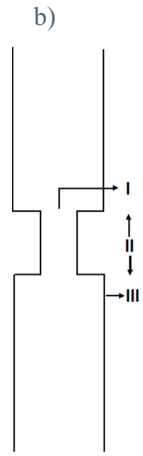

Fig. 8. a) Tensile strength of etched fibers on the basis of the region where fracture occurs, b) the different regions of fracture in the etched fiber.

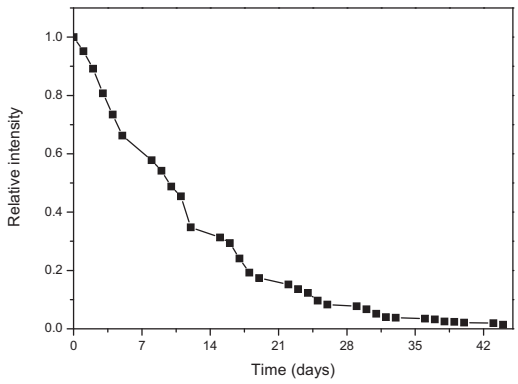

Fig. 9. Relative intensity of the output light at 680 nm through the core-clad fiber as a function of immersion time in TRIS.

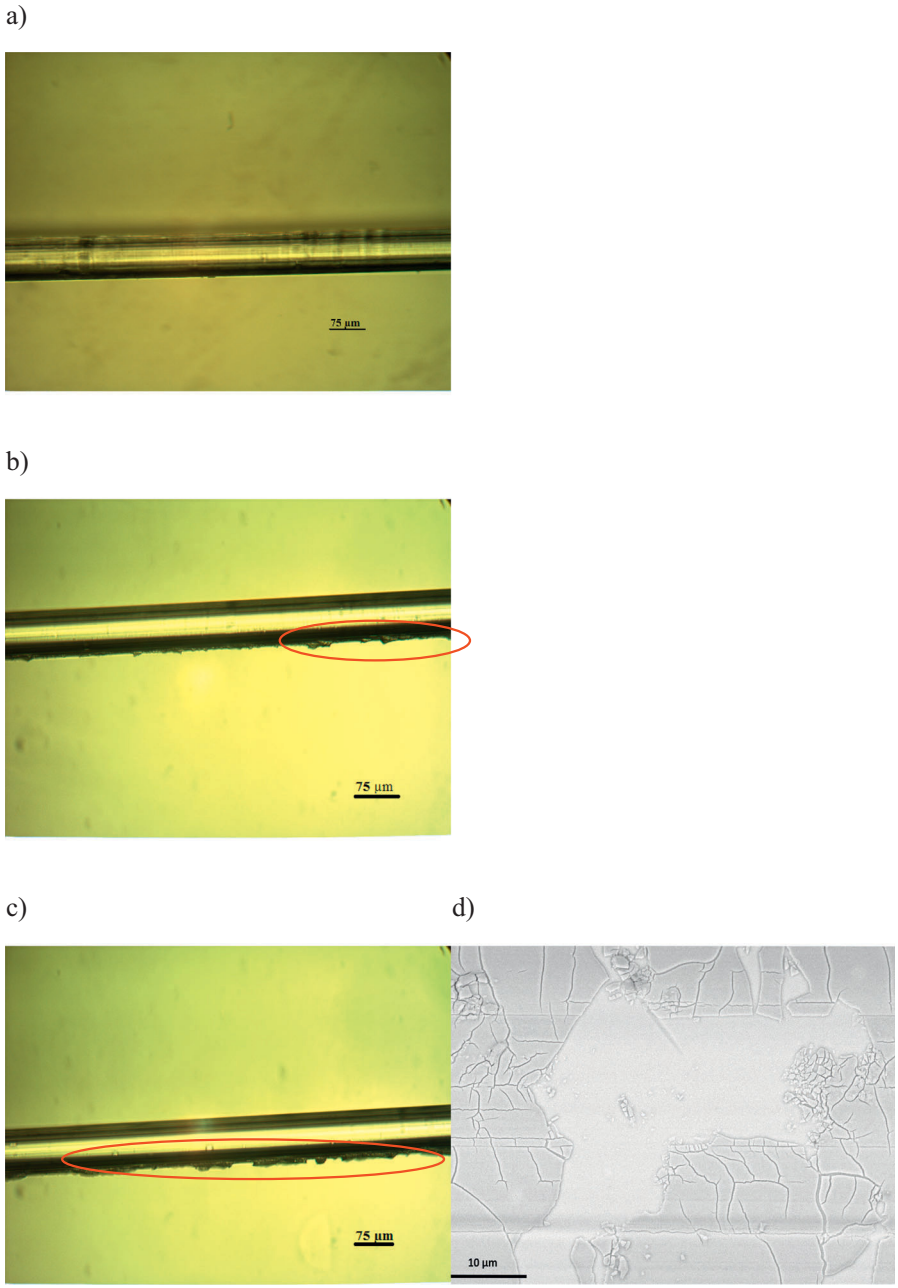

Fig. 10. Microscope images of the etched part of the core-clad fibers immersed for a) 7 days, b) 21 days and c) 42 days in TRIS and SEM image of the fiber surface at 42 days of immersion d). At 21 days surface layer starts to form (red circle). At 42 days thicker and more homogeneous reactive layer. (For interpretation of the references to colour in this figure legend, the reader is referred to the web version of this article.)

extended period of time in TRIS. This supported our hypothesis that upon significant surface etching, the increase in surface roughness and surface flaws dictate the fiber's failure.

The sensing region (5 cm) was immersed in TRIS buffer solution for up to 42 days. Fig. 9 shows the light loss through the etched portion of a core-clad fiber. A progressive reduction in the relative intensity of the output light at 680 nm of the core-clad fiber can be observed upon immersion in TRIS. Fig. 10 presents the optical micrographs of the etched fiber upon immersion for a) 7 days, b) 21 days and c) 42 days as well as the SEM image of the fiber surface upon immersion for 42 days. The rapid decrease in light intensity, during the first 14 days, was attributed to the fast initial dissolution of the glass in aqueous solutions

and a decrease in the fiber diameter. At longer immersion time, it is clear from Fig. 10(b, c and d) that a thin CaP reactive layer precipitated at the surface of the fiber, the thickness of which grew overtime leading to further increase in the light losses as discussed in [16]. When compared to our former study in [7], the layer precipitated at a slower rate when immersed in TRIS than in SBF, as SBF solution is known to be thermodynamically unstable and to lead to rapid precipitation of a reactive layer [41]. It is interesting to point out that, from SEM analysis the reactive layer was fine and not well attached to the glass surface as already shown in [20] confirming the role of the reactive layer formation on the decreased mechanical properties reported here.

4. Conclusions

Core (Sr50 and Ce-1) and core (Ce-1)-clad (Sr50) phosphate fibers were successfully drawn into fibers. The tensile strength of the core-clad fibers was lower compared to that of the core and was assigned to an increase in the density of the core-clad fiber surface defects surface of the fiber. Upon immersion in TRIS for 2 days, all the fibers exhibited an increase in mechanical properties (tensile strength, Young's modulus and Weibull modulus) due to the etching of the fibers' surface and a subsequent decrease in the density of surface defects. At longer immersion, the mechanical properties of the fibers dropped due to the dissolution/reaction of the glass with the aqueous media. The drop in mechanical properties of the fibers was delayed by the presence of CeO_2. The change in the mechanical properties of the core-clad fibers followed a similar trend than the Sr50 core fiber. With this study, we show that the change in mechanical properties upon immersion in TRIS is dictated by the cladding surface reaction with the medium rather than the fiber geometry. This core-clad fiber exhibited good light transmission and the change in light transmission was assessed upon immersion in TRIS. The clad of the core-clad fiber was etched in phosphoric acid to reveal the core. Such process led to a decrease of the fiber mechanical properties. Upon immersion, for 10 days in TRIS, a drop of 50% of the initial light intensity was recorded.

Owing to the ability to guide light effectively and to maintain decent tensile strength in vitro (~ 150–200 MPa after 6 wks in TRIS), this fiber looks promising for future use as a biosensing device in vivo.

Acknowledgement

The authors would like to acknowledge the financial support of the Academy of Finland through the Academy Research Fellow grant (275427), the Initial and follow-on funding for research costs (284492 and 312634) and Competitive Funding to Strengthen University Research Profiles (310359).

References

[1] L.L. Hench, R.J. Splinter, W.C. Allen, T.K. Greenlee, Bonding mechanisms at the interface of ceramic prosthetic materials, J. Biomed. Mater. Res. 2 (1) (1971) 117–141.
[2] S. Fagerlund, J. Massera, L. Hupa, M. Hupa, T-T-T behaviour of bioactive glasses 1–98 and 13–93, J. Eur. Ceram. Soc. 32 (11) (2012) 2731–2738.
[3] J. Massera, S. Fagerlund, L. Hupa, M. Hupa, Crystallization behavior of the commercial bioactive glasses 45S5 and S53P4, J. Am. Ceram. Soc. 95 (2012) 607–613.
[4] B.C. Bunker, G.W. Arnold, J.A. Wilder, Phosphate glass dissolution in aqueous solutions, J. Non-Cryst. Solids 64 (3) (1984) 291–316.
[5] A. Mishra, J. Rocherullé, J. Massera, Ag-doped phosphate bioactive glasses: thermal, structural and in-vitro dissolution properties, Biomed. Glasses 2 (2016) 38–48.
[6] J. Massera, Y. Shpotyuk, F. Sabatier, T. Jouan, C. Boussard-Plédel, C. Roiland, B. Bureau, L. Petit, N. Boetti, D. Milanese, L. Hupa, Processing and characterization of novel borophosphate glasses and fibers for medical applications, J. Non-Cryst. Solids 425 (2015) 52–60.
[7] J. Massera, M. Vassallo-Breillot, B. Törngren, B. Glorieux, L. Hupa, Effect of CeO_2 doping on thermal, optical, structural and in vitro properties of a phosphate based bioactive glass, J. Non-Cryst. Solids 402 (2014) 28–35.
[8] E.A. Abou Neel, D.M. Pickup, S.P. Valappil, R.J. Newport, J.C. Knowles, Bioactive functional materials: a perspective on phosphate-based glasses, J. Mater. Chem. 19 (2009) 690–701.
[9] R. Colquhoun, K.E. Tanner, Mechanical behaviour of degradable phosphate glass fibres and composites-a review, Biomed. Mater. 11 (2015) 014105.
[10] J. Clement, J.M. Manero, J.A. Planell, Analysis of the structural changes of a phosphate glass during its dissolution in simulated body fluid, J. Mater. Sci. Mater. Med. 10 (1999) 729–732.
[11] J.C. Knowles, Phosphate based glasses for biomedical applications, J. Mater. Chem. 13 (2003) 2395–2401.
[12] M.A. De Diego, N.J. Coleman, L.L. Hench, Tensile properties of bioactive fibers for tissue engineering applications, J. Biomed. Mater. Res. A 53 (2000) 199–203.
[13] J. Choueka, J.L. Charvert, H. Alexander, Y.H. Oh, G. Joseph, N.C. Blumenthal, W.C. LaCourse, Effect of annealing temperature on the degradation of reinforcing fibers for absorbable implants, J. Biomed. Mater. Res. 29 (1995) 1309–1315.
[14] I. Ahmed, M. Lewis, I. Olsen, J.C. Knowles, Phosphate glasses for tissue engineering: part 1. Processing and characterisation of a ternary-based P_2O_5-CaO-Na_2O glass system, Biomaterials 25 (2004) 491–499.
[15] B. Gholamzadeh, H. Nobovati, Fiber Optic Sensors, 18 World of Academy of Science, Engineering Technology, 2008, pp. 297–307.
[16] J. Massera, I. Ahmed, L. Petit, V. Aallos, L. Hupa, Phosphate-based glass fiber vs. bulk glass: change in fiber optical response to probe in vitro glass reactivity, Mater. Sci. Eng. C 37 (2014) 251–257.
[17] V.P. Gapontsev, S.M. Matitsin, A.A. Isineev, V.B. Kravchenko, Erbium glass lasers and their applications, Opt. Laser Technol. 14 (4) (1982) 189–196.
[18] S. Jiang, M.J. Myers, N. Peyghambarian, Er^{3+} doped phosphate glasses and lasers, J. Non-Cryst. Solids 239 (1998) 143–148.
[19] D. Pugliese, N.G. Boetti, J. Lousteau, E. Ceci-Ginistrelli, E. Bertone, F. Geobaldo, D. Milanese, Concentration quenching in an Er-doped phosphate glass for compact optical lasers and amplifiers, J. Alloys Compd. 657 (2016) 678–683.
[20] J. Massera, A. Kokkari, T. Narhi, L. Hupa, The influence of SrO and CaO in silicate and phosphate bioactive glasses on human gingival fibroblasts, J. Mater. Sci. Mater. Med. 26 (2015) 196.
[21] J. Massera, A. Haldeman, D. Milanese, H. Gebavi, M. Ferraris, P. Foy, W. Hawkins, J. Ballato, R. Stolen, L. Petit, K. Richardson, Processing and characterization of core–clad tellurite glass preforms and fibers fabricated by rotational casting, Opt. Mater. 32 (2010) 582–588.
[22] M. Curie, A. Lepape, Conductibilité thermique des gaz rares, J. Phys. Radium 2 (1931) 392–397.
[23] E. Pirhonen, L. Moimas, M. Brink, Mechanical properties of bioactive glass 9–93 fibres, Acta Biomater. 2 (2006) 103–107.
[24] E. Pirhonen, H. Niiranen, T. Niemelä, M. Brink, P. Törmälä, Manufacturing, mechanical characterization, and in vitro performance of bioactive glass 13–93 fibers, J Biomed Mater Res B Appl Biomater 77B (2006) 227–233.
[25] N. Syam Prasad, J. Wang, R.K. Pattnaik, H. Jain, J. Toulouse, Preform fabrication and drawing of KNbO3 modified tellurite glass fibers, J. Non-Cryst. Solids 352 (2006) 519–523.
[26] J.H. Campbell, T.I. Suratwala, Nd-doped phosphate glasses for high-energy/high-peak-power lasers, J. Non-Cryst. Solids 263–264 (2000) 318–341.
[27] G.W. Sherer, A.R. Cooper, Thermal stresses in clad-glass fibers, J. Am. Ceram. Soc. 63 (1980) 346–347.
[28] D.A. Krohn, A.R. Cooper, Strengthening of glass fibers: I, cladding, J. Am. Ceram. Soc. 52 (1969) 661–664.
[29] U.C. Paek, C.R. Kurkijan, Calculation of cooling rate and induced stresses in drawing of optical fibers, J. Am. Ceram. Soc. 58 (1975) 330–335.
[30] I. Ahmed, S.S. Shaharuddin, N. Sharmin, D. Furniss, C. Rudd, Core/clad phosphate glass fibres containing iron and/or titanium, Biomed. Glasses 1 (2015) 20–30.
[31] N. Sharmin, C.D. Rudd, A.J. Parsons, I. Ahmed, Structure, viscosity and fibre drawing properties of phosphate-based glasses: effect of boron and iron oxide addition, J. Mater. Sci. 51 (2016) 7523–7535.
[32] P.K. Gupta, Fractography of fiberglass, in: R.C. Bradt, R.E. Tressler (Eds.), Fractography of Glass, Springer, Boston MA, 1994, pp. 185–206.
[33] S. Cozien-Cazuc, A. Parsons, G. Walker, I. Jones, C. Rudd, Effects of aqueous aging on the mechanical properties of P40Na20Ca16Mg24 phosphate glass fibres, J. Mater. Sci. 43 (14) (2008) 4834–4839.
[34] R. Colquhoun, K.E. Tanner, Mechanical behaviour of degradable phosphate glass fibres and composites—a review, Biomed. Mater. 11 (2016) 014105.
[35] P. Haque, I. Ahmed, A. Parsons, R. Felfel, G. Walker, C. Rudd, Degradation properties and microstructural analysis of $40P_2O_5$–24MgO–16CaO–$16Na_2O$–$4Fe_2O_3$ phosphate glass fibres, J. Non-Cryst. Solids 375 (2013) 99–109.
[36] S. Inaba, S. Fujino, K. Morinaga, Young's modulus and compositional parameters of oxide glasses, J. Am. Ceram. Soc. 82 (1999) 3501–3507.
[37] L.G. Baikova, V.P. Pukh, Y.K. Fedorov, A.B. Sinani, L.V. Tikhonova, M.F. Kireenko, Mechanical properties of phosphate glasses as a function of the total bonding energy per unit volume of glass, Glas. Phys. Chem. 34 (2008) 126–131.
[38] J. Massera, A. Mishra, S. Guastella, S. Ferraris, E. Verné, Surface functionalization of phosphate-based bioactive glasses with 3-aminopropyltriethoxysilane (APTS), Biomed. Glasses 2 (2016) 51–62.
[39] W. Weibull, A statistical distribution of wide applicability, J. Appl. Mech. 18 (1951) 293–297.
[40] C.R. Kurkijan, M.J. Matthewson, J.M. Rooney, Effects of heat treatment and HF etching on the strength of silica lightguides, Proc. SPIE Int. Soc. Opt. Eng. 5465 (September 2004).
[41] M. Bohner, J. Lemaitre, Can bioactivity be tested in vitro with SBF solution? Biomaterials 30 (2009) 2175–2179.

UNPUBLISHED MANUSCRIPT

Surface modified phosphate glasses for improved protein adsorption and cell viability

A. Mishra*, L. Azizi*, C. Palma*, N. B. Huynh, R. Rahikainen, P. Turkki, A. S. Ribiero, V. P. Hytönen, J. Massera

*authors contributed equally